

https://dspace.org/

Reinforcement of synthetic rubber with carbon nanoballs to produce nanocomposite ion exchange membrane

Nyemba, Lloyd Elliott Nyasha

2011-10-21
http://hdl.handle.net/10539/10627

Downloaded from a DSpace repository. https://dspace.org/

REINFORCEMENT OF SYNTHETIC RUBBER WITH CARBON NANOBALLS TO PRODUCE NANOCOMPOSITE ION EXCHANGE MEMBRANE

Lloyd Elliott Nyasha Nyemba

A dissertation submitted to the Faculty of Engineering and the Built Environment, University of the Witwatersrand, in fulfillment of the requirements for the degree of Master of Science in Engineering

Johannesburg, 2010

DECLARATION

I declare that this dissertation is my own unaided work. It is being submitted to the Degree of Master of Science in Engineering to the University of the Witwatersrand, Johannesburg. It has not been submitted before for any degree or examination to any other University.

…….

Signature of Candidate

…….day of……..year……

ABSTRACT

The research was aimed at improving the mechanical properties of locally synthesised styrene butadiene rubber ion exchange membrane through blending with locally synthesised carbon nanoballs. Emulsified styrene butadiene rubber was sulphonated to 44% DS by chilled 0.09M $ClSO_3H$. Pure and uniform carbon nanoballs of 60nm diameter were synthesized through a Non Catalytic Chemical Vapour Deposition method using a 16mm diameter reactor, acetylene as the carbon source and argon as the carrier gas at 1000°C. Homogeneous blending was achieved using a Probe Ultrasonicator at 60% amplitude to produce a 160μm thick nanocomposite ion exchange membrane. Weight concentrations varying from 0.25 to 4wt%CNB were added to the sulphonated styrene butadiene rubber in solution. The blends were cast using the evaporative technique and dried partly by vacuum oven and finally r.t.p conditions. Mechanical testing was done using Hysitron Nanotensile5000 Tester to evaluate the effects of blending. Tensile strength, σ_s, increased linearly (2 - 3.88MPa) with carbon nanoball volume fraction (V_f), achieving a maximum improvement of 94% at 14.2% V_f. The Young's modulus, E increased as a power function of V_f, reaching a maximum of 79% (13.71 – 24.58MPa) improvement at 3.3% V_f and decreasing gently afterwards due to agglomeration. The fracture toughness, $U_{f.t}$ increased as a power function of V_f up to a maximum improvement of 215% (0.84 – 2.65MPa) at 14.2% V_f. Strain, e increased by a maximum of 63% (0.68 – 1.11) at 14.2% V_f. Higher ultrasonication amplitudes achieved superior dispersion effectiveness as compared to lower amplitudes. The nanofiller addition also significantly reduced degradation of mechanical properties with time. Below a critical nanofiller volume fraction, V_c, related to the fractional free volume of the polymer matrix, the E profile was consistent with existing models by Guth and Thomas. The only difference was in the coefficients of V_f, which was attributed to the higher mechanical properties of carbon nanoballs. Beyond V_c, agglomeration distorted the profile. The tensile strength profile for the well dispersed carbon nanoballs was

different from the existing models by Nicolais and Narkis and Nielsen. However, the profile for the poorly dispersed carbon nanoballs was similar to existing models. Prediction of mechanical properties of synthetic rubber nanocomposites based on nanofiller volume fraction was also feasible. It was concluded that the addition of [1-14vol% *(1-4wt%)*] carbon nanoballs improved the mechanical properties by a margin between 79% and 369%. Further work on dispersion improvement was shown to have the potential to increase the mechanical properties by up to 700%.

DEDICATION

I dedicate this work to my wife Mercy and our son Tinokunda as well as Rehoboth Bumberharvest World Ministry (RBWM), which is the love of our heart and reason for our existence.

ACKNOWLEDGEMENTS

I would like to thank AMSEN for granting me this blessed opportunity to advance and unleash my potential in Materials Engineering through their financial support for both the research work as well as my well being. The University of the Witwatersrand is worth appreciating for their financial assistance for my studies through the Postgraduate Merit Award. I also thank my supervisors, Professors Sunny Iyuke and Frank Kavishe for their intellectual guidance, direction and motivation throughout the research work. Doctor Clarence Yah is also worth mentioning for his intellectual support and guidance. I also thank fellow postgraduate students, with special mention going to the Nanotechnology Research Group. I also thank the School of Chemical and Metallurgical Engineering, the DST/NRF Centre of Excellence in Strong Materials and their staff, the School of Chemistry, the Biology Microscopy Unit and the Pharmacy Department of the Medical School and their staff for their support and laboratory facilities. In this regard, special mention goes to Professor Lesley Cornish, Professor Neil Coville, Professor Viness Pillay, Professor Mike Witcomb, Abe, Bruce and Doctor. Professor Viness Pillay and Deane are most appreciated for their assistance with nanotensile testing. I am grateful to Professor Christo Pienaar and Karbochem (Pty) Ltd for the donation of the synthetic rubber.

Last but not least, special appreciation goes to my lovely wife, the blessed gift from God for the priceless dimensionless support throughout and our son Tinokunda for the great refreshment and unique inspiration. All the glory and honour and thanksgiving be to my God forever in Jesus Name.

TABLE OF CONTENTS

DECLARATION ..... **II**

ABSTRACT ..... **III**

DEDICATION ..... **V**

ACKNOWLEDGEMENTS ..... **VI**

TABLE OF CONTENTS ..... **VII**

LIST OF TABLES ..... **XIX**

LIST OF ABBREVIATIONS AND SYMBOLS ..... **XXII**

CHAPTER 1: INTRODUCTION **1**

1.0 INTRODUCTION **1**

1.1 BACKGROUND **1**

1.2 MOTIVATION **2**

1.3 RESEARCH PROBLEM: NANOCOMPOSITE ION EXCHANGE MEMBRANE CHALLENGES **3**

1.3.1 PROBLEM STATEMENT 5

1.3.2 RESEARCH QUESTIONS 5

1.3.3 EXPECTED RESEARCH OUTCOMES AND CONTRIBUTIONS 6

1.4 AIM **7**

1.4.1 OBJECTIVES 7

1.4.2 HYPOTHESIS 8

1.5 SCOPE OF RESEARCH 8

1.6 ORGANIZATION OF DISSERTATION 8

CHAPTER 2: LITERATURE REVIEW 10

2.1 ION EXCHANGE MEMBRANE (IEM) OVERVIEW 10

2.1.1 DEFINITION OF ION EXCHANGE MEMBRANE 10

2.1.2 APPLICATION OF ION EXCHANGE MEMBRANES 11

2.1.3 PROPERTIES OF ION EXCHANGE MEMBRANES 13

2.2 POLYMERIC MEMBRANES 13

2.2.1 TYPES OF POLYMERIC MEMBRANES 14

2.3 FUNCTIONALISATION OF POLYMERS TO PRODUCE ION EXCHANGE MEMBRANES 16

2.3.1 SULPHONATION OF POLYMERS 17

2.3.1.1 Sulphonation methods 18

2.3.1.2 Sulphonating agents 19

2.3.1.3 Challenges to styrenic polymer sulphonation 20

2.4 MODIFICATION OF SULPHONATED SYNTHETIC RUBBER MEMBRANES 21

2.4.1 POLYMER NANOCOMPOSITE MEMBRANES 22

2.4.2 NANOFILLERS FOR NANOCOMPOSITE MEMBRANES 23

2.4.2.1 Classification and size dimension 23

2.4.2.2 Nanomaterials for polymer nanocomposites 24

2.4.3 CARBON NANOBALLS 26

2.4.3.1 What are carbon nanoballs (nanospheres 27

2.4.3.2 Categorisation of carbon nanoballs 27

2.4.3.3 Synthesis of Carbon Nanoballs 28

Chemical Vapour Deposition (CVD) method 29

2.4.3.4 Carbon ball morphology and formation mechanisms 31

2.4.3.5 Properties of carbon nanoballs 34

2.4.4 BLENDING TECHNOLOGIES 36

2.4.4.1 Solution processing 37

2.4.4.2 The sol–gel method 37

2.4.4.3 Melt processing 37

2.4.4.4 In-situ polymerization 38

2.4.4.5 Comparison of dispersion techniques for nanoparticles 38

2.4.4.6 Challenges to polymer matrix- nanoparticle blending 39

2.5 MECHANICAL PROPERTIES OF ION EXCHANGE MEMBRANES 40

2.5.1 MEASURES OF MECHANICAL PROPERTIES OF POLYMERIC MATERIALS 41

2.5.1.1 Stability measures (Elasticity and Stiffness measures) 42

2.5.1.2 Mechanical strength measures 43

2.5.1.3 Ductility measures 44

2.5.1.4 Hardness measure (MPa) *45*

2.5.1.5 Endurance measures *45*

2.5.2 REINFORCEMENT MECHANISMS 46

2.5.2.1 Bonding of particles in materials *47*

Secondary bonds 48

2.5.2.2 Relationship between types of bonding and mechanical properties *49*

2.5.2.3 Mechanisms of reinforcement in polymer nanocomposites *50*

2.5.2.4 Failure mechanisms in membranes *53*

2.5.2.5 Models of reinforcement *53*

2.5.2.6 Comparison of theoretical models and experimental trends *55*

CHAPTER 3: MATERIALS AND METHODS 58

3. EXPERIMENTAL PROCEDURES FOR REINFORCEMENT EVALUATION 58

3.1 NON CATALYTIC SYNTHESIS OF CARBON NANOBALLS 58

3.1.1 CHARACTERIZATION OF CARBON NANOPARTICLES 60

3.1.1.1 Morphology of carbon nanoballs (TEM Analysis) *60*

3.1.1.2 BET surface area analysis and porosity analysis *61*

3.1.1.3 Thermogravimetric analysis (TGA) *61*

3.1.1.4 Raman spectroscopy *61*

3.2 SULPHONATION OF STYRENE BUTADIENE RUBBER 61

3.2.1 CHARACTERISATION OF SULPHONATED STYRENE BUTADIENE RUBBER (SSBR) 63

3.2.1.1 Determination of Ion Exchange Capacity (IEC) 63

3.2.1.2 Fourier Transform Infrared (FT- IR) Spectroscopy 64

3.2.1.3 Thermal stability of sulphonated styrene butadiene rubber 65

3.3 PRODUCTION OF NANOCOMPOSITE ION EXCHANGE MEMBRANE 65

3.3.1 PREPARATION OF SSBR MEMBRANE FILMS 65

3.3.2 REINFORCEMENT OF SSBR WITH CARBON NANOBALLS 66

3.3.3 MORPHOLOGY OF THE ION EXCHANGE MEMBRANE 68

3.4 MECHANICAL CHARACTERISATION 68

3.4.1 SAMPLE PREPARATION FOR TENSILE TESTING 69

3.4.2 MECHANICAL TESTING 69

3.4.3 REINFORCEMENT PROPERTY EVALUATION 71

CHAPTER 4: RESULTS AND DISCUSSION 73

4.1 CARBON NANOBALL SYNTHESIS 73

4.1.1 CONDITIONS OF SYNTHESIS OF CARBON NANOBALLS 73

4.1.2 MORPHOLOGY OF CARBON NANOPARTICLES 75

4.1.3 FACTORS AFFECTING CARBON BALL SIZE 77

4.1.3.1 Effect of acetylene flow ratio (η_{AC}) on carbon ball diameter (Φ_{CB}) 78

4.1.3.2 Effect of reactor diameter (Φ_R) on carbon ball diameter 85

4.1.4 Effect of production conditions on productivity 88

4.1.4.1 Effect of acetylene flow ratio on production rate 90

4.1.4.2 Effect of acetylene flow ratio on yield 90

4.1.4.2 Effect of acetylene flow ratio on purity 92

4.1.4.3 Challenges to productivity using the NCCVD equipment 93

4.1.5 Optimum region for carbon nanoball production 93

4.1.6 Thermal stability of the carbon nanoballs 94

4.1.7 Electron conductivity properties of the carbon nanoball 96

4.1.8 Porosity and density of carbon nanoballs 97

4.2 SULPHONATION OF STYRENE BUTADIENE RUBBER, BLENDING AND CASTING 99

4.2.1 Sulphonation of emulsified styrene butadiene rubber 99

4.2.1.1 Effect of chlorosulphonic acid concentration on sulphonation 99

4.2.1.2 Causes of polymer degradation 103

4.2.1.3 Optimum sulphonation of styrene butadiene rubber 105

4.2.1.4 FTIR analysis of sulphonated styrene butadiene rubber 106

4.2.2 Blending and production of membrane films 108

4.2.3 Characterisation of SSBR nanocomposite Ion Exchange Membrane 112

4.2.3.1 FTIR analysis of sulphonated nanocomposite IEM 112

4.2.3.2 Thermal stability of nanocomposite IEM 113

4.3 MECHANICAL TESTING OF SSBR NANOCOMPOSITE IEM 115

4.3.1 EFFECT OF CNB VOLUME FRACTION ON MECHANICAL PROPERTIES OF SSBR IEM 115

4.3.1.1 Effect of CNB volume fraction on mechanical stability of nanocomposite IEM 117

43.1.2 Effect of CNB volume fraction on the mechanical strength of nanocomposite IEM 118

4.3.1.3 Effect of CNB volume fraction on ductility of nanocomposite IEM 120

4.3.1.4 Effect of CNB volume fraction on fatigue strength of SSBR IEM 121

4.3.1.5 Overall reinforcement effect of CNBs on mechanical properties of SSBR IEM 122

4.3.2 EFFECT OF BLENDING CONDITIONS ON MECHANICAL PROPERTIES OF NANOCOMPOSITE IEM..... 124

4.3.2.1 Optimisation of ultrasonication conditions for SSBR reinforcement..... 126

4.3.3 EFFECT OF TIME (AGE) ON MECHANICAL PROPERTIES OF NANOCOMPOSITE IEM 127

4.3.4 COMPARISON OF THE EXPERIMENTAL RESULTS WITH EXISTING MODELS..... 130

4.3.4.1 Comparison of experimental E with existing models 130

Validity of the experimental relationship with E 132

Relationship between fractional free volume of matrix and E_{max} for nanocomposite IEM 134

4.3.4.2 Comparison of experimental profile for tensile strength with existing models 136

Relationship between tensile strength and CNB volume fraction 138

4.3.4.3 Relationship between fracture toughness and CNB volume fraction 139

4.3.5 PROPOSED MECHANISM FOR REINFORCEMENT OF SSBR WITH CARBON NANOBALLS..... 140

4.3.5.1 Mechanism for improvement of Young's modulus 141

CHAPTER 5: CONCLUSIONS AND RECOMMENDATIONS **148**

5.1 CONCLUSIONS **148**

5.1.1 CARBON NANOBALL SYNTHESIS 148

5.1.2 SYNTHETIC RUBBER SULPHONATION AND BLENDING 149

5.1.3 REINFORCEMENT EFFECTS OF CARBON NANOBALLS ON SSBR ION EXCHANGE MEMBRANE 149

5.2 RECOMMENDATIONS **152**

5.2.1 CARBON NANOBALL SYNTHESIS 152

5.2.2 SYNTHETIC RUBBER FUNCTIONALISATION, BLENDING AND CASTING 152

5.2.3 REINFORCEMENT OF SYNTHETIC RUBBER WITH CARBON NANOBALLS 153

REFERENCES **154**

APPENDICES **171**

APPENDIX 1 ..... **171**

APPENDIX 2 ..... **176**

APPENDIX 3 ..... **179**

APPENDIX 4 ..... **180**

LIST OF FIGURES

FIGURE 2.1: STYRENE BUTADIENE REVERSIBLE SULPHONATION REACTION EQUATION 18

FIGURE 2.2: NANOMATERIAL SHAPES 24

FIGURE 2. 3: CARBON NANOBALLS; A) RANDOM; B) RADIAL; C) CONCENTRIC; D) FULLERENES (C_{60} AND C_{70})..... 28

FIGURE 2.4: CARBON BALL GROWTH MECHANISMS 33

FIGURE 2. 5: GRAPHICAL REPRESENTATION OF MECHANICAL PROPERTY MEASURES 42

FIGURE 3.1: SCHEMATIC PRESENTATION OF NCCVD REACTOR FOR CARBON NANOBALLS SYNTHESIS 59

FIGURE 3.2: SULPHONATION APPARATUS FOR STYRENE BUTADIENE RUBBER 63

FIGURE 3.3: TENSILE TESTING SAMPLE PREPARATION 69

FIGURE 3.4: TENSILE TEST SPECIMEN LOADED ONTO THE HYSITRON NANOTENSILE 5000 MACHINE 71

FIGURE 4.1: TEM IMAGES OF CNBS PRODUCED AT 1000^0C; A) PURE AND UNIFORM AND B) POROUS CNBS 75

FIGURE 4.2: TEM IMAGES A) HIGHLY UNIFORM AND PURE CNB (NARROW VARIATION) FROM 16MM Φ REACTOR; B) LESS UNIFORMLY DISTRIBUTED AND PURE CARBON NANOBALLS (WIDER VARIATION) FROM 22MM Φ REACTOR 76

FIGURE 4.3: TEM IMAGES; A) IMPURE CARBON NANOBALLS, COVERED IN CARBONACEOUS MATERIALS, COLLECTED FROM THE REACTOR; B) PURE CNBS SHOWING RARE CNBS OF 10NM Φ. 76

FIGURE 4.4: TEM IMAGES; A) HIGH MAGNIFICATION TEM SHOWING SPHERICAL CNBS; B) COMMONLY OBSERVED AGGLOMERATION OF THE FORMED CNBS 77

FIGURE 4.5: EFFECT OF REACTOR DIAMETER ON CARBON NANOBALL PRODUCTION..... 78

FIGURE 4.6: EFFECT OF ACETYLENE FLOW RATIO ON CARBON BALL DIAMETER 79

FIGURE 4.7: FLOW RATIO CONDITIONS FOR CARBON NANOBALL PRODUCTION..... 80

FIGURE 4.8: MODEL FOR CARBON BALL COMPRISING THE CONCENTRIC LAYERS OF CARBON 81

FIGURE 4.9: LIMITING ACETYLENE FLOW RATIO FOR CNB PRODUCTION 86

FIGURE 4.10: EFFECT OF REACTOR DIAMETER ON CNB PRODUCTION RANGE 86

FIGURE 4.11: EFFECT OF REACTOR DIAMETER ON MINIMUM CNB DIAMETER 87

FIGURE 4.12: EFFECT OF ACETYLENE FLOW RATIO ON PRODUCTION RATE 90

FIGURE 4.13: EFFECT OF ACETYLENE FLOW RATIO ON YIELD 91

FIGURE 4.14: EFFECT OF ACETYLENE FLOW RATIO ON PURITY OF CARBON BALLS 92

FIGURE 4.15: EFFECT OF ACETYLENE FLOW RATIO ON PURITY OF CARBON BALLS 94

FIGURE 4.16: THERMAL STABILITY OF 60NM CARBON NANOBALLS PRODUCED IN 16MM Φ, AT 0.82 H_{AC} AND 1000^{o}C (SAMPLE COLLECTED FROM CYCLONE). 95

FIGURE 4.17: RAMAN SPECTRA OF 60NM CARBON NANOBALLS FORM 16MM Φ REACTOR 97

FIGURE 4.18: EFFECT OF $ClSO_3H$ CONCENTRATION ON YIELD AND EFFICIENCY OF SULPHONATION 102

FIGURE 4.19: FTIR OF PURE SSBR, SSBR AND DEGRADED SSBR AT DIFFERENT CONCENTRATIONS. 104

FIGURE 4.20: SEM IMAGE OF 44% DS SSBR AT 0.09M CSA AND 1.12 MOLAR RATIO 106

FIGURE 4.21: FTIR OF SSBR MEMBRANES SULPHONATED BY 0.09M CSA AT DIFFERENT MOLAR VOLUMES 107

FIGURE 4.22: SEM IMAGES OF 160MM THICK MEMBRANES, BLENDED AT 20% AMPLITUDE, 3 HRS SONICATION TIME AT 200W POWER. A) 2.5WT% CNB LOADING B) 4 WT % CNB LOADING 108

FIGURE 4.23: SEM IMAGES OF 160MM THICK MEMBRANE A) 4WT% CNB LOADED IEM AT 20% SONICATION AMPLITUDE; B) HOMOGENEOUS 1WT% CNB LOADED IEM AT 60% SONICATION AMPLITUDE 109

FIGURE 4.24: SEM IMAGE OF 160MM THICK MEMBRANE, A) 2.5WT% CNB LOADED IEM AT 60% SONICATION AMPLITUDE; B) 4WT% CNB LOADED IEM AT 60% SONICATION AMPLITUDE 110

FIGURE 4.25: EFFECT OF AMPLITUDE OF SONICATION AND FILLER WEIGHT FRACTION ON DISPERSION EFFECTIVENESS... 110

FIGURE 4.26: FTIR OF NANOCOMPOSITE IEM AT DIFFERENT WT% CNB LOADING 113

FIGURE 4.27: THERMAL STABILITY OF SSBR NANOCOMPOSITE IEM 114

FIGURE 4.28: EFFECT OF NANOFILLER VOLUME FRACTION, V_F ON; A) YOUNG'S MODULUS, E (STIFFNESS). B) ISOTROPY118

FIGURE 4.29: EFFECT OF CNB VOLUME FRACTION ON; A) TENSILE STRENGTH, Σ_S; B) YIELD STRENGTH, Σ_Y..... 119

FIGURE 4.30: EFFECT OF CNB V_F ON; A) ENGINEERING STRAIN; B) FRACTURE TOUGHNESS OF SSBR IEM 120

FIGURE 4.31: EFFECT OF CNB WT% ON FATIGUE STRENGTH 121

FIGURE 4.32: OVERALL REINFORCEMENT EFFECT OF CARBON NANOBALLS 123

FIGURE 4.33: EFFECT OF AMPLITUDE OF SONICATION ON; A) YIELD STRENGTH; B) YOUNG'S MODULUS;..... 126

FIGURE 4.34: EFFECT OF AMPLITUDE OF SONICATION ON; A) ULTIMATE STRAIN; B) FRACTURE TOUGHNESS..... 126

FIGURE 4.35: OPTIMISATION OF SONICATION AMPLITUDE FOR REINFORCEMENT 127

FIGURE 4.36: EFFECT OF AGE ON; A) E; B) Σ_S; C) E_U AND D) $U_{F.T}$..... 129

FIGURE 4.37: %CHANGE OF REINFORCEMENT PROPERTIES WITH AGE 129

FIGURE 4.38: COMPARISON OF EXPERIMENTAL RESULTS AND EXISTING MODELS FOR E FOR RUBBER NANOCOMPOSITES 131

FIGURE 4.39: VALIDITY OF THE EXPERIMENTAL PROFILE FOR E 133

FIGURE 4. 40: COMPARISON OF EXPERIMENTAL PROFILES AND EXISTING MODELS FOR TENSILE STRENGTH 137

FIGURE 4.41: RELATIONSHIP BETWEEN I) TENSILE STRENGTH AND V_F AND II) FRACTURE TOUGHNESS, $U_{F.T}$ AND V_F FOR SSBR-CNB NANOCOMPOSITE IEM 139

FIGURE 4.42: CNBS IN POLYMER MATRIX; A) ILLUSTRATION OF INTERACTION BETWEEN MONODISPERSE NANOPARTICLES AND POLYMER CHAINS IN AN ELASTOMERIC NANOCOMPOSITE; B) MODELING OF POLYMER CHAINS AS REPRESENTED BY THEIR RADIUS OF GYRATION (HOOPER AND SCHWEIZER, 2006) 141

FIGURE IV.I: STRESS- STRAIN AND FORCE DISPLACEMENT GRAPHS FOR AGED PLAIN SSBR MEMBRANES 181

FIGURE IV.II: STRESS- STRAIN AND FORCE DISPLACEMENT GRAPHS FOR AGED 2.5WT% SSBR-CNB NANOCOMPOSITE ION EXCHANGE MEMBRANES 181

FIGURE IV.III: STRESS- STRAIN AND FORCE DISPLACEMENT GRAPHS FOR AGED 1WT% SSBR-CNB NANOCOMPOSITE ION EXCHANGE MEMBRANES 182

FIGURE IV.IV: STRESS- STRAIN AND FORCE DISPLACEMENT GRAPHS FOR AGED 4WT% SSBR-CNB NANOCOMPOSITE ION EXCHANGE MEMBRANES 182

FIGURE IV.V: STRESS- STRAIN GRAPHS OF; A) 20% AND B) 60% AMPLITUDE SSBR-CNB NANOCOMPOSITE ION EXCHANGE MEMBRANE 183

FIGURE IV.VI: A) COMPARISON OF STRESS-STRAIN GRAPHS FOR A) 20% AND 60% AMPLITUDE OF SONICATION, B) DIFFERENT FILLER CONCENTRATIONS 183

FIGURE IV.VII: ISOTROPY RESULTS (STRESS-STRAIN) FOR 1WT% LOADED SSBR-CNB NANOCOMPOSITE ION EXCHANGE MEMBRANE 184

FIGURE IV.VIII: ISOTROPY RESULTS (STRESS-STRAIN) FOR PLAIN SSBR MEMBRANES 184

FIGURE IV.IX: ISOTROPY RESULTS ON A) 2.5 AND 4WT% LOADED CNB, B) UNSULPHONATED PLAIN SBR (RED) AND 1WT%SBR-CNB NANOCOMPOSITE (BLUE) 185

FIGURE IV.X: FORCE TIME GRAPHS OF 20%A, 2.5WT% LOADED SSBR-CNB IEM AT 0.14MPA MEAN STRESS 185

FIGURE IV.XI: FORCE TIME GRAPHS FOR 20%A, 1WT% LOADED SSBR-CNB IEM AT 0.14MPA MEAN STRESS 186

FIGURE IV.XII: FORCE TIME GRAPHS FOR 60%A; A) 1WT% LOADED SSBR-CNB IEM AT 0.63MPA MEAN STRESS AND B) 2.5WT% LOADED SSBR-CNB IEM AT 0.81MPA MEAN STRESS 186

LIST OF TABLES

TABLE 2.1: THE CHARACTERISTICS OF MEMBRANES USED IN DIFFERENT MEMBRANE SEPARATION PROCESS, PROCESS DRIVING FORCE AND APPLICATIONS 12

TABLE 2.2: COMPARISON OF EFFECT OF DIFFERENT BLENDING TECHNOLOGIES ON YOUNG'S MODULUS 39

TABLE 2.3: BOND TYPES AND STIFFNESS CONSTANTS (ASHBEY AND JONES, 1980)..... 50

TABLE 2.4: MODELS FOR PREDICTION OF ELASTIC MODULUS, E OF NANOCOMPOSITES 54

TABLE 2.5: MODELS FOR PREDICTING THE TENSILE STRENGTH OF NANOCOMPOSITES 55

TABLE 4.1: CARBON BALL SYNTHESIS CONDITIONS.....74

TABLE 4.2: LIMITING VALUES OF ACETYLENE FLOW RATIO FOR CNB PRODUCTION..... 85

TABLE 4.3: CARBON BALL PRODUCTIVITY FROM 16MM Φ X 300MM LENGTH REACTOR..... 89

TABLE 4.4: SURFACE AREA AND PORE VOLUME ANALYSIS 98

TABLE 4.5: EFFECT OF $ClSO_3H$ CONCENTRATION ON 24HR SULPHONATION OF SBR..... 100

TABLE 4.6: THE RELATIONSHIP BETWEEN $ClSO_3H$ CONCENTRATION AND INSTANTANEOUS RATIO OF $ClSO_3H$ MOLES TO STYRENE MOLES..... 103

TABLE 4.7: SULPHONATION DATA FOR SBR SULPHONATED AT 0.09M $ClSO_3H$ FOR 24HRS AT R.T.P AND 1250 RPM STIRRING..... 105

TABLE 4.8: MECHANICAL PROPERTIES OF SBR-CNB NANOCOMPOSITE IEM 116

TABLE 4.9: DATA FOR RATIO OF TRANSVERSE MECHANICAL PROPERTIES TO PERPENDICULAR PROPERTIES..... 117

TABLE 4.10: MAXIMUM REINFORCEMENT ACHIEVEMENTS WITH CNB ADDITION..... 122

TABLE 4.11: PERCENTAGE CHANGE IN MECHANICALS PROPERTIES WITH CHANGE IN AMPLITUDE OF SONICATION FROM 20 TO 60%..... 124

TABLE I.I: NCCVD REACTOR DIMENSIONS.....171

TABLE I. II: AVERAGE CARBON BALL SIZE ESTIMATION..... 171

TABLE I.III: CARBON BALL PRODUCTION RATE..... 173

TABLE I.IV: CARBON BALL PRODUCTIVITY MEASURES 175

TABLE II.I: DILUTION OF CHLOROSULPHONIC ACID.....176

TABLE III.I: DISPERSION DATA FOR SSBR-CNB BLENDED AT DIFFERENT AMPLITUDES.....179

TABLE IV.I: DIMENSIONS OF STRIP SPECIMENS FOR NANOTENSILE TESTING.....180

TABLE IV.II: YOUNG'S MODULUS EXPERIMENTAL RESULTS (60% AMPLITUDE, 20 DAYS AFTER DRYING)..... 187

TABLE IV.III: YIELD STRENGTH EXPERIMENTAL RESULTS (60% AMPLITUDE, 20 DAYS AFTER DRYING)..... 187

TABLE IV.IV: TENSILE STRENGTH EXPERIMENTAL RESULTS (60% AMPLITUDE, 20 DAYS AFTER DRYING) 187

TABLE IV.V: ENGINEERING STRAIN EXPERIMENTAL RESULTS (60% AMPLITUDE, 20 DAYS AFTER DRYING)..... 188

TABLE IV.VI: FRACTURE TOUGHNESS EXPERIMENTAL RESULTS (60% AMPLITUDE, 20 DAYS AFTER DRYING)..... 188

TABLE IV.VII: YOUNG'S MODULUS EXPERIMENTAL RESULTS (20% AMPLITUDE, 20 DAYS AFTER DRYING)..... 188

TABLE IV.VIII: YIELD STRENGTH EXPERIMENTAL RESULTS (20% AMPLITUDE, 20 DAYS AFTER DRYING)..... 189

TABLE IV.IX: TENSILE STRENGTH EXPERIMENTAL RESULTS (20% AMPLITUDE, 20 DAYS AFTER DRYING) 189

TABLE IV.X: ENGINEERING STRAIN EXPERIMENTAL RESULTS (20% AMPLITUDE, 20 DAYS AFTER DRYING)..... 189

TABLE IV.XI: FRACTURE TOUGHNESS EXPERIMENTAL RESULTS (20% AMPLITUDE, 20 DAYS AFTER DRYING)..... 190

TABLE IV.XII: YOUNG'S MODULUS EXPERIMENTAL RESULTS (60% AMPLITUDE, 40 DAYS AFTER DRYING)..... 190

TABLE IV.XIII: YIELD STRENGTH EXPERIMENTAL RESULTS (60% AMPLITUDE, 40 DAYS AFTER DRYING)..... 190

TABLE IV.XIV: TENSILE STRENGTH EXPERIMENTAL RESULTS (60% AMPLITUDE, 40 DAYS AFTER DRYING)..... 191

TABLE IV.XV: ENGINEERING STRAIN EXPERIMENTAL RESULTS (60% AMPLITUDE, 40 DAYS AFTER DRYING)..... 191

TABLE IV.XVI: FRACTURE TOUGHNESS EXPERIMENTAL RESULTS (60% AMPLITUDE, 40 DAYS AFTER DRYING)..... 191

TABLE IV.XVII: EFFECT OF AMPLITUDE OF SONICATION ON MECHANICAL PROPERTIES 192

TABLE IV.XVIII: EFFECT OF AGE ON SSBR NANOCOMPOSITE ION EXCHANGE MEMBRANE 192

TABLE IV.XIX: % CHANGE IN REINFORCEMENT PROPERTY WITH AGE (20 DAYS TO 40DAYS)..... 192

TABLE IV.XX: COMPARISON OF EXPERIMENTAL PROFILE FOR YOUNG'S MODULUS WITH EXISTING MODELS..... 193

TABLE IV.XXI: COMPARISON OF EXPERIMENTAL PROFILE FOR TENSILE STRENGTH WITH EXISTING MODELS..... 193

LIST OF ABBREVIATIONS AND SYMBOLS

AFM	Atomic Force Microscopy
APCVD	Atmospheric Pressure Chemical Vapour Deposition
BN	Boron Nitride
CB	Carbon Ball
CCVD	Catalytic Chemical Vapour Deposition
$ClSO_3H$	Chlorosulphonic Acid
CNB	Carbon Nanoball
CNF	Carbon Nanofibres
CNT	Carbon Nanotube
CSA	Chlorosulphonic Acid
CVD	Chemical Vapour Deposition
DCE	1,2 Dichloroethane
DS	Degree of Sulphonation
FTIR	Fourier Transform Infrared
GPa	Giga Pascals
GPCVD	Gas Phase Chemical Vapour Deposition
HCF	High Cycle Fatigue
HCVD	Liquid Injection Chemical Vapour Deposition
HPACVD	High Pressure Autoclave Chemical Vapour Deposition
HRTEM	High Resolution Transmission Electron Microscopy
ID	Inner Diameter
IEC	Ion Exchange Capacity
IEM	Ion Exchange Membrane
LCF	Low Cycle Fatigue
LHS	Left Hand Side
LPCVD	Low Pressure Chemical Vapour Deposition

MMT	Montmorillonite
NCCVD	Non Catalytic Chemical Vapour Deposition
nm	Nanometer
PBI	Polybenzimidazole
PEEK	Poly Ether-Ether Ketone
PEM	Proton Exchange Membrane
RHS	Right Hand Side
SBR	Styrene Butadiene Rubber
SCVD	Sublimation Chemical Vapour Deposition
SEBS	Styrene-Ethylene Butylene Styrene
SEM	Scanning Electron Microscopy
SiC	Silicon Carbide
SPEEK	Sulphonated Poly Ether-Ether Ketone
SPI	Sulphonated Polyimide
SSBR	Sulphonated Styrene Butadiene Rubber
TEM	Transmission Electron Microscopy
TGA	Thermogravimetric Analysis
UHVCD	Ultra High Vacuum Chemical Vapour Deposition
USD	United States Dollar
E	Young's Modulus (MPa)
d	Interlayer distance between adjacent nanoball shells (nm)
D	Density of off-the-shelf Chlorosulphonic Acid (kg/L)
e	Ultimate Engineering Strain of a material
E_c	Young's Modulus of Nanocomposite (MPa)
E_{CNB}	Young's Modulus of Carbon Nanoballs (MPa)
E_m	Matrix Material Young's Modulus (MPa)
E_R	Relative Young's Modulus (MPa)
f	packing fraction of nanofiller

G	Shear Modulus of a Material (MPa)
I_D	Intensity of the distorted graphitic band of carbon nanoparticles
I_G	Intensity of the ordered graphitic band of carbon nanoparticles
K	Bulk Modulus of a Material (MPa)
M_{ci}	Mass input flow rate of carbon into Reactor (g/min)
M_G	Gross mass production rate of carbon particles (g/min)
M_n	Number average molecular weight of a polymer (g/mol)
mN	milliNewtons
M_P	Mass production rate of carbon balls (g/min)
M_w	Molecular Weight of a Material (g/mol)
M_{wC}	Molecular Weight of Carbon (g/mol)
M_{wcsa}	Molecular Weight of Chlorosulphonic Acid(g/mol)
n	number of shells in a carbon nanoball
P	Purity of off the shelf Chlorosulphonic Acid (%)
Q_{ac}	Acetylene Flow Rate (ml/min)
Q_T	Total Flow Rate of Gases into NCCVD Reactor (ml/min)
R_{CB}	Carbon Ball Radius
r_θ	Radius of Curvature of Carbon balls
t	Membrane thickness(mm)
Td	Thermal Decomposition Temperature of a Material (^{0}C or K)
$U_{f.t}$	Fracture Toughness of Material (J/cm3)
V_0	Fractional Free Volume of a Matrix Material
V_{aci}	Acetylene Input Volumetric Flow rate (ml/min)
V_c	Critical Volume Fraction of carbon nanoballs corresponding to E_{max}

V_f	Volume fraction of carbon nanoballs
wt%	Weight Percent
β	Carbon Balls Purity (%)
γ	Yield of carbon balls NCCVD (%)
γ_{cyc}	Yield of carbon balls from the cyclone (%)
δ	Dispersion Efficiency of a Blending Technology
η_{AC}	Acetylene flow ratio
η_{AC0}	Critical Acetylene flow ratio corresponding to minimum CB Diameter
η_R	Carbon nanoball production Range
ν	Poisson Ratio of a Material
ρ_{SSBR}	density of Sulphonated Styrene Butadiene Rubber
σ_c	Composite Tensile Strength (MPa)
σ_m	Tensile Strength of Pure Matrix Material (MPa)
σ_y	Yield Strength of Material (MPa)
Φ_{CB}	Carbon Ball Diameter
Φ_{CB0}	Minimum Carbon Ball Diameter
Φ_R	NCCVD Reactor Diameter

CHAPTER 1: INTRODUCTION

1.0 Introduction

Advances in membrane technology especially in novel materials and ion exchange related processes will continue to play a crucial role in providing reliable energy efficient and environmentally sustainable applications for the 21st Century. Continuous growth of chemical engineering technology and biotechnology coupled with diversity in the applications has fuelled the demand for efficient reliable green technologies for the downstream processes of which advances in ion exchange membrane technologies is inevitable (Nagarale et al., 2006 and Xu, 2005). New membranes with unusual properties like low permeability, low electrical resistance, good mechanical stability, high chemical stability and durability are thus required.

1.1 Background

Nanocomposite membranes have drawn a lot of attention due to their potential for properties improvement, emanating from the strengths of individual constituents (Sata, 1986 and Sata, 1991). Recent developments in processing and nanotechnology have enhanced the competitiveness of nanocomposite membranes for industrial applications to achieve the desired environmentally sustainable outcomes (Xu, 2005 and Nagarale et al., 2006). These emerging membrane types are hence expected to overcome the challenges faced by conventional ion exchange membranes. The advantages of the new membranes include the reduction in cost of production, maintenance cost and improved mechanical properties, dimensional stability, thermal stability, ionic conductivity and reliability amongst others.

Since many important chemical and physical interactions are governed by surfaces and surface properties, a nanostructured material can have substantially different properties from a larger dimensional material of the same composition.

Nanocomposite membrane technology takes advantage of these factors leading to efficient reinforcement at low filler loadings because of their high aspect ratios (Hussain et al., 2006; Tripathi et al., 2008; Xu, 2005; Zhou and Magriotis, 2005 and Tagmatarchis and Prato, 2005).

Xu, 2005 reports that although ion exchange membrane technology has received multidiscipline attention in both theoretical investigations and industrial applications, a lot still has to be done in the discovery of new ion exchange membrane types, synthesis and novel ion exchange membrane based processes. Research has been done using different polymeric materials blended with various nanomaterials and yielding excellent membranes, superior to conventional ones (Tripathi et al 2008; Hussain et al., 2006 and Choi et al., 2008). Abdulkareem, 2009 and Idibie, 2009 have reported successful blending of polystyrene-butadiene - carbon nanoballs composite membrane for fuel cell applications, which has better properties than the commercially available Nafion 112.

1.2 Motivation

Although major breakthroughs have been made towards commercializing highly efficient and clean ion exchange membranes, the costs are still way above competing technologies. The major cost component is the membrane material itself, which is the heart of the ion exchange technology. For example, Nafion, used in Proton Exchange Membrane for fuel cells cost 800 USD per square metre, which translates to 160 USD per KW against a target of 10 USD per KW (Hickner et al., 2004 and Chen et al., 2004). As a result, the cost of the technology is raised far beyond the conventional power generating systems despite the benefits of higher efficiency and cleaner environment.

Secondly, the durability and reliability of ion exchange membranes are generally lower than competing technologies resulting in slow progress towards

commercialization. A consistent operational performance of 5000 hrs in fuel cell technology would be comparable to competing technologies (Huang et al., 2006). Thus great efforts and energy have been channeled towards the development of alternative and more economical membranes from perfluorinated and non – perfluorinated polymer membranes with desired qualities. Novel work done by Idibie, 2009 on styrene butadiene rubber ion exchange membrane has attracted much attention because of the low cost of material, superior properties to commercially available membranes like Nafion and simple production processes.

1.3 Research problem: Nanocomposite ion exchange membrane challenges

Despite the positive scores, the highly sulphonated styrenic polymers are brittle and susceptible to damage in the form of cracks which leads to mechanical degradation (Abdulkareem, 2009 and Idibie, 2009). Micro cracking induced by the operating conditions of most ion exchange membranes, which involve thermal cycles of heating up and cooling, humidity cycles, intermittent starts and stops as well as differential pressure create the great need for adequately reinforced membranes (Tuichiev et al., 2008 and Patwardhan, 2002).

Efforts to improve the mechanical properties of synthetic rubber ion exchange through the incorporation of nanofillers have gained momentum all over the world. Work done on silicon filler based polymer nanocomposite and other nanoparticles have yielded contradicting results, including some negative effects of nanoparticle inclusions on mechanical properties of matrix materials. Different results have also been observed with different blending conditions due to agglomeration and aggregation of nanoparticles. The increase in nanofiller content comes with problems like surface roughness, shear heating, and breakage of fillers. A balance between various complementary properties may be maintained by the addition of nanofiller particles. Consequently, the composite industry struggles with various trade-off issues (Guillermo, 2007; Nagarale et al., 2006 and Oren et al., 2004).

The manufacturing of composite constituents like the matrix and nanofiller material can be quite challenging and limiting. The matrix functionalisation process is often a long, costly and challenging one (Abdulkareem, 2009 and Idibie, 2009). The production of nanofiller material may also require high temperatures, as well as strict control of parameters like flow rates, pressure and temperature (Abdulkareem, 2009 and Idibie, 2009). Material handling and blending at nanoscale has never been easy due to the fact that nanotechnology is relatively new. As a result, there is need for more research and development in nano-manipulation technology to address the dispersion, alignment and orientation challenges. Therefore the cost of producing the nanofiller and blending may have negative effect on the overall cost of the nanocomposite ion exchange membrane (Guillermo, 2007).

Mechanical testing at nanoscale has also been limited due to limited technology to test and characterize nanobased materials. Sue et al., 1994 reported that by 1994, fatigue testing of polymeric thin films and membranes was very difficult and virtually non-existent due to the difficulties in adequate membrane sample preparation and precise control of testing at low loadings of around 0.4 to 0.5N. Such challenges contributed to lack of adequate literature on the reinforcement properties of membranes. The recent advancement in characterization and analysis technology like AFM, HRTEM, and nanomechanical testing equipment have enhanced the need for testing, characterization and optimization of the critical mechanical properties (Calleja et al., 1996; Lach et al., 2004,). Current generic models are not consistent, and hence failed to accurately predict effects of reinforcement at nano-scale, making inference very undependable.

The novel work done on styrene butadiene rubber – carbon nanoball nanocomposite ion exchange membrane for fuel cell membranes by Abdulkareem, 2009 and Idibie, 2009 is of great interest because of four major reasons. Firstly, they achieved good membrane properties superior to Nafion 117 like ion exchange capacity, power density, thermal stability and reduced methanol permeabilities at low filler loadings

(1-4wt% carbon nanoballs). Secondly, the synthetic rubber used (SBR) used is a low cost material with the potential of significantly reducing the ion exchange membrane cost. Thirdly, the carbon nanoball filler material was reportedly produced by a simple process using low cost material which could potentially reduce the overall cost (Mhlanga et al., 2010). Lastly, the spherical nature of the nanofiller is also expected to overcome orientation and alignment challenges and thus promising a highly isotropic ion exchange membrane.

1.3.1 Problem statement

Despite the excitement with SSBR-CNB nanocomposite ion exchange membrane, no information to our knowledge has been reported in literature concerning the reinforcement effects of the carbon nanoballs on synthetic rubber ion exchange membrane. Important and accurate information concerning nanoball production, properties, testing, blending and applications of carbon nanoballs is also yet to be obtained (Zetl and Cumings, 2001). This is against the background that the reinforcement need is driven by the critical durability and reliability requirements of ion exchange membranes. There is also limited literature on sulphonation of styrene butadiene rubber and hence the need for more work towards the reinforced SSBR – CNB nanocomposite ion exchange membrane. Therefore low cost synthetic rubber ion exchange membranes with competitive electrochemical properties but poor mechanical properties will find commercial application if successfully reinforced with nanoparticles.

1.3.2 Research questions

In solving the research problems mentioned above the following questions must be answered;

- What is the effect of the presence of carbon nanoballs on reinforcement of styrene butadiene rubber ion exchange membrane?
- What is the effect of the concentration of carbon nanoballs on the reinforcement of ion exchange membrane?
- What is the effect of blending conditions on reinforcement?
- How do the reinforcement properties and characteristics compare with similar nanocomposites?
- How do the reinforcement properties compare with existing models?
- What are the optimal compositions of the nanocomposite ion exchange membranes and the achieved improvements by reinforcement?
- What further work needs to be done to maximize the benefits of nanotechnology?
- What are the possible applications for the ion exchange membrane?

1.3.3 Expected research outcomes and contributions

The polymeric matrix material must be adequately functionalized without distortion of the backbone, through a simple low cost process. A simple and cost effective synthesis of nanofiller materials must yield the desired size, purity and uniformity of carbon nanoballs (under 100nm). An effective blending technique must lead to homogeneous dispersion of nanofiller into functionalized matrix and casting of membrane to produce an optimized reinforced ion exchange membrane.

Ultimately, this work is expected to contribute towards a mechanically strong, dimensionally stable and durable nanocomposite membrane, which is reliable and cheaper to maintain. The characterization is expected to contribute towards a model for the prediction of reinforcement properties at any given filler concentration. This research work is expected to provide a strong basis for further work on durability and reliability of nanocomposite ion exchange membrane for applications such as Proton

Exchange Membrane (PEM) Fuel Cell (FC) and industrial purification ion exchange membrane amongst others.

1.4 AIM

The research is aimed at the improvement of the mechanical properties of locally sulphonated styrene butadiene rubber ion exchange membrane through addition of low volumes of locally synthesized carbon nanoballs.

1.4.1 Objectives

This aim would be achieved via the outlined activities and objectives:

- To synthesise ion exchange matrix material by sulphonation of the phenyl group in polystyrene butadiene rubber.
- To synthesise pure carbon nanoballs of uniform size and structure in adequate volumes as the nanofiller for the synthetic rubber based nanocomposite ion exchange membrane
- To effectively blend the sulphonated polymer matrix with the nanoparticles to make a homogeneous nanocomposite blend.
- To cast thin film membranes from the unblended and blends of sulphonated polystyrene butadiene and carbon nanoballs of different weight ratios to produce nanocomposite ion exchange membranes.
- To test, characterize and optimize the blending to achieve optimal reinforcement properties of the nanocomposite ion exchange membrane
- To compare the reinforcement properties of synthesized nanocomposite membrane with existing membranes and predict possible applications.

1.4.2 Hypothesis

Low additions of (1-10%) by volume of carbon nanoballs will significantly improve the mechanical properties of styrene butadiene rubber ion exchange membrane (>50%).

1.5 Scope of research

The scope of the research encompasses the sulphonation of synthetic rubber, synthesis of carbon nanoballs, preparation of nanocomposite ion exchange membrane from sulphonated polystyrene butadiene rubber blended with carbon nanoballs, mechanical testing, characterization and optimization of the blending conditions for mechanical property improvement.

1.6 Organization of dissertation

Chapter One gives the background/ motivation of the research, research problem, aim and objectives, hypothesis and scope of the research. Chapter Two starts by a brief overview of polymeric ion exchange membrane, their properties, types and applications. This is then followed by a brief description of polymer matrix functionalisation methods with special emphasis to sulphonation of styrene based copolymers. The literature review of carbon nanoballs synthesis follows encompassing process routes, formation mechanisms, and properties of the carbon spheres. Emphasis shall however be given to the Pyrolytic Chemical Vapor Deposition method of synthesis. A survey of the blending technologies will then follow before a comprehensive literature survey on polymer nanocomposites. The latter survey will include the work done on polymer nanocomposite and their properties as well as the summary of various models designed to predict the reinforcement characteristics of polymer nanocomposites. Chapter Three describes the research methodology and experimental procedures for the research work.

Chapter Four dwells on the results and discussion associated with the production of nanofiller material, synthetic rubber functionalisation, blending, casting and mechanical testing. Chapter Five presents the conclusions based on constituent synthesis, blending and the reinforcement outcomes. Recommendations for future work are included in the same chapter. Lastly the list of referenced material and appendices are given.

CHAPTER 2: LITERATURE REVIEW

2.1 Ion Exchange Membrane (IEM) overview

The Literature review looks at firstly the ion exchange membrane principle, morphology, properties and applications overview. It is then followed by a brief survey of available polymeric membrane materials in relation to property improvement and functionalisation processes. A review of polymer nanocomposites, nanomaterials and blending technology with a bias towards carbon nanoballs follows. Finally the review of the reinforcement measures, failure mechanisms and models for polymer nanocomposite concludes the chapter.

2.1.1 Definition of Ion Exchange Membrane

Ion exchange materials are thin insoluble semi permeable membranous materials bonded to loosely held ions which are able to be exchanged with other ions in solutions (Jannasch, 2003). The loosely held ions enable the membrane to exchange either positively charged ions (cation exchangers) or negatively charged ones (anion exchangers) without any physical alteration to the ion exchange material As a rule, ion-exchange membrane consists of the inert carrier of a microporous structure and the ion-active pore wall component carrying fixed positive or negative charges (Shatalov et al., 2007 and Dortimundt and Doshi, 1999). The membrane serves as a selective barrier between two phases and remains impermeable to specific particles, molecules, or substances when exposed to the action of a driving force (Pinnau and Freeman, 1999; Sata, 1986 and Sata 1991).

Several types of ion exchange membranes are available based on the type of the functional groups attached to the matrix and their layout and distribution in the matrix. Cation permeable membranes, called cation exchange (or cationic) membranes and anion permeable membranes, called anion exchange (or anionic)

membranes, are monopolar membranes; which means that they are permeable to only one type of ion (Sata, 1986 and Xu, 2005). Besides these, bipolar, amphoteric and mosaic ion exchange membranes exist (Sata, 1991 and Strathmann, 2004). Bipolar ion exchange membranes are the ones that have cation exchange groups on one side and anion exchange groups on the other (Sata, 1986). Amphoteric ion exchange membranes have both negatively and positively fixed ionic groups randomly distributed, whilst mosaic ion exchange membranes are composed of macroscopic domains of polymers with negatively fixed ions and those of positively fixed ions randomly distributed in a neutral polymer matrix (Sata, 1986 and Xu, 2005).

2.1.2 Application of Ion Exchange Membranes

Ion exchange membrane technology has played an important and central role in addressing the need for more efficient energy conversion technologies as well as lean, cleaner and environmentally friendly technologies. It has found its industrial applications in Hi - Tech areas such as biotechnology, nanotechnology and membrane based energy devices in addition to different membrane based separation and purification processes (Nagarale et al., 2006). The use of ion exchange membrane not only makes the process cleaner and more energy efficient but also recovers useful effluents that are now going to wastes, and thus makes the development of the society sustainable (Xu et al., 2005).

The most known synthetic membranes separation processes include water purification, reverse osmosis, dehydrogenation of natural gas, removal of cell particles by microfiltration and ultrafiltration, removal of microorganisms from dairy products and solid polymer electrolytes for fuel cell applications. It has also been used in electrodialysis concentration or desalting of solutions, diffusion dialysis to recover acids and electrolysis of sodium chloride solution. Membrane based sensors find applications in humidity sensors, carbon monoxide sensors, drug sensors and enzyme carriers (Nagarale et al., 2006). New ionomer composites possessing high

proton conductivity have been introduced as solid electrolytes in polymer fuel cells for stationary, mobile telephony and automotive power generators (Xu et al., 2005). They are also efficient tools for treating industrial effluents, concentration or separation of food and pharmaceutical products containing ionic species.

Table 2.1 summarises the membrane based processes and the process driving force. The process driving force and applications are important for the design of strong membranes capable of withstanding the operating conditions (Ho and Zydney, 2001).

Table 2.1: The characteristics of membranes used in different membrane separation process, process driving force and applications (Ho and Zydney, 2001 and Strathmann, 2004).

Separation Process	**Process Driving Force**	**Membrane Materials**	**Applications**
Reverse Osmosis	Hydrostatic Pressure, 2-10MPa	Polymers, cellulosic acetate, aromatic polyamide	Separation of salts and microsolutes from solution
Electrodialysis	Electrical Potential Gradient	Sulphonated crosslinked polystyrene	Desalting of Ionic solutions
Gas separation	Hydrostatic pressure and concentration gradient	Polymers and copolymers	Separation of Gas Mixtures
Pervaporation	Vapour pressure gradient	Polyacrylonitrile polymers	Separation of zeotropic mixtures
Nanofiltration	9.3 – 15.0bar	Cellulosic acetate, aromatic polyamide	Removal of hardness and desalting
Microfiltration	Hydrostatic Pressure, 10-500kPa	Cellulose nitrate/ acetate,PVDF,polyamides,polysulfones,PTFE, metal oxides	Sterile filtration, clarification
Ultrafiltration	Hydrostatic Pressure, 0.1-1.0MPa	Polysulfone, polypropylene,nylon 6,PTFE, PVC,acrylic copolymer	Separation macromolecular solutions

2.1.3 Properties of Ion Exchange Membranes

The desired membrane properties determine to a large extent the technical feasibility and the economics of the processes. The properties of ion exchange membranes are determined by two parameters, namely the basic materials they are made from and the type and concentration of the fixed ion moiety. The membrane separation properties are governed by both chemical and physical natures of the membrane materials as well as the method of production (Nasef and Hegazy, 2004).

The critical properties to all high performance ion exchange membranes include high ionic conductivity, low electronic conductivity, good permselectivity, oxidative and hydrolytic stability, good mechanical properties and dimensional stability, good thermal stability, low cost, and easy processability (Strathmann, 2004 and Hickner, et al., 2004).

The need for the above mentioned properties has led to extensive research in materials and technology to produce competitive ion exchange technologies. Therefore recent progress in this area is assessed towards the development of next-generation materials (Zeaman et al., 1996). Polymeric membranes lead the membrane separation industry market because they are very competitive in performance and economics (Perry and Green, 1997).

2.2 Polymeric membranes

Many efforts have been made on polymers to form ion exchange membranes. Polymers' amorphous and semi-crystalline morphologies affect the membrane performance characteristics resulting in dimensional instability and low mechanical properties (Hickner et al., 2004). The polymer has to be readily available, cheap to functionalise and reasonably priced to comply with the low cost criteria of membrane separation process. These challenges have delayed the large-scale commercialization

of polymeric ion exchange membranes. Many membrane polymers are grafted, custom-modified, or produced as copolymers to improve their properties (Zeaman et al, 1996). Therefore, many efforts have been devoted to extensive research in different types of polymers and their sustainable modification to produce competitive membranes.

2.2.1 Types of polymeric membranes

Fluorocarbon based ion exchange membranes, such as Nafion, Aciplex and Flemion, with excellent chemical and thermal stability were developed by DuPont. Despite the good properties, they degrade in the presence of the oxidizing agent, especially at elevated temperatures above 100ºC (Jannasch, 2003 and Hickner et al., 2004). The fluorinated ionomers based ion-exchange membranes are also very costly due to limited availability and complex processing route.

Nonfluorinated nonstyrenic polymers have also been explored for ion exchange membranes. Polysulfone based ion-exchange membranes, are thermally stable with a minimum temperature of -50ºC and a maximum temperature of up to 600ºC (Dick and Anniceli, 2001; Johnson, 2001 and Nagarale et al., 2006). They have been widely used as a base polymer for ultrafiltration and gas separation because of their excellent workability and mechanical strength (Nagarale et al., 2006 and Hickner et al., 2004). Despite the mentioned benefits, they are costly and difficult to process. Sulphonated poly(ether-ether ketone) (SPEEK), sulphonated polyimide (SPI) and polybenzimidazole (PBI) doped with phosphoric acid, have low cost, but the conductivity of all of these membranes was not high enough for ion exchange membrane applications (Meier-Haack et al., 2005). Partially sulphonated poly (ether ether ketone) (PEEK) membranes are reported to be mechanically fragile with limited lifetime in electrolysis system (Nagarale et al., 2006).

Polybenzimidazole based ion-exchange membranes were observed to possess excellent chemical, thermal and mechanical stability. Phthalic polyimides are used for proton exchange membranes (PEM) in fuel cells. Their disadvantage is the quick degradation in operating environment. The hydrolysis of the phthalic imide structure leads to chain scission (decrease in molecular weight) and causes the membrane to become brittle. Although naphthalenic polyimides are much more stable to hydrolysis, their stability is still questionable (Nagarale et al., 2006).

Styrene derived ion exchange membranes are widely reported in literature. This is due to their availability in abundance and easy modification, rendering them low cost materials. Furthermore, their polymers are easily synthesized via conventional free radical and other polymerization techniques. Ballard Advanced Materials (BAM) Corporation introduced a semicommercial styrenic membrane based on a novel family of sulphonated copolymers incorporating trifluorostyrene. This generation of BAM membranes exhibited some superior performance to perfluorinated membranes, such as Nafion 117 (Hickner et al., 2004 and Jannasch, 2003). Dais Analytic introduced sulphonated styrene-ethylene-butylene-styrene (SEBS) membrane and styrene/ethylene-butadiene/styrene triblock membranes. They are reported to be thermally stable with a minimum degradation temperature of -50ºC and can withstand up to 600ºC (Dick and Anniceli, 2001 and Johnson, 2001). Dais membranes are reported to be much less expensive to produce than Nafion 112. They are also reported to exhibit a rich array of microphase separated morphologies because of the ability to tailor the block length and composition of the unsulphonated starting polymer. BAM based semicommercial membranes are limited by their presumed high cost and monomer availability (Nagarale et al., 2006).

Styrene butadiene and their hydrogenated counterparts are very promising low cost high performance materials for ion exchange membranes (Sheikh-Ali and Wnek, 2000). Abdulkareem (2009) and Idibie (2009) reported a novel styrene butadiene rubber ion exchange membrane with better properties than Nafion 112. Despite the

scores, their main drawbacks are their poor mechanical properties and oxidative stability compared to perfluorinated or partially perfluorinated membranes due to their partially aliphatic character (Sheikh-Ali and Wnek, 2000). However, little has been explored on improvement of the presumed weak mechanical strength and oxidative stability.

The limitations of the polymeric ion exchange membranes have led to the continuous research into ways to improve the overall properties of the ion exchange membrane technology at low cost. One of the most common approaches to modify polymeric membranes has been to blend them with nanomaterials of different structures and forms to make nanocomposite ion exchange membranes with improved properties at lower cost. Therefore researchers have gained a lot of interest in polymeric matrix based nanocomposite membranes as a result of their combined properties of chemical stability, thermal stability, flexibility, cost and availability (Nagarale et al., 2006). Low concentrations of filler material below 4% by weight have been reported to drastically improve properties of the membranes (Sata, 1986; Osada and Nakagawa, 1992 and Abdulkareem, 2009). Before reviewing the exciting polymer nanocomposite, a brief review of the prerequisite functionalisation of polymer to produce polymeric ion exchange membranes shall be done. Furthermore, mechanical properties need to be addressed with much more rigor than they have been in the past.

2.3 Functionalisation of polymers to produce ion exchange membranes

Although there has been significant progress towards the synthesis of polymeric ion exchange materials, there are many outstanding issues to fully realize commercialisation. This review will highlight the synthetic aspects of ion conducting polymers and the polymer chemical structure considerations for producing useful ion exchange membranes.

Functionalisation of polymers is the process of attaching ionic groups to polymer backbones to produce the desired polymeric ion exchange material. There are several methods of functionalisation with sulphonation being a popular route due to its simplicity (Zhang et al., 2000). Polymers from monomers containing phosphoric-based ion exchange materials have been reported in literature. However they have not been well studied because of the limited synthetic procedures available for their preparation, compared with sulphonic acid derivatives (Zhang et al., 2000 and Hickner et al., 2004). Thus the review shall be focused on sulphonation since the functionalised polymer is not going to be purchased off the shelf.

2.3.1 Sulphonation of polymers

Sulphonation of polymers to produce ion exchange membranes has been reported widely in literature as a convenient method of producing desired ion exchange membranes. It is the process of attachment of the sulphonate group to a polymer through electrophilic substitution to produce a polymeric sulphonic acid (Figure 2.1) (Idibie, 2009). Sulphonation can be heterogeneous where the phase of the sulphonating agent is different from the phase of the polymer solution or homogeneous (in hydrocarbons or chlorinated solvents) where the polymer solution and the sulphonating agent are in the same phase (Martins et al., 2003). It is a reversible reaction which often depends on the type and concentration of sulphonating agent, the polymer properties, the temperature and time of reaction (Knaggs and Nepras, 2005).

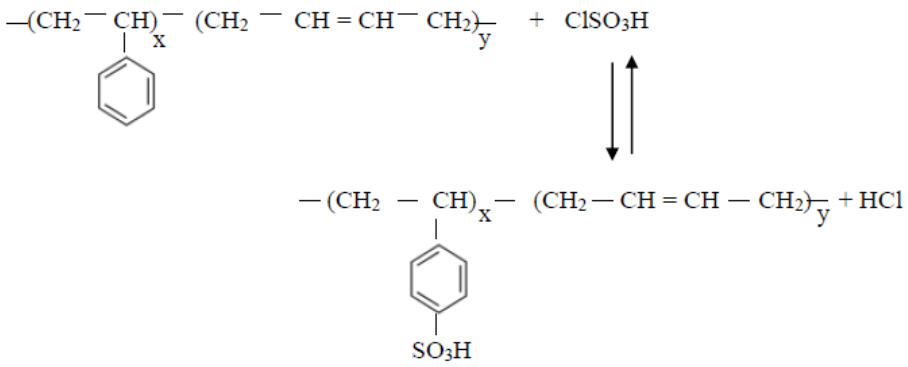


Figure 2.1: Styrene butadiene reversible sulphonation reaction equation (Idibie, 2009)

2.3.1.1 Sulphonation methods

There are two main methods of sulphonation namely post sulphonation and direct copolymerization. Post sulphonation is the common route, which has been established for a while. In this route, the 'as is' produced polymer is sulphonated by the sulphonating agent. The chemical structure and composition of the polymer dictates the extent of sulphonation rather than trying to externally control sensitive and sometimes unpredictable macromolecular sulphonation reactions (Foster, 1997). The method is therefore cheaper and simpler. The drawbacks of post modification include the lack of control over the degree and location of functionalisation. The opportunity to control and/or increase molecular weight to enhance durability using post-reaction on an existing commercial product is also limited.

In direct copolymerization, monomers are sulphonated prior to copolymerization. However, higher reaction temperatures and longer times are required to obtained high molecular weight sulphonated copolymers. Random statistical sulphonated copolymers are produced through this method. The other copolymerization methods include a series of complicated steps including metalation, sulfination and oxidation (Zhang et al., 2000). The draw backs of the latter method are that they are complex,

expensive and resulting in low ion exchange capacities. The method is also relatively new with little reported in literature. As a result post sulphonation remains the favoured route to polymer functionalisation to date (Hickner et al., 2004).

2.3.1.2 Sulphonating agents

The common sulphonating agents reported in literature include acetyl sulfate, chlorosulphonic acid and its complexes, sulfur trioxide and complexes thereof, concentrated sulfuric acid and fuming sulfuric acid (Walsby et al., 2001). The common solvents used for dissolving the polymer are the ones which are highly stable and do not react with the polymer material or sulphonating agent. The solubility parameters of these polymeric materials in terms of polarity, dispersion forces and hydrogen bonding forces must be comparable to the solvent of choice for solubility. These solvents include 1,2 dichloroethane, chloroform, n-propanol, tetrahydrofuran, toluene/methanol mixture amongst others (Knaggs and Nepras, 2005).

The sulphonation process involves cooling of the diluted sulphonating agent solution to low temperatures, followed by the addition of the sulphonating agent in an inert environment of a vigorously agitated polymer solution (Idibie, 2009). The sulphonation process is commonly terminated by the addition of ethanol and methanol. The mechanism of sulphonation has been extensively reported to be a first order or second order mechanism depending on the polymer structure. The second-order reaction takes place at the aromatic ring due to the higher electron density of the ring as compared to the carbonyl group. The sulphonation level of the polymer may be controlled by the stoichiometric ratio of the sulphonating agent to the polymer, temperature as well as concentration variation. Since aromatic polymers are relatively easier to sulphonate, the research focus shall be biased towards styrene based polymers (Knaggs and Nepras, 2005).

2.3.1.3 Challenges to styrenic polymer sulphonation

Challenges of sulphonation span from material/ingredient and processing cost to product quality. The cost drivers include the direct costs of sulphonating agent and solvent employed and the processing cost. The processing costs include the set up cost for the process, safety, the energy cost associated with temperature control, the processing time as well as the yield and efficiency factors (Knaggs and Nepras, 2005).

Strong sulphonating agents are reported to cause inhomogeneous reactions that reduce product quality. Chlorosulphonic acid is reported to induce chain cleavages during some sulfonations resulting in serious polymer degradation. Unwanted crosslinking, gelation and side reactions have also been associated with strong sulphonating agents (Zhang et al., 2000 and Rabia et al., 1996). Mitigations such as reduction of temperatures below $10^{\circ}C$, have been observed to smoothen some reactions. However, the cost of energy increases by the additional refrigeration required. Despite these setbacks, strong sulphonating agents have their own advantages over their mild counterparts. The reaction speed, the efficiency of sulphonation and high level of sulphonation is often achieved in a short period of time. Such advantages tend to reduce the material and processing costs through the consumption of less quantities and high throughput (Zhang et al., 2000).

Mild sulphonating agents often result in homogeneous reactions, ensuring minimal polymer degradation, crosslinking and side reactions. The end product is often of a better quality than those based on strong sulphonating agents. However, they have their own reported drawbacks. They include low sulphonation efficiency, huge volumes of ingredients used, thus increasing the material costs and long throughput times, which raise the cost further. Since the sulphonation process is a reversible reaction, they tend to favour the backward reaction and hence result in lower yields, efficiencies and level of sulphonation (Knaggs and Nepras, 2005).

Clearly, tradeoffs exist between strong and mild sulphonating agents, but prevention of polymer degradation and side reactions could probably outweigh longer reaction times and somewhat lower sulphonation efficiency. High sulphonation levels of between 20mol% and 80mol% have been reported for styrene butadiene based polymers using acetyl sulfate as the sulphonating agent and 1,2 dichloroethane as the solvent (Sheikh-Ali and Wnek, 2000). Idibie, 2009 reported successful and fairly smooth sulphonation of styrene butadiene rubber with chlorosulphonic acid in 1,2 dichloroethane at mild operating conditions. He reported a 55mol% level of sulphonation. Nevertheless, the ion exchenge membrane was brittle at this high degree of sulphonation. Continuous research in functionalisation techniques has resulted in continuous decrease of production costs and hence further reducing the cost of high quality ion exchange membranes at laboratory scale. If the mechanically weak synthetic rubber ion exchange membranes are properly reinforced at low cost, they will find commercial application. Therefore the next section reviews the modification of polymeric ion exchange membranes using nanomaterials.

2.4 Modification of sulphonated synthetic rubber membranes

One of the abundant polymeric synthetic rubber materials, polystyrene butadiene rubber, has attracted great attention towards a synthetic rubber based ion exchange membrane. This is due to the fact that it is readily available, cheap and easily processed (Abdulkareem, 2009). However, it has limited strength and dimensional stability (Idibie, 2009). Although chemical modification processes like crosslinking have improved mechanical properties, they are complex and costly. On the other hand reinforcement could be possible with nanofillers. Work done on polystyrene butadiene rubber and carbon nanoball composite ion exchange membrane has shown great potential for use in fuel cells, with better properties than Nafion 112 (Abdulkareem, 2009). Despite the fact that functionalisation of styrene butadiene polymers to produce ion exchange membranes has successfully been achieved,

challenges associated with mechanical integrity, and other property shortcomings are yet to be addressed.

2.4.1 Polymer nanocomposite membranes

In principle, the polymeric nanocomposite membranes are an extreme case of composite membranes in which nanometer-size (1 -100nm) particles (spheres, rods, plates, fibres) (Hussain et al., 2006) are homogeneously dispersed as separate particles in a polymer matrix (Allegra et al., 2008). The term "polymer nanocomposite" has evolved to refer to a multi-component system in which the major constituent is a polymer or blend thereof and the minor constituent has at least one dimension below 100nm (Winey and Vaia, 2007).

The transition from microparticles to nanoparticles yields dramatic changes in physical properties. Nanoscale materials have a large surface area for a given volume. Since many important chemical and physical interactions are governed by surfaces and surface properties, a nanostructured material can have substantially different properties from a larger dimensional material of the same composition. Typical nanomaterials currently under investigation include nanoparticles, nanotubes and nanofibres, fullerenes and nanowires (Baeta et al., 2009). These nanomaterials generally provide reinforcing efficiency because of their high aspect ratios. The properties of a nanocomposite are greatly influenced by the size scale of its component phases and the degree of mixing between the phases (Hussain et al., 2006).

Low volume additions (1–5%) of nanoparticles were reported in literature to provide property enhancements which are comparable to those achieved by conventional loadings (15–40%) of traditional fillers (Yasmin et al., 2006). Apart from the unique value - added properties not normally possible with traditional fillers, such as reduced permeability, optical clarity, self - passivation and increased resistance to oxidation

and ablation, the lower loadings facilitate processing and reduce component weight (Brechet et al., 2001). Thus, polymer nanocomposites have shown vast potential with regard to overcoming traditionally antagonistic combinations of properties. New blending technologies have made it possible to blend these composites to the desired level of homogeneity and hence obtain the desired properties (Hussain et al., 2006).

The matrix material has been reviewed in the previous section. Nevertheless the nanofiller material and blending technology affect the quality of the polymer nanocomposite. Hence the next section reviews the nanomaterials and blending technologies.

2.4.2 Nanofillers for nanocomposite membranes

The use of nanofillers is driven by cost reduction, improved processing, density control and improved mechanical properties notably abrasion, hardness, stiffness and tear resistance (Rothon et al., 2008). Fillers may push the cost higher if they use different equipment and processes, and hence higher energy input as well as low throughput. The raw material input cost also increases if filler does not substitute raw material. Therefore the review of different types of nanofillers, critical to the properties modification of polymers is done below towards the justification of the filler selected for blending.

2.4.2.1 Classification and size dimension

Materials that have at least one dimension less than 100nm are denoted as either nanoparticles, nanoclusters, nanocrystals, nanosheets or nanowires (Thostenson et al., 2005 and Brechet et al., 2001). Nanomaterials are found in three basic shapes namely the plate, sphere and the rod/fibre as shown in Figure 2.2 below. It was discovered that as particles decrease in size to less than 100nm, the interfacial volume around a particle can dominate the physical properties and this is particularly evident for spheres and rods (Winey and Vaia, 2007).

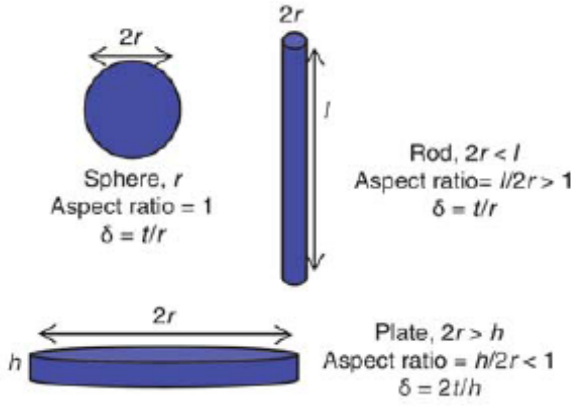


Figure 2.2: Nanomaterial shapes (Winey and Vaia, 2007)

2.4.2.2 Nanomaterials for polymer nanocomposites

Common nanomaterials used in polymer nanocomposites can be classified into montmorillonite organoclays (MMT), carbon nanofibres (CNFs), carbon nanotubes (CNTs), metallic nanoparticles and others (Thostenson et al., 2005). Montmorillonite organoclays consist of tetrahedral silicate layers of SiO_4 groups linked together to form a hexagonal network. They also comprise the octahedral alumina layers which are sandwiched by the tetrahedral layers, sharing their apex oxygens with the latter (Rothon et al., 2008). As stiffness, strength, and flame resistance increase, gas permeability and swelling in solvents decrease, implying improvement of traditionally antagonistic properties. Their disadvantage is that they are hydrophilic materials and hence must be made hydrophobic to become compatible with most polymers which are hydrophobic (Brechet et al., 2001).

Carbon nanofibres are a form of vapour-grown carbon fiber which is a discontinuous graphitic filament produced in the gas phase from the pyrolysis of hydrocarbons. The resulting nanofibers typically have an outer diameter of 60 to 200 nm, a hollow core of 30-90 nm, and a length on the order of 50 to 100 microns. The use of vapor-grown

carbon nanofibers has been proposed for providing improved mechanical, electronic and thermal transport properties to polymers (Iyuke et al., 2007).

Carbon nanotubes have high Young's modulus and tensile strength, and can be metallic, semiconducting, or semimetallic, depending on the hellicity. They are excellent candidates for stiff and robust structures. There has been intense interest in nanocomposites of polymers and carbon nanotubes because of the large change of the properties (conductivity, elasticity, viscosity, thermal conductivity) exhibited at relatively low concentrations ($\leq$ 1 % volume fraction) (Carrandi, 2008).

Metallic nanoparticles exhibit novel properties (plasmon resonance, super paramagnetism, etc). Metals undergo the most considerable property change by size reduction, and their composites with polymers are very interesting for functional applications because the properties of nano-sized metals (optical, magnetic, dielectric, and thermal transport properties) leave unmodified after embedding in polymers (Carrandi, 2008).

Nanofillers such as exfoliated graphite and silicon carbide (SiC) have been used to form polymer nanocomposites with enhanced properties (mechanical, thermal and electrical). Boron nitride (BN) is an excellent thermal conductor and electrical insulator, polymers filled with boron nitride could be good materials for dissipating heat (Rothon et al., 2008).

Limitations associated with the use of the above mentioned nanofillers for ion exchange membranes range from cost and dispersion to contradicting properties. Carbon nanotubes are difficult to disperse and align and result in a membrane of high anisotropy. Most of the above mentioned nanomaterials are electron conductive and hence disqualified for ion exchange membranes for energy generation due to short circuiting.

Other nanofillers include mineral fillers (calcium carbonate, dolomite, mica, nanoclays, crystalline silicas and calcium sulphate). Their limitations include toxicity, cost of processing to get the right purity for nanocompositing and unwanted electron conductivity. Synthetic fillers commonly used like carbon black whilst good for certain applications are disqualified for proton exchange membranes due to electron conductivity across the membrane (Jayasree and Predeep, 2008).

New nanomaterial candidate in the form of carbon nanoballs offers great potential for applications in nanocomposite ion exchange membrane due to three major reasons. Firstly, carbon nanoballs are electron insulating (Abdulkareem, 2009). Secondly, novel methods of synthesis promise to be simple, yielding nanoballs of high purity and uniformity, thus giving hope to the provision of cheap and high quality nanofillers for ion exchange membranes (Deshmukh et al., 2010). Thirdly, undesirable anisotropy is also expected to be minimized considering the spherical shape of the novel filler. Abdulkareem, 2009 reported improvements in styrene butadiene based ion exchange membrane properties by addition of 1-4% by weight carbon nanoballs. He reported reduced methanol permeability and higher power density as compared to the commercially available Nafion 112. Nevertheless, little research has been done on carbon nanoballs since more effort has been channeled towards carbon nanotubes in recent years. Therefore the next section reviews carbon nanoball as potential filler for use in reinforcement of ion exchange membranes.

2.4.3 Carbon nanoballs

The past two decades have seen the synthesis and characterisation of variously shaped carbon materials (SCM) which include tubes and fibers, onions, spheres, horns, calabashes and flasks amongst others (Deshmukh et al., 2010. Much focus has been on carbon nanotubes because of their unique and distinctive properties. Relatively, less work has been done on carbon nanoballs (spheres) besides carbon black yet recent studies have revealed their importance in critical applications like batteries,

capacitors, fuel cells, reinforcement, cathode materials for field emission, catalyst support materials, composites and purification processes (Shanov et al., 2007). The exciting focus on carbon nanoballs is due to the fact that addition of small volumes to matrix materials have been reported to improve many material properties of the matrix. If the reinforcement effect is positive, then carbon nanoballs can be ideal nanofiller for polymer ion exchange membrane.

It becomes therefore important to review the relatively new carbon nanomaterial since the incorporation of nanomaterials and prediction of the properties of the formed composite hinges on the detailed knowledge of the constituent materials including the nanofiller. The synthesis techniques affect the morphology, size, property and cost structure of the end product and hence the review.

2.4.3.1 What are carbon nanoballs (nanospheres)?

Carbon nanoballs (CNBs) are a group of shaped carbon materials with a spherical or near spherical shapes under 100nm diameter. They include balls, spheres, microbeads, carbon blacks, onions and mesoporous micro-beads (Caldero et al., 2005 and Deshmukh et al., 2010). The spheres and balls can be hollow or solid and in this survey, spheres and balls will mean the same thing. Since much of the early work has focused on the production of carbon blacks under oxidizing environments, focus of this survey will be on carbon nanoballs from inert environments. The survey will be biased towards the carbon nanoballs outside the pure fullerene family even though some fullerene based theories will be adopted because of certain similarities.

2.4.3.2 Categorisation of carbon nanoballs

Carbon nanoballs can be classified in a variety of ways. Firstly they can be described as solid, core shell or hollow. They can also be classified according to the nanometric orientation of spheres, i.e. whether the spheres are made of concentric, radial or random layers (Figure 2.3). Thirdly, they can be classified according to their

diametric size into i) fullerenes (0.7-2nm) ii) well graphitized spheres (2-20nm) and iii) less graphitized spheres (50-100nm) (Deshmukh et al., 2010). The fullerene family consists of a family of closed cage carbon atoms like $C_{n\ (n>=60)}$ and multishell fullerenes symbolized by $C_{n1}@C_{n2}@C_{n3}$.....where n stands for number of carbon atoms in each shell and 1,2,3… stand for the number of shells (Zettl and Cumings, 2001 and Prato, 1997). Finally carbon nanoballs can be classified according to the synthesis techniques since most properties, morphologies and sizes are often as a result of the synthesis route. The common synthesis methods include chemical vapour deposition (CVD), arc discharge, laser ablation and autoclave processes amongst others (Sobkowicz et al., 2009). These different techniques produce different carbon balls for nanocomposites and hence worth reviewing.



Figure 2. 3: Carbon nanoballs; a) random; b) radial; c) concentric; d) fullerenes (C_{60} and C_{70}) (Deshmukh et al., 2010)

2.4.3.3 Synthesis of Carbon Nanoballs

An extensive review of synthetic methods of carbon nanoballs has been done by Deshmulch et al., 2010. The following synthesis review was further summarized with the aim of facilitating the selection of a suitable synthesis technique with great potential for production of low cost quality nanofillers for nanocomposite ion exchange membranes.

The arc discharge methods uses materials such as acetylene, ethanol and coal as carbon sources in the presence of a catalyst at temperatures around 1100^0C. The

catalysts include carbon rod containing Fe – Ni, Ni and polyethylene terephthalate amongst others. A voltage of 40 – 50V is applied, generating a current of 50-70A between the electrodes to create the arc under low pressure (0.05–0.06MPa). Carbon balls with diameters ranging from 10nm to the micron range are produced. The disadvantages of the process are that low purity balls are formed at relatively high cost considering the process, temperature and catalyst involved. The range of carbon balls formed by size is also relatively wide, resulting in low particle uniformity (Wang and Kang, 1996 and Caldero et al., 2005).

Laser ablation is another method which uses high laser energy at high frequency, typically 40KW. The technique uses a catalyst such as iron cake, Co, Ni, MgO-Ni supported on Si amongst others. Methane gas is the common carbon source at high temperatures (700 – 1000^0C) and low pressures (1.6 -5MPa). Production of nanoballs of 5 -100nm have been reported using this technique. The cost and the wide range of size distribution of the product have been significant draw backs to the use of this technique (Deshmukh et al., 2010).

The shock compression method uses extremely high pressure of around 57GPa at high temperatures of up to 3000^0C to disintegrate fullerene or pyrolytic graphite to produce carbon spheres ranging from 8 – 300nm. This technique is expensive due to the extremely high shock pressures involved and the high temperatures used (Deshmulch et al., 2010).

Chemical Vapour Deposition (CVD) method

The common and versatile synthesis technique is the chemical vapour deposition method in which a volatile carbon source is converted into a solid non-volatile carbon product (Iyuke et al., 2007). Many variants of the process have been used due to its simplicity and hence worth emphasizing in this review. The variants are as a result of the means by which chemical reactions are initiated, the type of reactor used and the

process conditions (Deshmukh et al., 2010). The CVD process uses the following generic approaches; namely variation of the physical characteristics of the vapour, operating pressure and temperature and catalyst based reactions (Wang and Kang, 1996).

Within the variation of operating pressure class, four regimes can be identified. They are the atmospheric pressure CVD (APCVD), low pressure CVD (LPCVD), ultra high vacuum CVD (UHVCVD) and high pressure autoclave CVD (HPACVD). The variation of the physical characteristics of the vapour includes gas phase CVD (GPCVD); where process gas is added directly to the reactor, sublimation CVD (SCVD); where a solid is converted directly into a gas for use in the CVD process and the direct liquid injection CVD (LICVD); in which the precursors are in liquid form (Deshmukh et al., 2010).

In the above mentioned processes, the pyrolysis of a carbon source is generally carried out in a quartz tube reactor at high temperatures ($600 – 1100^0$C) created by an electronically controlled furnace. A number of carbon sources are available which include aromatic organic compounds, alkenes, alkanes, carbon dioxide, sugars and other organic materials rich in carbon. If a catalyst is used in the production process, then the process is called the Catalytic Chemical Vapour Deposition Method (CCVD). A wide variety of catalysts has been reported in literature. They include silica spheres, Au on SiO_2, iron doped polypyrrole, Mg, $NiCl_2$, Li, ferrocene, $AgNO_3$ and many more (Deshmukh et al., 2010). The method used in the absence of a catalyst is called Non Catalytic Chemical Vapour Deposition Method (NCCVD). There are two basic reactor configurations towards carbon nanoballs synthesis by CVD, which are the vertical and the horizontal ones. The vertical reactors have been reported to produce smaller carbon nanoballs as compared to the horizontal ones (Deshmukh et al., 2010; Jin et al., 2005 and Abdulkareem, 2009).

The objective of synthesis is to produce high quality, high yield carbon nanoballs in the simplest way at optimal cost. Such an achievement will result in low cost filler for the ultimately desired reinforced nanocomposite ion exchange membrane. Therefore an atmospheric pressure non catalytic chemical vapour deposition method (APCNCCVD) operating at fair temperatures would be ideal for producing the carbon nanoballs (Jin et al., 2005).

2.4.3.4 Carbon ball morphology and formation mechanisms

The knowledge of formation mechanisms of carbon nanoballs is critical to process and morphology control. Indirectly, such review is critical towards cost reduction and property improvement of the desired nanocomposite. The formation of the carbon nanoballs occurs too rapidly to isolate intermediate species. As a result, most of the mechanistic proposals are based on theoretical techniques (quantum mechanical and molecular dynamics) supported by experimental evidence (Fahlman, 2007). The mechanisms tend to depend on carbon source, reaction conditions (temperature, pressure, feed rate and time), catalyst, etc (Wang & Kang et al., 1996).

The main features of synthesis are the conversion of a carbon source typically into C and H radicals (and O containing radicals if O_2 is present), and nucleation to produce the carbon balls. Typically high temperatures or a catalyst will defragment the carbon source, resulting in carbon particle building blocks for the carbon ball layers. For the smaller diameter carbon spheres which fall into the fullerene family, two formation models have been proposed. The pentagon road model proposed by Smalley assumes that the graphitic sheets contain hexagons and pentagons responsible for closure of the sheets forming buckyballs and hence growth termination. The growth process initiates from linear chains which preferably connect to form more stable rings which ultimately curve to form closed sheets due to the combination of pentagonal and hexagonal rings. Depending on the number of carbon atoms, planar rings can be formed. Kroto and Mckay proposed a mechanism for large fullerenes where the

sphere is nucleated from a pentagonal ring followed by a spiral shell growth (Figure 2.4i). In contrast, the "fullerene road" model assumes the initial formation of smaller non-IPR fullerenes, which undergo thermal rearrangement to yield C_{60} and higher fullerenes (Prato, 1997 and Fahlman, 2007).

Since most carbon balls produced are non fullerenes with diameters greater than 10nm, their morphologies suggest a similar but different formation mechanism of growth. These carbon balls do not have closed graphitic layers but rather have carbon graphitic flakes arranged perpendicular to the core and produce concentric layers of carbon domains with many dangling bonds at their edges (Figure 2.4). The key difference of these spheres to fullerenes is that the curling and randomly twisted graphitic flakes are not closed shells (Caldero et al., 2005; Wang and Kang, 1996 and Miao et al., 2003).

The formation of a graphitic carbon ball typically requires the modulation of the atomic structure of each flake and the graphitic lattice to accommodate the curvature of the sphere. The illustration of the proposed growth mechanisms is shown in Figure 2.4. The presence of pentagonal and heptagonal rings is inevitable to achieve curvature as shown in (Figure 2.4). Kang and Wang, 1996 analysed the flakes in terms of heptagon, pentagon and hexagon ring structures. A combination of pentagonal, heptagonal and the planar hexagonal structure of graphene is claimed to be responsible for curved graphitic flakes, 1 to 30nm in length. The superposition of these wavy flakes, concentric layer by concentric layer, gives rise to carbon balls.

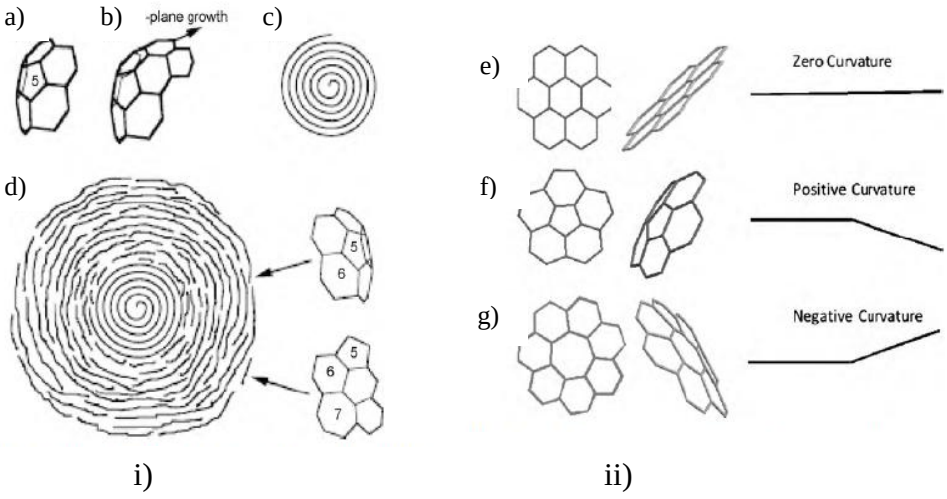


Figure 2.4: i) Nucleation of a pentagon, growth of quasi-icosahedral shell, formation of a spiral carbon particle and growth of large carbon sphere; ii) Graphitic flakes representation – hexagonal, pentagonal and heptagonal carbon rings introduce changes in the curvature of the graphitic flakes (Deshmulch et al., 2010 and Caldero et al., 2005)

The morphology of the carbon balls depends much on the type of nucleation site and combinations of the three different types of carbon rings. The pentagonal and heptagonal rings within hexagonal rings cause curvatures in opposite directions. Thus if a pair of pentagon and heptagon appear in the same hexagonal lattice, the curving of the entire lattice would be significantly reduced. The pure hexagonal rings result in flat layers. Therefore the random combination of the three different carbon rings result in different morphologies and sizes of carbon balls (Deshmukh et al., 2010; Caldero et al., 2005; Wang and Kang, 1996 and Miao et al., 2003). A curling graphitic carbon particle is claimed to be nucleated from the pentagonal carbon ring as opposed to a fullerene site. This is due to the fact that production of a fullerene precisely requires 12 pentagons per shell, which is extremely difficult to achieve experimentally. Therefore the former mechanism is proposed and backed with experimental observation.

The newly created pentagons and heptagons in the reaction chamber fall continuously on the surface of the growing spiral sphere (nucleation site). These latter carbon rings act as new nucleation sites for growing curved graphitic flakes with orientations that may not have any relation to the initial spiral layer. If the growth rates of these graphitic flakes are faster than that of the spiral layer, the particle surface is covered by a stack of randomly twisted graphitic flakes nucleated at different depth (Caldero et al., 2005).

The above mentioned proposal is consistent with experimental observations and hence generally adopted for larger carbon spheres that are commonly produced at high yields. If the properties of these relatively common carbon balls are distinctive, they will definitely contribute towards a reinforced ion exchange membrane with improved properties. The mechanistic descriptions of the formation of the other types of carbon balls, especially the radial ones have not been reported widely in literature (Deshmukh et al., 2010).

2.4.3.5 Properties of carbon nanoballs

Properties of carbon nanoballs are still under investigation considering the limitations that are still present for testing nanomaterials and the wide variety of carbon nanoball species. Despite such challenges theoretical models and estimates from experimental and analysis techniques have given approximate values which could be dependable (Wang and Kang et al., 1996). The properties can be classified into morphological, physico-mechanical, chemical and electrical properties amongst others.

Morphological properties have partly been reviewed in the previous section. The carbon balls normally exist as agglomerates of several nanoballs through van der Waals bonding. They have a brown to black colour as the thickness increases. The carbon balls have a BET surface area ranging from as low as 2 to 1200m^2g^{-1} (Jin et al., 2005 and Deshmukh et al., 2010). The density ranges from as low as 0.4 to 1.6 g

cm^{-3} depending on the synthesis procedures (Mhlanga et al., 2010). They can be porous or hard spherical solids depending on process and treatment routes. The interspacing of the graphitic layers varies from 0.3 to 0.4 nm, with a core shell of between 3 and 4nm. These morphological properties are essential for tailor making the properties of ion exchange membrane such as weight to strength ratio, dispersion efficiency, etc (Miao et al., 2003).

The chemical reactivity of carbon spheres is somewhat similar to those of graphitic materials. They appear to be insoluble in non polar solvents and sparingly soluble in most solvents because of their hydrophobic nature. However, solvents such as chloroform, benzene, methanol and toluene have resulted in miscibility (Sobkowicz et al., 2009). The presence of dangling bonds has enabled carbon balls to be functionalised by acids like nitric acid (Kang and Wang, 1996). Therefore fullerene-like sites in spherical carbons are expected to act as free radical acceptor sites, which have implications for rubber filler interactions (Wang et al., 2005).

The degree of graphiticity of carbon nanoballs determines their electrical properties. A low ratio of the ordered graphitic layers to the disordered layers (I_G/I_D) implies low electron conductivity whilst a high ratio (typically greater than 2) implies good electron conductivity. Ramman spectra have shown the ratio varying from as low as 0.5 to as high as 5 depending on synthesis route and post treatment (Shanov et al., 2007 and Jin et al., 2005).

Although the physical properties have not yet been fully established, approximations have been made based on the use of AFM and other nanotechnology instruments as well as theoretical models. TGA has shown carbon spheres to be thermally stable up to a temperature range of 400 to 600^0C (Jin et al., 2005). The theoretical values of Young's modulus for fullerenes have been estimated between 8.8 and 16GPa depending on temperature (Zettl and Cumings, 2001). Levin et al., 2003 estimated the bulk modulus of fullerene at 12GPa. Above 260K, molecular rotational orientation

ordering transition occurs to fullerene from sc to face centred cubic (fcc) crystal structure. Such transition is claimed to be responsible for the change in mechanical properties. Classical measurements on carbon spheres have estimated a compressive strength of 0.7 to 0.9GPa and tensile strength of 7 to 9GPa (Deshmukh et al., 2010). Since little is reported in literature, estimates based on fullerenes and classical theories shall aid significantly in analysis and discussions of the reinforcement work (Ruoff and Hickman, 1993).

The knowledge of carbon nanoballs properties and the synthesis techniques that give rise to them is critical towards the selection and tailoring of the synthesis methodology to achieve the desired objectives. A cost effective method of producing high quality carbon nanoballs for polymeric nanocomposite is aided by the above review of carbon nanoballs. However, the blending technologies are critical towards the desired reinforced rubber ion exchange. Therefore the next section briefly reviews the blending technologies.

2.4.4 Blending technologies

Despite the great potential of nanofillers in reinforcement of ion exchange membranes, lack of appropriate, effective and efficient blending methods might hinder the realization of the anticipated benefits. A good blending technology must achieve homogeneity and maximum matrix - nanofiller interaction through effective dispersion of nanofiller (Bhattacharya et al., 2009). The blending must not give rise to high cost of processing due to significant reduction of throughput, complicated additional equipment and energy intensive processes. Hence the blending technology selection takes into account the above mentioned factors to come up with an optimal process that ensures the intended benefits of reinforcement and property improvement (Cho, et al., 2009). The commonly used nanofiller dispersion methods are briefly reviewed below.

2.4.4.1 Solution processing

In this process, the nanoparticles are easily separated and dispersed (weak forces that separate the nanoparticles) in an adequate solvent in which the sulphonated rubber and nanofiller are soluble. Agitation and stirring mechanisms can also be used to facilitate homogeneous dispersion. The filler is trapped in between the polymer chains, and when the solvent is evaporated, the nanofiller blends with the polymer to form an ordered, nanocomposite structure (Yasmin et al., 2006).

Mixing is enhanced by different methods. Ultrasonication, whereby nanoparticles are dispersed by ultrasonic waves is commonly used in recent times due to better dispersion (Sobkowicz et al., 2009 and Ramanathan et al., 2007 and Shanov et al., 2007). The airjet method is another effective method where the nanofiller - polymer mixture/ suspension/solution is violently agitated for a specific time with an airjet dispersion apparatus operating at high pressure (Crowley and Welch, 1954). Mechanical agitation methods use baffles to disperse the nanofillers into the matrix.

2.4.4.2 The sol–gel method

Basically, sols are dispersions of colloidal particles (size 1–100 nm) in a liquid and a gel is an interconnected, rigid network with pores of sub micrometer dimensions and polymeric chains whose average length is greater than a micron. In the sol gel method, the nanofiller material reacts with the matrix material and hence a solution to gel transition occurs to form a rigid two phase composite system of solid nanomaterial and solvent filled pores (Nagarale et al., 2006).

2.4.4.3 Melt processing

The nanoparticles are mixed with the polymer in the molten state. If the nanomaterial surface is compatible enough with the selected polymer, it can be inserted into the

interlayer space and form the final nanocomposite. In this case, no solvent is required (Miller, 2008).

2.4.4.4 In-situ polymerization

In this process, the monomeric units of the polymer, the initiator and the nanoparticles are added to the polymerisation reactor. As polymerisation takes place, the generated polymer chains separate the nanoparticles as they grow forming the polymer nanocomposite (Brechet et al., 2001).

2.4.4.5 Comparison of dispersion techniques for nanoparticles

A few researchers have investigated different dispersion techniques in an effort to maximize the nanoparticle effect. Earlier work by Crowley and Welch, 1954, showed that ultrasonication yielded exceedingly better results of nanofiller dispersion and blending as compared to the air jet method and mechanical agitation methods. Factors like increasing the energy of transmission, direct ultrasonication as opposed to bath sonication as well as increasing the time of sonication yielded better dispersion. Ramanathan et al., 2007 reviewed the different methods of blending of graphitic nanofillers on polymer nanocomposites as shown in Table 2.1. Both negative and positive results were obtained from the methods used. All of the methods were still far from perfect and hence the need for further work on dispersion of nanofillers.

Table 2.2: Comparison of effect of different blending technologies on Young's modulus (Ramanathan et al., 2007)

Nanocomposite	Nanofiller, wt%	Blending Technique	% Increase in E
PMMA/EG	0.5 - 3	Solution	3.5 - 11
PMMA/Graphite	0.5 - 5	Solution	-3.5 - -1.1
Epoxy/EG	0 - 9	Solution	0
GNP/Epoxy	2	Solution + Sonicate, 2hrs	-16
GNP/Epoxy	2	Solution + Sonicate, 8hrs	13
Nylon 6/GNP	0 – 4	Insitu	20
Nylon 6/FG	0 – 3.5	Insitu	0
PMMA/GNP	0-6	Insitu	0
PMMA/EG	0 - 10	Insitu	0
Epoxy/EG	1 - 3	Shear Mixing	25.7
HDPE/EG	3	Melt Blending	16.8

2.4.4.6 Challenges to polymer matrix- nanoparticle blending

Despite the rapid development of understanding of the synthesis processes, dispersion of nanomaterials is one of the major issues due to the agglomeration nature of these materials (Brechet et al., 2001). On the other hand, the blending process is an addition to the production process implying higher cost due to new capitalization cost and increased production cost.

Agglomeration of nanoparticles as observed in carbon nanospheres, bundling nature of fibrillar nanomaterials like carbon fibres and tubes, presence of impurities and poor nanofiller – polymer compatibility makes dispersion difficult to achieve (Shanov et al., 2007; Brechet et al., 2001 and Yasmin et al., 2006). Nanofibres and tubes are also difficult to align and hence cause undesirable anisotropy. Failure to achieve desired dispersion was reported to impact negatively on the mechanical and other desirable properties of nanocomposite ion exchange membranes. With effective homogeneous dispersion of nanoparticles to polymeric materials, small filler loadings of 1wt% have improved mechanical properties by more than 100%. Barrier properties have also been reduced by 50 -500 times at very low loadings. Therefore the control of

dispersion quality is critical in enhancing the mechanical properties of ion exchange membranes (Guillermo, 2007).

The cost of blending is driven by the blending technique. Conventional methods use energy intensive high shear force to produce homogenous blends. However, fibers such as carbon nano-fibers are damaged, leading to reduction of aspect ratio and consequently compromising the mechanical properties (Guillermo, 2007). Energy intensive methods results in high energy cost which can impact negatively on the cost. Novel blending techniques which allow structured and synthetic dispersion are being investigated to optimize the cost and dispersion level. Therefore an ideal blending technique must be low cost, highly reliable, high production throughput, simple to operate, low maintenance, low energy consumption, low weight and space requirement (Dortimundt and Doshi, 1999). A combination of high dispersion quality and low cost process would definitely accelerate the commercialization of polymer nanocomposite ion exchange membranes.

The review so far, has covered the synthesis of polymer nanocomposites constituents and their properties and potential benefits. This review was aimed to give the fundamental background to the core of the research which is centred on reinforcement of synthetic rubber ion exchange membrane by nanofillers. Since the constituents are to be produced locally rather than off-shelf, the previous review was critical. The next section reviews the mechanical properties of polymer nanocomposite as the key measurement in the reinforcement of synthetic rubbers.

2.5 Mechanical properties of Ion Exchange Membranes

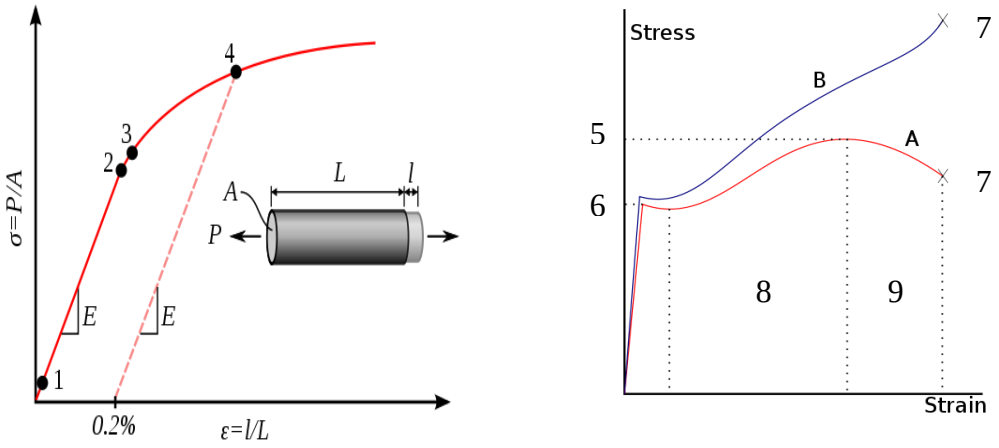
The reinforcement goal of improved mechanical properties is driven by durability (Huang et al., 2006). The strength of a polymeric ion exchange membrane has been observed to decrease over time as a result of polymer degradation. The loss in strength will cross a critical threshold resulting in a breach which grows rapidly until

a catastrophic loss in performance (Sue et al., 1994 and Sata, 1991). Depending on the operating environment and type of assembly, a membrane can take the following states; taut (where the membrane carries a tensile load), slack (free of stress and do not possess any stiffness) and wrinkled (uniaxial stress states) (Hornig and Schoop, 2003). Thus one of the major functions of the composite membrane is to mechanically support the membrane during operation, thus offering dimensional stability, robustness as well as durability as required by the customer. Therefore reinforcement evaluation and understanding of the mechanical behaviour of polymer membranes are worthy reviewing in this section (Yan et al., 2006).

This section thus briefly looks at the various mechanical property measures for reinforcement and their understanding, reinforcement mechanisms and finally the review of models that have been established for polymeric nanocomposites.

2.5.1 Measures of mechanical properties of polymeric materials

In order to have an insight into the resistance of a material to failure or crack growth, it is essential to carry out the mechanical property measurements. The measures of mechanical properties have been extensively and thoroughly studied and established in literature as presented in Figure 2.5. The mechanical property measures can be classified into stability, strength, ductility, hardness and endurance measures.



1: True elastic limit
2: Proportionality limit
3:Elastic limit
4: Offset yield strength
5: Ultimate Strength
6:Yield Strength
7:Tensile Strength
8:Strain hardening region
9: Necking region
A: Apparent stress (F/A_0)
B: Actual stress (F/A)

Figure 2. 5: Graphical representation of mechanical property measures

2.5.1.1 Stability measures (Elasticity and Stiffness measures)

The modulus of elasticity, also called the Young's modulus, E (MPa) or the Tensile or Elastic modulus, *($E = \Delta\sigma/\Delta\varepsilon$)* is a measure of the stiffness of the material in the linear region of the stress strain curve where Hooke's Law applies (Figure 2.5). E was found to be correlated to two other fundamental stiffness measures; G, (MPa), the Shear modulus, which is the initial, linear elastic slope of the stress-strain curve in shear and K (MPa), the Bulk Modulus, which measures the elastic response to hydrostatic pressure. A material subjected to uniaxial tension will exhibit some shrinkage in the lateral direction. The ratio of lateral strain and axial strain is defined as Poisson ratio, ν. Elastomers have a poisson ratios just under 0.5 implying that they are incompressible, whilst solids have a value of ν close to 1/3. For isotropic materials E is related to K and G by the Poisson ratio, υ, through $E = 3(1-2\upsilon)K$ and $E = 2(1+\upsilon)K$. Hence for solids, υ = 1/3, and hence E = K, and E = (8/3) G. For rubbers, ν = 0.48, E = 0.12K and E = 2.96G

Since the measures for elasticity are correlated, one measure can be adequate for stiffness evaluation (Askeland and Predeep, 2003). Approximations of other unknown stiffness measures for nanomaterials are also facilitated by the knowledge of one measure through the above mentioned relations.

Anisotropy, (X/Y), is the property of being directionally dependent, as opposed to Isotropy, which implies homogeneity in all directions. It can be defined as a difference, when measured along different axes, in a material's physical property, e.g. Tensile Strength, σ_s in the y and x direction (σ_{sx}/ σ_{sy}). For many polycrystalline materials the grain orientations are random before any deformation is done. Although the individual grains are anisotropic, the property differences tend to average out and, overall, the material is isotropic. Formation methods often make grains distorted and hence anisotropic. Therefore the formation measures are essential in improving the isotropy of the membrane (Askeland and Predeep, 2003).

Creep is the tendency of a solid material to slowly move or deform permanently as a result of long term exposure to levels of stress that are below the yield strength of the material. The rate of this deformation is a function of the material properties, exposure time, exposure temperature and the applied load. Creep always increases with temperature. The deformation may become so large that a component can no longer perform its function. The creep of a material can be divided into three stages. In the first stage, or primary creep, deformation starts at a rapid rate and slows with time. Second stage (secondary) creep has a relatively uniform rate. Third stage (tertiary) creep has an accelerating creep rate and terminates by failure of material at time for rupture.

2.5.1.2 Mechanical strength measures

The Yield Strength**,** σ_y (MPa) is defined as the stress applied to the material at which plastic deformation starts to occur while the material is loaded. The Tensile strength,

σ_S (MPa), is the nominal stress at which the material, loaded in tension separates. For brittle solids: ceramics, glasses and brittle polymers - it is much less than the compressive Yield strength. For metals, ductile polymers and most composites - it is larger than the Yield strength by a factor ranging from 1.1 to 3. The Ultimate Tensile Strength (UTS), σ_{UTS} (MPa), is a material property which defines the maximum load the material can sustain (Askeland and Predeep, 2003).

2.5.1.3 Ductility measures

Strain refers to the amount of stretch or elongation the specimen undergoes during tensile testing expressed as the ratio of the change in length to the original length. It can be expressed either as engineering strain, e, or true strain ε (based on instantaneous parameters).The tensile ductility is the permanent increase in length of a tensile specimen before fracture, expressed as a fraction of the original gauge length (Pavlina and Van Type, 2008).

The Fracture Toughness, K_C (MPa.$m^{1/2}$), is a measure of the resistance of a material to the propagation of a crack. It can be measured by loading a sample containing a deliberately-introduced crack of length 2c and then recording the tensile stress σ at which the crack propagates. Fracture toughness is then calculated by $Kc = Y\sigma\sqrt{(\pi c)}$, where Y is a geometric factor, near unity, which depends on details of the sample geometry. Ductile materials are complex to characterize due to a plastic zone that develops at a crack tip with new crack propagation features. Therefore this conventional evaluation for elastomers is difficult. The Fracture toughness of elastomers is therefore approximated by the energy required to fracture the specimen and hence the area under the stress strain curve in (J/cm^3) (Anderson, 1995).

2.5.1.4 Hardness measure (MPa)

The Hardness of a material, H, measured by pressing a pointed diamond or hardened steel ball into its surface, is defined as the indenter force divided by the projected area of the indent. It is related to the Yield strength, σ_y of ductile materials by $H = 3\,\sigma_y$. Due to this relationship, hardness of a material may be inferred from the yield strength measurement or vice versa (Askeland and Predeep, 2003).

2.5.1.5 Endurance measures

In membrane applications, materials are subjected to vibrating or oscillating forces. The behavior of materials under such conditions differs from the behavior under a static load since the material is subjected to repeated load cycles. Therefore Fatigue strength, σ_f, is the stress level below which a particular material will survive an indefinite number of load cycles. The Endurance Limit, σ_L is defined as the maximum applied cyclic stress amplitude for an 'infinite' fatigue life. Generally 'infinite' life means more than 10^7 cycles to failure. Fatigue life, N_F, is defined as the total number of cycles to failure under specified loading conditions (Budynas, 1999).

Low Cycle Fatigue (LCF) is the service environment of materials characterized by low frequency, large loads/strains above the yield strength like (heat-up/cool down cycling) and other load conditions like thermal and/or mechanical cycling. High Cycle Fatigue (HCF) results from vibratory stress cycles at frequencies which can reach thousands of cycles per second induced from various mechanical sources. HCF is predominantly elastic, and stress levels are below the yield strength of the material.

Fatigue is explained in four stages namely crack nucleation, crack growth (stage1), crack growth (stage 2) and ultimate ductile failure. The fatigue life is affected by the cyclic stress state (stress amplitude, mean stress, biaxiality, load sequence), geometry (notches and stress concentrations), surface quality (stress concentrations), material

type, residual stresses, size and distribution of defects, direction of loading, grain size, environment and temperature.

Generally for steel, it has been shown that the Fatigue Strength lies from 32% to 50% of the Ultimate Tensile Strength. The relationship for brittle and ductile materials can be estimated from this relationship. This relationship also makes inference of fatigue property acceptable given the ultimate strength of a material (Budynas, 1999).

Therefore a combination of reinforcement path and material selection is helpful in improving the fatigue properties of materials. Nanoparticles, especially spherical ones will improve fatigue life because of the size scale as well as their isotropic geometry. The nanocomposite yield strength gives an idea of the suitability of a membrane for specific service environments as reported in literature.

From the above review, it can be seen that the complete evaluation of the mechanical properties from stability measures to endurance measures, might adequately determine the critical mechanical properties of reinforced ion exchange membranes. However, other factors, outside the scope of this work, which include chemical stability in the dynamic operating environment, must be incorporated for a comprehensive durability assessment.

2.5.2 Reinforcement mechanisms

The understanding of material properties like Young's modulus hinges on the understanding of materials from the atomic or molecular level. The mechanical properties are affected by intermolecular/atomic bonds and the way molecules/atoms pack together. The behavior of the materials under applied loads is critical to review towards the design of reinforced materials for applications (Ashbey and Jones, 1980).

2.5.2.1 Bonding of particles in materials

There are two main bonding types affecting the mechanical properties namely covalent bonding (intramolecular forces), and non-covalent bonding (intermolecular forces). They can also be classified according to magnitude of strength into primary and secondary bonds. Primary bonds include ionic, covalent or metallic bonds, which are all relatively strong. Ceramics and metals are entirely held together by primary bonds – the ionic and covalent bond in ceramics and the metallic and covalent bond in metals (Ashbey and Jones, 1980).

The ionic bond is as a result of the presence of oppositely charged particles held together by extremely strong electrostatic interactions. The force of separating these particles was found to be directly proportional to the charge on the ion and inversely proportional to the square of the separation distance *($F = q2/4\pi\varepsilon_0 r^2$, where q is the charge on each ion, e the permittivity of vacuum, and r is the separation of the ions*). The work done as the ions are brought to a separation r (from infinity) is integration $Fdr = U = q2/4\pi\varepsilon_0 r$. As r decreases, more work is gained until r = 1nm. For r < 1nm, further work is gained the ionic bond becomes more stable. When the ions get close enough together, the electronic charge distributions start to overlap one another causing a very large repulsion. The ionic bond is then most stable at the minimum point in the U(r) curve, which is well approximated by $U = Ui - q2/4\pi\varepsilon_0 r + B/r^n$. The ionic bonding model could be useful in nanocomposite analysis since separation distances, r for fillers vary with filler concentration within the matrix material and vice versa. The ionic moieties present in the polymer also introduce ionic bonding which cannot be ignored (Ashbey and Jones, 1980 and Green and Spain, 1973).

In covalent bonds, the proximity of adjacent nuclei creates a new electron orbital shared by the two atoms, into which the two electrons go. This sharing of electrons leads to reduction in energy and the formation of a stable bond. Depending on orbital shape many other covalent bonds show various kinds of directionality which in turn

determines how atoms pack together to form crystals. This packing is critical to filling polymers with nanoparticles. The energy of a covalent bond is described by the empirical equation; $U = - A/r^m – B/r^n$. Carbon atoms in organic materials like synthetic rubber are held together by covalent bonds. However, this type of bond was found not to be of significant importance to the mechanical properties of the synthetic rubbers as compared to the weaker secondary bonds which operate across polymer chains (Ashbey and Jones, 1980).

Secondary bonds

Although much weaker than primary bonds, secondary bonds are of great importance to polymers and carbon nanomaterial composites. This is due to the fact that they are the dominant bonds binding polymer chains and the nanoparticles together. Therefore they have a significant bearing on the mechanical properties of rubber nanocomposites. There are three main types of secondary bonds namely Van der Waals forces, dipole-dipole interactions and hydrogen bonding (Ashbey and Jones, 1980 and Zhang et al., 2000).

Van der Waals forces are weak interactions between uncharged particles caused by momentary changes in electron density in a molecule. The instantaneous change in electron density distribution causes unsymmetry which results in a dipole moment. This moment induces a like moment on a nearby atom and the two dipoles attract such that their energy varies as $1/r^6$. Thus the energy of the Van der Waals bond has the form, $U = -A/r^6 + B/r^n \quad (n \approx 12)$. The van der Waals forces are the only attractive forces in nonpolar materials. Although these forces exist in all materials, they are more dominant in polymers, linking the polymer chains together. Despite the fact that C-C chains in polymers are linked by strong covalent bonds, the van der Waals interchain interactions are responsible for the strength of most polymers. The strength of the van der Waals interactions increases with increasing surface area of a particle (Zhang et al., 2000 and Ashbey and Jones, 1980).

Dipole—dipole interactions are the attractive forces between the permanent dipoles of two polar molecules. The dipoles in adjacent molecules align so that the partial positive and partial negative charges are in close proximity. These attractive forces caused by permanent dipoles are much stronger than weak van der Waals forces. The presence of functional groups in ion exchange materials increase the polarity of the material and may often result in dipole – dipole interactions. Thus the bonding and shape, type and strength of intermolecular forces, physical properties, chemical reactivity are affected by the presence of the ionic groups (Ashbey and Jones, 1980).

Hydrogen bonding occurs when a hydrogen atom bonded to O, N, or F, is electrostatically attracted to a lone pair of electrons on an O, N, or F atom in another molecule. Each hydrogen atom gives up its charge to the nearest oxygen atom (which then acquires a negative charge). The positively charged H atom (proton) acts as a bridging bond between neighbouring anions, partly because the charge redistribution gives each molecule a dipole moment (Ashbey and Jones, 1980).

2.5.2.2 Relationship between types of bonding and mechanical properties

From the survey, the following can generally be noted; i) the force F, for any separation of the particles, r, is given by, $F = dU/dr$, where U is the work required to separate the particles, ii) F is zero at the equilibrium separation r_0; however, if the atoms are pulled apart by distance $(r-r_0)$, a resistive force proportional to $(r-r_0)$ at small $(r-r_0)$ is observed for all materials, in both tension and compression. The stiffness, S, of the bond is given by $dF/dr = d^2U/dr^2$. When the stretching is small, S is constant and equal to $S_0 = (d^2U/dr^2)_{r=r0}$, that is the bond behaves in a linear elastic manner. This is the physical origin of Hooke's Law and the Young's modulus which are critical to reinforcement evaluation, iii) The strength of the bond is inversely proportional to the distance from the equilibrium position (Ashbey and Jones, 1980).

From the bonding theory upper limits of stiffness constants for different materials have been established as shown in Table 2.2 **(**Ashby and Jones, 1980). For metals and ceramics the theoretical and experimental values of E match. However for a whole range of polymers and rubbers, there exist some with moduli which are far much lower than theoretical values (by up to a factor of 100) (Zhang et al., 2000). This is due to the fact that various bonding types act in these polymeric materials. The influence of these bonding types on mechanical properties become more complex creating the need for further research for polymeric composites.

Table 2.3: Bond types and stiffness constants (Ashbey and Jones, 1980)

Bond Type	**S_0/Nm^{-1}**	**Approximate E from $(S_0/r_0)/GNm^{-2}$**
Covalent, C – C Bond	180	1000
Pure Ionic,e.g. Na – Cl bond	9 - 21	30 - 70
Pure Metallic, e.g. Cu-Cu	15 - 40	30 - 150
H-Bond, e.g. H_2O – H_2O	2	8
Van der Waals (waxes, polymers)	1	2

2.5.2.3 Mechanisms of reinforcement in polymer nanocomposites

Blends reinforced with fillers generally show an increase in modulus, hardness, tensile strength, abrasion, tear resistance as well as resistance to fatigue and cracking. The critical parameters that control the mechanical behavior of filled polymer blends are the physicochemical properties of the constituents, polymer-filler interactions, complexity of filler particles and their aggregation, the large range of particle dimensions and the distribution and dispersion of filler in each phase of the blend (Jayasree and Predeep, 2008). Ahmed and Jones, 1990 observed that the modulus of a filled resin results from a complex interplay between the properties of the individual constituent phases; the resin, the filler and the interfacial region.

In comparing a microcomposite and a nanocomposite with the same volume fraction of a filler, it has been shown that the mean particle–particle separation for the nanocomposite is smaller by three orders of magnitude, the total internal interfacial area increases by six orders of magnitude, and the number density of constituents increases by nine orders of magnitude (Yan et al., 2006). For the rubber matrix, properties are related to the size of the polymer chain, which can be expressed as the radius of gyration, R_g (the second moment of the three - dimensional distribution of the monomers of the polymer chain—approximately the expanse of the molecule). R_g is on the order of 3–30 nm (Crosby and Lee, 2007 and Hooper and Schweizer, 2003). Therefore the increase in surface area and number density and the reduction in particle separation distance all contribute towards high stiffness, tensile strength and fracture toughness.

The complete dispersion of nanoparticles in a polymer maximizes the number of available fillers that carry an applied load and deflect the evolving cracks. Nanofillers also deviate tear paths thereby restricting crack propagation and improving fracture toughness and tensile strength. The coupling between the large surface area of the particles and the polymer matrix facilitates the stress transfer to the reinforcing phase allowing for the improvement of the tensile stress and toughness (Miller, 2008).

It is worthy to note that when the fillers are reduced to the nanoscale size, the volume of the interfacial region exceeds the volume of the particle. The *V*interface/*V*particle ratio, therefore increases from plates to rods to spheres as the fillers change from two – dimensional (sheets) to one - dimensional (wires) to zero - dimensional (sphere) objects. The magnitude of this change increases dramatically as the filler size drops; demonstrating the impact that a small volume fraction of filler has on the surrounding polymers (Crosby and Lee, 2007). The importance of polymer–particle interactions is amplified in polymer nanocomposites such that the interface and the co-operativity between particles dominate the macroscopic properties. Van der Waals forces between particles, are more pronounced for nano -sized particles because of lower

surface roughness, smaller average particle separations, and thus higher dispersive forces (Moniruzzaman and Winey, 2006). These high - aspect - ratio, nanoscale fillers can reach percolation thresholds at 1–5 vol% and thereby exhibit large increases in bulk mechanical and transport properties at these low loadings (Yan et al., 2006).

The high degree of reinforcement observed in the primary particle size range of 10 – 100nm on work done on synthetic rubber and filler blends is attributed specifically to the adhesion type of interaction between the amorphous filler and the polymer macromolecules. The small particle size of the fillers has been reported to be of prime importance in elastomer reinforcement where as the chemical nature of the filler appears to be of secondary importance. In the case of carbon-black filled elastomers, the presence of different active centers on its surface participate in the formation of chemical as well as physical bonding between the filler and the matrix molecules improving the tensile strength of the blends. The surfaces of the filler act as stress homogenizers allowing slippage and redistribution of stress among polymer chains. They also serve to deflect or arrest growing cracks (Thostenson et al., 2005).

The mechanism of mechanical rupture of polymer chains during processing gives free chain ends which react with free radicals on the C-black, resulting in giant crosslinks at the morphological scale. The crosslinked composite results in a stiffer, stronger and tougher product with enhanced mechanical properties (El-Lawindy, 2002). The sliding of polymer molecular segments across the filler interface is a mechanism for energy dissipation. The dissipation of strain energy by additional relaxation mechanisms introduced by C-black also contributes towards the improvement in the tensile strength of the blend (Osman et al., 2000). The case of carbon black - elastomer nanocomposite was worthy taking note of due to the graphitic similarities between carbon black and carbon nanoballs.

2.5.2.4 Failure mechanisms in membranes

Mechanisms such as shorts due to punctures by carbon fibers, pinholes due to defects in the membrane, thinning due to oxidative degradation, thinning due to creep in compression and tears due to stresses present in the plane of the membrane have been proposed. Edge failure is commonly observed as a tear or hole in the membrane at or near the GDL edge in operating fuel cells. The very thin membranes used in many commercial fuel cells are simply not strong enough to resist either the sharp edges of the GDL or the stresses present in the region that is unsupported between the GDL and gasket. It is believed that improvements in membrane strength will significantly reduce these and other failures (Seon et al., 2004). The membrane production methods also contribute to the failure mechanisms. Extruded membranes are mechanically stronger in the machine direction than the transverse direction whilst cast membranes show random behavior.

Therefore the understanding of bonding mechanisms, reinforcement and failure mechanisms is essential in the development of an effective reinforcement methodology for ion exchange membranes. The selection of composite constituents and membrane production process are enhanced from this review as well. The next section therefore reviews the models developed for the prediction of reinforcement effects of various nanofillers on matrix materials.

2.5.2.5 Models of reinforcement

Scientists have given mathematical models for predicting the mechanical properties of heterogeneous materials. The investigations of Einstein, Smallwood, Guth , Kraus, Cuneen – Russell, Kerner, Mooney, Thomas, Nielsen, Queamada and Frankie-Acrivos are of prime importance in predicting the Elastic Modulus of composites at low filler loadings (Yan et al., 2006). The different models are summarized in Table 2.3. The theories for the strength of filled systems is less developed than that for the

moduli as pointed out by Nielsen. Verbeck, Nicolais and Narkis and Nielsen have developed models for the tensile strength as shown in Table 2.4. All of the models have been developed based on the properties of the constituents of the composite and factors like geometry, packing factors, e.t.c (Odegard et al., 2005 and Zeng et al., 2008). Most models show an increase of mechanical properties with increasing filler content. This trend is consistent with the theories reviewed in previous sections on bonding.

Table 2.4: Models for prediction of elastic modulus, E of nanocomposites (Ahmed and Jones, 1990; Seon et al., 2004 and Yan et al., 2006)

Model	**Equation**
Einstein	$E_R = 1 + 2.5\Phi$
Guth	$E_R = 1 + 2.5\Phi + 14.1\Phi^2$
Mooney	$E_R = \exp\left[\frac{2.5\Phi}{1-\frac{\Phi}{\Phi_m}}\right]$
Kerner	$E_R = \frac{G_f\Phi/[(7-5\upsilon)G_p + (8-10\upsilon)G_f] + \Phi/[15(1-\upsilon)]}{G_p\Phi/[(7-5\upsilon)G_p + (8-10\upsilon)G_f] + \Phi/[15(1-\upsilon)]}$
Thomas	$E_R = 1 + 2.5\Phi + 10.05\Phi^2 + 0.00273\exp 16.6\,\Phi$
Quemada	$E_R = \frac{1}{(1-0.5K\Phi)^2}, K - Usually\ 2.5$
Nielsen	$E_R = \frac{1+A\Phi}{1-\Psi\Phi}, A = f(geometry), \Psi = 1 + (\frac{1-\Phi_m}{\Phi_m^{\,2}})\Phi$
Frankie-Acrivos	$E_R = 1 + \frac{9}{8}\left[\frac{(\Phi/\Phi_m)^{\frac{1}{3}}}{1-(\Phi/\Phi_m)^{1/3}}\right]$

E_R = relative modulus, Φ = volume fraction of filler, G_I = shear modulus of filler, G_p = shear modulus of polymer, v Poisson ratio of polymer, Φ_m, maximum packing fraction of filler.

Table 2.5: Models for predicting the tensile strength of nanocomposites (Ahmed and Jones, 1990; Seon et al., 2004 and Yan et al., 2006)

Name	Model	Notes
Verbeek model	$\sigma_c = V_p\sigma_p + K_3\tau_p MPF$ $\mu = \alpha(\frac{G_p V_f}{E_m(1-V_f)})^{1/2}$ $MPF = V_f(\frac{\propto}{\mu})(\frac{1}{\tanh(u)} - \frac{1}{\mu})$	G_p = Shear modulus of the polymer σ_c = Tensile strength of the composite τ_p = Shear strength of the polymer K_3 = Correction factor MPF = Strength reduction factor
Nielsen model	$\sigma_C = \sigma_p(1 - V_f^{\frac{2}{3}})K$	σ_p = Tensile strength of the polymer K = Stress concentration factor
Nicolais–Narkis model	$\sigma_C = \sigma_p(1 - 1.21V_f^{\frac{2}{3}})$	V_f = Volume fraction of filler

2.5.2.6 Comparison of theoretical models and experimental trends

Models developed by different investigators have generally been inconsistent in predicting the reinforcement effect of nanofillers on matrix materials. Wu proved theoretically that disc-shaped particles gave better reinforcement than, needle or spherical shaped particles but ignored the anisotropy associated with non-spherical particles in the composite (Bigg, 1987). Whilst some models have postulated that the elastic modulus for a given particle and matrix depend only upon the volume fraction of filler and not the particle size, it has been generally observed that the modulus increases as the particle size decreases. One theory assumed that the non-bonded particles acted as holes and therefore, predicts a decrease in modulus with increasing filler content. In work done on some silica filled polymers, the experimental values

lied far above the theoretical values for all filler content, implying strong polymer filler adhesion (Seon et al., 2004). Therefore the existing models find it difficult to adequately incorporate activities that occur at the matrix – filler interface.

There are many reasons for such variances reported in literature. The contradictions are due to the complex factors to consider in the interactions between matrix and filler particles and hence the need for further investigations. Firstly, most of the theories which explain the reinforcing action of a filler assume perfect adhesion between the filler and the polymer matrix, yet there is imperfect adhesion in reality. The degree of adhesion may have little effect on reinforcement since there may not be any relative motion across the filler-matrix interface (Ikeda et al., 1997). The incorporation of a coupling agent also further complicates the modeling. Spanoudakis and Young therefore concluded that the modulus of a filled system is a detailed function of interfacial adhesion. The nature of imperfection may either result in stronger or weaker bonds resulting in the variations between experimental and theoretical results. Secondly, a mismatch in the coefficients of thermal expansion of filler and matrix is reflected as a mechanical bond resulting from thermally induced stresses (Zhanga et al., 2005).

It has also been difficulty to incorporate the effect of particle size. Some models depict an increase in reinforcement effectiveness with increasing particle size, especially at higher volume fractions. For example, fine silica and chalk particle sizes were reported to be more effective than the larger ones in polystyrene reinforcement. On the other hand, there were no observed differences between fine and coarse glass beads, in a thermosetting polyester resin. In the latter case, reinforcement appeared not to be affected by particle size (Seon et al., 2004). The effects of agglomeration have also been difficulty to model and hence theoretical models are still not yet adequate to predict reinforcement effects of fillers on matrix materials.

In conclusion, the literature review has provided the strong basis for selection of nanocomposite constituents, blending methodology and reinforcement evaluation.

CHAPTER 3: MATERIALS AND METHODS

3. Experimental procedures for reinforcement evaluation

The general steps involved in this synthetic rubber ion exchange reinforcement work were: (i) selecting the polymer matrix material, ii) selecting the nanoscale constituent material, iii) synthesizing the nanofiller, iv) functionalisation of the polymer, (v) performing intermediate processing to prepare the nanofiller for incorporation into the sulphonated polymeric matrix material, vi) blending the two, (vii) forming the nanocomposite ion exchange membrane and viii) reinforcement testing (Shanov et al., 2007). The literature review has therefore given a strong background and justification of procedures used to achieve the desired aim and objectives.

The first part describes the approach to synthesis of carbon nanoballs and their characterization. The second part deals with the synthetic rubber functionalisation technique to produce the desired IEM and the characterization. Thirdly the blending and casting technique for nanocomposite production is described. Finally the mechanical testing and characterisation procedures are described to evaluate the effects of blending. At every stage, the produced constituents are evaluated by characterisation methods prior to blending.

3.1 Non catalytic synthesis of carbon nanoballs

The apparatus used for the carbon nanoballs production was the Non Catalytic Chemical Vapour Deposition Equipment (NCCVD) similar to the one developed by Iyuke (2005), presented schematically in Figure 3.1. It consisted of a vertical silica tube flow reactor (I.D-16mm) immersed in a furnace (heating zone -300mm) with a sensitive temperature regulator. A system of rotameters, pressure controllers and valves to control the flow of argon and acetylene gases into the reactor were also attached to the equipment. The above mentioned system was connected to the swirled

mixer which in turn led into the reactor. The upper end of the reactor was connected to a condenser which led to a delivery cyclone where the produced CNBs were continuously collected. Argon was first turned on at a flow rate of 118ml/min for 30 minutes to purge the system of any impurities and air. The furnace was heated to 1000^{o}C at a heating rate of 20 °C/min under an argon inert environment. Acetylene as the carbon source and argon as the carrier gas were introduced into the reactor at varying flow rates for 10 min/run (Iyuke et al., 2007; Abdulkareem et al., 2007). The smoky product or carbon vapour evolved from the reactor was cooled at the condenser and collected in the cyclones. Acetylene and argon gas flow rates were varied in order to study their effect on the structure and yields of the CNBs obtained. The carbon particles produced were collected from the cyclone and silica reactor and weighed using a digital scale.

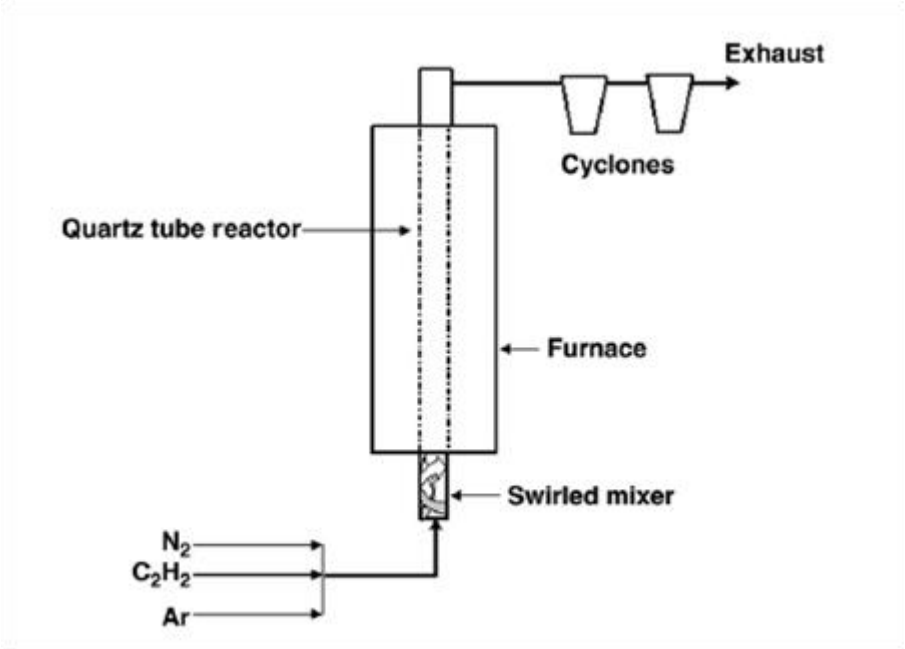


Figure 3.1: Schematic presentation of NCCVD Reactor for carbon nanoballs synthesis (Mhlanga et al., 2010)

The collected samples were analysed with Transmission Electron Microscope (TEM) (JEOL 100S Electron Microscope), Thermo gravimetric Analyser (TGA) (Perkin Elmer Pyris 1 TGA Analyzer), BET surface area analysis (Micrometrics TriStar Surface Area and Porosity Analyzer) and Raman spectroscopy. The production rate for carbon balls was computed as the total sum of mass of balls collected from the reactor and cyclone divided by the total running time. The yield (conversion) was computed as the ratio of the mass of carbon balls produced (product) to the supplied mass of carbon in acetylene (reactant). The purity was computed as the ratio of the mass of carbon balls produced to the gross mass of particles produced as a percentage (Abdulkareem, 2009).

3.1.1 Characterization of carbon nanoparticles

Characterisation of carbon nanoparticles was critical to evaluate the critical properties of nanoparticles which include morphology, surface area, conductivity and thermal stability amongst others. These properties are in turn responsible for the benefits realized in nanotechnology and hence characterisation becomes vital.

3.1.1.1 Morphology of carbon nanoballs (TEM Analysis)

Both High and Low magnification TEM were used to investigate the surface morphology of carbon nanoparticles. To prepare the samples for TEM analysis, a trace amount of each of these carbon nanoballs samples which is in powder form and black in colour, was ultrasonically vibrated in methanol in small tubes for about 15 minutes until it was well dispersed and formed a suspension in the solvent. A drop of this suspension was spread on 300 mesh copper grid with lacy carbon thin film and allowed to dry. After drying, the grid was loaded into the instrument (TEM JEOL 100S) for analysis by checking for the presence of carbon nanoballs. A clear picture is achieved by varying the magnification using magnification knob (Abdulkareem, 2009). After photographing the desired picture, the carbon grid is discharged from the

machine and the next sample is analyzed by following the same procedure, and microscopic image printed. The estimate nanoball diameters were measured from the images and the frequency of occurrence noted for averaging purposes (Mhlanga et al., 2010).

3.1.1.2 BET surface area analysis and porosity analysis

0.2g of produced carbon nanoball samples were collected and tested for surface area of pores and pore volume. This was done using a Micrometrics TriStar Surface Area and Porosity Analyzer BET Analyser (Abdulkareem, 2009).

3.1.1.3 Thermogravimetric analysis (TGA)

The thermal stability of the CNBs was examined with a TGA Perkin Elmer Pyris 1 analyzer running from 25 to 600°C at heating rate of 20°C/min and in an atmosphere of N_2 (Abdulkareem, 2009 and Jin et al., 2005).

3.1.1.4 Raman spectroscopy

This device was used to check for the presence of carbon nanoparticles by checking for the Raman peaks corresponding to the carbon nanoparticles range. It can also be used to determine whether the nanoparticles produced are single walled or multi-walled carbon nanotubes, nanofibres or nanoballs. The sample excitation was performed using 6mW of 514.5 nm light with a 1μm spot size. The integration time for the spectral collection was 120s per acquisition (Abdulkareem, 2009).

3.2 Sulphonation of styrene butadiene rubber

The synthetic rubber functionalisation was via chlorosulphonation using a method similar to the one adopted by Idibie, (2010). A 4% w/v solution of emulsified styrene-butadiene rubber (SBR) (Afpol 1502, 23.5% Styrene, M_n = 135000g/mol, M_w =

530000g/mol, ρ=0.935g/cm^3) (Karbochem, South Africa) was prepared by vigorously stirring small chopped granules in 1, 2 dichloroethane (Analytical grade ≥98%: Merck South Africa) in a 1000ml four neck reactor at room temperature and pressure for 24hrs. The stirring was achieved by using a magnetic stirrer set at 1250 rpm. The rubber solution was chilled in a chiller to temperatures between 0 and 5°C to eliminate latent heat and regulate the initial reaction rate. This was followed by purging the solution with a continuous flow of argon for 30 minutes to create an inert environment (Idibie, 2009).

The volume, V_{csa} (ml) of chlorosulphonic acid, ($ClSO_3H$) (purity, *P = 97%:* Merck South Africa, density, *D = 1.75kg/l*, M_{wcsa} *= 116.52g/mol*), required to prepare a dilute solution, volume, V_d of concentration, C_{csa} (M) in DCE was calculated using Equation 3.1;

$$V_{csa} = \frac{C_{csa} V_d M_{wcsa}}{10DP} \qquad (3.1)$$

where V_d and M_{wcsa} are the volume of diluted chlorosulphonic acid and the molecular weight of the 'off the shelf' chlorosulphonic acid respectively.

The CSA solutions of desired concentrations were prepared using standard procedures and chilled in a chiller to 0^0C. The CSA solution was freshly prepared prior to each sulphonation reaction. The chilled CSA in 1, 2 dichloroethane was added drop wise into vigorously stirred solution (MR3002 Dual Plate Magnetic Stirrer, 1250rpm) of SBR in a four-neck round bottom flask reactor under argon atmosphere at room temperature as shown in Figure 3.2. Chilling was necessary to eliminate latent heat (Idibie, 2010). The sulphonation reaction was allowed to proceed for 24 hours. The reaction was terminated by adding ethanol (Assay ≥ 98%: Merck South Africa) and the precipitated sulphonated polymer was recovered, washed with

deionized water until the pH of wash reached values of 6 – 7 (Martins et al., 2003). The product was then dried in an oven at 80^{o}C for 2-3 hours. The Sulphonated Styrene Butadiene Rubber (SSBR) was characterized using Thermo gravimetric analysis, Titration and FTIR.

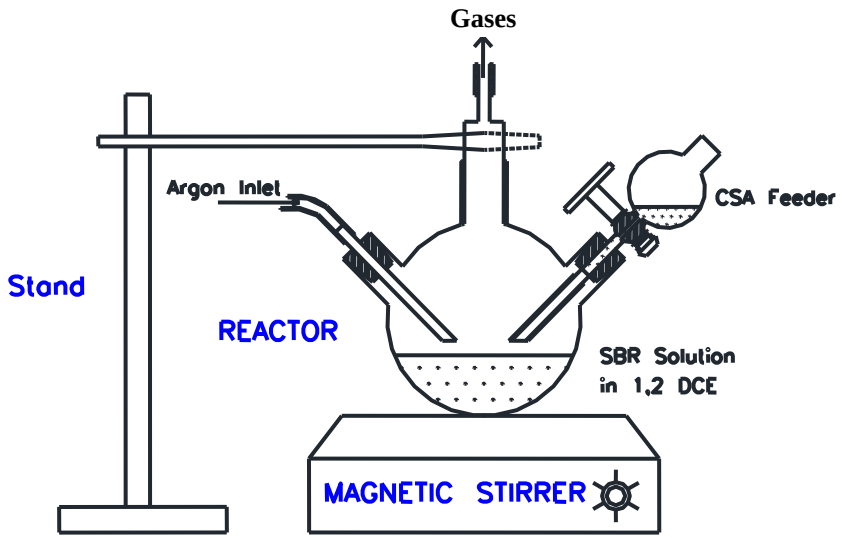


Figure 3.2: Sulphonation apparatus for styrene butadiene rubber

3.2.1 Characterisation of Sulphonated Styrene Butadiene Rubber (SSBR)

The SSBR was characterized for ion exchange capacity degree and thermal stability. These two parameters are critical properties to ion exchange membrane functions and hence the need for characterization.

3.2.1.1 Determination of Ion Exchange Capacity (IEC)

Ion exchange capacity is an indirect and reliable way of ion conductivity measurement as it indicates the content of acid groups present in a polymer matrix. The back titration method was adopted to measure the IEC. In this method, a known volume of 0.01M NaOH solution in methanol (methanolic sodium hydroxide) was added in excess to 0.5wt% (w/v) solution of SSBR in toluene/methanol (90/10 - v/v).

This overall solution was equilibriated for 48hrs and titrated against a 0.01M HCL solution. The amount of Na^+ consumed by the SSBR is equivalent to the difference between the molar Na^+ supplied for equilibriation and the ones consumed in the titration. From this result, the IEC was calculated. This method was preferred since equilibriation allows for the complete reaction of the Na^+ cations in the solution and the SO_3^- anions in the SSBR (Walsby et al., 2001; Guan et al., 2005). IEC indicates the number of milligram equivalents of ions in 1 g of the dry polymer and was calculated using Equation 3.2 below.

$$\text{IEC} = [(C_{NaOH}\ x\ V_{NaOH}) - (C_{HCl}\ x\ V_{HCl})]/(1000M_{SSBR} \quad \left(\frac{moles}{g}\right) \qquad (3.2)$$

Where IEC is the ion exchange capacity in moles SO_3^-/g, C_{NaOH} (mols/litre), V_{NaOH} (ml) are the concentration and volume of NaOH supplied for equilibriation respectively. C_{HCl} (mols/litre), V_{HCl} (ml) are the concentration and volume of HCl consumed in titration respectively. M_{SSBR} is the mass of SSBR used in the titration in g. The degree of sulphonation (DS) is expressed as mole percent of the sulphonated styrene repeating units. The DS was the average number of moles of sulphonic groups present per mole of styrene units in the sulphonated polymer (Walsby et al., 2001). The relationship between the DS and IEC values was calculated with the following equation

$$DS = \frac{104IEC}{0.235(1 - 80IEC)} \qquad (3.3)$$

3.2.1.2 Fourier Transform Infrared (FT- IR) Spectroscopy

The FT IR spectra of unsulphonated and sulphonated PSBR were scanned using Vector O Brucker 400 model FT-IR spectrometer and data were collected in the range of 400 – 4000cm^{-1}. The observed peaks were used to qualitatively prove the occurrence of sulphonation (Idibie, 2009).

3.2.1.3 Thermal stability of sulphonated styrene butadiene rubber

The thermal stability of the membranes was examined with a TGA Perkin Elmer Pyris 1 analyzer running from 25 to 1100°C at heating rate of 20°C/min and in an atmosphere of N_2. The samples were subjected to TGA both before and after sulphonation and blending to determine the decomposition temperatures (Idibie, 2009).

3.3 Production of nanocomposite ion exchange membrane

Production of a membrane was achieved via the complete dissolution of the sulphonated rubber in a selected solvent followed by evaporated casting under specified conditions

3.3.1 Preparation of SSBR membrane films

Due to the fact that SSBR was difficult to dissolve after prolonged drying, the freshly sulphonated rubber was redissolved within three hours after oven drying. The freshly dried SSBR was chopped and dissolved *(4%w/v solution)* in DCE/ethanol mixture (95/5 v/v) in a vigorously stirred conical flask reactor at r.t.p for 12 hrs. The homogeneous solution was filtered using a 150micron sieve to remove solids. The solution was degassed and further concentrated to about 20% w/v using a probe Ultrasonicator at 30% amplitude of sonication and full cycle for 1 hour. The casting was done using a simple evaporative technique (Sheikh-Ali and Wnek, 2000; Chen et al., 2004). The degassed viscous SSBR solution was poured gently into a 90mm circular petri dish of known surface area and depth. The thickness of the desired membrane was estimated as follows; Volume of SSBR solution, V_{SSBR} (ml) to give desired membrane thickness, t (cm) was given by;

$$V_{SSBR} = \frac{100At\rho_{SSBR}}{\mu C_{SSBR}} \quad (3.4)$$

where A is the internal area of the petri dish in cm^3, t, the desired membrane thickness (cm) and ρ (gcm^{-3}) the density of the membrane and **μ,** the loss factor to account for losses. The petri dish was placed on a level platform in a vacuum oven at room temperature and allowed to evaporate for 24hrs. Further vacuum drying of the membrane was done at 50 °C for 12 hrs to eliminate all residual solvents and acids. The cast solution was cured for 4 days by exposing it to the air and then peeled off from the casting foil mold. The dry membranes were then stored at room temperature in a fume hood at room temperature and pressure. For the non sulphonated membrane, 100 ml of unsulphonated rubber solution were taken and deposited as film. The membranes were then characterized using SEM, TGA, IEC and FTIR.

3.3.2 Reinforcement of SSBR with carbon nanoballs

Sulphonated polystyrene butadiene rubber was synthesized at conditions that gave a steady reaction and high degree of IEC. The SSBR was then blended with the carbon nanoballs. Therefore SBR was sulphonated with 0.09M CSA at a styrene mole to CSA mole ratio of 1.12 using the procedure previously described for sulphonation. The sulphonation time was 24hrs at r.t.p under an inert environment of argon. The stirring rate was 1250 rpm and sulphonation was terminated by ethanol (Methanol Absolute, Merck Chemicals, SA), filtered and dried using previously described procedures.

Carbon nanoballs were also synthesized at optimal conditions. These conditions were based on a route that produced minimum diameter, uniformly sized, high purity and relatively high yield carbon nanoballs at optimal temperatures and flow rates of acetylene and argon. A 16mm diameter reactor, operating at 1000°C, acetylene and argon flow rate of 456ml/min and 100ml/min respectively were used. As a result,

highly pure carbon nanoballs of 60nm average diameter, and I_D/I_G ratio of 1.04 and approximate density of 0.5g cm^{-3} were produced by NCCVD in adequate quantities for blending.

SSBR was dissolved in 1, 2 Dichloroethane/ ethanol (95/5 v/v) mixture at room temperature in a clean environment to produce a 4% (w/v) solution using the method described previously. Separately, 0.1% (w/v) solutions of carbon nanoballs of different masses (from the same batch) in DCE were prepared for blending purposes (Sobkowicz et al., 2009; Crowley and Welch, 1954 and Manivannan et al., 2009).

The carbon nanoball solutions were magnetically stirred for 5 minutes before ultrasonication at three different amplitudes (20, 60 and 75%) for 1 hr. The procedure for ultrasonication was adopted from reported work on similar work and adapted for this particular work. The probe sonicator of 14mm Φ tip was used for ultrasonication (Ramanathan et al., 2007 and Sobkowicz et al., 2009). The tip was maintained at the same position close to the surface of the mixture to ensure effective dispersion. The ultrasonicated solution was prepared for blending by filtration through a 3μm filter to remove aggregates (Manivannan et al., 2009).

20 grams of SSBR was dissolved in 1, 2 dichloroethane according to the outlined procedure. The dissolved solution was divided into equal portions, each one equivalent to 1.67 g SSBR by weight. Carbon nanoballs of masses 0.004, 0.0085, 0.013, 0.017, 0.030, 0.042 and 0.067g corresponding to approximate filler weight concentrations of 0.25, 0.5, 0.75, 1, 1.75, 2.5 and 4% in SSBR, respectively were dispersed in DCE according to the procedure described above. This was then followed by the dispersion of the various mass dispersions of the carbon nanoballs in equivolume identical solutions of SSBR in DCE. One of the SSBR solutions was left plain to represent the 0% filler concentration. The blends were ultrasonicated (UP200S Processor) for 3hrs at constant power (200W), amplitude and frequency, until the blends appeared homogenous and viscous (20% w/v). Three different sets of

samples were prepared and blended at three different sonication amplitudes, namely 20, 60 and 75% amplitudes (Sobkowicz et al., 2009 and Shanov et al., 2007). The total sonication time remained constant at 3hrs and frequency to maintain a steady temperature for the solution. The process was set into the intermittent mode at constant frequency to prevent heat build up associated with continuous sonication process. The blended polymer was then cast using the evaporative procedure previously discussed to produce the nanocomposite membrane.

3.3.3 Morphology of the ion exchange membrane

Morphological structure of plain, sulphonated and nanocomposite SSBR IEM were carried out using SEM, Model FEI Phenom, Hillsboro, Oregon, USA). The Scanning Electron Microscopy analysis of representative samples was conducted in two stages. Firstly, samples were cut and mounted onto spuds using double sided tape. Thereafter spuds were loaded into the SPL module –Sputter Coater followed by coating with gold palladium for 9 minutes to make the rubber surface conductive. The coated samples were finally examined under the microscope for morphological determination. FTIR and TGA were used for the qualitative IEC analysis and thermal stability analysis respectively (Lee et al., 2004).

3.4 Mechanical characterisation

The mechanical properties of the nanocomposite and plain membranes were evaluated by a Hysitron Nanotensile 5000 Tester on thin rectangular specimens, cut out from the cast films using a sharp blade. All the tests were carried out guided by the ASTM D 412-99 method at 23 ± 2 ^{0}C at strain rate of 6 mm/min (El-Lawindy, 2002 and Sue et al., 1994). The average values of three tests for tensile strength, elastic modulus, fracture toughness and strain were reported for each sample. Yield strength was measured at 0.2% offset. Creep test was not feasible due to the absence of an environment chamber.

3.4.1 Sample preparation for tensile testing

The sample preparation was similar to ISO 3167 and 527-2 Type 5A but particularly adapted to fit the Hysitron based membrane testing (El-Lawindy, 2002). Strip specimens (Sue et al., 1994) of 30 mm x 4mm x 0.15mm (lxwxt) were prepared for testing as shown in Figure 3.3. Dimensions were measured by a digital vernier caliper. Cutting was done on a template using a sharp blade to avoid notches. The specimens were aligned onto sample holders on a standard square template by a thin double sided tape. After alignment, the specimens were glued onto specimen holders by acryanitrite low viscosity glue and left to dry for 24 hrs after which testing would commence. Three specimens were prepared per sample and the average value computed after testing. Specimens broken at the grip ends were discarded and replaced. Prepared samples were also tested on the same day.

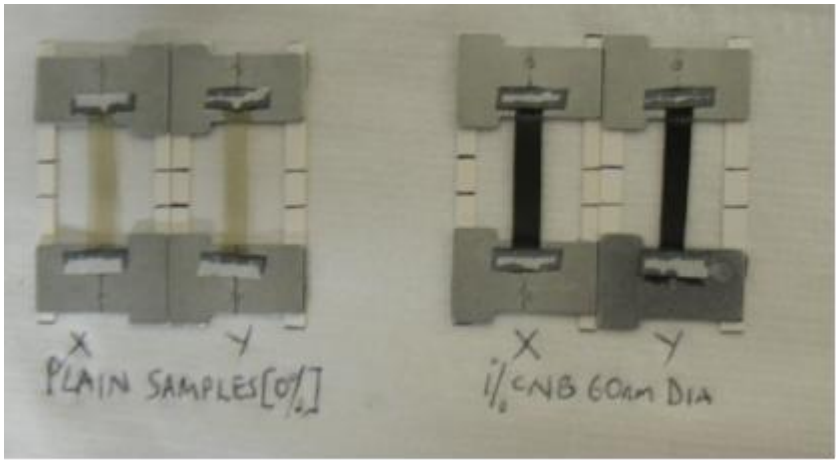


Figure 3.3: Tensile testing sample preparation

3.4.2 Mechanical Testing

Prior to testing the system was calibrated using a nanotensile5000 software. The piezo stop voltage was set to 8V. The X, Y and Z force gains were set to 10, whilst the Z displacement gain was set to 100. The X, Y, Z relative positions were set to 0 and the system was set onto the Force (μm) vs Displacement (nm) mode. A positive

gradient graph of Force (μm) vs Displacement (nm) confirmed successful calibration upon which testing commenced.

Prior to loading the specimen onto the machine, all gains were reset to 10. The specimen identity was recorded onto the machine and saved. The test to be performed was selected (Tensile/Fatigue/Creep). The specimen information including shape, and dimensions were also captured for computations, documentation and analysis. The machine was then set into the large displacement mode (maximum extension of 150mm) with a maximum operating load of 10.624mN. The displacement/ strain rate was set to 100 μm/ second (6mm/min) for all samples.

The specimen was then loaded onto the upper gripper of the machine and tightly secured using a torque wrench set to 20lb.inch (Figure 3.4). The specimen mass was then measured and saved onto the machine. After mass measurement, the specimen was lowered to the bottom gripper, aligned in the three principal directions (X, Y, Z) using the mouse and tightly secured once perfect alignment was achieved. The alignment template was then cut off by a pair of scissors after which tensile testing commenced. At the fracture point, the testing was stopped and the data saved onto the software for analysis.

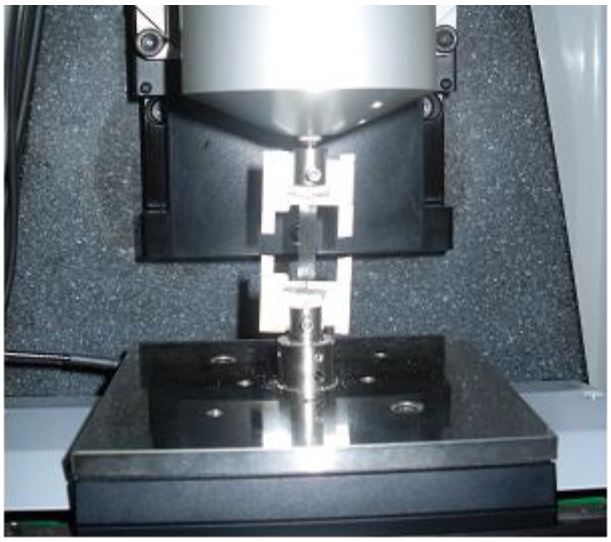


Figure 3.4: Tensile test specimen loaded onto the Hysitron Nanotensile 5000 machine

For fatigue testing, the machine was set onto the dynamic loading testing and load control. Different maximum and minimum load settings were set based on the yield and strength of the materials being tested. The maximum and minimum load sets used were (60mN, 40 mN); (220 mN, 180 mN); (260 mN, 220 mN) and (350mN, 300 mN). Thus tensile tests for all sample specimens were done before the fatigue tests. The frequency was set to 0.1Hz and all tests were terminated at 100 cycles.

3.4.3 Reinforcement property evaluation

The engineering stress-strain profile was constructed by using the formula;

$$\sigma = \frac{F}{A_0} \tag{3.5}$$

Where F is the instantaneous load applied in Newtons and A_0 is the cross sectional area prior to deformation. Engineering strain was computed as;

$$e = \frac{l_i - l_o}{l_0} \tag{3.6}$$

where l_i is the instantaneous length of sample and l_o is the original length of sample.

The Young's modulus, E (Elastic Modulus) is the slope of the initial linear portion of the stress strain graph and measures the stiffness of the material.

$$E = \frac{\Delta\sigma}{\Delta e} \tag{3.7}$$

The Yield stress is a measure of the maximum stress the material can handle before plastic deformation commences and was measured at 0.2% offset, the point at which the slope cuts the stress strain profile.

Fracture toughness was measured by computing the area under the stress strain graph.

$$U_{F.T} = \int_0^e \sigma(e)de \tag{3.8}$$

Anisotropy was measured by measuring the mechanical properties in the X and Y transverse direction and computed by,

$$Anisotropy = \frac{Mechanical\ Property\ (X\ direction)}{Mechanical\ property\ (Y\ direction)} \tag{3.9}$$

Fatigue analysis was limited to low cycle fatigue and 100 cycles due to equipment limitations.

CHAPTER 4: RESULTS AND DISCUSSION

4.1 Carbon nanoball synthesis

As previously discussed in the literature review, the knowledge of the nanofiller properties is critical towards the development of high quality nanocomposite ion exchange membrane. The knowledge of the synthesis route was critical in tailoring the desired properties of the nanofiller end product as well as the cost implications. Therefore in this section, the analysis and discussion of, i) the synthesized nanoparticles and ii) synthesis route for carbon nanoballs are presented. The suitability of the nanofiller in meeting the desired reinforcement objectives is also discussed.

4.1.1 Conditions of synthesis of carbon nanoballs

The operating conditions and the average carbon ball diameters are tabulated in Table 4.1 for the different reactors used. The 16mm diameter reactor produced uniform carbon nanoballs at the widest range of operating conditions and hence used as a basis for analysis of results. The carbon nanoballs were produced at acetylene flow ratios ranging from 0.72 to 0.82. The smallest carbon nanoball with an average diameter of 60nm was produced from the 16mm diameter reactor (Table 4.1). There was no carbon ball produced at acetylene flow ratios below 0.5. Below this flow ratio, shiny flakes were produced. The collected results are analysed graphically and discussed with the aim of selecting pure and uniform carbon nanoballs for nanocomposite applications.

Table 4.1: Carbon ball synthesis conditions

C_2H_2 Flow[a] (Q_{ac}) (ml/min)	Argon Flow[b] (Q_{arg}) (ml/min)	Total flow[c] (Q_T) (ml/min)	C_2H_2 Flow Ratio[d] (η_{AC})	Temperature (^oC)	CNB Dia[e] (Φ_{CB}) (nm)
22mm Φ x 300mm Length Reactor					
191	210	401	0.48	1000	-
324	314	638	0.51	1000	150
324	210	534	0.61	1000	200
389	210	600	0.65	1000	160
389	153	543	0.72	1000	80
324	59	384	0.85	1000	200
389	59	449	0.87	1000	300
456	0	456	1.00	1000	450
19mm Φ x 300mm Length Reactor					
191	413	603	0.32	1000	-
191	210	401	0.48	1000	-
324	210	534	0.61	1000	250
357	182	539	0.66	1000	300
389	153	543	0.72	1000	70
456	100	556	0.82	1000	100
513	59	572	0.90	1000	200
568	0	568	1.00	1000	350
16mm Φ x 300mm Length Reactor					
261	261	522	0.50	1000	-
324	210	534	0.61	1000	140
357	182	539	0.66	1000	250
389	153	543	0.72	1000	80
456	100	556	0.82	1000	60
513	59	572	0.90	1000	120
568	0	568	1.00	1000	300

a = Adjusted C_2H_2 Flowrate; b = Adjusted Argon Flowrate; c = Total Flowrate (Q_{ac}+Q_{arg}); d = C_2H_2 flow ratio (Q_{ac}/Q_T); e = Average Carbon Ball Diameters. Assumptions: i) Compressibility of argon and acetylene = unity; ii) Adjustment Factors for Argon and Acetylene Flow Rates = 1.18 and 0.95 respectively; iii) Ideal Gas Law Applies at 20°Cand 101.3kPa

4.1.2 Morphology of carbon nanoparticles

The morphologies of the produced carbon nanoballs were best observed from TEM images as shown in Figure 4.1a and b below. TEM analysis showed that the carbon nanomaterials formed were spherical balls (Figures 4.1a and b) similar to the ones reported in literature (Mhlanga et al., 2010 and Miao et al., 2003). These carbon nanoballs, collected from the cyclone, were highly pure and uniform as shown in (Figures 4.1a and b, 4.2a and 4.3b). However, the ones collected within the reactor were impure and contaminated with predominantly shining flakes of carbon (Figure 4.3a), similar to the ones reported in literature (Abdulkareem, 2009). The carbon nanoballs from the smaller diameter reactor were more uniform in size than the ones from the larger diameter reactor (Figure 4.2a and b). This could be due to the fact that the smaller the reactor diameter, the narrower the operating conditions variation and hence the uniformity. An extremely low (<<1%) quantity of about 10nm diameter carbon nanoballs was observed from the cyclone containing predominantly 60nm carbon nanoballs (Figure 4.3b). These rare carbon spheres could be fullerenes and were discussed later in the section.

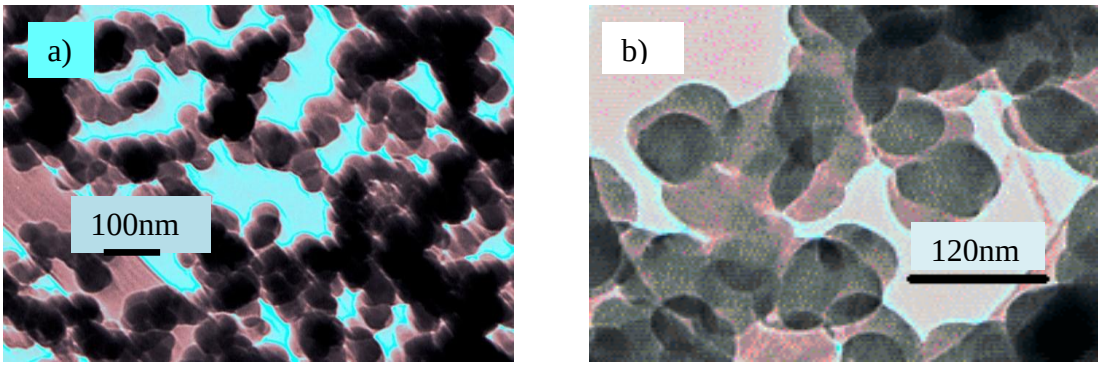


Figure 4.1: TEM images of CNBs produced at 1000^0C, 456ml/min and 100ml/min C_2H_2 and Argon flow rates respectively (η_{AC} = 0.82) using 16mmΦ reactor; a) Pure and uniform and b) Porous CNBs

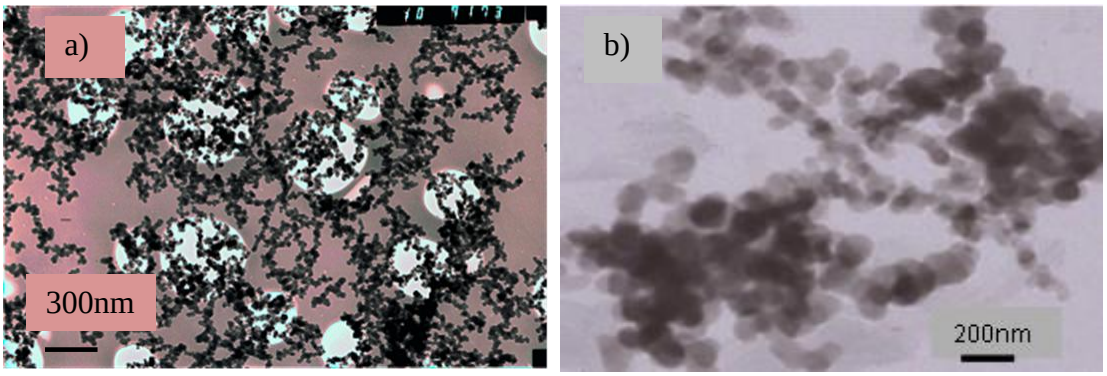


Figure 4.2: TEM Images a) Highly uniform and pure CNB (narrow variation) from 16mm Φ reactor; b) Less uniformly distributed and pure carbon nanoballs (wider variation) from 22mm Φ reactor

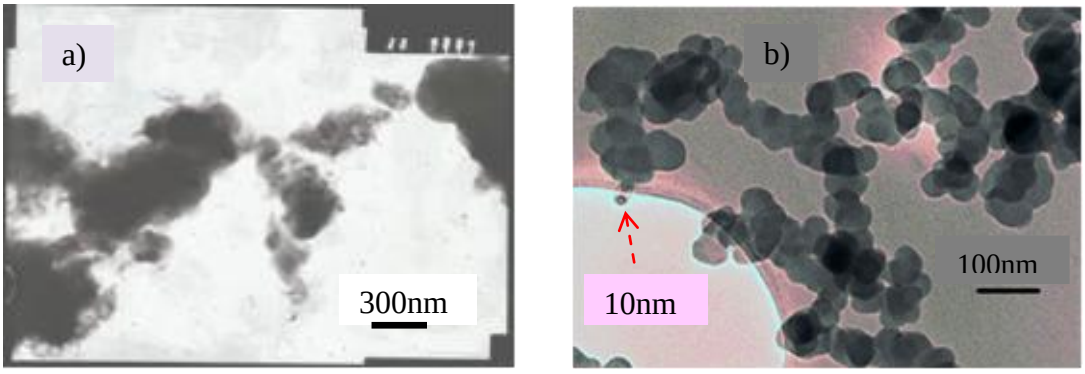


Figure 4.3: TEM images; a) Impure carbon nanoballs, covered in carbonaceous materials, collected from the reactor; b) Pure CNBs showing rare CNBs of 10nm Φ.

TEM images also showed that the produced carbon nanoballs were not monodisperse but stayed as carbon chains or agglomerates as shown in (Figure 4.4a and b). There must therefore exist relatively strong forces which attract the carbon nanoparticles towards one another (Shanov et al., 2007). This observation was critical in the consideration of the dispersion of the carbon nanoballs into the rubber matrix. The

randomly dispersed carbon nanoball chains amongst the agglomerates could also be of interest in some applications and may need further focus.

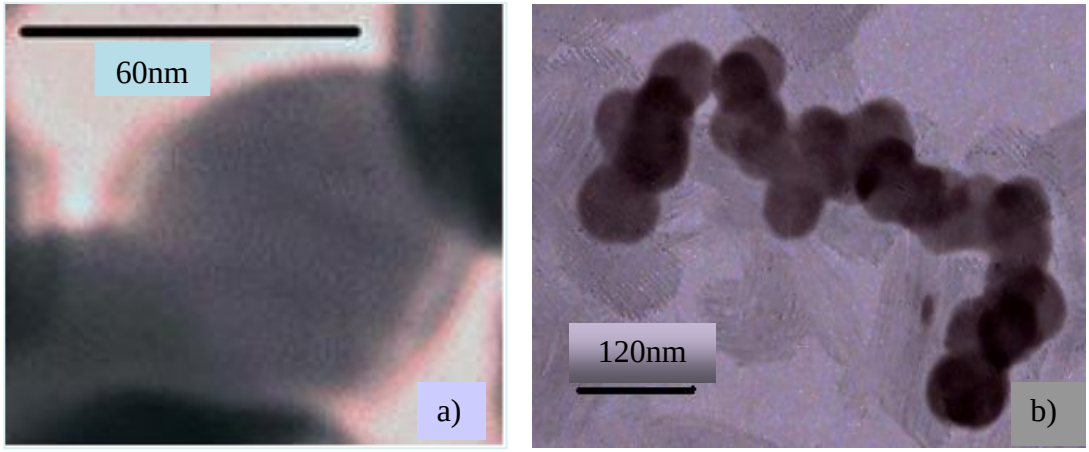


Figure 4.4: TEM images; a) High magnification TEM showing spherical CNBs collected from the cyclone. Patterned dots on the outer surface suggests porous graphitic layer. Adjacent carbon balls overlap showing accretion of the CNBs; b) Commonly observed agglomeration of the formed CNBs

Although the produced carbon balls were physically similar in shape and perhaps structure, they were different in size and seemed to be affected by the flow ratio (η_{AC}) of acetylene and reactor diameter since the operating temperature was kept constant. In addition, the observed flakes collected from the reactor would prompt further investigation into the effect of these various parameters towards the production of highly pure and uniform carbon nanoballs ideal for nanocomposite ion exchange membrane.

4.1.3 Factors affecting carbon ball size

Although chemical vapour deposition methods for producing carbon balls have widely been reported in literature, the greater majority reported are submicron carbon particles which are outside the nanoscale range. Therefore the synthesis technique

adopted was aimed at consistent production of carbon nanoballs (under 100nm diameter). Graphical analysis of the product obtained showed that the flow ratio of the carbon source (η_{AC}) and reactor diameter, (Φ_R) affect the carbon ball size (Φ_{CB}) at constant operating temperature and total flow rate (Q_T). Figures 4.5 and 4.6 showed that the carbon ball size varies with η_{AC} and reactor diameter (Φ_R). The graphs also show a consistent nonlinear relationship between Φ_{CB} and η_{AC}.

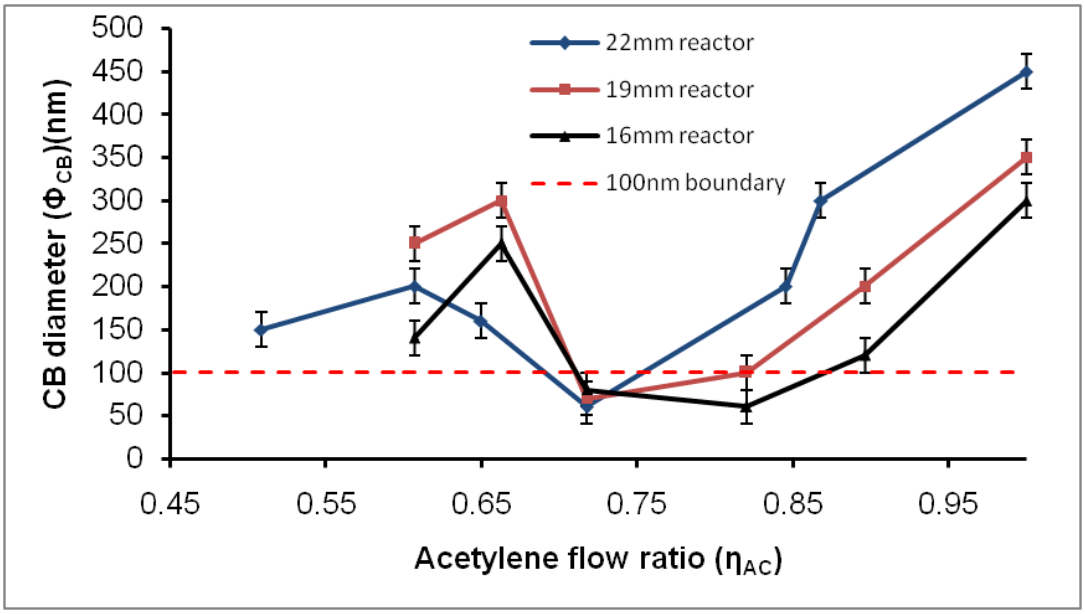


Figure 4.5: Effect of reactor diameter on carbon nanoball production

4.1.3.1 Effect of acetylene flow ratio (η_{AC}) on carbon ball diameter (Φ_{CB})

Figures 4.6 and 4.7 illustrate the effect of acetylene flow ratio (η_{AC}) on carbon ball production. From the experimental results, two regions were observed; i) the dominantly flake production region and ii) the predominantly carbon ball production region as shown in Figure 4.6. In the carbon ball production region, the carbon nanoball production region was of great interest since the reinforcement desired was to be achieved through nanoparticles under 100nm.

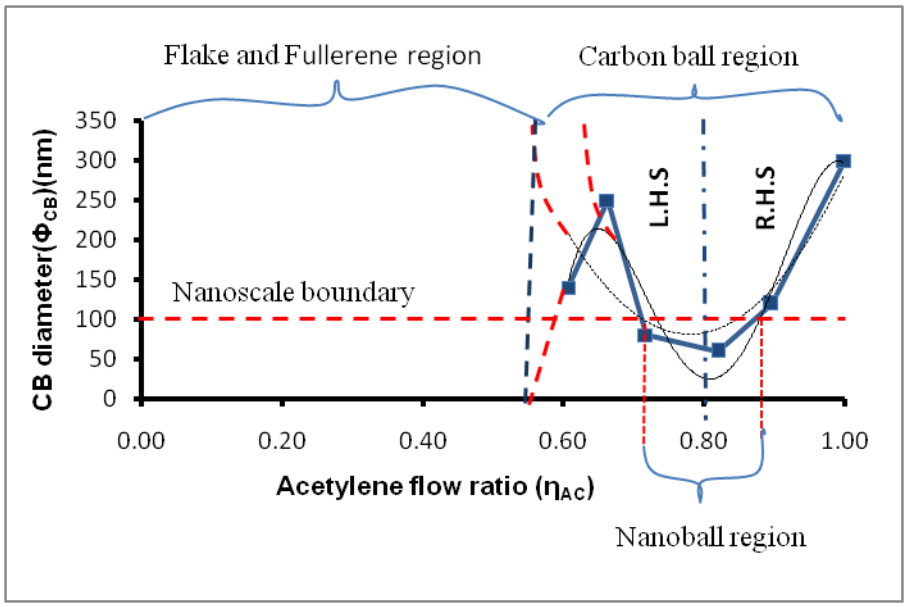


Figure 4.6: Effect of acetylene flow ratio on carbon ball diameter

The Φ_{CB} vs η_{AC} graph was exciting because of the existence of a minimum turning point corresponding to the critical acetylene flow ratio, η_{AC0}, which gave the minimum carbon ball diameter, Φ_{CB0}. The nanoball production region of interest was bound by the range of values of η_{AC} in the asymmetric trough for which $\Phi_{CB} \leq$ 100nm as shown in Figure 4.6 above. The production range, was defined by $\eta_{AC(min)} \leq \eta_{AC0} \leq \eta_{AC(max)}$. Generally, Φ_{CB}, decreases nonlinearly with increasing η_{AC} up to η_{AC0}, the minimum turning point, after which, Φ_{CB} increases nonlinearly with increasing η_{AC} (Figure 4.7).

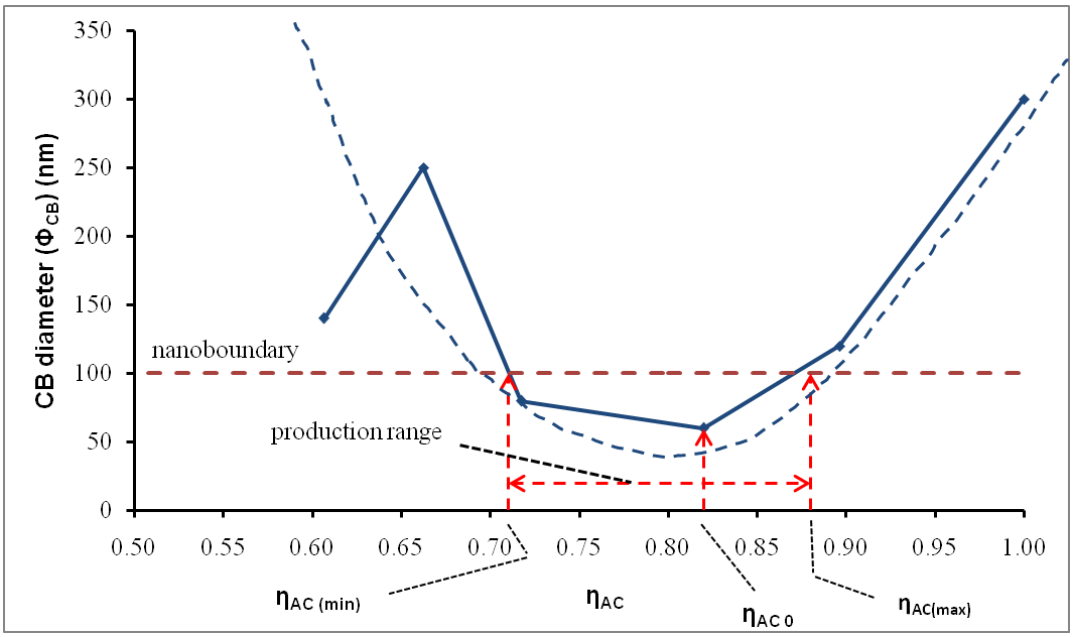


Figure 4.7: Flow ratio conditions for carbon nanoball production

Apparently, it seemed unusual to obtain higher $\mathbf{\Phi_{CB}}$ at lower $\mathbf{\eta_{AC}}$ and vice versa in the left hand side of the graph presented by Figure 4.6 above. However, the mechanism of growth of carbon nanoballs reported by Caldero et al., 2005 helps to explain the behaviour. According to the mechanism of growth for carbon nanoballs, the size of the carbon nanoballs were determined by two main factors namely i) the average radius of curvature of shells and ii) the number of concentric shell layers formed, **n**.

Since curvature depends on the ratio of the proportions of hexagons, pentagons and heptagons forming and combining in the reactor, low $\mathbf{\eta_{AC}}$ tend to favour the formation of a greater proportion of flat hexagonal rings as compared to heptagons and pentagons (Caldero et al., 2005; Wang and Kang, 1996). As a result, the curvature, θ is low and hence the radius of curvature $\mathbf{r_\theta}$, was very high at low $\mathbf{\eta_{AC}}$. This was consistent with experimental results, since there existed a limiting $\mathbf{\eta_{AC}}$, below which no carbon balls were produced except the flakes. These flakes were

assumed to be made of completely planar (hexagonal) layers whose curvature was 0 and hence, $\mathbf{r_0} = \infty$.

One could argue that below the minimum acetylene flow ratio, $\boldsymbol{\eta_{AC(min)}}$ (Figure 4.6 and 4.7), carbon nanoballs of very small diameters (<10nm) must be formed. This was not very likely considering that the TEM analysis of both the cyclone and reactor product did not show nanoballs under 10nm. However an extremely low percentage (<<1%) of isolated and rare carbon nanoballs were observed on TEM as shown in Figure 4.3b. This could be attributed to the fullerene formation mechanisms reported in literature for small diameter nanospheres. The insignificant quantity of these small nanospheres could be due to the fact that production of a fullerene precisely requires 12 pentagons per shell, which is extremely difficult to achieve at mild experimental conditions used (Fahlman, 2007). From Figure 4.6, the experimental results produced a trendline approximated by Equation 4.1;

$$\Phi_{CB} = -C_4'\eta_{AC}^4 + C_3'\eta_{AC}^3 - C_2'\eta_{AC}^2 + C_1'\eta_{AC} - C_0' \qquad (4.1)$$

where C_4', C_3', C_2', C_1' and C_0' are constant coefficients of the polynomial equation However, Equation 4.1 could not account for flakes formed at low acetylene flow ratios. A model based on the experimental observations and the concentric carbon layer formation is therefore proposed as shown in Figure 4.8.

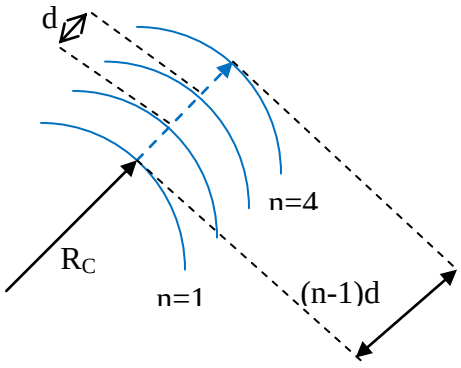


Figure 4.8: Model for carbon ball comprising the concentric layers of carbon

Therefore, assuming a series of ***n*** closed shell layers, one on top of the other around a spiral core shell, radius, $\mathbf{R_C}$ and separated by distance, ***d*** (nm), (Figure 4.8), then the radius of the carbon nanoball, $\mathbf{R_{CB}}$, is given by;

$$R_{CB} = R_C + (n-1)d \tag{4.2}$$

where $\mathbf{R_{CB}}$ is the carbon nanoball diameter and $\mathbf{R_C}$ is the diameter of the core shell which is assumed to be constant. As $\boldsymbol{\eta_{AC}}$ increases, the proportion of pentagons and heptagons increases relative to the hexagonal rings and hence promoting curvature of layers. A direct relationship between $\boldsymbol{\eta_{AC}}$ and the non hexagonal carbon rings proportion was proposed and assumed. As a result, $\mathbf{r_\theta}$ was assumed to be inversely proportional to $\boldsymbol{\eta_{AC}}$. The average radius of curvature of shells, $\mathbf{r_\theta}$, must be related to $\boldsymbol{\eta_{AC}}$ and the number of concentric shells, **n,** to the carbon source flow rate, $\mathbf{Q_{ac}}$ since the total flow rate, $\mathbf{Q_T}$ is a constant. The relationship between $\boldsymbol{\Phi_{CB}}$ and $\boldsymbol{\eta_{AC}}$ was therefore approximated from the three important assumptions;

$$r_\theta \; \alpha \, 1/\eta_{AC}^{p} \tag{4.3}$$

where *p* is a power of the flow ratio.

$$n \; \alpha \; Q_{ac}/r_\theta^2 \tag{4.4}$$

where *n* and Q_{ac} are the number of shells and C_2H_2 flow rate. Equation 4.4 is derived from the surface area density equation of a spherical surface.

$$\eta_{AC} \; \alpha \; Q_{ac} \tag{4.5}$$

By combining Equation 4.4 to 4.5, the following relationship was derived;

$$n \; \alpha \; \eta_{AC}/r_\theta^2 \tag{4.6}$$

By substituting r_ϑ in Equation 4.3 into Equation 4.6 and substituting into Equation 4.2, the radius of the carbon ball, R_{CB} is given by;

$$R_{CB} = \frac{C_1}{\eta_{AC}^{p}} + C_2 d\left(\eta_{AC}^{2p+1} - 1\right) \quad (4.7)$$

And by substituting $p = 1$, then R_{CB} is described by Equation 4.8 below;

$$R_{CB}\, \alpha \frac{C_1}{\eta_{AC}} + C_2 \eta_{AC}^{3} - C_3 \quad (4.8)$$

Where C_1, C_2 and C_3 could be constants related to the equipment specification, total flow rate of the system and reaction temperature. Since the carbon ball diameter, $\Phi_{CB} = 2R_{CB}$, then a relationship between Φ_{CB} and η_{AC} can be estimated from Equation 4.7 as,

$$\Phi_{CB}\, \alpha \frac{C_1}{\eta_{AC}} + C_2 \eta_{AC}^{3} - C_3 \quad (4.9)$$

The relationship seems consistent with the experimental trend since at low $\boldsymbol{\eta_{AC}}$, the term $\mathbf{C_2\eta^3_{AC}}$ approaches zero and $\mathbf{C_1/\eta_{AC}}$ approaches infinity, implying infinite diameter, $\Phi_{\mathbf{CB}}$ of carbon nanoballs. This is consistent with the fact that as the acetylene flow ratio, $\boldsymbol{\eta_{AC}}$, is reduced from $\boldsymbol{\eta_{AC0}}$, going to the left of the $\boldsymbol{\eta_{AC}}$ axis, $\mathbf{C_1/\eta_{AC} >> C_2\eta^3_{AC}}$, implying that $\boldsymbol{\Phi_{CB} \sim C_1/\eta_{AC}}$. Therefore at the left hand side (LHS) of Figure 4.6, the carbon ball diameter is inversely proportional to acetylene flow ratio. This was consistent with the fact that below a certain limiting, $\boldsymbol{\eta_{ACl}}$, no carbon balls were made but flakes, which can be assumed to be carbon balls with infinite diameter, thus as $\boldsymbol{\eta_{AC} \rightarrow 0,\ \Phi_{CB} \rightarrow \infty}$. At the R.H.S of Figure 4.6, the effect of $\mathbf{C_2\eta^3_{AC}}$ could be dominating the effect of $\mathbf{C_1/\eta_{AC}}$ and hence the increase in $\boldsymbol{\Phi_{CB}}$. In other words, as $\boldsymbol{\eta_{AC} >> \eta_{AC0}}$, the inverse part $\mathbf{(C_1/\eta_{AC})}$ becomes almost a constant and hence $\boldsymbol{\Phi_{CB}}$ increases as a cubic function of $\boldsymbol{\eta_{AC}}$.

Comparing Equation 4.1 and 4.9, the equations are only similar in non linearity. The difference was due to the complex deviations of produced carbon nanoballs from the ideal one portrayed in Figure 4.8. For example, the concentric layers are not completely closed as suggested by the model (Kang and Wang, 1996). On the other hand, the experimental trend fails to incorporate the infinite diameter observed at low η_{AC}. Further work is definitely necessary to establish an accurate important relationship between carbon ball diameter and acetylene flow ratio, η_{AC}. The turning point of Equation 4.9, $(d\Phi_{CB}/d\eta_{AC} = 0)$, given by Equations 4.10 and 4.11 below gives the critical acetylene flow ratio, η_{AC0}, at which the equipment produces the smallest carbon ball (Φ_{CB0}).

$$\frac{d\Phi_{CB}}{d\eta_{AC}} \alpha \frac{-C_1}{\eta_{AC}^2} + 3C_2\eta_{AC}^2 \qquad (4.10)$$

Substituting the L.H.S of Equation 4.10 by 0 (turning point), Equation 4.11 is obtained as shown below.

$$\eta_{AC0} \alpha \left(\frac{C_1}{3C_2}\right)^{1/4} \qquad (4.11)$$

Equation 4.11 shows that the minimum diameter is related to the equipment and total flowrate constants. The NCCVD equipment and process redesign and optimization was not part of the research scope and hence further work is recommended to establish a comprehensive relationship for the smooth production of carbon nanoballs and prediction of sizes based on operating conditions. The analysis and discussion has therefore given a basis for further work.

4.1.3.2 Effect of reactor diameter (Φ_R) on carbon ball diameter

The 50mm Φ reactor failed to produce significant quantities of carbon nanoballs under 100nm and hence prompted the investigation of reactor diameter, $\mathbf{\Phi_R}$ effects on carbon ball diameter, $\mathbf{\Phi_{CB}}$. The same trend of carbon ball size variation with acetylene flow ratio was observed for all the three reactors under investigation (16mm Φ reactor, 19mm Φ reactor and 22mm Φ reactor) as shown in Figure 4.5 from the previous section. Table 4.2 shows the data used to analyse the effect of $\mathbf{\Phi_R}$ on $\mathbf{\Phi_{CB}}$. Figure 4.7 from the previous section illustrates the important boundary conditions for the successful synthesis of carbon nanoballs.

The reactor diameter, $\mathbf{\Phi_R}$, has three main positive contributions to carbon ball size reduction. The first contribution observed was that the minimum carbon ball diameter, $\mathbf{\Phi_{CB0}}$, decreased with decreasing $\mathbf{\Phi_R}$ at constant total flow rate, $\mathbf{Q_T}$. Secondly, the nanosize production range, $\mathbf{\eta_R}$, widens with decreasing $\mathbf{\Phi_{CB}}$. Thirdly size uniformity improves with decreasing reactor diameter.

Table 4.2: Limiting values of acetylene flow ratio for CNB production

$\mathbf{\Phi_R}$[a] **(mm)**	$\mathbf{\eta_{AC(min)}}$[b]	$\mathbf{\eta_{AC(max)}}$[c]	$\mathbf{\eta_R}$[d]	$\mathbf{\Phi_{CB0}}$[e] **(nm)**	$\mathbf{\eta_{AC0}}$[f]
22	0.68	0.78	0.1	80	0.72
19	0.73	0.85	0.12	70	0.72
16	0.72	0.88	0.16	60	0.82

a = Reactor Diameter; b = Minimum C_2H_2 flow ratio for CNB production; c = Maximum C_2H_2 flow ratio for CNB production; d = Range of nanoball production (c-b); e = Minimum carbon ball diameter ($\mathbf{\Phi_{CB0}}$); f = C_2H_2 flow ratio to produce smallest carbon ball

The carbon nanoball production range was observed to narrow with increasing $\mathbf{\Phi_R}$ (Figures 4.9 and 4.10). This was attributed to the increasing residence time in the reactor implying more time for concentric layers accumulation and hence pushing $\mathbf{\Phi_{CB}}$ off the nanoregion. The minimum carbon ball diameter, $\mathbf{\Phi_{CB0}}$ also increased with increasing $\mathbf{\Phi_R}$ (Figure 4.11). This was attributed to the increasing residence time for concentric layer formation with increasing $\mathbf{\Phi_R}$ at constant $\mathbf{Q_T}$ and temperature.

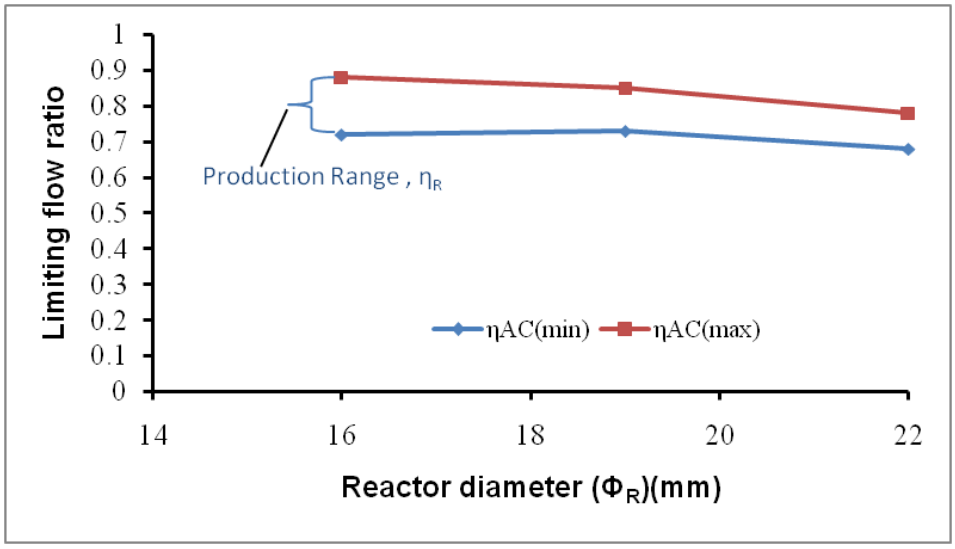


Figure 4.9: Limiting acetylene flow ratio for CNB production

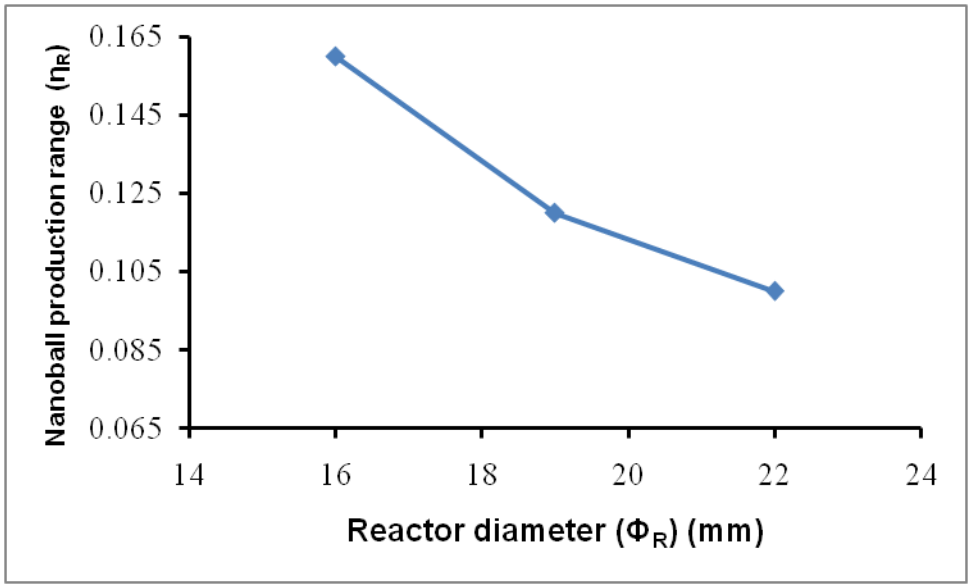


Figure 4.10: : Effect of reactor diameter on CNB production range

TEM images showed a higher degree of uniformity with carbon nanoballs from the smallest diameter reactor. This is consistent with better distribution of operating conditions at narrower cross sectional areas. For example, the minimum temperature region was observed to be at the centre since the furnace heating elements are outside the reactor (Mhlanga et al., 2010). Therefore, the wider the reactor, the wider the range of operating conditions and hence the wider the carbon ball variations. The 16mm diameter reactor produced the smallest carbon nanoballs, over the widest range and hence preferred.

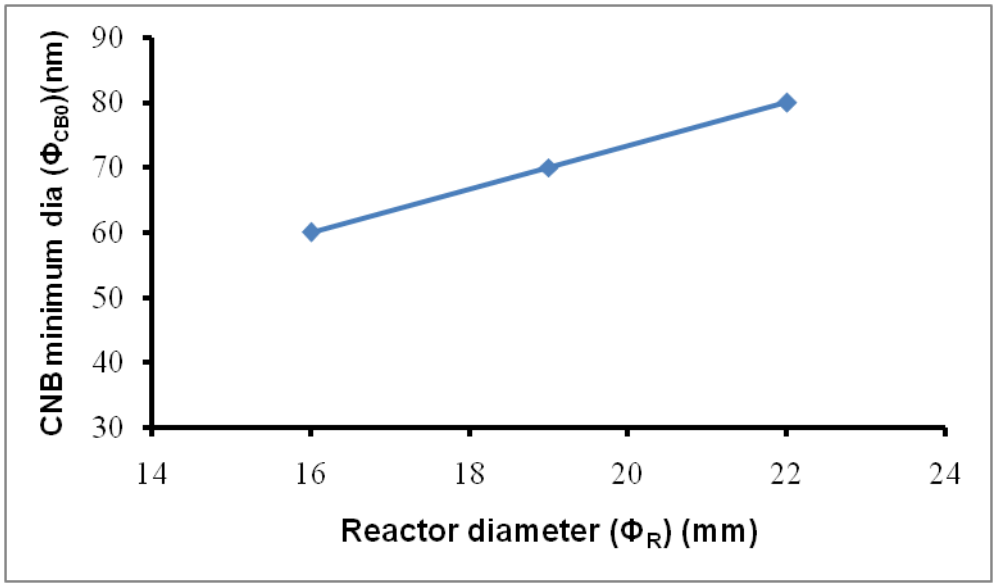


Figure 4.11: Effect of reactor diameter on minimum CNB diameter

Two important relationships related to the equipment size can be proposed from the analysis. The first one is that the smallest size of carbon ball, the equipment can produce, $\mathbf{\Phi_{CB0}}$ is directly proportional to the reactor diameter, $\mathbf{\Phi_R}$. Secondly, the carbon nanoball production range, $\mathbf{\eta_R}$ is inversely proportional to the reactor diameter, $\mathbf{\Phi_R}$. Therefore smaller reactors are more suitable for production of uniform and smaller nanoballs at wider range of production conditions. Carbon nanoballs of 60nm average diameter have been successfully produced using 16mm diameter

reactor at 0.82 acetylene flow ratio (456ml/min and 100ml/min acetylene and argon flow rates respectively).

The critical acetylene flow ratio, $\boldsymbol{\eta_{AC0}}$ required to produce the minimum carbon ball diameter, $\boldsymbol{\Phi_{CB0}}$, approaches 1 as $\boldsymbol{\Phi_R}$ decreases. Further work might prove the existence of a reactor diameter, $\boldsymbol{\Phi_{R0}}$ which produces the smallest carbon ball of minimum diameter, $\boldsymbol{\Phi_{CB0}} \leq$ 100nm, at $\boldsymbol{\eta_{AC0}} = 1$ using the NCCVD method. Such achievement would eliminate the carrier gas from the production process. Consequently, the cost of production is reduced, enhancing competitiveness in nanocomposite applications. The next section looks at the effects of operating conditions on productivity and yield of carbon balls. Measures like production rate, yield and purity give insight into the economic feasibility of the process.

4.1.4 Effect of production conditions on productivity

Productivity measures are very important in evaluating a synthesis technology. These measures include i) the Production rate, $\boldsymbol{M_P}$ **(g/min)** which was evaluated as the average mass of carbon balls produced per unit time, ii) the Purity, **β (%)** computed as the percentage ratio of the mass of produced carbon balls to the gross mass of nanoparticles produced, $\boldsymbol{M_G}$ **(g/min)** and the Yield, **γ**, which is the ratio of the mass ouput rate of carbon balls produced, $\boldsymbol{M_P}$ **(g/min)** to the mass flowrate of carbon supplied as the carbon source, $\boldsymbol{M_{ci}}$. The above described production measures were computed using Equations 4.12 to 4.16 below.

$$M_p = \frac{M_R + M_{CYC}}{T_r} \tag{4.12}$$

Where M_R and M_{CYC} are the masses of carbon balls collected from the reactor and cyclone respectively and T_r is the total run time of the synthesis.

$$M_{ci} = 2M_{wC}\frac{pV_{ACi}}{RT} \quad (4.13)$$

Where M_{wC} is the Relative Molecular weight of carbon, V_{ACi} is the volumetric flow rate of C_2H_2, at the inlet, p is the atmospheric pressure (1.03kPa), R is the ideal gas constant and T is the operating temperature (1273K).

$$\gamma = \frac{M_P}{M_{ci}} \quad (4.14)$$

$$\gamma_{CYC} = \frac{M_{CYC}}{T_r M_{ci}} \quad (4.15)$$

Where γ_{CYC} and M_{CYC} are the cyclone yield and mass of carbon nanoballs collected from the cyclone respectively. The purity is given by Equation 4.16 below;

$$\beta = \frac{M_P}{M_G} \quad (4.16)$$

Table 4.3 shows the productivity data of the synthesised carbon balls.

Table 4.3: Carbon ball productivity from 16mm Φ x 300mm length reactor

η_{AC} [a]	Φ_{CB} (nm) [b]	M_{ci} (g/min) [c]	M_{CBc} (g/min) [d]	M_R (g/min) [e]	M_F (g/min) [f]	M_G (g/min) [g]	M_P (g/min) [h]	γ_{cyc} (%) [j]	B (%) [k]	ω [m]	γ_G (%) [n]	γ (%) [p]	γ_F (%) [q]
0.50	-	0.26	0.0000	0.0000	0.0020	0.002	0.000	0	0	-	1	0	1
0.61	140	0.32	0.0100	0.0009	0.0081	0.019	0.011	3	57	0.92	6	3	3
0.66	250	0.36	0.0042	0.0009	0.0038	0.009	0.005	1	58	0.82	3	1	1
0.72	80	0.39	0.0100	0.0300	0.0270	0.067	0.040	3	60	0.25	17	10	7
0.82	60	0.45	0.0382	0.0714	0.0480	0.158	0.110	8	70	0.35	35	24	11
0.90	120	0.51	0.0218	0.0410	0.0176	0.080	0.063	4	78	0.35	16	12	3
1.00	300	0.57	0.0211	0.0513	0.0190	0.091	0.072	4	79	0.29	16	13	3

a = acetylene flow ratio; b = CB diameter; c = mass flow rate of carbon into the reactor; d = mass accumulation rate of CBs in the cyclone; e = mass accumulation rate of CBs in the reactor, f = mass accumulation rate of flakes; g = gross mass production rate of carbon nanoparticles; h = mass production rate of carbon balls; j = cyclone yield of carbon balls; k = purity of CBs; m = mass ratio of cyclone CBs to total mass of CBs; n = gross yield of carbon nanoparticles; q = yield of carbon flakes

4.1.4.1 Effect of acetylene flow ratio on production rate

The production rate increased with increasing acetylene flow ratio (Figure 4.12). The highest production rate of 0.11g/min [6.6g/h] was achieved with 16mm diameter reactor acetylene flow ratio of 0.82 (Table 4.4 and Figure 4.12). The highest production rate also occurred in the carbon nanoball production region. The increasing trend was attributed to increasing carbon supply rate. However, it was difficult to obtain an accurate relationship between $\mathbf{M_p}$ and $\boldsymbol{\eta_{AC}}$ due to equipment limitation.

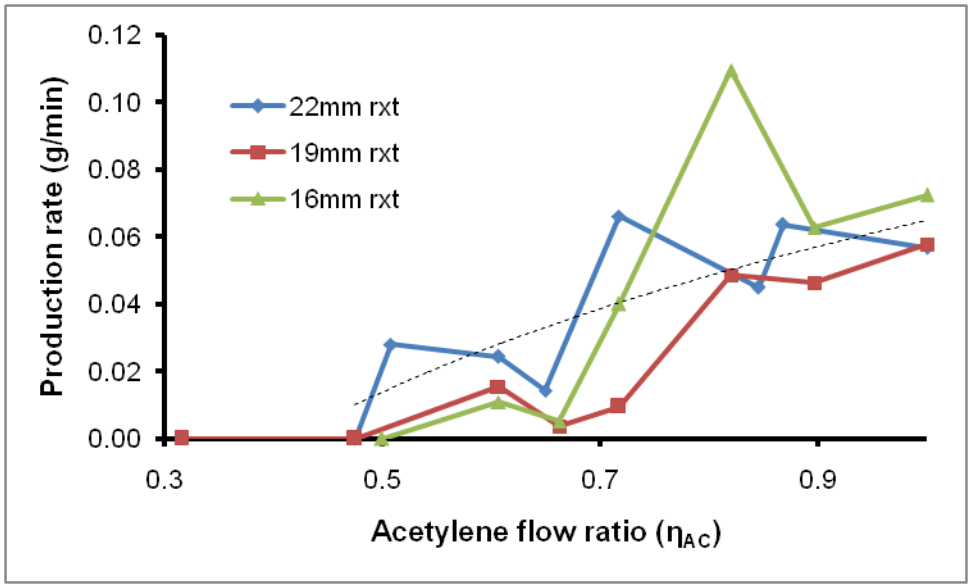


Figure 4.12: : Effect of acetylene flow ratio on production rate

4.1.4.2 Effect of acetylene flow ratio on yield

Figure 4.13 shows that the yield increased with increasing acetylene flow ratio. This was attributed to the fact that higher flow ratios promoted the growth of carbon nanoballs as opposed to flakes and other carbonaceous materials and hence the increase in yield. However, the maximum yield achieved was low at 24% (Figure

4.13). It is comparable to a yield of 26% reported elsewhere (Deshmukh et al., 2010). The maximum gross yield of carbon nanoparticles produced was 28% (Table 4.3). The blockages caused by equipment and orientational limitations like 90° elbows could be the major sources of low yields. The blockages choked the system, blocked and insulated the reactor, which might have been responsible for significant variations in the synthesis process.

Further work is proposed to account for the 72% as well as improvement of the yield to reduce cost. The unaccounted 72% could be made up of gaseous species such as benzene, C_4H_4, C_4H_2, vinyl, ethynyl radicals, hydrogen and unreacted acetylene (Deshmukh et al., 2010). Gas analysis techniques at the output end could be implored in further work to confirm the presence of such species and perhaps consider acetylene recycling.

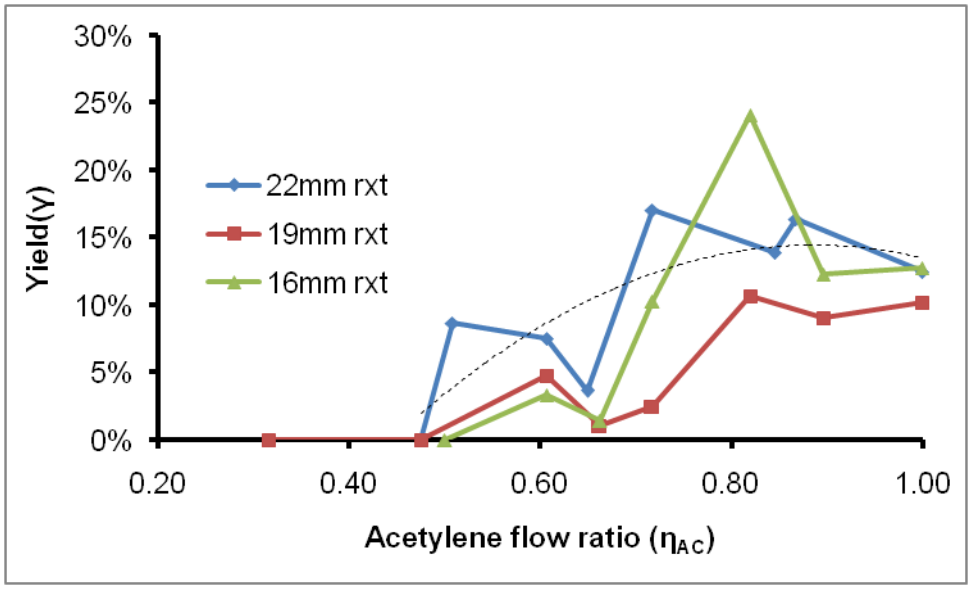


Figure 4.13: Effect of acetylene flow ratio on yield

4.1.4.2 Effect of acetylene flow ratio on purity

Despite the relatively low yields, the produced carbon balls from all reactors were highly pure as shown by Figure 4.14 and the TEM images in the previous section. The product collected at cyclone was of high purity (>99%) and hence of great interest due to the elimination of purification cost. Elimination of blockages from the system would imply that more carbon nanoballs would be collected in the cyclones rather than accumulate in the reactor and hence improve the yield whilst maintaining the high purity. The significance of high purity carbon nanoballs collected from the cyclone was that they could be used 'as produced' as a nanofiller for blending purposes. The purity was also observed to increase with increasing acetylene flow ratio (Figure 4.14). This was also attributed to the increasing probability of forming carbon balls as opposed to flakes as described in earlier sections.

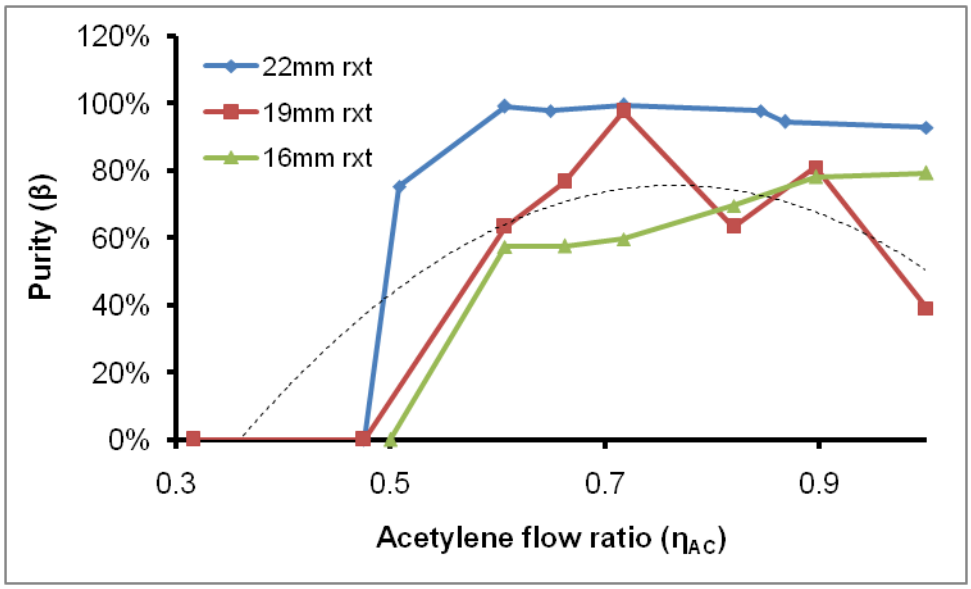


Figure 4.14: : Effect of acetylene flow ratio on purity of carbon balls

4.1.4.3 Challenges to productivity using the NCCVD equipment

Many productivity measures are expected to increase with the elimination of blockages for the following reasons. Firstly, the blockages reduce flow rate and hence increase the residence time of forming nanoparticles in the reactor. The nanoparticle diameters increase as a result and their morphologies are distorted. The purity of the nanoballs is compromised as a result and the production rate retarded due to the reduced flow rate. Secondly, blockages distort the proportions of the fresh graphitic constituents responsible for carbon nanoball formation, and hence reduce purity, yield and production rate. Thirdly, the nanoparticles returning to the reactor due to blockages reduce the reactor temperature, thus promoting the production of flakes and other carbonaceous material. The flakes stick to the wall of the reactor and further insulate the reactor from the elements supplying heat. The quality yield, purity and production rate were hence affected by the blockage.

4.1.5 Optimum region for carbon nanoball production

Figure 4.15 shows the optimum region for production of pure and uniform carbon nanoballs for blending purposes. The production range lies between acetylene flow ratio of 0.71 and 0.86, producing carbon nanoballs ranging from a minimum average diameter of 60nm to 100nm. Although the conversion efficiency (yield) and production rate were 24% and 6.6 g/h respectively (though comparable to similar reported work), there was great room for improvement (Mhlanga et al., 2010). For the purposes of synthetic rubber reinforcement, the pure and uniform carbon nanoballs collected from the cyclone of the 16mm Φ reactor were selected.

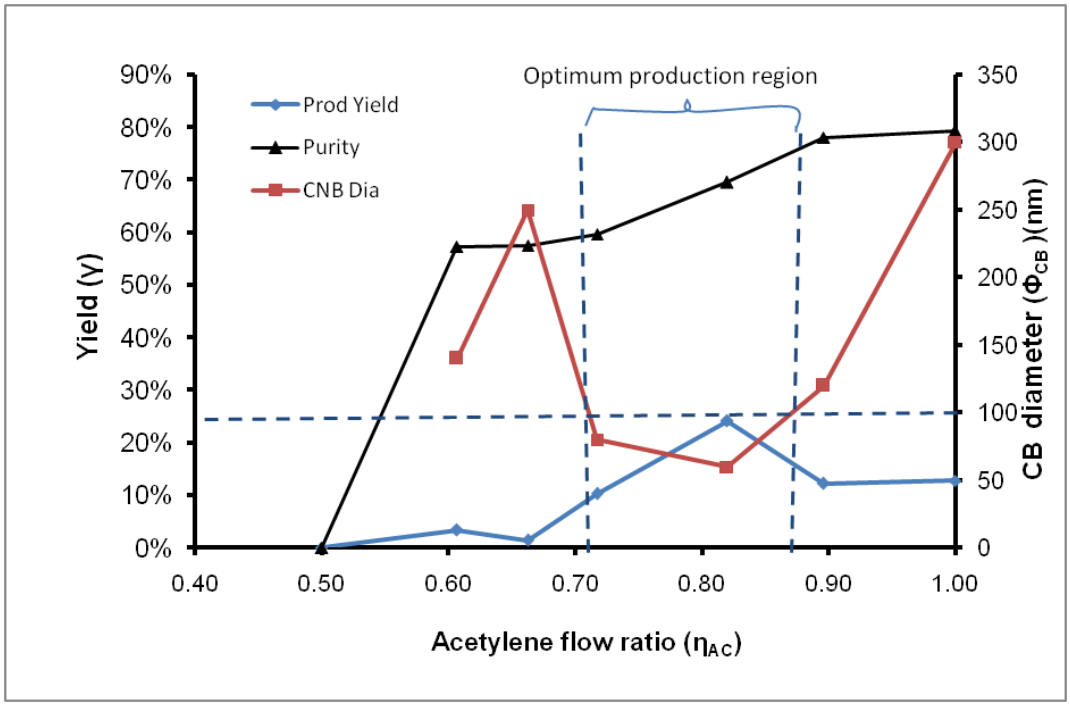


Figure 4.15: Effect of acetylene flow ratio on purity of carbon balls

Process and equipment redesign and optimisation are recommended to eliminate the blockages that prohibit smooth continuous production. Such further work is expected to significantly improve the production yield, rate and carbon nanoball sizes at minimal cost. Having successfully produced the carbon nanoballs, further caharacterisation was necessary for thermal stability since most ion exchange membranes operate at temperatures far above room temperature.

4.1.6 Thermal stability of the carbon nanoballs

The thermal stability of as-synthesised carbon balls was investigated by TGA. Figure 4.16 shows the result of TGA in nitrogen. In the first stage, the weight decreased at a very slow rate from room temperature to 540 °C, and the product lost about 3 wt.%. In the second stage, the weight loss was very fast and the product burned off at 900 °C (1173K).

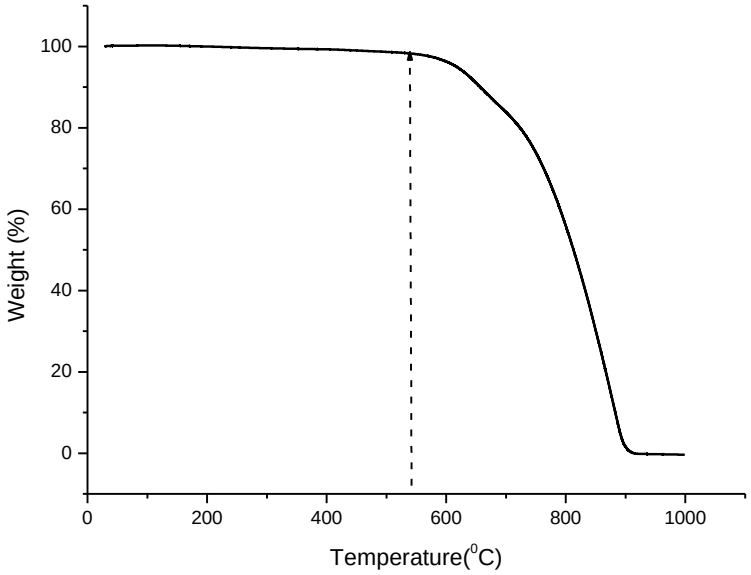


Figure 4.16: Thermal stability of 60nm carbon nanoballs produced in 16mm Φ, at 0.82 η_{AC} and 1000°C (Sample collected from cyclone).

The 3wt% loss in the first stage could be attributed to the amorphous carbon of the unclosed curved outermost carbon layers of the nanoballs. The result also illustrated that the spheres are thermally stable up to 540 °C (813K) and similar to the ones reported elsewhere (Miao et al., 2003; Jin et al., 2005 and Abdulkareem, 2009). The complete decomposition of the carbon nanoballs at 1173K confirmed that they were not fullerenes. The fullerene decomposition temperatures range from 4000K for multi-shelled ones to 7500K for C_{20}, which are way higher than the $\boldsymbol{T_d}$ for the produced carbon nanoballs (Zetl and Cummings, 2001). This further strengthens the earlier assumption that the carbon nanoballs were made of unclosed curved layers of carbon piled together concentrically to the core. The possibility of dangling bonds at the edges offers opportunities for interaction with other molecules and ultimately possibility of strong nanocomposites (Kang and Wang, 1996).

Since most IEM applications operate below 500°C, a decomposition temperature of 540°C could generally be adequate. The knowledge of the type of carbon ball

produced is critical in the prediction and modeling of reinforcement measures. The 97% weight retention at 540°C further confirms the high purity first shown from TEM images.

4.1.7 Electron conductivity properties of the carbon nanoball

The degree of crystallinity of carbon balls is dependent on the quantity of ordered graphitic layers in the nanomaterial. The ratio of I_G (intensity of graphitic band) to the I_D (intensity of distorted layer band) was used to determine the conductivity properties. If ($I_G/I_D > 2$), the material is graphitized and hence an electron conductor. Otherwise, it is a poor conductor and hence an electron insulator (Shanov et al., 2007 and Abdulkareem, 2009).

Figure 4.17 shows the Raman spectrum of the 'as synthesized' carbon nanoballs. A strong peak at 1589.5 cm^{-1} and a relatively weak peak at 1332 cm^{-1} which correspond to the G and D bands of carbon spheres respectively. The peak at 1589.5 cm^{-1} (G band) is attributed to the stretching modes of C–C (sp^2) bonds of typical graphite, while the peak at 1332 cm^{-1} (D band) (sp^3) is related to the defects and disorders of structures in carbonaceous solid. The intensity ratio, I_G *(145)* /I_D *(139)* of 1.04, was indicative of the presence of approximately equal amounts of sp^3 and sp^2 carbon. This result shows low graphitization degree and hence electron insulating amorphous carbon nanoballs (Deshmukh et al., 2010 and Abdulkareem, 2009).

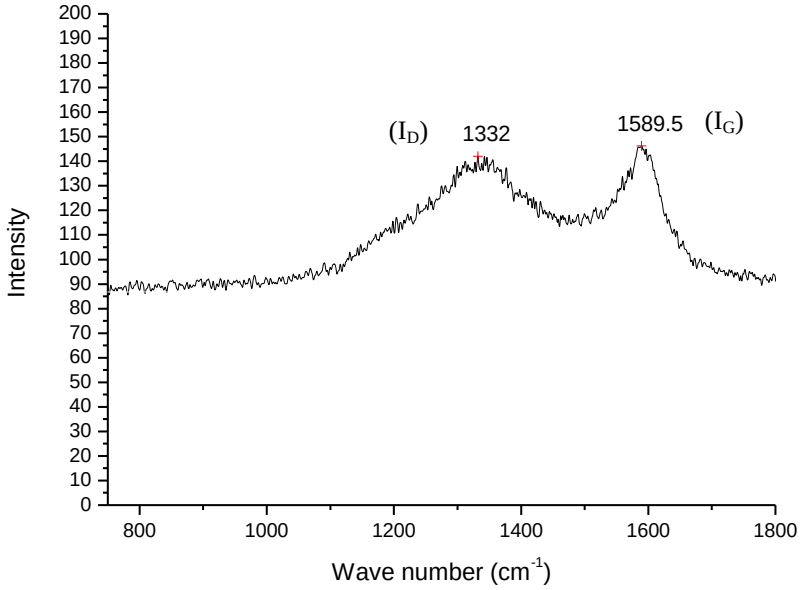


Figure 4.17: Raman Spectra of 60nm carbon nanoballs form 16mm Φ reactor

This electron insulation property is critical to IEM for fuel cells to prevent undesirable short circuiting. On the other hand, if conducting carbon nanoballs could be made, they could find applications in nanocomposite polymeric conductors.

4.1.8 Porosity and density of carbon nanoballs

The surface area of pores and the pore volume of the 60 nm carbon nanoballs were 13.81m^2/g and 0.029cm^3/g respectively as shown in Table 4.5. Therefore the nanoballs produced were highly porous and lightweight. The samples collected from the reactor were less porous than the ones from the cyclone. This was attributed to the longer residence time in the former (Abdulkareem, 2009). This greater exposure time means more layers are compactly stacked together and hence density increases whilst pore volume decreases (Wang and Kang, 1996).

Table 4.4: Surface area and pore volume analysis

Sample ID	Φ_{CB}(nm)	Surface area (m^2/g)	Pore volume (cm^3/g)
Cyclone collected samples			
S_6	60	13.81	0.029
S_3	200	10.28	0.021
Reactor collected samples			
S_{1x}	150	2.49	0.0059
S_{8x}	400	3.022	0.0055
S_{5x}	600	5.37	0.012

The density of the formed carbon nanoballs was approximated by using a combination of Archimedes principle and the pore volume. A weighed mass of the carbon nanoballs was immersed in a measuring cylinder with a predetermined volume of ethanol. The change in volume was noted. The density of the carbon nanoballs were estimated as follows; Let change in volume, ΔV due to immersed mass, m_c, then apparent density, $\rho_{ca}=m_c/\Delta V$ g/cm^3. Then the true density must account for the pore volume, therefore, change in volume correction, $\Delta V_{cor} = 1/V_p$, where V_p is the Pore Volume in cm^3. Therefore the true density, $\rho_{ct}= m_c/(\Delta V+ \Delta V_{cor})$ g/cm^3 (Joyce, 2009). The approximate density of the carbon nanoballs was 0.5g/cm^3, a value much lower than that of diamond, 3.50 g/cm^3, and graphite, 2.26 g/cm^3 (Jin et al., 2005). The density showed a typical lightweight nanofiller desirable for high strength to weight ratio reinforced nanocomposites. The high porosity could be desirable for the selective permeability required in ion exchange membrane processes.

4.2 Sulphonation of styrene butadiene rubber, blending and casting

The sulphonation of locally available SBR, blending and casting with the aim of producing a strong nanocomposite ion exchange membrane are analysed and discussed in this section. Quantitative and qualitative sulphonation data was initially analysed and discussed, followed by blending and finally, nanocomposite characterization. Nevertheless, a separate section is dedicated to the analysis and discussion of the mechanical properties testing results of the nanocomposite.

4.2.1 Sulphonation of emulsified styrene butadiene rubber

Chlorosulphonic acid was preferred to concentrated sulphuric acid, sulfur trioxide and acetyl sulphate as the sulphonating agent of choice for several reasons. Sulfur trioxide was reported to be too reactive whilst the other two were reported to result in low degrees of sulphonation due to low reactivity and difficulty to penetrate the polymer chain to sulphonation sites (Knaggs and Nepras, 2005; Owzhera and Cerfontain, 1968 and Foster, 1997). Since the concentration, temperature and reaction time were critical parameters for sulphonation, optimal parameters from previous work were used as the basis for sulphonation (Idibie, 2010; Gibson and Bailey, 1980 and Barreto, 2009).

4.2.1.1 Effect of chlorosulphonic acid concentration on sulphonation

High concentrations of $ClSO_3H$ (0.2 - 1.6M) were first used in an attempt to achieve homogeneity as well as high DS at lowest possible time. Serious challenges associated with polymer degradation and gelation was observed. This prompted the study of the effect of concentration of $ClSO_3H$ on sulphonation. Table 4.5 shows the concentration effect on IEC and DS of the sulphonated SBR.

Table 4.5: Effect of $ClSO_3H$ concentration on 24hr sulphonation of SBR, sulphonated at r.t.p and constant stirring speed of 1250rpm

Conc. ($ClSO_3H$) (M)	Molar ratio[a] (η_d/η_s)	IEC mmol/g	DS (%) (η_{SO3}/η_{C8H8})	Efficiency (%)[b] (DS/M.R)	Recovery (%)[c] [(1-m_{burnt})/m_{sbr}]
0.05	0.622	0.033	2	2	100
0.09	1.12	0.97	44	39	100
0.8	0.6	0.93	42	70	50
1.6	0.3	0.551	25	83	20

a= ratio of moles of acid added to moles of styrene; b = ratio of DS to the molar ratio; c = ratio of mass of undegraded polymer to mass of originally added polymer

The effect of concentration on sulphonation was not consistent as shown in Table 4.5. The DS was very low, 2% at 0.05M CSA and 0.6 molar ratio, and increased to 44% at 0.09M and 1.12 Molar Ratio. From this peak, DS decreased with increasing $ClSO_3H$ concentration.

The DS was limited by two major factors. Firstly, low concentration of acid resulted in high acid volume requirements to match the stoichiometric requirements for significant sulphonation. The maximum possible volume that can be added was limited by the sulphonation equipment and hence the low DS at 0.05M CSA.

Secondly, concentrations above 0.1M CSA resulted in instant polymer degradation. Although filtration of the rubber solution under sulphonation was carried out to remove the degraded material, sulphonated rubber with burnt phases randomly distributed in solution was produced. The purity improved with decreasing acid concentration. Furthermore, the degradation meant polymer wastage and hence low recoveries. This degradation was associated with localized extremely high heat of reaction as compared to dissipation at the point of contact of acid dropping into the polymer solution (Rabia et al., 1996; Knaggs and Nepras, 2005).

Apart from polymer degradation, gelation was also observed for acid concentration above 0.1M. It was observed after addition of CSA above a critical volume. The

gelation could be associated with the formation of sulphone bridges between adjacent sulphonate groups from neighbouring aromatic rings of styrene units (Bacquet et al., 1992 and Walsby et al., 2001). Other side reactions might include arenesulfonyl chlorides and diarylsulfones (Knaggs and Nepras, 2005 and Rabia et al., 1996).

Therefore, due to the observed limitations described above, the sulphonation process is assumed to be stoichiometrically limited. The molar ratio of chlorosulphonic acid to styrene was used to calculate the efficiency of the reaction (Table 4.5). The recovery, which was defined as the ratio of the *original mass of rubber in solution less degraded mass* to the *mass of original rubber*, was also an important analysis measure. The reaction efficiency was defined as *the ratio of moles of styrene units sulphonated to the moles of acid added*.

Figure 4.18 shows that recovery at concentrations below 0.1M CSA was high at 100% and hence no polymer degradation. Above 0.1M CSA, recovery dropped from 100% to 20% at 1.6M due to polymer degradation described above. However, the reaction efficiencies were low (2 – 39%) at low concentrations (0.05 - 0.1M). Above 0.1M the reaction efficiencies increased up to a maximum of 83% at 1.6M CSA (Table 4.5). The high efficiencies at higher concentrations could be attributable to better penetration of the acid into the polymer chain as compared to lower concentrations. Since sulphonation is also a reversible reaction, high concentrations tended to favour the forward reaction and hence achieved better yields (Bacquet et al., 1992).

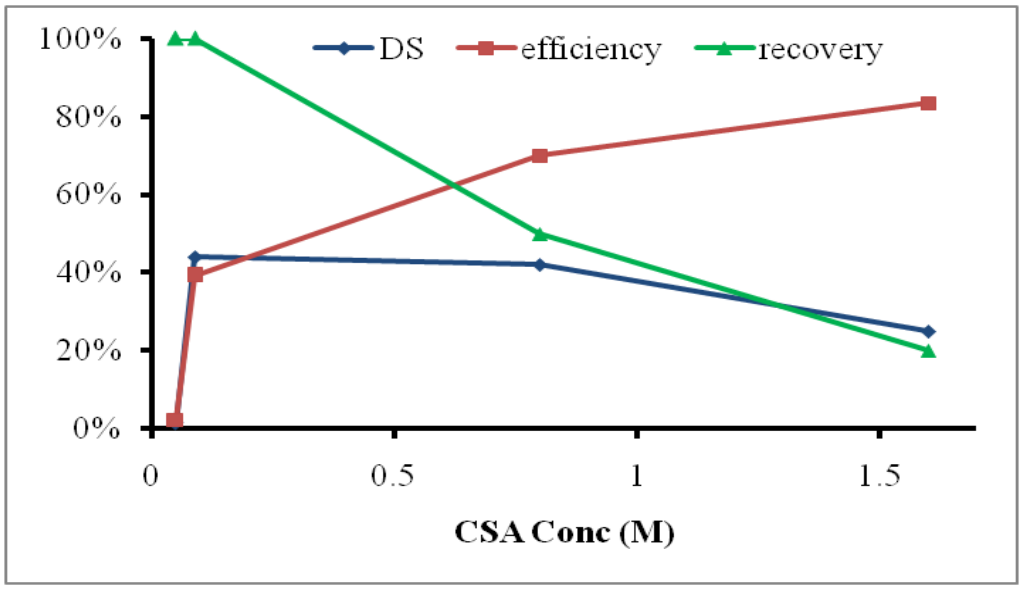


Figure 4.18: Effect of $ClSO_3H$ concentration on yield and efficiency of sulphonation

On the other hand, the maximum degree of sulphonation (44%) was achieved at the low concentration of 0.09M CSA. This was due to the fact that sulphonation is sensitive to the initial concentration of CSA. The 0.09M acid molar ratio of 1.12 stoichiometrically promoted high degree of sulphonation. The volumes of CSA that can be added at high concentration were limited by gelation and hence limiting the DS (Figure 4.18).

Therefore, if there is a way of preventing polymer degradation and gelation at high concentrations of sulphonating agent, then high DS could be achieved using low volumes of reagents. Sulphonation times could also be reduced and hence significantly reducing the cost of sulphonation. Although cost reduction was beyond the scope of this work, insights based on the encountered challenges might enhance further work towards cost reduction of the sulphonation process. Analysis of the root causes of polymer degradation and gelation was therefore necessary for recommendations for further work.

4.2.1.2 Causes of polymer degradation

The instant localized polymer degradation observed at dropwise addition of acid concentrated above 0.1M was assumed to emanate from the extremely high local exotherm from the highly exothermic sulphonation reaction. The maximum stirring rate of the solution was not adequate to dissipate this heat and hence the burning out. To prove this assumption, number of moles per drop of acid, η_d, was determined as a function of acid concentration and tabulated in Table 4.6. The matching estimate number of moles of styrene, η_s in the equivalent volumetric drop of polymer solution was also determined. It was observed that at an acid concentration of 1.6M, the instantaneous mismatch of moles of acid to styrene was 18 times in favour of the acid. This mismatch, referred to in this analysis as *(DOM = η_d/η_s)* was greater than 1 for all acid concentrations greater than 0.09M acid. Therefore the high mismatch between the localized moles of sulphonating agent and styrene moles in polymer solution was the root cause of polymer degradation. The same mismatch must also be responsible for gelation due to sulphone bridges and other side reactions (Knaggs and Nepras, 2005; Owzhera and Cerfontain, 1968 and Bacquet et al., 1992).

Table 4.6: The relationship between $ClSO_3H$ concentration and instantaneous ratio of $ClSO_3H$ moles to styrene moles

Acid Conc. (M)	η_d (moles/drop)	η_s(moles/drop)	η_d/η_s (DOM)
0.05	4.22E-06	7.63E-06	0.6
0.09	7.59E-06	7.63E-06	1.0
0.8	6.75E-05	7.63E-06	8.9
1.6	1.35E-04	7.63E-06	17.7

An acid concentration of 0.09M, corresponding to Degree of Mismatch (DOM) of 1, which implied zero mismatch (Table 4.6), resulted in smooth sulphonation with neither polymer degradation nor polymer gelation. The assumption was therefore proved correct. The highest degree of sulphonation was achieved at 0.09M CSA. The

lowest recovery of polymer occurred at the highest concentration corresponding to the highest degree of mismatch. FTIR peaks at around 1261cm^{-1}, 2250cm^{-1} and 3600cm^{-1} as shown in Figure 4.19 are suspected to be due to the side reactions on the polymer backbone at high concentrations of chlorosulphonic acid (Mokrini et al., 2004). The 0.09M sulphonated rubber, shows a consistently similar FTIR profile to pure SBR, with intact polymer backbone (Figure 4.19). The additional peaks between 1033 and 1126cm^{-1}, 1632 and 1650cm^{-1} and 3400cm^{-1} (Figure 4.19) were evidence of stretching of sulphonate groups (Martins et al., 2003; Lee et al., 2004 and Baeta et al., 2009).

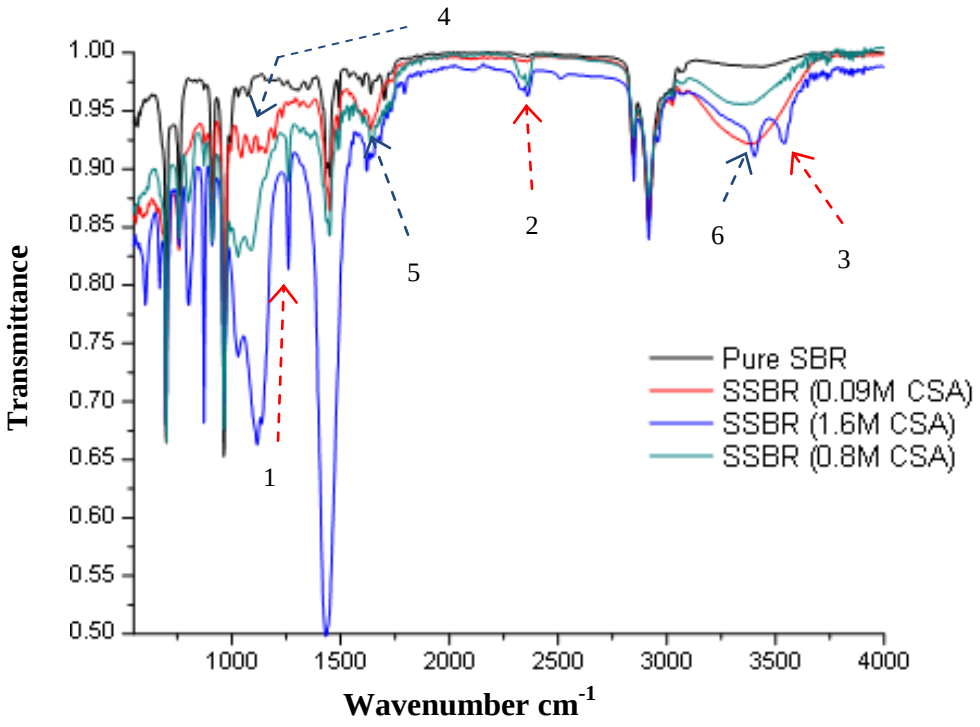


Figure 4.19: FTIR of pure SSBR, SSBR (0.09M) and degraded SSBR at different concentrations. (1→1261cm^{-1}, 2→2355cm^{-1} and 3→3500cm^{-1}) are suspected degradation sites to the polymer backbone due to side reactions. (4→1033– 1126 cm^{-1}; 5→1650cm^{-1};6→3400cm^{-1}) are wavenumbers which show the evidence of aromatic sulphonation

4.2.1.3 Optimum sulphonation of styrene butadiene rubber

Sulphonation of SBR with 0.09M CSA for 24 hrs at 1250 rpm stirring and room temperature conditions under an argon inert environment is referred to as optimum sulphonation. The DS during optimum sulphonation increased almost linearly with increasing molar ratio (moles of $ClSO_3H$ to moles of styrene units) to a desirable IEC of 0.97mmol/g and relatively high DS of 44% (Table 4.7). The reaction efficiency also increased with molar ratio. However the reaction efficiency was low at 39%, which has cost and environmental consequences due to solvent wastage.

Table 4.7: Sulphonation data for SBR sulphonated at 0.09M $ClSO_3H$ for 24hrs at r.t.p and 1250 rpm stirring

Sample	Molar Ratio η_d/η_s	IEC mmol/g	DS (%) η_{SO3}/η_{C8H8}	Efficiency (%) DS/M.R
1	0.2	0.04	2	9
2	0.4	0.044	2	5
3	0.6	0.26	12	20
4	0.8	0.39	18	23
5	1	0.7	33	33
6	1.12	0.97	44	39

Due to the fact that homogeneous sulphonation resulted in a relatively high DS at 0.09M $ClSO_3H$ and 1.12 molar ratio, more SBR was sulphonated at the same conditions to produce sulphonated matrix material for blending purposes. The plane membrane was cast and characterized by SEM and FTIR (Figures 4.20 and 4.21). SEM shows unevenness which is distributed uniformly throughout the whole surface. A slightly darker phase was observed within a lighter phase. The darker phase could be assigned to the softer hydrophilic sulphonic acid groups containing small amounts of water. The lighter phase is assigned to the hydrophobic polymer backbone which stays unchanged after sulphonation (Figure 4.20).

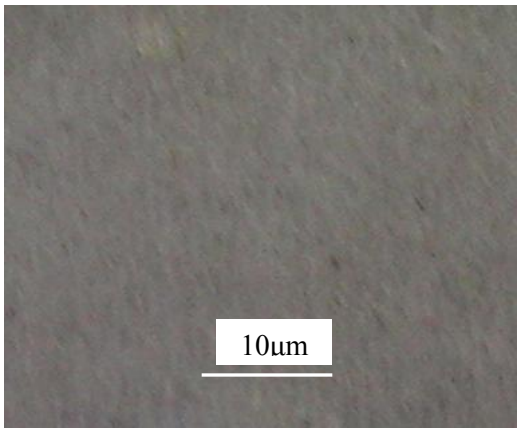


Figure 4.20: SEM image of 44% DS SSBR at 0.09M CSA and 1.12 molar ratio

4.2.1.4 FTIR analysis of sulphonated styrene butadiene rubber

Figure 4.21 shows specific features for non sulphonated and sulphonated SBR. The FTIR of the unsulphonated rubber acted as a control to check whether the polymer backbone remained intact. Secondly, new peaks and change of peak structure would indicate the position of sulphonation. For the unsulphonated SBR, the broad symmetric peaks at 2,916 and 2,844 cm^{-1} indicate stretching vibrations of CH and CH_2 of the polymer backbone. The peaks between 1436-1452 cm^{-1} and 699 cm^{-1} confirmed the presence of the phenyl group. The peak at 1600 cm^{-1} confirms the CH group, whilst 966 cm^{-1}, the CH and C=C of trans 1,4 butadiene and 910, for 1,2 butadiene (Baeta et al., 2009; Mokrini et al., 2004).

For SSBR, three important regions are observed. The consistent broad and symmetric absorption peak at 3400 cm^{-1}, corresponds to the hydroxyl group that is formed due to the oxidation during the synthesis. The second region showing stretching from 1624-1641 cm^{-1} confirms substitution on the phenyl ring by the sulphonate group. The third region is an unsymmetrical stretch between 1028 and 1261 cm^{-1}. Within this broad stretching a small peak at 1033, 1042 and 1093 cm^{-1} confirm the sulfoxide stretching, S=O of the sulphonate anion. The small peaks at 1124, 1157, 1192 and

1261 cm^{-1} indicated the phenyl ring substituted by a sulphonate group (Figure 4.21) (Mokrini et al., 2004).

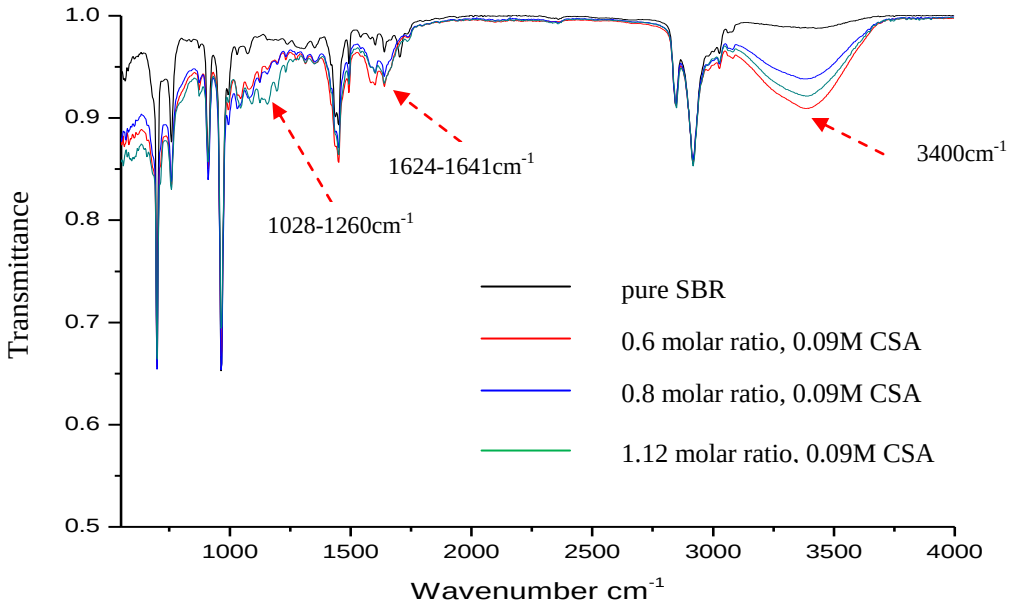


Figure 4.21: FTIR of SSBR membranes sulphonated by 0.09M CSA at different molar volumes

Conclusively, a SSBR of 44mol% DS, and 0.97mmol/g has been successfully produced using 0.09M $ClSO_3H$ at a relatively fair reaction efficiency of 39%. This sulphonation method showed potential in the production of low cost synthetic rubber IEM matrix for filler reinforcement. Further work to minimize gelation and polymer degradation has been proposed in an attempt to improve yields and DS, reduce sulphonation time and cost.

Therefore, the successful production of the constituent materials for the nanocomposite ion exchange membrane led to the blending of the constituents to produce the desired strong nanocomposite ion exchange membrane.

4.2.2 Blending and production of membrane films

As reported in literature effective blending is critical to achieving a nanocomposite with IEM of high uniformity. The agglomeration of the produced carbon nanoballs had to be overcome for effective dispersion. Therefore ultrasonication was the selected blending method. SEM of preliminary cast composites at 20% amplitude showed serious agglomeration and non uniformity (Figure 4.22). From the SEM images agglomeration is indicated by the dark spots with an approximate diameter range of 200nm to 500nm for 2.5wt% CNB loaded composite membrane. For 4wt% CNB loaded composite membrane, the approximate agglomerate diameter range was 400nm to 600nm. Considering that the average diameter of the used CNB was 60nm, the blending at 20% amplitude could not disperse the nanoballs into the sulphonated polymer matrix. Therefore the amplitude of ultrasonication was increased to 60%, holding the other variables constant.

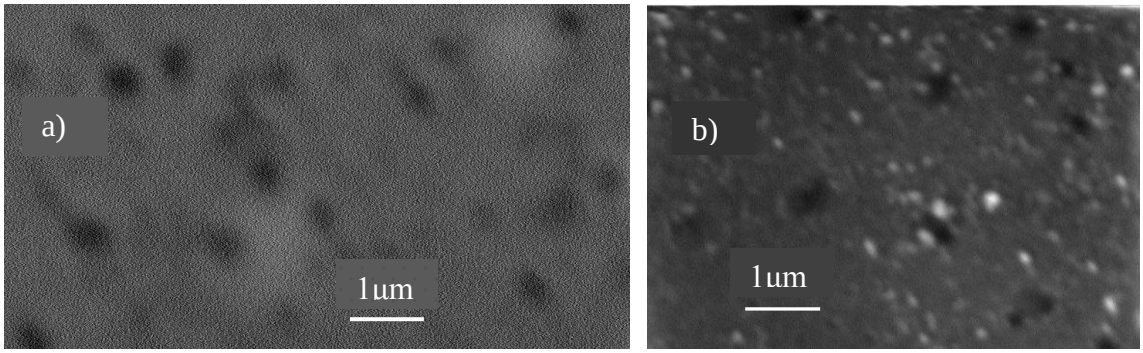


Figure 4.22: SEM Images of 160µm thick membranes, blended at 20% Amplitude, 3 hrs sonication time at 200W power. a) 2.5wt% CNB loading b) 4 wt % CNB loading

Figures 4.23b and 4.24 show that the increase in the amplitude of sonication significantly reduced agglomeration and improved dispersion efficiency. The dispersion efficiency in this case was defined as the percentage distribution of nanosize filler particles to the total distribution of fillers in the matrix. The dispersion

effectiveness was estimated from SEM images and hence very approximate (Figure 4.25). An estimated 85% dispersion efficiency was achieved at 75% amplitude of sonication and 1wt% carbon filler concentration. The lowest dispersion efficiency of 1% was observed at 20% amplitude and 4wt% filler concentration. At constant filler wt%, the dispersion efficiency increased drastically with increasing sonication amplitude. As an example for 1wt% filler, dispersion efficiency increased from 10% efficiency for 20% amplitude to 85% efficiency for 75% Amplitude, approximately 8 fold increase. At constant amplitude of sonication, dispersion efficiency decreased with increasing filler wt%. For example, at 75% amplitude, the efficiency decreased from 85% at 1wt% filler to 55% for 4wt% filler. Since the quality of dispersion was critical to reinforcement, the effect of sonication and filler concentration on dispersion efficiency needed to be discussed.

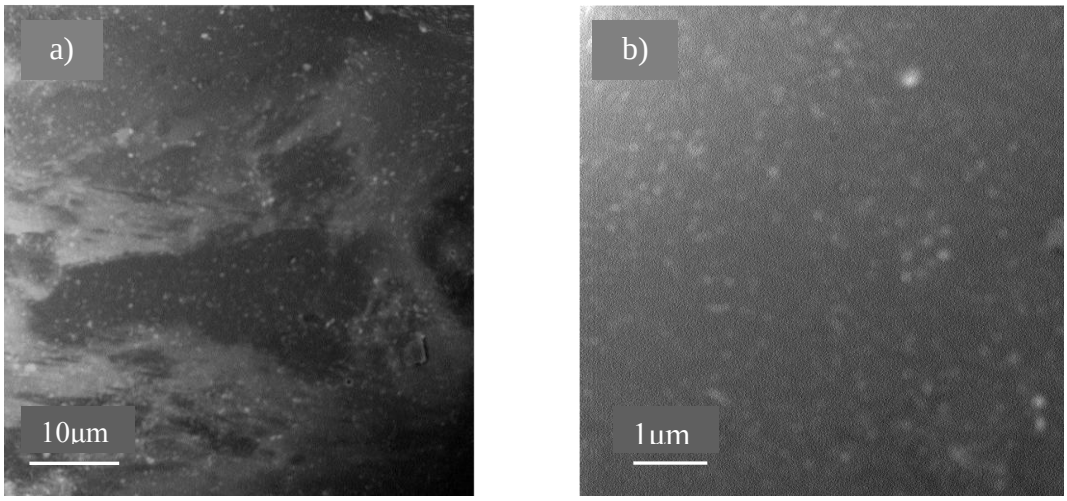


Figure 4.23: SEM images of 160µm thick membrane a) 4wt% cnb loaded IEM at 20% sonication amplitude showing the existence of distinct polymer phases and and blended phases; b) homogeneous 1wt% cnb loaded IEM at 60% sonication

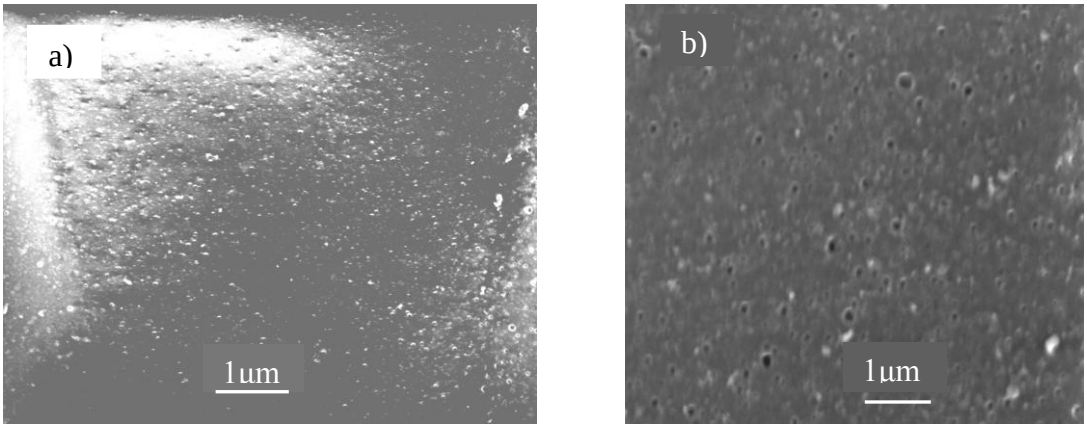


Figure 4.24: SEM image of 160µm thick membrane, a) 2.5wt% CNB loaded IEM at 60% sonication amplitude; b) 4wt% CNB loaded IEM at 60% sonication amplitude

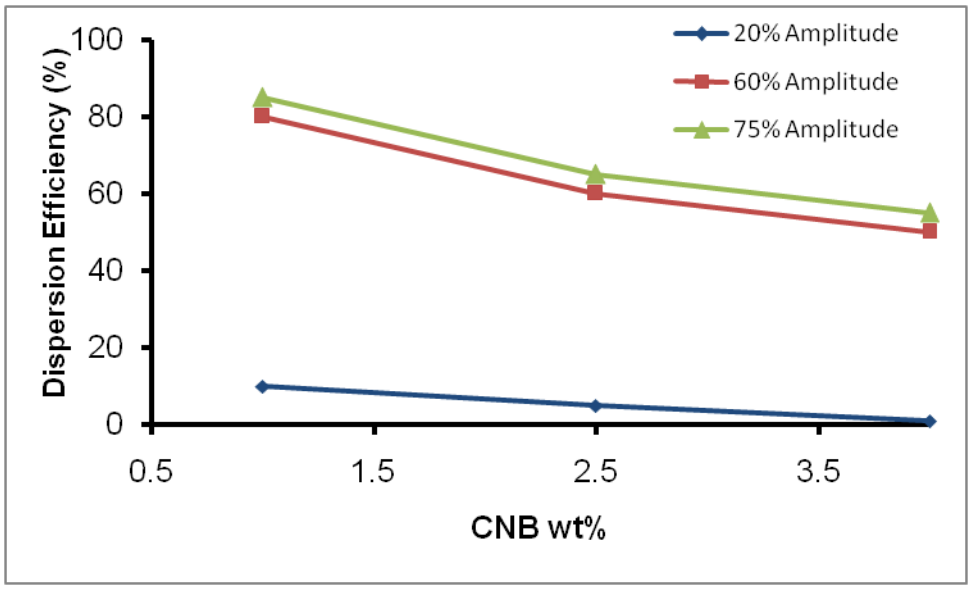


Figure 4.25: Effect of amplitude of sonication and filler weight fraction on dispersion effectiveness

The SEM analyses above and Figure 4.25 show two key aspects. Firstly, the effectiveness of dispersion increased with increasing sonication amplitude. This could be attributed to the structural difference between the structure of carbon nanoballs (spherical) and polymer chain (long and cylindrical). The aspect ratio of a SSBR chain is about 854 (790/0.924) (l/2r). This implies that the aspect ratio of a chain was 850 times greater than that of a carbon nanosphere (Allegra et al., 2008). This great mismatch was responsible for the agglomeration that took place due to the difficulties encountered on mixing. Higher sonication amplitudes therefore break and separate the long polymer chains. The broken polymer chains have lower aspect ratios which are more compatible with the carbon nanospheres. As the shorter polymer chain fragments attempt to recombine on drying, they randomly interact with the carbon nanospheres (Allegra et al., 2008). The dangling carbons at the outer layers of the carbon nanospheres interact with terminal free radical ends of the chain fragments (Kang and Wang, 1996). This strong polymer filler interaction was believed to be responsible for reinforcement.

At low sonication amplitudes, polymer- nanoball interaction was assumed to be very low, polymer - polymer and filler - filler were very high, thus promoting agglomeration of the carbon nanoballs. Therefore high amplitudes of sonication (60 and 75%) resulted in high dispersion of carbon nanoballs with minimum agglomeration. However, an attempt to increase the amplitude of sonication above 75% resulted in rapid heat build up which made the process difficult to control.

Secondly, as Figure 4.25 shows, agglomeration increased with increasing filler concentration at constant amplitude of sonication. This could be attributed to the fact that the higher concentration of filler requires further separation of polymer chains to incorporate more carbon nanospheres into the matrix. This further separation requires greater power which was limited by the amplitude of sonication. Therefore the degree of dispersion decreased with increasing filler concentration. This observation pointed to the fact that more energy intensive methods may have to be found to further

improve the dispersion effectiveness. Non energy intensive methods may also be used to improve dispersion.

The successful dispersion of carbon nanoballs at higher amplitudes of sonication was a major milestone towards the achievement of reinforcement. However, the fragmentation of long polymer chains at high sonication amplitudes could mean a compromise on the mechanical properties. The compromise could be expected since the mechanical properties of polymeric materials increase with increasing molecular weight (Allegra et al., 2008).

4.2.3 Characterisation of SSBR nanocomposite Ion Exchange Membrane

The nanocomposites were characterised by FTIR and TGA for qualitative sulphonation analysis and thermal stability respectively

4.2.3.1 FTIR analysis of sulphonated nanocomposite IEM

FTIR was used to qualitatively assess the nanocomposite material. Figure 4.26 shows that the polymer backbone was not distorted by blending. The strong peaks at 3400, 1641, 1126 and 1033 cm^{-1} were consistent with plain SSBR. A broad strong band observed for 4wt% CNB loaded IEM at 1632 cm^{-1} was attributed to the C=C bonds of carbon nanospheres. The generally lower transmittance values observed for 4wt% CNB loaded IEM was attributed to the presence of high density of C-C and C=C bonds of carbon nanospheres (Mokrini et al., 2004 and Sobkowicz et al., 2009).

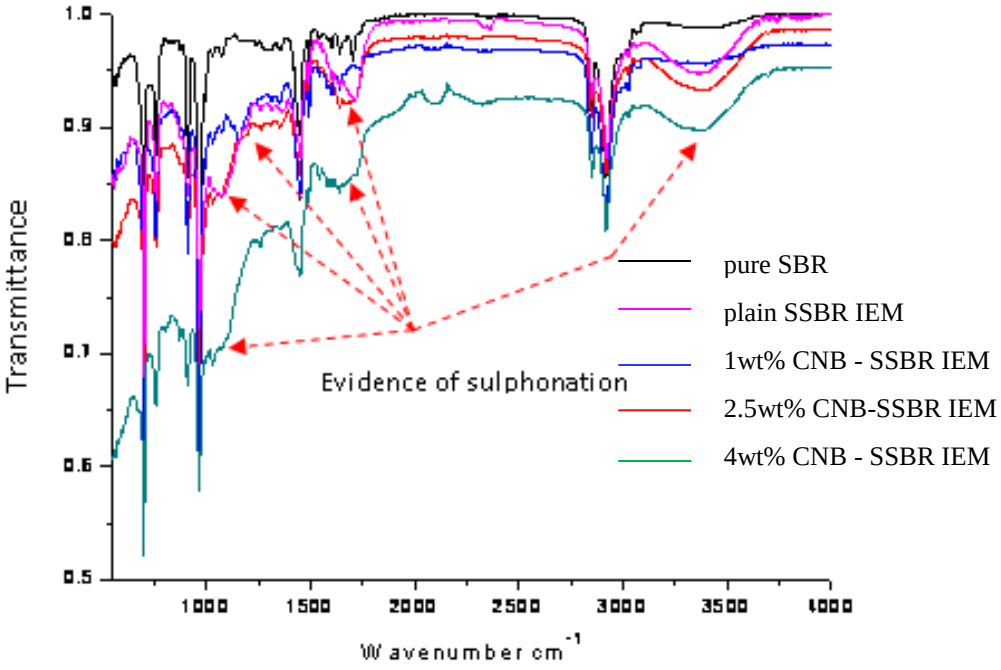


Figure 4.26: FTIR of nanocomposite IEM at different wt% CNB loading

4.2.3.2 Thermal stability of nanocomposite IEM

Figure 4.27 shows the thermal stability for nanocomposite IEM. For both unblended and blended IEM, they went up to 140°C without any weight loss. Rapid decomposition of all samples started at 415^0C and total decomposition occurred at 622^0C. The 2.5 and 4wt% CNB loaded IEM sample lost 5% weight before rapid decomposition, whilst the rest of the samples lost 8%. This loss could be attributed to the loss of water absorbed by the hygroscopic membrane. Therefore the IEM could be thermally stable for up to 415°C.

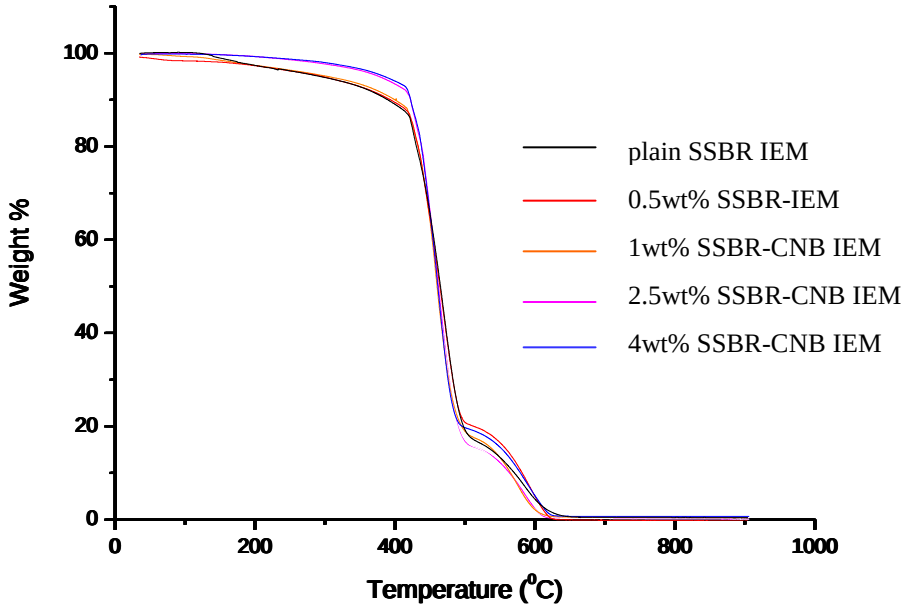


Figure 4.27: Thermal stability of SSBR nanocomposite IEM

The 4wt% CNB loaded IEM could withstand 199^{0}C without any material loss. This relatively high thermal stability could be of use in ion exchange membranes for fuel cell applications, where temperatures above 120^{0}C are desirable. Having successfully blended and cast thin nanocomposite membranes of 160μm average thickness, the testing and evaluation of mechanical properties were feasible. Therefore the next section analyses and discusses the ultimate goal of the whole work – the reinforcement effects of carbon nanoballs to SBR ion exchange membrane.

4.3 Mechanical testing of SSBR nanocomposite IEM

In this section, the results of mechanical testing of nanocomposite ion exchange membranes were analysed, evaluated, discussed and compared to existing work. The first subsection focused on the general results of mechanical testing. From these results, detailed analysis and discussion of the effects of carbon nanoball concentration on dimensional stability, mechanical strength, ductility and endurance was done. The trends were then compared to existing models and finally an attempt to establish relationships for predictions was done. Recommendations for further work were presented too.

4.3.1 Effect of CNB volume fraction on mechanical properties of SSBR IEM

The mechanical tests carried out on specimens from the nanocomposite membranes blended at 60% amplitude, 20 days after blending were frequently used for analysis and discussion due to greater consistency and more uniform dispersion. Data derived from mechanical testing using the Hysitron Nanotensile5000 tester is recorded in Table 4.8.

The filler volume fraction, V_f was defined as the ratio of the volume occupied by the carbon nanoballs to the total volume of the nanocomposite. It was derived from the weight fraction of carbon nanoballs used (CNB wt%) using the density - volume relationship described in the methodology section. The Young's modulus, E (MPa) was computed as the gradient of the initial linear portion of the stress - strain graph obtained from uniaxial tensile testing. The yield strength, σ_y (MPa) was the stress value obtained at the point where the initial slope of the stress - strain graph, offset by 0.2% on the strain axis, met the plotted stress - strain curve. The tensile strength, σ_s (MPa), was the stress level on the stress strain graph at which the membrane broke apart. The strain, e_u, was evaluated as the ratio of the extension of membrane specimen before breaking to the original specimen length. Since the fracture

toughness evaluation of elastomers is difficulty using conventional methods, it was computed by the Hysitron Nanotensile tester software as the area under the stress-strain curve.

Table 4.8: Mechanical properties of SBR-CNB nanocomposite IEM

CNB wt%	V_f	E(MPa)	σ_y(MPa)	σ_s(MPa)	e_u	$U_{F.T}$(J/cm^3)
0.00	0.00	13.71±0.29	0.25±0.02	2.00±0.09	0.68±0.03	0.84±0.04
0.25	0.008	14.34±0.15	0.24±0.01	1.90±0.12	0.57±0.05	0.71±0.01
0.5	0.017	17.15±0.19	0.27±0.01	1.92±0.14	0.69±0.03	0.83±0.07
0.75	0.025	21.91±0.18	0.34±0.01	2.17±0.12	0.73±0.03	0.91±0.02
1	0.033	24.58±0.29	0.47±0.01	2.37±0.10	0.53±0.08	0.85±0.04
1.75	0.058	22.05±0.06	0.45±0.02	2.44±0.03	0.67±0.04	0.99±0.07
2.5	0.086	19.73±0.32	0.44±0.01	2.55±0.03	0.84±0.06	1.41±0.02
4	0.142	20.18±0.52	0.42±0.01	3.88±0.15	1.11±0.01	2.65±0.12

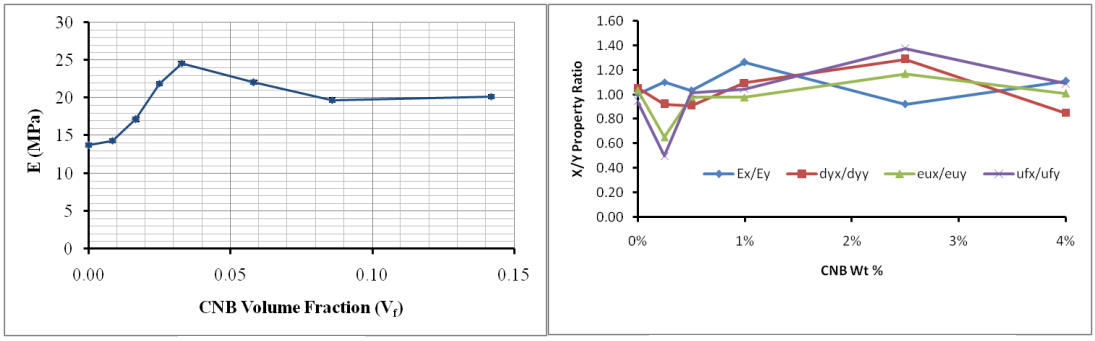
Isotropy data is recorded in Table 4.9. The data was obtained by performing the uniaxial tensile test for identical specimens cut in two perpendicular directions *(X and Y)* from the same membrane sample. The ratio of the mechanical property value obtained from the x direction to the y direction was defined as the measure of isotropy. Therefore the degree of isotropy was defined by E_x/E_y, σ_{yx}/σ_{yy}, σ_{sx}/σ_{sy}, e_{ux}/e_{uy} and $U_{f.tx}/U_{f.ty}$, which are the ratios of E, σ_y, σ_s, e_u and $U_{f.t}$ in the x direction to the corresponding values in the y direction respectively. The *overall mean* of the mechanical property ratios at constant filler weight fraction gave an indication of the degree of anisotropy as shown in Table 4.9. The *property mean* is defined as the mean of the property ratios of a constant mechanical property with varying weight fractions of carbon nanoballs. The % dev is the deviation of the mechanical property ratio from isotropy, defined by; *(mechanical property ratio less 1).*

Table 4.9: Data for ratio of transverse mechanical properties to perpendicular properties

wt% CNB	E_x/E_y	σ_{yx}/σ_{yy}	σ_{sx}/σ_{sy}	e_{ux}/e_{uy}	$U_{f,tx}/U_{f,ty}$	Overall Mean	%dev
0.00	1.01	1.05	0.97	1.04	0.94	1.00	0.18
0.25	1.10	0.92	0.76	0.65	0.50	0.79	-21
0.50	1.03	0.91	1.02	0.98	1.01	0.99	-1
1	1.26	1.10	1.09	0.98	1.05	1.09	9
2.5	0.92	1.29	1.21	1.17	1.38	1.19	19
4	1.11	0.85	1.00	1.01	1.09	1.01	1
Property Mean	1.07	1.02	1.01	0.97	0.99	1.01	1

4.3.1.1 Effect of CNB volume fraction on mechanical stability of nanocomposite IEM

Figure 4.28a shows that the Young's modulus E, initially increased curvilinearly with increasing filler, from 13.71MPa at 0% loading, up to 24.58MPa at 3.3% volume fraction, after which a gradual decrease commenced in a curvilinear fashion down to 20.18MPa. Therefore a maximum improvement of 79% was achieved for E at 3.3 vol% CNB. The initial increase was associated with the high stiffness of the filler material in the homogeneous nanocomposite membrane below 3.3 vol% CNB. The decrease above this critical V_f (3.3vol% CNB) was attributed to agglomeration. Further analysis of E is presented at a later section.



a) E vs V_f b) Anisotropy (X/Y) vs V_f

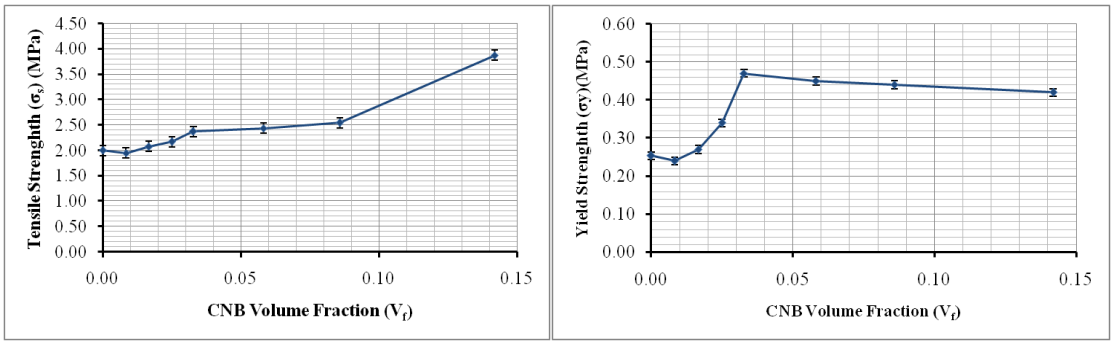
Figure 4.28: Effect of nanofiller volume fraction, V_f on; a) Young's Modulus, E (stiffness). b) isotropy

A maximum deviation of 21% at 0.25 CNB wt% loading and a minimum deviation of 1.21% from isotropy were observed (Table 4.9 and Figure 4.28b). However, the overall mean mechanical property ratio was 1.01, translating to a 1.32% deviation from isotropy (Table 4.9 and Figure 4.28b). This implies that the membrane was highly isotropic. This isotropy was attributed to the spherical nature of the carbon nanoballs as well as the casting technique used which was non-directional. The deviations from isotropic behavior could be due to agglomeration, and processing defects associated with blending and the evaporative casting technique (e.g uneven casting surface, impurities and pressure differentials on the casting liquid surface).

43.1.2 Effect of CNB volume fraction on the mechanical strength of nanocomposite IEM

Figure 4.29a shows that the tensile strength, σ_s increases almost linearly with carbon nanoball volume fraction from 2MPa at 0% loading to a maximum of 3.88MPa at 14.2vol% CNB loading. Thus tensile strength was improved by a maximum of 94% at 14.2 vol% CNB (4wt%). The yield strength, σ_y, increased curvilinearly from 0.25MPa at 0% CNB loading to a maximum of 0.47MPa at 3.3vol% CNB loading.

Above 3.3vol% CNB loading, σ_y decreases linearly and gently with increasing V_f down to 0.42MPa at 14.2vol% CNB loading. Therefore, a maximum of 88% improvement of yield strength was achieved at 3.3vol% CNB loading (1wt%).



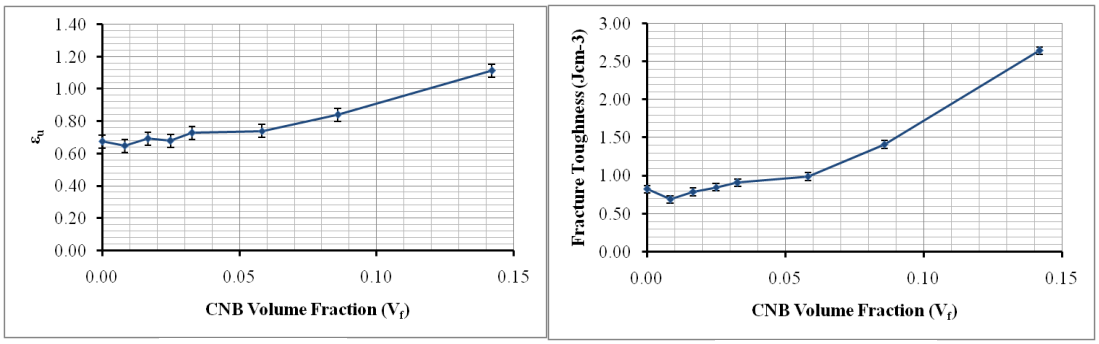
a) σ_s vs V_f b) σ_v vs V_f

Figure 4.29: Effect of CNB volume fraction on; a) tensile strength, σ_s; b) yield strength, σ_y

The increase of σ_s was attributable to the increasing total surface area of interaction between the polymer and the filler, facilitating the load transfer from the weaker polymer to the stronger nanofiller (Ahmed and Jones, 1990 and Baeta et al., 2009). The tensile strength of the carbon nanoballs, estimated to be 7 – 9GPa, i.e. about 350 times greater than that of the polymer (Deshmukh et al., 2010). Therefore if more load is transferred to the carbon nanoballs, the tensile strength is expected to increase. This further explained why σ_s increased with V_f. The analysis of σ_s vs V_f was discussed in further detail at later section. The yield strength trend was similar to that of the Young's modulus (compare Figure 4.28a and 4.29b). The increasing bouncing effect of nanoballs with increasing V_f could be responsible for the sharp increase of yield strength in the first section of Figure 6.2b. The latter decrease was attributed to agglomeration (Cho et al., 2006). The 88% increase in σ_y is significant, since the yield strength is directly related to the fatigue strength. Therefore it can be inferred that the fatigue strength increases with at least the same proportion.

4.3.1.3 Effect of CNB volume fraction on ductility of nanocomposite IEM

The engineering strain at break, e_u increased linearly from 0.68 at 0% CNB volume fraction loading to 1.11 at 14.2vol% CNB volume fraction, translating to 65% improvement (Figure 4.30a). According to Figure 4.30b, the fracture toughness, $U_{f.t}$ increased curvilinearly with increasing CNB volume fraction from 0.84 J/cm^3 at 0% loading to 2.65J/cm^3 at 14.2% filler loading. Accordingly, a 215% fracture toughness improvement was achieved. The strain improvement could be attributed to the increasing volume of interactions with increasing V_f. The entanglements of dangling bonds of carbon nanoballs with polymer chain ends as well as the rearrangements of sliding nanoballs could result in increased strains (Vassiliou et al., 2008). The carbon nanoballs could also have improved the fracture toughness through filler induced crazing, crack pinning and crack bridging (Yan et al., 2006). The lower fracture toughness of the plain membrane was associated with the introduced sulphonate groups reported to cause brittleness at high DS. The carbon nanoballs are believed to stop crack migration and propagation through the reorientation of chains, filling of voids as well as the entanglement interactions between chain fragments and dangling ends of the outer shell. These interactions increase the total energy of the composite, which must be overcome to break the membrane apart.



a) e_u vs V_f b) $U_{f.t}$ vs V_f

Figure 4.30: Effect of CNB V_f on; a) engineering strain; b) fracture toughness of SSBR IEM

4.3.1.4 Effect of CNB volume fraction on fatigue strength of SSBR IEM

Due to limitations of nanocomposite membrane fatigue testing equipment, fatigue testing was limited to 100 cycles at a frequency of 0.1Hz. Figure 4.31 shows the mean stresses endured by the nanocomposite membrane specimens without breaking for 100 cycles at 0.1Hz frequency. The fatigue strength trend increased with increasing nanofiller concentration, V_f. The trend was similar to the tensile strength trend as shown in Figure 4.31. This fatigue strength improvement could be associated with the crack pinning effect which dismantles and stops crack propagation. It was also attributable to the improvement of the yield strength, and hence the increase in elasticity which was earlier shown. As cycles of stress persist, the reorientation of the isotropic spherical particles does not alter much of the morphology of the nanocomposite and hence maintain a steady structure and properties.

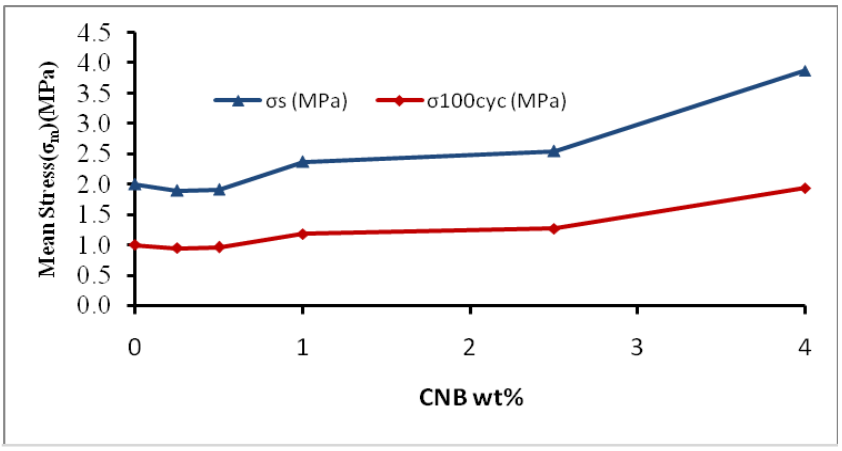


Figure 4.31: Effect of CNB wt% on fatigue strength

4.3.1.5 Overall reinforcement effect of CNBs on mechanical properties of SSBR IEM

Table 4.10 shows the maximum mechanical property improvements achieved through addition of carbon nanoballs. Maximum improvement of E and σ_y of 79 and 88% respectively were achieved at 60% amplitude and 3.3 vol% CNB. The maximum tensile strength improvement of 94% was achieved at 60% amplitude and 14.2 vol% CNB. The maximum strain and fracture toughness improvement of 369 and 367% respectively were achieved at 20% amplitude and 14.2vol%.

Table 4.10: Maximum reinforcement achievements with CNB addition

Property	Max. Value	% Improvement	CNB Vol%	%Amplitude
E (MPa)	24.6	79	3.3	60
σ_y (MPa)	0.47	88	3.3	60
σ_s (MPa)	3.9	94	14.2	60
e	3.3	369	14.2	20
$U_{f.t}$ (Jcm^{-3})	4.2	367	14.2	20

When a balance of mechanical properties is required, a CNB volume fraction of 8.6vol% CNB was optimal as shown in Figure 4.32. At this CNB volume fraction, E, the Young's modulus was 19.73MPa (44% improvement); yield strength, σ_y, 0.44MPa (74% improvement); Tensile Strength, σ_s, 2.55MPa (27% improvement); strain, e_u, 0.84 (25% improvement); and fracture toughness, $U_{f.t}$, 1.41J/cm^3 (72% improvement). Based on the reinforcement improvements mentioned above, applications such as nanofiltration (0.93 – 1.5MPa), microfiltration (0.01 – 0.5MPa) and ultrafiltration (0.1 – 1MPa) could be achieved with reinforcements below 14vol% CNB. Applications which require taut membranes carry a tensile load and might require high stiffness (E). Such applications then require CNB reinforcement loadings close to, but greater than or equal to 3.3vol%, (Figures 4.28a and 4.32). On the other hand a slack membrane does not possess any significant stiffness and tensile strength, but require great flexibility and hence good ductility and fracture toughness (Hornig and Schoop, 2003).

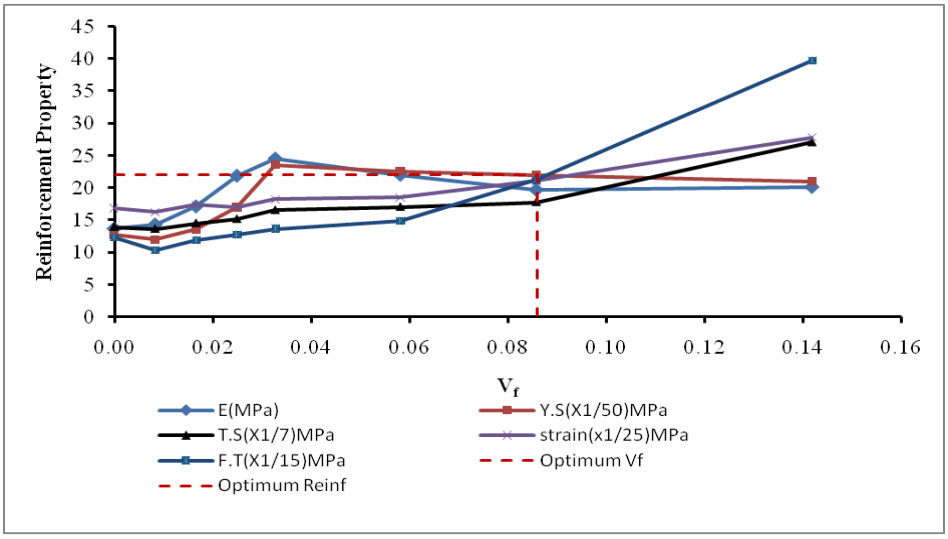


Figure 4.32: Overall reinforcement effect of carbon nanoballs

This is achieved at higher CNB volume fraction close to 14%. Wrinkled membranes also require good ductility and fracture toughness and hence higher values of V_f (Hornig and Schoop, 2003). The membrane could also find applications in reverse osmosis (2 – 10MPa) if the mechanical properties could be further improved at the same CNB loading.

More exciting applications of the carbon nanoballs would be in fuel cell applications. Previous work by Abdulkareem, 2009 and Idibie, 2009 has already shown that addition of carbon nanoballs drastically improved the electrochemical properties of styrene butadiene ion exchange membranes. The positive reinforcement effects of the carbon nanoballs further positions the SBR – CNB nanocomposite ion exchange membrane for fuel cell applications.

4.3.2 Effect of blending conditions on mechanical properties of nanocomposite IEM

Since agglomeration has been reported as one of the key hindrances to realizing the benefits of nanofillers, blending was investigated at different amplitudes of ultrasonication. The percentage changes in mechanical properties due to changing the blending conditions from 20 to 60% amplitude of sonication are shown in Table 4.11. E, σ_y, and σ_S increased by 92 – 233%, 88 – 282% and 60 - 81% respectively. On the other hand, fracture toughness and strain reduced by 44 – 64% and 50 – 66% respectively. The drastic change in mechanical properties shows that blending conditions are very critical in reinforcement of polymeric ion exchange materials with carbon nanoballs.

Table 4.11: Percentage change in mechanicals properties with change in amplitude of sonication from 20 to 60%

V_f (%)	ΔE (%)	$\Delta\sigma_y$ (%)	$\Delta\sigma_s$ (%)	ΔU_{ft} (%)	Δe(%)
3.3	92	88	60	*-44*	*-50*
5.8	120	177	56	*-55*	*-65*
8.6	185	238	73	*-50*	*-67*
14.2	233	282	95	*-64*	*-66*
Average	**158**	**196**	**71**	***-53***	***-62***

Figures 4.33 and 4.34 show the mechanical property vs V_f profiles for nanocomposites at 20, 60 and 75% amplitude of sonication. At 60 to 75% amplitude, all the mechanical properties improved with CNB loading. Nevertheless, the improvement of mechanical properties of membrane sonicated at 75% amplitude over the ones at 60% was marginal (Figure 4.33). The maximum elastic modulus, E of 25MPa, implying a 79% improvement (over plain ones), was achieved at both 60 and 75% amplitudes of sonication and 3.3vol% CNB. The maximum yield strength, σ_y, of 0.48MPa (92% improvement) was achieved at 75% amplitude and 3.3vol% CNB. The maximum tensile strength, σ_s, of 3.9MPa (95% improvement) was achieved at 60% amplitude and 14vol% CNB (Figure 4.33).

On the other hand, E, σ_y and σ_s vs V_f profiles decreased with increasing filler concentration at 20% amplitude (Figure 4.33). E, σ_y, and σ_s decreased by a maximum of 57, 55 and 25% respectively. Nevertheless, the maximum fracture toughness, $U_{f.t}$, and strain, e_u, improved by 367% (0.9 – 4.2J/cm^3) and 369% (0.7 – 3.28Jcm^{-3}) respectively, at 14vol% CNB (Figure 4.34).

The improvements at higher amplitudes of sonication were attributed to high dispersion of the carbon nanofiller, which promotes positive polymer - filler, polymer – polymer and filler - filler interactions. The marginal improvement from 60 to 75% amplitude of sonication could be attributed to the fragmentation of polymer chains. Fragmentation reduces the molecular weight of the polymer matrix and consequently compromises the mechanical properties. The negative effect of carbon nanofiller on synthetic rubber reinforcement at low sonication amplitude was attributable to agglomeration. Poor dispersion introduced tactoids and voids which acted as stress inhomogenizers thus reducing the tensile properties. Agglomeration also meant that most of the stress was not adequately transferred to the nanofiller material (Cho et al., 2006 and Brechet et al., 2001). As a result, the mechanical properties of the composite were limited by the mechanical properties of the polymer at low amplitude.

The effective surface area of interaction between polymer and filler as well as filler to filler is reduced by agglomeration, hence reducing the tensile properties. The significant improvement of fracture toughness and strain at low sonication amplitude could be attributed to minimal damage of polymer chains during blending. Higher sonication amplitude is responsible for fragmenting polymer chains and hence the density of fracture points responsible for failures (Allegra et al., 2008).

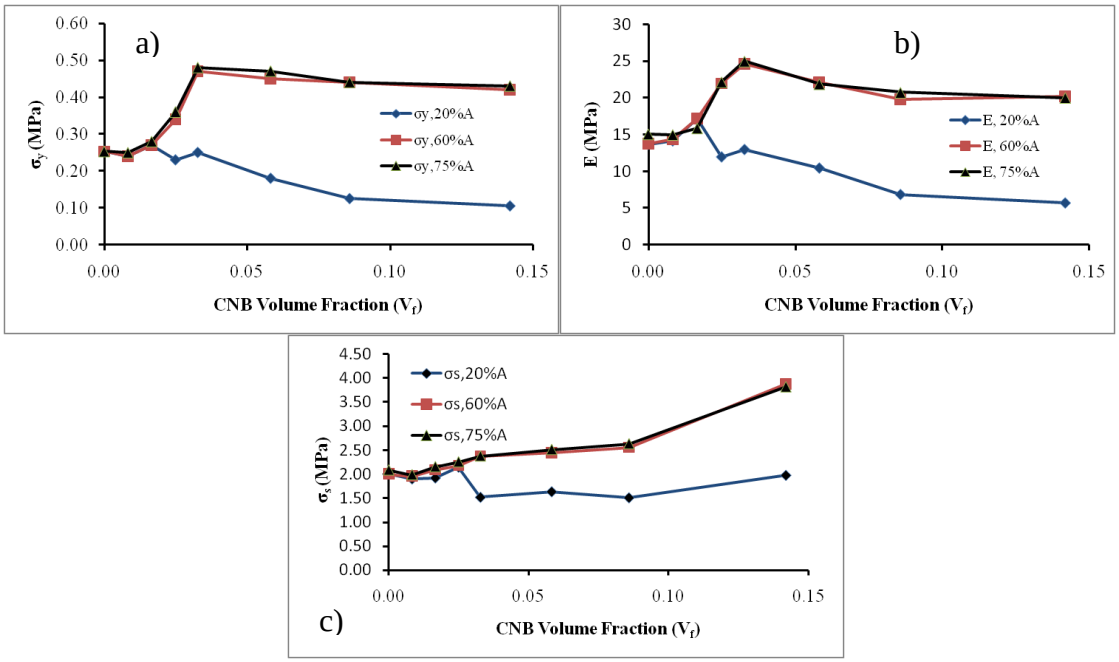


Figure 4.33: Effect of amplitude of sonication on; a) yield strength; b) Young's modulus; c) tensile strength

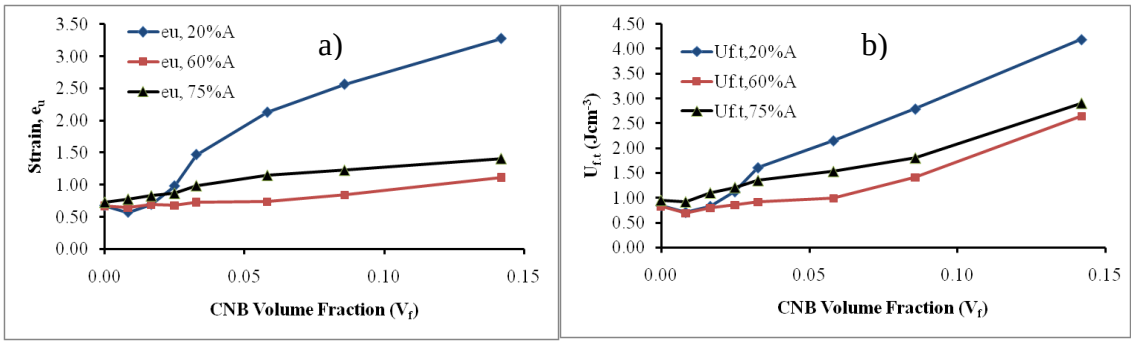


Figure 4.34: Effect of amplitude of sonication on; a) ultimate strain; b) fracture toughness

4.3.2.1 Optimisation of ultrasonication conditions for SSBR reinforcement

A compromise has to be reached, to achieve high E, σ_y, σ_s as well as $U_{f.t}$ and e_u. As shown in Figure 4.35, the optimal sonication region for overall reinforcement lies between 30 - 45% amplitude of ultrasonication. In this region, E_{max} lies in the range 18.5 – 22MPa (35 - 60% improvement); σ_{ymax}, 0.32 – 0.4MPa (28 - 60%

improvement); σ_{smax}, 2.5 – 3.25MPa (25 - 63% improvement); $U_{f.tmax}$, 3.2 – 3.75 Jcm^{-3} (256 - 317% improvement) and e_{umax}, from 1.8 – 2.6 (157 - 270% improvement).

If a blending method which minimizes polymer chain fragmentation whilst maintaining high dispersion of nanofiller could be found, then high fracture toughness and strain could be achieved without compromising the rest of the other desired mechanical properties. Therefore further work on blending of carbon nanoballs with SSBR using other blending technologies is recommended.

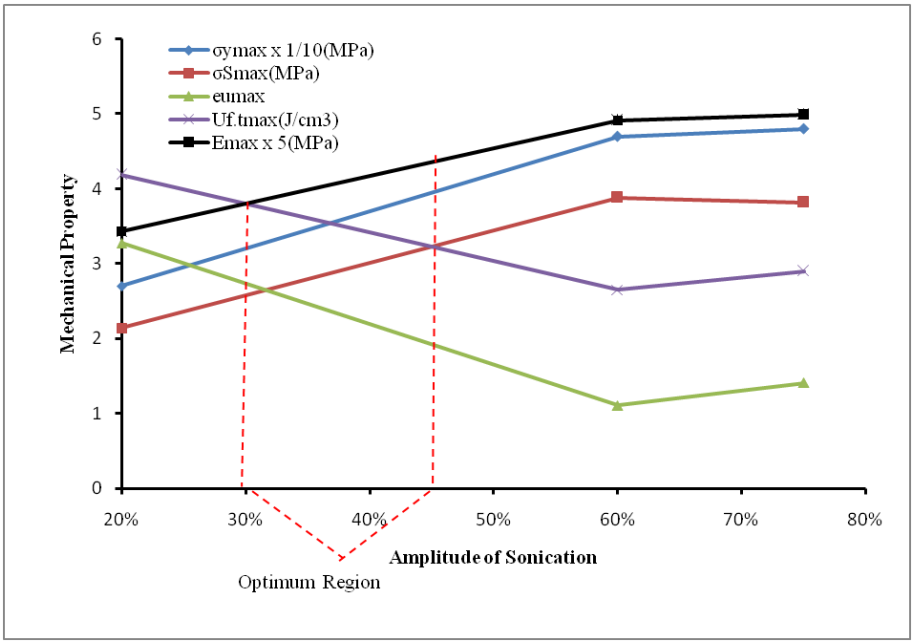


Figure 4.35: Optimisation of sonication amplitude for reinforcement

4.3.3 Effect of time (age) on mechanical properties of nanocomposite IEM

The nanocomposites blended at 60% ultrasonication were also tested 40days after production under the same conditions of mechanical testing as those carried out at 20days. Figures 4.36 and 4.37 show the comparisons of the mechanical properties

between 20day old nanocomposites and 40day old nanocomposites stored at room temperature and pressure conditions.

The increase in the Young's modulus with age can be attributed to the increase in crosslink density of the polymer as a result of aging. This increase in crosslink density could be responsible for enhancing stronger polymer filler interactions (Yasmin et al., 2006 and Cho et al., 2006). Aging may also result in the reduction of moisture suspected to be trapped within the membrane. This moisture reduction could result in the reduction of mean polymer – filler and filler – filler separation distances resulting in the significant improvements of elastic properties. The improvement of E was observed to increase with carbon nanoball volume fraction, reaching a maximum improvement of 52% at 3.3 vol% carbon nanoball loading. The yield strength increased along similar trends as E for the same reasons. The carbon nanoballs might also be responsible for reducing the degree of oxidation responsible for polymer degradation (Mitov et al., 2006). Further work on the effects of carbon nanoballs on oxidative stability of ion exchange membranes is therefore recommended.

The trend in tensile property with age was in line with that observed for their fresher counterparts (Figure 4.36b). The tensile strength of the nanocomposites shows marginal and insignificant change with age. The marginal change could be attributable to the little changes expected in the effective surface area of interaction between the carbon nanoballs and the polymer with age.

The trend of fracture toughness with age showed lower values than the ones of fresh samples, with a maximum reduction of 61%. The negative trend with CNB volume fraction could be attributed to increased oxidation at fragment ends of the polymer and dangling bonds of the outer layer of the carbon nanosphere (Mitov et al., 2006; Allegra et al., 2008 and Kang and Wang, 1996). The ultimate strain gains were also significantly reduced with age, with a maximum decrease of 52%.

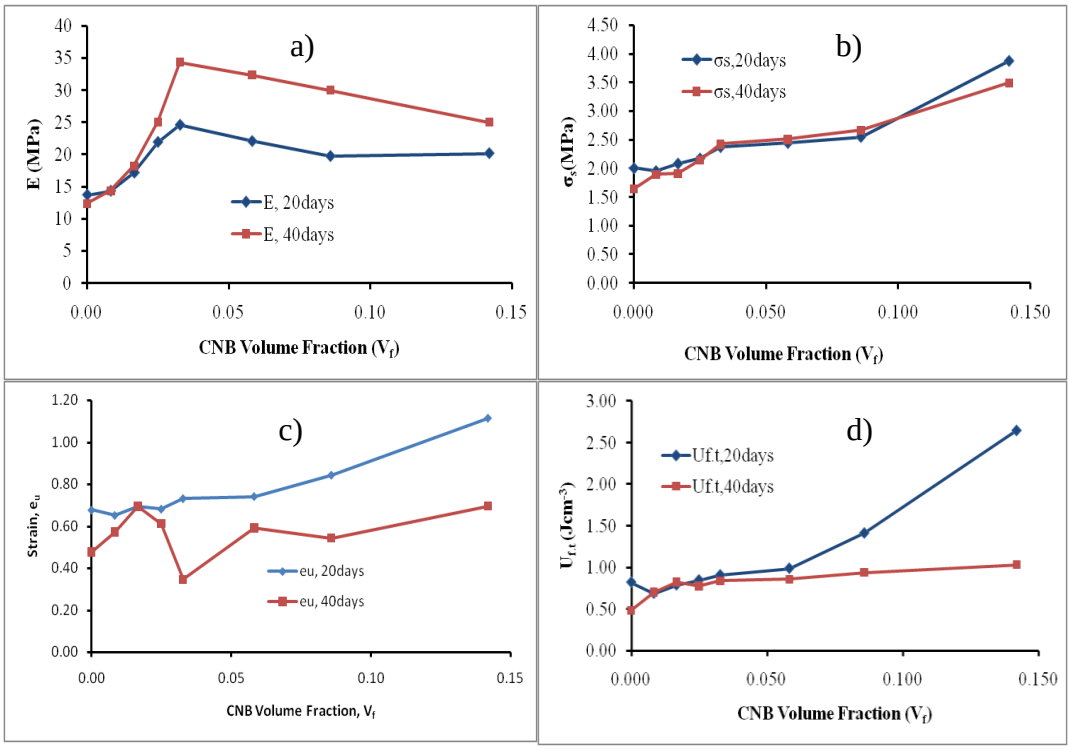


Figure 4.36: Effect of age on; a) E; b) σ_s; c) e_u and d) $U_{f.t}$

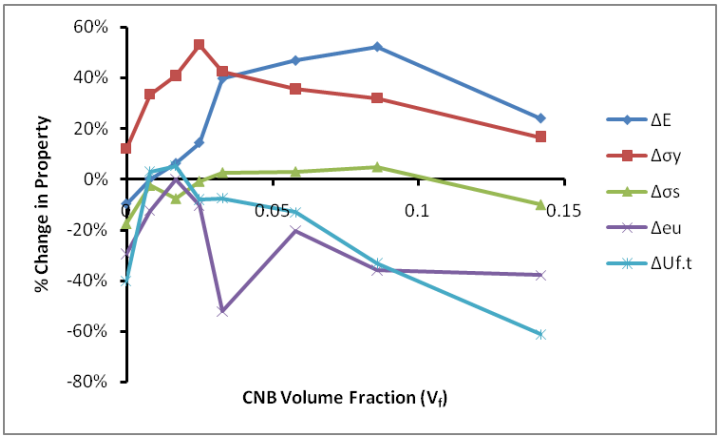


Figure 4.37: %change of reinforcement properties with age

Nevertheless, the impact of CNB volume fraction on mechanical properties of the older ion exchange membrane remained positive. The maximum improvements of e_u

and $U_{f.t}$ for the older specimens were 44 and 200% respectively, over the plain ones. Maximum improvements of 177, 139 and 112% on E, σ_y and σ_s of older nanocomposite specimens respectively, over their plain counterparts, were still realized.

Therefore addition of low volumes of carbon nanoballs improved the mechanical properties of styrene butadiene rubber ion exchange membrane. However, there is need to improve the fracture toughness stability with time. Carbon nanofiller functionalisation, heat treatment as well as insitu polymerization are recommended for further work.

4.3.4 Comparison of the experimental results with existing models

Theoretical and empirical models for tensile strength and Young's modulus were extensively reviewed in the literature review section. However, nanocomposite models for fracture toughness, yield strength and strain have rarely been reported in literature. Therefore, the comparisons of experimental profiles with existing models were only done for Young's Modulus and tensile strength. Figure 4.38 shows the comparison of the experimental results with existing models.

4.3.4.1 Comparison of experimental E with existing models

Figure 4.38 shows the comparison of experimental profile for E with existing models (Ahmed and Jones, 1990). Although the profile of E vs V_f between 0 and 3.3vol% CNB loading was similar to the existing models by Guth and Thomas, the experimental profile rose far much more sharply than the former.

From the experimental plot of *E vs* V_f, Equation 4.17 was obtained. By factorising out (E_p~13.37) as shown in Equation 4.18, $E_{R(experimental)}$ was obtained for the purpose of comparing with existing models (Equation 4.19).

$$E_{(experimental)} = 13.37 + 128.2V_f + 6967V_f^2 \quad (4.17)$$

$$E_{(experimental)} = 13.37[1 + 128.2V_f + 521V_f^2] \quad (4.18)$$

$$E_{R\,(experimental)} = 1 + 9.6V_f + 521V_f^2 \quad (4.19)$$

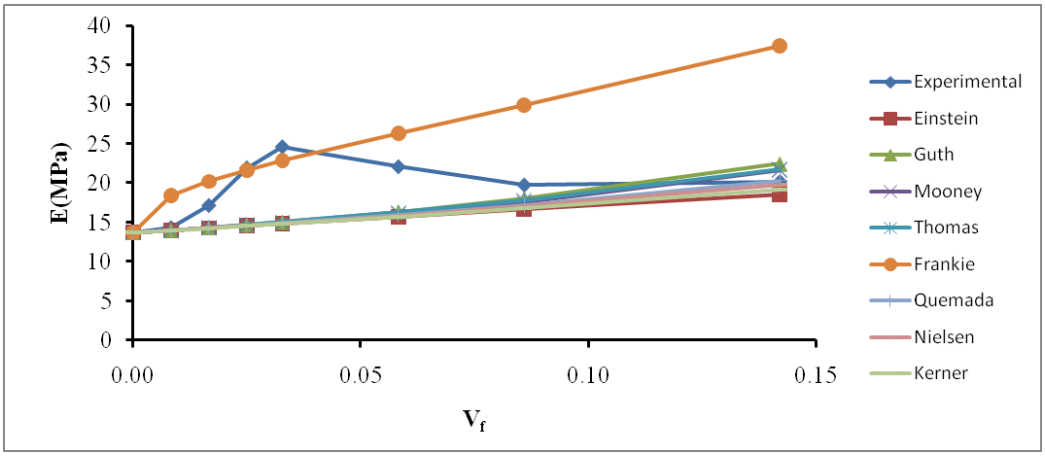


Figure 4.38: Comparison of Experimental Results and Existing Models for E for rubber nanocomposites

The existing models by Guth and Thomas are presented as Equations 4.20 and 4.21 respectively.

$$E_{R\,(Guth)} = 1 + 2.5V_f + 14.1V_f^2 \quad (4.20)$$

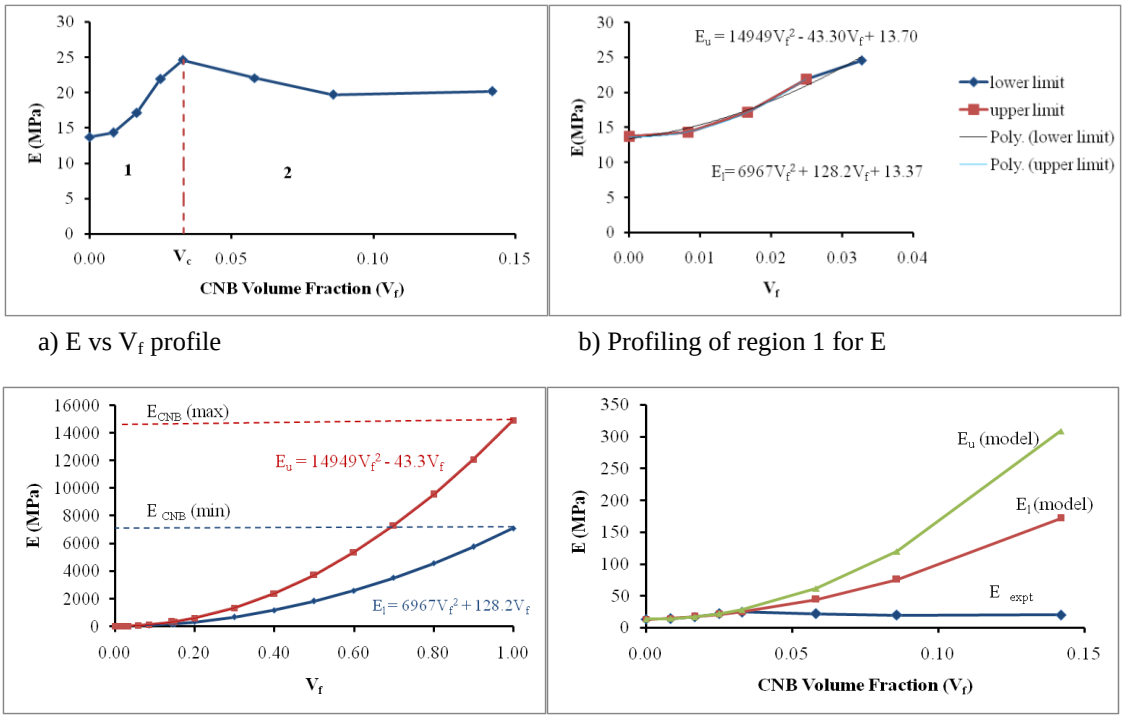
$$E_{R\,(Thomas)} = 1 + 2.5V_f + 14.1V_f^2 + 0.00273exp16.6V_f \quad (4.21)$$

The sharp rise of the experimental profile was due to the higher coefficients of V_f and V_f^2 in the experimental profile (Equation 4.19) as compared to the existing models (Equations 4.20 and 4.21). For example, the coefficients of V_f and V_f^2 from the experimental profile are *2.5* and *37* times greater than the Guth coefficients respectively. For the Thomas model, the experimental coefficient of V_f^2 is 52 times greater (Equation 4.19 and 4.21). This was due to the fact that the Young's modulus,

E_{cnb}, of the carbon nanoball is estimated to be far much greater than that of the polymer, E_p (*~680* times greater – *9.5/0.014*). E_{cnb} could also be uniquely greater than the *E* for the nanoparticles assumed in models by Guth and Thomas. Thirdly the carbon nanoballs are not solid but porous with a unique surface of interaction and hence the higher coefficients (Wang and Kang, 1996 and Miao et al., 2003). Above 3.3vol%, the equation does not hold due to agglomeration.

Validity of the experimental relationship with E

The experimental relationship for E can be divided into two section as shown in Figure 4.39. The distinctive features of the experimental trend (Figure 4.39a) was i) a sharp curvilinear rise of E with V_f up to V_f = 3.3% and ii) an gradual curvilinear decrease of E values in a different fashion after V_f = 3.3%. It is therefore premised that in region 1, E behavior was dominantly determined by the nanofiller properties whilst the region 2 trend was dominantly influenced by the polymer matrix properties due to nanofiller agglomeration. The volume fraction dividing the two regions was referred to as V_c, the critical filler volume fraction above which agglomeration begins. It was also assumed that E_m remained constant for $0 \leq V_c \leq V_f$ and hence the improvement of E_c in this region was due to carbon nanoballs. To prove this, region 1 was profiled as shown in Figure 4.39c and the limiting equations 4.22 and 4.23 were obtained;



a) E vs V_f profile

b) Profiling of region 1 for E

c) Extrapolation of profile to get E_{cnb}

d) Potential E improvement at ideal dispersion

Figure 4.39: Validity of the experimental profile for E

$$E_{(Upper)} = 14949V_f^2 - 43.3V_f + 13.71 \quad (4.22)$$

$$E_{(Lower)} = 6967V_f^2 + 128.2V_f + 13.37 \quad (4.23)$$

From Equation 4.22 and 4.23, the upper and lower limits of E_{cnb} were obtained by extrapolation (Figure 4.39c). If the theoretical Young's modulus of the carbon nanoballs found in literature lies between the experimental upper (E_{CNBU}, V_f =1) and lower (E_{CNBL}, V_f = 1) limits, then the premise made for region 1 is valid.

$$E_{CNBU} = 14949V_f^2 - 43.3V_f \quad (4.24)$$

$$E_{CNBL} = 6967V_f^2 + 128.2V_f \quad (4.25)$$

By substituting $V_f = 1$ into Equation 4.24 and 4.25, the Young's modulus of carbon nanoballs used lie between 7.1GPa and 14.9GPa. The theoretical values given in literature for fullerenes and related carbon materials similar to carbon nanoballs lie between 7 and 12GPa (Levin et al., 2003 and Zetl and Cumings, 2001). Therefore the assumption given to region 1 is consistent with literature. However, the Young's modulus for carbon nanoballs has not yet been fully established in literature and hence further verification work is necessary.

Relationship between fractional free volume of matrix and E_{max} for nanocomposite IEM

It was assumed that it was very difficult to disperse the nanofillers beyond the fractional free volume, V_o of the matrix material (Figure 4.39a). Therefore the critical volume, V_c must be related to V_o. Filling the matrix material below its free volume is expected to have the following advantages; i) less energy is required for effective dispersion since the nanofillers enter the unoccupied spaces with little resistance and ii) induced stresses (prestressing) are minimal and the matrix properties within the nanocomposite are expected to remain fairly constant since the matrix-matrix interparticle separation distance remains fairly constant for all $V_f < V_0$ (Wang et al., 2004).

For any given matrix material, $0 \leq V_c \leq V_0$. Factors like packing fraction and dispersion effectiveness must therefore deviate V_c away from V_0. The higher V_c is, the better the reinforcement. Therefore a preliminary relationship is proposed to relate V_c and V_0 (Equation 4.26).

$$V_c = \delta f V_0 \quad (4.26)$$

where V_c is the filler critical volume fraction, V_0 is the fractional free volume of the matrix material, f is the packing fraction of nanofiller and δ is the dispersion efficiency of nanofillers into the polymer matrix. The theoretical V_0 for SSBR was approximated by taking the one for SBR, $V_0 = 0.095$ and $f = 0.5236$, assuming a face centred cubic lattice packing fraction of spheres (Wang et al., 2004, Recio et al., 2008 and Kozako et al., 2005). Since for the experiment done, $V_c = 3.3\%$, substitution into Equation 6.30 would give a dispersion efficiency, δ *of 66%*. The estimated δ achieved through blending was around *85%*. The discrepancies could be due to the fact that most of the figures used in the computations are estimates rather than accurate figures. Further work on dispersion analysis techniques for nanocomposites is therefore recommended. Agglomeration will have a serious effect on reducing V_c and hence the maximum achievable E. Equation 4.23 can take the form shown by Equation 4.27;

$$E_c = K_1 V_f^2 + K_2 V_f + E_{m0} \quad (4.27)$$

where K_1 and K_2 are constants and E_{m0} is E of the plain matrix without filler. Assuming that the maximum E of the composite E_{cmax} occurs at V_c, then,

$$E_{cmax} = K_1 V_c^2 + K_2 V_c + E_{m0} \quad (4.28)$$

By substitution of Equation 4.26 into 4.28, then;

$$E_{cmax} = K_1 \delta^2 f^2 V_0^2 + K_2 \delta f V_0 + E_{m0} \quad (4.29)$$

Assuming that f and V_0 are constants for a given pair of matrix and nanofiller, then Equation 4.29 can be reduced to;

$$E_{Cmax} = K_3\delta^2 + K_4\delta + E_{m0} \qquad (4.30)$$

Equation 4.30 clearly shows the significant effect of dispersion efficiency on the maximum elastic modulus of a polymer nanocomposite. If a matrix material and filler have known characteristics like V_o and f, then the maximum E for the nanocomposite can be predicted by Equation 4.30 if the dispersion efficiency of the equipment was known.

Beyond V_c, in region 2 of Figure 4.39a, agglomeration began impacting negatively on the Young's modulus profile (Jayasree and Predeep, 2008). The polymer – polymer interactions begin to dominate the E profile. If non energy intensive methods can adequately disperse carbon nanoballs beyond V_c, (up to V_f = *14%*), there is potential for improving E up to 180MPa (700% improvement) (Figure 4.39d). Therefore further work on blending techniques to improve dispersion might enhance the full realisation of the benefits of reinforcement.

4.3.4.2 Comparison of experimental profile for tensile strength with existing models

Figure 4.40 shows the comparison of the experimental profiles for tensile strength with existing models by Nielsen and Nicolais and Narkis (Seon et al., 2004). Equations 4.31 and 4.32 were derived from the experimental plots of σ_s vs V_f at 20 and 60% amplitude of sonication respectively.

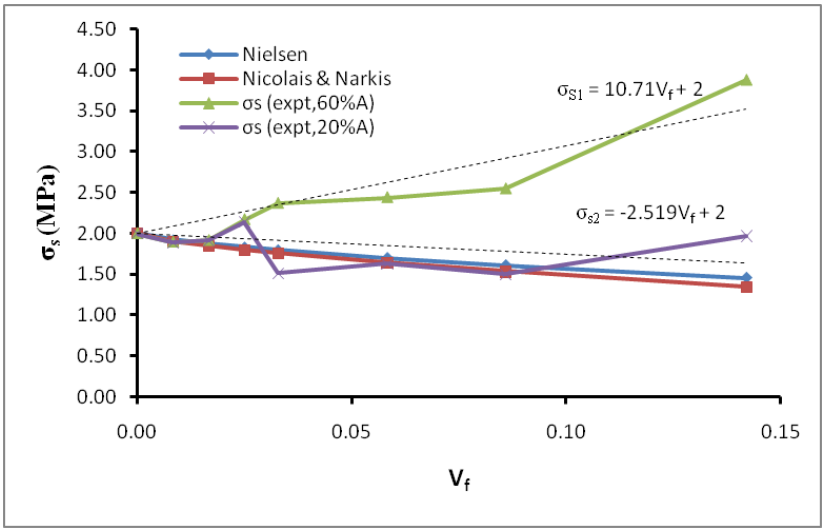


Figure 4. 40: Comparison of experimental profiles and existing models for tensile strength

$$\sigma_{s20\%A} = \sigma_{sm}\left(1 - 1.26V_f\right) \tag{4.31}$$

$$\sigma_{s60\%A} = \sigma_{sm}\left(1 + 5.36V_f\right) \tag{4.32}$$

where σ_{sm} is the tensile strength of the unblended polymer matrix.

The model proposed by Nicolais and Narkis was similar to the experimental profile at 20% amplitude of sonication (Figure 4.40, Equations 4.31 and 4.33). They both are functions with similar negative coefficient of V_f (compare 1.21 and 1.26). They imply that the tensile strength decreases approximately linearly with nanofiller volume fraction. This similarity could be due to the fact that agglomerates of carbon nanoballs in the composite interact in the same manner as the nanoparticles assumed by Nicolais and Narkis. However, there was a difference in the power of V_f for the experiment as compared to existing models (compare 1 and 2/3 from Equations 4.31 and 4.33 respectively). This could be attributable to the size of nanoparticles used.

$$\sigma_{s(Nicolais\&Narkis)} = \sigma_{sm}\left(1 - 1.21V_f^{\frac{2}{3}}\right) \quad (4.33)$$

$$\sigma_{s(Nielsen)} = \sigma_{sm}\left(1 - V_f^{\frac{2}{3}}\right)K, \qquad K = 1 \quad (4.34)$$

The existing models might have assumed smaller sizes of nanoparticles than the ones used, as well as ideal packing, which is different from reality.

The experimental profile for the well dispersed carbon nanoballs at 60% amplitude, contradicts the given models (Figure 4.40, Equations 4.32, 4.33 and 4.34). The equation has a positive gradient, implying the increase of tensile strength with nanofiller concentration. The coefficient of V_f is also more than 4 times greater than the one for existing models. This change in trend at different amplitudes of sonication can be attributed to better dispersion of nanofillers at 60% amplitude. This observation further shows the importance of dispersion in the reinforcement of synthetic rubbers. Equation 4.32 can form a good basis for the prediction of the tensile strength of a well dispersed synthetic rubber nanocomposite at any given volume fraction of carbon nanoballs.

Relationship between tensile strength and CNB volume fraction

The observed relationship between the tensile strength of the nanocomposite, σ_c and the carbon nanoball volume fraction, V_f, approximates a linear function (Figure 4.41i).

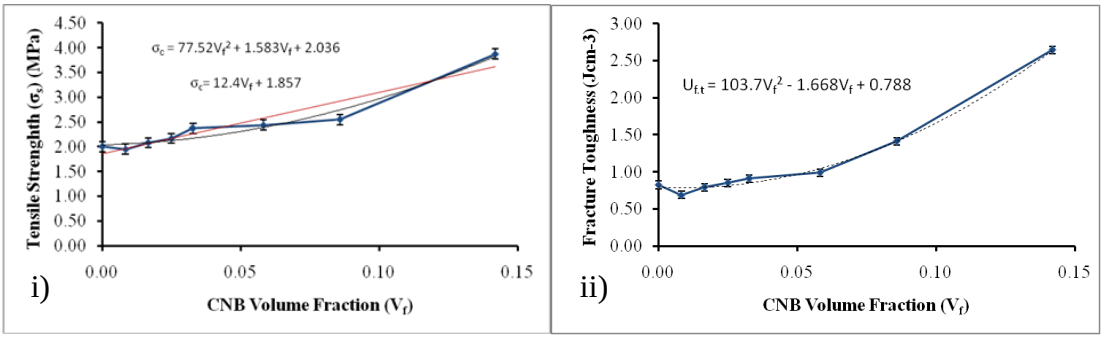


Figure 4.41: Relationship between i) tensile strength, σ_c and V_f and ii) fracture toughness, $U_{f.t}$ and V_f for SSBR-CNB nanocomposite IEM

The relationship was described by Equation 4.35 below;

$$\sigma_c = \sigma_m\left(1 + 6.67V_f\right) \tag{4.35}$$

where σ_c and σ_m are the tensile strength of the nanocomposite and plain polymer, respectively. The equation suggest that the tensile strength is directly related to the surface area of interaction and stress transfer, which increases linearly with increasing volume fraction of carbon nanoballs (Seon et al., 2004). The surface area of interaction increases with volume fraction and hence the linear increase in stress.

4.3.4.3 Relationship between fracture toughness and CNB volume fraction

The fracture toughness relationship was estimated to be a polynomial relationship of order 2 (Figure 4.41ii and Equation 4.36).

$$U_{f.tc} = U_{f.tm}\left(1 + 2.12V_f + 131.6V_f^2\right) \tag{4.36}$$

where $U_{f.tc}$ and $U_{f.tm}$ are the fracture toughness of the nanocomposite membrane and plain membrane respectively. From the bonding theory, fracture toughness is directly related to total energy of bonds in the system (Ashbey and Jones, 1980). In turn the

total energy is directly proportional to the number and strength of interactive bonds. Therefore by combining Equation 4.42, 4.44, 4.45, 4.46 and 4.50 proposed at a later section (4.35), Equation 4.37, which is similar to Equation 4.36 except for the $V_f^{1/3}$ is obtained.

$$U_{f.tc} = U_{f.tm}\left(1 + K_5 V_f + K_6 V_f^2 + K_7 V_f^{1/3}\right) \quad (4.37)$$

The difference could be attributable to the fact that the size of the carbon nanoball used might have been too large to compare with the molecular bonding theory. Agglomeration could have also caused further deviation. On the other hand reduction in the size of carbon nanoball used for blending and high dispersion of nanofiller might reduce the variation between the theoretical and experimental expressions.

4.3.5 Proposed mechanism for reinforcement of SSBR with carbon nanoballs

The proposed mechanism for reinforcement is similar to the one proposed for styrene butadiene rubber by carbon black (Jayasree and Predeep, 2008). During the initial stages of carbon nanoball incorporation, the carbon nanoball aggregates are compressed by the polymer and contains many discrete voids. During mixing, the aggregates are dismantled by the ultrasonic energy and forced into the voids and air is expelled. In the process, long chain rubber molecules are split by the forces generated by the ultrasonic waves. The chain fragments are formed with terminal free radicals and if stable, short chain molecules remain. They can also recombine into longer chain molecules on stabilisation. The combination of polymer chains with the bound carbon nanoballs result in different types of interactions affecting the overall mechanical properties (Allegra et al., 2008).

The polymer chains can be considered as sequences of interface segments (subchain segments totally running in the interface shell of a given carbon nanoball), bridge segments (sequences of non-interface units with the two adjoining units in the

interface shells of two different particles), loop segments (similar to bridge segments, but starting and ending in the interface shell of the same particle) and dangling terminal segments (Odegard et al., 2005). Bound rubber is trapped between or within the filler aggregates where it is no longer part of the elastically active rubber matrix. The assumed model of interaction is illustrated in Figure 4.42.

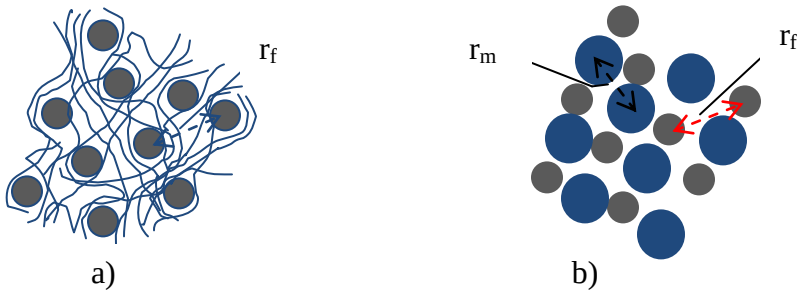


Figure 4.42: CNBs in polymer matrix; a) illustration of interaction between monodisperse nanoparticles and polymer chains in an elastomeric nanocomposite; b) modeling of polymer chains as represented by their radius of gyration (Hooper and Schweizer, 2006)

4.3.5.1 Mechanism for improvement of Young's modulus

The assumptions made in this discussion are that; i) the carbon nanoballs are uniform in size and shape (spherical), ii) the polymer matrix, though made of strings of long polymer chains far much thinner than the carbon nanoballs (1-3nm vs 60-80nm), are considered as spherical particles (Hooper and Schweizer, 2006) with their diameter equivalent to their radius of gyration (Figure 4.42b); iii) the nanocomposite is considered as a multiphase continuum comprising monodisperse filler within elastomer chains separated by interfacial shells; iv) E for each constituent is thought of as a result of effective interactions of identical constituent particles, transmitted and mediated through the intervening second constituent of the nanocomposite (Crosby and Lee, 2007 and Zeng et al., 2008); v) E for the composite is assumed to be the sum of E for the constituents of the composite vi) van der Waals forces and electrostatic forces (due to calixarenes, electron donor–acceptor- type interactions) are the only significant forces acting between carbon nanoballs in the nanocomposite

vii) van der Waals and ionic interaction are the significant interactions between polymer particles (Ashbey and Jones, 1980) and viii) interparticle repulsive forces are negligible.

Based on the above assumptions, the theoretical value of E, for the composite can be estimated. The fundamental equations for the theoretical model are as follows;

$$E_C = E_f + E_m \tag{4.38}$$

where E_c, E_f and E_m are the composite, nanofiller and matrix Young's moduli respectively. Assuming that the van der Waals and dipole-dipole interactions are the only significant forces between the nanofillers (Ashbey and Jones, 1980), then,

$$E_f = E_{f(VDF)} + E_{f(dip)}. \tag{4.39}$$

where $E_{f(VDF)}$ and $E_{f(dip)}$ are the contributions of nanofiller van der Waals and electrostatic (dipole) interactions to Young's moduli respectively. Similarly,

$$E_m = E_{m(VDF)} + E_{m(IONIC)}. \tag{4.40}$$

According to bonding theory, the stiffness of a substance, E is related to the potential energy, U of the substance by;

$$E = \frac{d^2U}{dr^2} \tag{4.41}$$

where r is the interparticle distance (Ashbey and Jones, 1980). For van der Waals interaction, the magnitude of Energy, U, neglecting the repulsive component is given by;

$$U_{VDF} = \frac{A}{r^6} \tag{4.42}$$

where *A* is the constant of attraction (Ashbey and Jones, 1980 and Zhang et al., 2000). Therefore by differentiation, E_{VDF}, the stiffness due to van der Waals interactions is given by;

$$E_{VDF} = \frac{A_0}{r^8} \tag{4.43}$$

Similarly, the energy due to ionic and dipole interactions and the corresponding E are given by;

$$U_{IONIC/dipole} = \frac{B}{r} \tag{4.44}$$

$$E_{IONIC/dipole} = \frac{B_0}{r^3} \tag{4.45}$$

Since the interparticle distance, r is related to the volume fraction of particles, *V* by Equation 4.46 (Kozako et al., 2005 and Palza et al., 2010);

$$r = \frac{C}{V^{1/3}} \tag{4.46}$$

where *C* is a constant of proportionality related to the size, shape and packing fraction of the particles. By substituting Equations 4.43 and 4.45 into 4.39;

$$E_f = \frac{A_f}{r_f^8} + \frac{B_f}{r_f^3} \tag{4.47}$$

By substituting 4.46 into 4.47, an important equation of E_f as a function of V_f, the filler volume fraction is established;

$$E_f = \frac{A_f}{C_f^8} V_f^{8/3} + \frac{B_f}{C_f^3} V_f \tag{4.48}$$

where A_f, C_f and B_f are constants related to the permittivity of the matrix material to filler to filler interactions. Similarly, the Young's modulus of the matrix constituent, E_m, is given by;

$$E_m = \frac{A_m}{C_m^8} V_m^{8/3} + \frac{B_m}{C_m^3} V_m \tag{4.49}$$

Where A_m, C_m and B_m are constants related to the permittivity of the filler material to matrix to matrix interactions. But, V_m is related to V_f by;

$$V_m = 1 - V_f \tag{4.50}$$

By substitution of Equation 4.50 into 4.49,

$$E_m = \frac{A_m}{C_m^8} (1 - V_f)^{\frac{8}{3}} + \frac{B_m}{C_m^3} (1 - V_f) \tag{4.51}$$

By substituting Equation 4.48 and 4.51 into 4.38, an important relationship between filler volume fraction and E is established,

$$E_c = \frac{A_f}{C_f^8} V_f^{8/3} + \frac{A_m}{C_m^8} (1 - V_f)^{\frac{8}{3}} + \left(\frac{B_f}{C_f^3} - \frac{B_m}{C_m^3} \right) V_f + \frac{B_m}{C_m^3} \tag{4.52}$$

For small V_f, and since $0 \leq V_f \leq 1$, the expression $(1- V_f)^{8/3}$ in Equation 4.51 can be expanded and approximated as Equation 4.53 (Taylor Series);

$$(1 - V_f)^{\frac{8}{3}} \approx 1 - \alpha_1 V_f + \alpha_2 V_f^2 - \alpha_3 V_f^3 + \cdots . - \cdots \quad (4.53)$$

where α_1, α_2, α_3, *e.t.c* are established constants. By neglecting the higher powers of Equation 4.53 since it is a convergent series, the approximation becomes;

$$(1 - V_f)^{\frac{8}{3}} \approx 1 - \alpha_1 V_f \quad (4.54)$$

Substituting Equation 4.54 into Equation 4.52, Equation 4. 55 is obtained

$$E_c = \frac{A_f}{C_f^8} V_f^{8/3} + \left(\frac{B_f}{C_f^3} - \left[\frac{B_m}{C_m^3} + \alpha_1 \frac{A_m}{C_m^8} \right] \right) V_f + \left(\frac{B_m}{C_m^3} + \frac{A_m}{C_m^8} \right) \quad (4.55)$$

Equation 4.55 can be generalized further to Equation 4.56, summarised as;

$$E_c = K_f V_f^{8/3} + K_{fm} V_f + K_m \quad (4.56)$$

where K_f defined by Equation 4.57 below, is a constant related to the E of the filler material;

$$K_f = \frac{A_f}{C_f^8} \quad (4.57)$$

and K_m, defined by Equation 4.58 below is a constant related to the E of the pure unblended matrix material.

$$K_m = \left(\frac{B_m}{C_m^3} + \frac{A_m}{C_m^8}\right) \quad (4.58)$$

K_{fm}, the matrix - filler interaction constant defined by Equation 4.59 below is of great interest.

$$K_{fm} = \left(\frac{B_f}{C_f^3} - \left[\frac{B_m}{C_m^3} + \alpha_1 \frac{A_m}{C_m^8}\right]\right) \quad (4.59)$$

Equation 4.59 can be further summarised as;

$$K_{fm} = K_{f0} - K_{m0} \quad (4.60)$$

where K_{f0} and K_{m0} are constants related to the E of the filler and matrix respectively. The equation therefore suggests that the difference between the magnitude of the properties of the filler and matrix materials are critical for reinforcement purposes. The equation suggests that the properties of the mechanical properties of the nanofiller must be significantly greater than those for the matrix material for significant reinforcement. If the filler properties are inferior to the matrix material, the effects on reinforcement could be negative. Agglomeration as a result of poor dispersion must therefore affect the interaction constant, K_{fm} resulting in negative effects on reinforcement. Similarly, K_f is significantly reduced by agglomeration resulting in limited or even negative reinforcement.

As Equation 4.56 shows, the Young's modulus, E, of a synthetic rubber nanocomposite ion exchange membrane can be equated to an approximate polynomial function of the volume fraction of the filler using the bonding theory. This is justified by the fact that the experimental equation for E, given by Equation 4.17 is similar in structure to the one from the bonding theory (Equation 4.56). The only difference is on the higher order power of V_f (*2 vs 8/3*). This difference could be

attributable to the differences between the actual packing of nanofiller in matrix and the assumed one (Kozako et al., 2005 and Palza et al., 2010). It is also important to note that the interactions between polymer and filler are much more complex than the assumptions made. Therefore reduction in the size of carbon nanoball used as a filler and improved dispersion are expected to bridge the gap between theoretical and experimental equations.

Therefore, the assumption that the Young's modulus of a synthetic rubber carbon nanoball nanocomposite ion exchange membrane is the result of summation of the filler-filler interactions mediated through the synthetic rubber matrix, the polymer-polymer interactions mediated through the nanofiller and the polymer-filler interactions can be reasonable. For the SSBR – CNB nanocomposite ion exchange membrane, Equation 4.56 can be written as;

$$E_c = K_{cnb}E_{cnb}V_{cnb}^{8/3} + K_cV_{cnb} + K_{ssbr}E_{ssbr} \qquad (4.61)$$

where E_c, K_{cnb}, E_{cnb}, V_{cnb}, K_c, K_{ssbr} *and* E_{ssbr} are the *Young's modulus* of the SBR – CNB nanocomposite, the *permittivity constant* for *CNB-CNB* filler interaction through SSBR, the *Young's modulus* of *CNBs*, the *volume fraction* of *CNB* filler, the *SSBR – CNB compatibility factor*, the *permittivity constant* for *SSBR – SSBR* interaction through CNBs and the *Young's modulus* of SSBR respectively.

Therefore if the Young's moduli of CNB and SSBR are known, reasonable reinforcement predictions can be made for the synthetic rubber nanocomposites. It can therefore be inferred that predictions for the other mechanical properties is possible and can be extended to similar synthetic rubber reinforcements.

CHAPTER 5: CONCLUSIONS AND RECOMMENDATIONS

5.1 Conclusions

The research was aimed at reinforcing locally synthesized rubber (polymeric) ion exchange membrane with locally synthesized carbon nanoballs to improve the mechanical properties. Successes in carbon nanoball synthesis, synthetic rubber functionalisation, blending, casting and mechanical testing made reinforcement feasible.

5.1.1 Carbon nanoball synthesis

A simple and stable NCCVD method using acetylene gas as the carbon source and argon as the carrier gas, has successfully produced uniform carbon nanoballs for reinforcement applications. A carbon nanoball of 60nm average diameter, 13.81m^2 BET surface area, I_G/I_D ratio of 1.04, T_d of 540°C and 99% purity was produced at 0.82 acetylene flow ratio and 1000°C in 16mm Φ reactor. The acetylene flow ratio and the reactor diameter were observed to be critical for the optimal production of the carbon nanoballs. At constant temperature and reactor size, the carbon ball size varies nonlinearly with acetylene flow ratio, reaching a minimum turning point between the lowest acetylene flow ratio and unity. The acetylene flow ratio, which determines curvature of graphitic shells, and the acetylene flow rate, which determines the number of shells formed, were the key factors influencing the size of the carbon ball formed. The carbon nanoball production range is inversely proportional to the reactor size. The minimum carbon ball size the equipment can produce is directly proportional to the reactor size. The acetylene flow ratio corresponding to the minimum turning point of the graph approaches unity as the reactor size decreases. Therefore smaller reactor sizes favour carbon nanoball production. The maximum production rate was 0.11$gmin^{-1}$ and the yield was 24% comparable to 26% reported elsewhere. The production rate and yield increase with acetylene flow rate.

5.1.2 Synthetic rubber sulphonation and blending

Styrene butadiene rubber was successfully sulphonated using 0.09M chlorosulphonic acid in 1,2 dichloroethane at 1.12 molar ratio to produce 44% degree of sulphonation. Low concentration of sulphonating agent (< 0.1M CSA) was found to promote homogeneous sulphonation due to the stoichiometric matching of the instantaneous concentration of sulphonating agent to the polymer solution. High concentration of acid (>1M) promotes polymer degradation. The high degree of mismatch of the instantaneous concentration of the sulphonating agent to the polymer solution was responsible for the degradation at relatively high concentrations.

The successfully sulphonated synthetic rubber ion exchange material was successfully blended with the carbon nanoballs using the solution processing method aided by ultrasonication at 60% sonication amplitude for 3hrs. A 160μm thick fairly homogenous nanocomposite ion exchange membrane was successfully produced. The quality of dispersion increased significantly with the amplitude of ultrasonication with a 700% quality of dispersion improvement from 20 to 60% amplitude of sonication. A critical amplitude of sonication exists for optimal blending. Above this critical value, polymer chain fragmentation occurs. Below this critical value, the quality of dispersion is compromised. The quality of dispersion also decreases with increasing filler concentration. There exists a saturation point above which the matrix material may not accommodate more nanofiller. Therefore optimisation of the blending conditions is critical inorder to achieve the desired reinforcement objectives.

5.1.3 Reinforcement effects of carbon nanoballs on SSBR ion exchange membrane

The reinforcement of synthetic rubber ion exchange membrane with 3 – 14 vol% CNB improved the mechanical properties in the range 79 – 370%. The results of mechanical testing of the plain unsulphonated and sulphonated rubber were

comparable with those reported elsewhere *(1.18 – 2MPa from literature, vs 2 - 4MPa from experimental for tensile strength)* implying that the testing method used was valid (Sakr et al., 1995; Baeta et al., 2009; Furtado et al., 1995; Saeb et al., 2010; Kim and Reneker, 1999 and El- Lawindy and El Guiziri, 2000). Although the fracture toughness and strain properties of the ion exchange membrane decreased with time, the carbon nanoballs reduced the rate of property deterioration. Polymer chain fragmentation at high amplitudes of sonication was responsible for increasing the density of fracture points as well as oxidation sites. As a result increased oxidation must be responsible for deterioration of fracture toughness with time. The elastic properties improved by a maximum of 50% with age due to increased crosslink density. The tensile strength remained stable with age. Therefore the addition of carbon nanofillers between 3 and 14vol% improves the stability of mechanical properties with time. The blending conditions significantly affected reinforcement. The change of amplitude of sonication from 20 to 60% drastically improved E, σy and σs by (92 – 233%), (88 – 282%) and (60 - 95%) respectively. These improvements were as a result of better dispersion at higher amplitudes of sonication. On the other hand the change of amplitude from 20 to 60% significantly reduced fracture toughness and strain by (36 – 55%) and 66% respectively. Polymer chain fragmentation at high amplitude of sonication is responsible for reduction in the latter properties. Therefore optimisation of the blending process must lead to high quality of dispersion responsible for significant improvement of the mechanical properties.

Comparison of experimental model for E was similar to the model proposed by Guth in the range of 1 – 4vol% CNB. However the coefficients of the experimental model were superior to the ones for the existing models. Therefore the mechanical properties of carbon nanoballs must be superior to the spherical nanofillers assumed in the models. This superiority could be attributable to the unique morphology of carbon nanoballs as compared to other spherical nanofillers. The extrapolation of the experimental profile for E gave values of E for CNBs that lie in the range reported in

literature confirming the validity of the model. Extrapolation also showed the potential of improvement of E by up to 700% within 3 – 14vol% CNB. Above 4 vol% CNB, the experimental profile was distorted due to agglomeration. The experimental model for tensile strength of well dispersed carbon nanoballs in the range 1 – 14vol% differed with models proposed by Nicolais and Narkis and Nielsen. The positive influence of carbon nanoballs in the experimental model was attributable to the properties of the carbon nanoballs and good dispersion. When agglomeration is dominant, the experimental model for tensile strength was similar to the existing models, the only difference being the power of V_f *(1 vs 2/3)*. This difference could be attributable to difference between the experimental packing of carbon nanofiller and assumed packing due to agglomeration. Models for fracture toughness of synthetic rubber nanocomposites are rarely reported in literature and hence no comparison was made. Nevertheless the experimental model showed a polynomial relationship of order 2, with CNB volume fraction. Approximate predictions for E, σ_s and $U_{f.t}$ can therefore be done for similar work on synthetic rubber – carbon nanoball nanocomposites.

An attempt to compare the experimental models for reinforcement for E and $U_{f.t}$ with the bonding theory showed close similarities. The difference on the higher powers of V_f was attributable to the difference in actual packing as compared to the assumed packing assumed. There is also still inadequate literature to address the complex interactions between the synthetic rubber and the carbon nanoballs.

Therefore, the addition of low concentration of carbon nanoballs improves the mechanical properties and stability of synthetic rubber ion exchange membranes. Improvement of the degree of dispersion drastically improved the reinforcement effects. The produced nanocomposites can be used in fuel cell applications, nano and ultrafiltration processes and reverse osmosis amongst others.

5.2 Recommendations

Further work spanning from carbon nanoball synthesis, polymeric matrix functionalisation to blending could facilitate continuous improvement of the nanocomposite membrane.

5.2.1 Carbon nanoball synthesis

Equipment redesign is recommended to eliminate blockages to the NCCVD process and hence ensure continuous production of uniform carbon nanoballs. Equipment and process optimisation is also recommended to produce carbon nanoballs under 50nm as well as improve the carbon nanoball production range. The economic feasibility of the process also needs to be looked at for commercialisation purposes.

5.2.2 Synthetic rubber functionalisation, blending and casting

Further work on the feeding mechanism for the sulphonating agent (e.g sprays as opposed to dropwise addition) might result in the use of higher concentration of sulphonating agent. This would imply less volumes of reagent used, higher reaction efficiencies and lower sulphonation times and hence significant reductions in the cost of the process.

Since the degree of dispersion is one of the major factors affecting reinforcement, improvement of the blending technology is recommended. Firstly, there is need for further work into the optimisation of the ultrasonication method for synthetic rubber reinforcement with carbon nanoballs. Secondly, there is need to try other blending techniques like insitu polymerisation, carbon nanoball functionalisation as well as the use of surfactants. Thirdly, further work into more accurate insitu and post blending dispersion analysis of synthetic rubber nanocomposite blends is recommended.

5.2.3 Reinforcement of synthetic rubber with carbon nanoballs

The effect of size of carbon nanoballs on reinforcement was not investigated and hence recommended. The use of functionalised and heat treated carbon nanoballs is also recommended for reinforcement improvement. The effect of carbon nanoballs and similar nanofillers on the oxidative stability of synthetic rubber ion exchange membrane must also be investigated. Along the same lines, the effect of carbon nanoballs on the chemical stability of synthetic rubber ion exchange membranes must be investigated.

Since creep test were not done, work on the effect of carbon nanoballs on creep behaviour of polymer nanocomposite is recommended. Little work was also done on fatigue testing and hence the need for further research. In situ testing of the membrane in operating environments with the aim of improving durability is also recommended.

Last but not least, little has been reported in literature on the mechanical properties of carbon nanoballs. Research work focused on establishing accurate measurements of the mechanical properties of carbon nanoballs is recommended. Such work will go a long way in predicting reinforcement effects of carbon nanoballs of synthetic rubber nanocomposites.

REFERENCES

Abdulkareem S.A (2009). Design and Development of Proton Exchange Membrane (PEM) from Synthetic Rubber and Carbon nanoparticles for PEM Fuel Cell, University of the Witwatersrand, South Africa (PhD Thesis, School of Chemical and Metallurgical Engineering).

Abdulkareem S.A, Afolabi A.S, Iyuke S.E, Pienaar C.H (2007): Synthesis of carbon nanotubes by swirled floating catalyst chemical vapour deposition reactor. *Journal of Nanoscience and Nanotechnology, Vol. 7 (9)*. Pp 3233 – 3238.

Ahmed, S and Jones, F. R (1990). A review of particulate reinforcement theories for polymer composites. *Journal Of Materials Science*, 25: 4933-4942

Allegra, G., Raosa, G and Vacatellob, M (2008). Theories and simulations of polymer-based nanocomposites: From chain statistics to reinforcement. Progress in Polymer Science, 33: 683–731

Amick, D.R (1979). Sulfone crosslinked polystyrene ion exchange resin and process of manufacture.*United States Patent 4,177,331,* Application No. 927,224.

Anderson, T. L (1995). Fracture Mechanics: Fundamentals and Applications *(CRC Press, Boston 1995).*

Ashby, M. F and Jones D. R (1980). Engineering Materials 1: An introduction to their properties and applications. Vol 34 – *Pergamon Press*

Askeland, D. R and Pradeep P. P (2003). The Science and Engineering of Materials (4th ed.). *Brooks/Cole.*

Baeta, D. A., Zattera, J. A., Oliveira, M. G and Oliveira, P. J (2009). The use of styrene-butadiene rubber waste as a potential filler in nitrile rubber: order of addition and size of waste particles. *Brazilian Journal of Chemical Engineering, Vol. 26, No. 01*: 23 – 31

Barnard, A. S., Russo, S. P and Snook, I. K (2003). Size dependent phase stability of carbon nanoparticles: Nanodi**a**mond versus fullerenes. *Journal Of Chemical*

Physics, Volume 118:11

Bacquet, M., Salunkhe, M. B and Caz, C (1992). Influence Of Chlorosulfonation On Textural, And Chemical Parameters Of Styrene-Divinylbenzene Porous Copolymers. *Reactive Polymers*, 16: 61-69

Bashir H., Linares, A and Acosta, J. L (2001). Heterogeneous sulfonation of blend systems based on hydrogenated polybutadiene–styrene/ block copolymer. Electrical and structural characterization. *Solid State Ionics,* 139: 189–196

Bhattacharya, M., Maiti, M and Bhowmick, A. K (2009). Tailoring Properties of Styrene Butadiene Rubber Nanocomposite by Various Nanofillers and Their Dispersion. *Polymer Engineering and Science*

Bigg D. M (1987)**.** Mechanical Properties of Particulate Filled Polymers. *Polymer Composites,* 8(2).

Blunk R, Zhong F, John O (2006). Automotive composite fuel cell bipolar plates: Hydrogen permeation concerns. *Journal of Power Sources 159*: 533–542.

Brechet, Y., Cavaille, J. Y., Chabert, E., Chazeau, L., Dendievel, R., Flandin, L and Gauthier, C (2001). Polymer Based Nanocomposites: Effect of Filler-Filler and Filler-Matrix Interactions. *Advanced Engineering Materials*, 3(8).

Byeon, J. H and Kim, J (2010). Production of carbonaceous nanostructures from a silver-carbon ambient spark. *Applied Physics Letters*, *96*.

Bystrzejewski, M., Rummeli, M.H., Gemming, T., Lange, H and Huczko, A (2010). Catalyst-free synthesis of onion-like carbon nanoparticles. *New Carbon Materials*, 25(1): 1–8

Budynas, R. G (1999). Advanced Strength and Applied Stress Analysis (2nd ed.). *McGraw-Hill, Inc: 532–533.*

Caldero -Moreno, J. M., Labarta, A., Batlle, X., Pradell, T., Crespo, D and Thien Binh, V (2005). Magnetic properties of dense carbon nanospheres prepared by chemical vapor deposition. *Chemical Physics Letters*, 447: 295–299

Calleja, F. J. B., Giri, L., Asano, T., Mieno T., Sakurai, M., Ohnuma, M and Sawatari, C (1996). Structure and mechanical properties of polyethylene-fullerene composites. *Journal of Materials Science*, 31: 5153-5157.

Castellanos, A (2005). The relationship between attractive interparticle forces and bulk behaviour in dry and uncharged fine powders. *Advances in Physics*, 54 (4): 263–376

Carrandi, J. C (2008). Nanomaterials in Context. *Journal of Nanoscience and Nanotechnology,* 7 (7): 3220 – 3227.

Chen J, Asano M, Maekawa Y, Yoshida M (2005): Suitability of some fluoropolymers used as base films for preparation of polymer electrolyte fuel cell membranes. *Journal of Membrane Science* 277: 249–257.

Chen S, Bocarsly A.B, Benzinger J (2005): Nafion-layered sulphonated polysulfone fuel cell membranes. *Journal of Power Sources*, 152: 122-135.

Chen, S., Krishnan, L., Srinivasan, S., Benziger, J and Bocarsly, A.B (2004). Ion exchange resin/polystyrene sulfonate composite membranes for PEM fuel cells. *Journal of Membrane Science,* 243: 327–333

Cho, J., Joshi, M.S and Sun, C.T (2006). Effect of inclusion size on mechanical properties of polymeric composites with micro and nano particles. *Composites Science and Technology,* 66: 1941–1952

Cho, J., Boccaccini, A. R and Shaffer, M. S. P (2009). Ceramic matrix composites containing carbon nanotubes. *Journal of Material Science,* 44:1934–195

Choi J, Lee K.M, Wycisk R, Pintauro P.N, Mather P.T (2008): Nanofiber Network Ion Exchange Membranes. *Macromolecules,* 41 (13): 4569-4572.

Choi, S (2000): Pyrolysis. *Journal of Analytical and Applied Pyrolysis*, 55: 161–170

Crosby, A. J and Lee, J (2007). Polymer Nanocomposites: The "Nano" Effect on Mechanical Properties. *Polymer Reviews,* 47:217–229

Crowley, M. S. and Welch, A. P (1954). Clay-Particle Dispersion by Ultrasons. *Journal of The American Ceramic Society*, 37(9).

Deshmukh, A. A., Mhlanga, S. D. and Coville, N. J (2010). Carbon spheres. *Materials Science and Engineering Review,* xxx xxx–xxx

Dick J.S, Anniceli R.A (2001): Rubber Technology: Compounding and Testing for Performance. *Hanser Gardner Publications*, Cincinnati, OH.

Dortmundt D, Doshi K (1999): Recent Developments in CO_2 Removal Membrane Technology. *UOP LLC*, pp 1-31.

Elabd, Y. A and Napadensky, E (2004).Sulfonation and Characterization of Poly(styrene-isobutylene-styrene) Triblock Copolymers at High Ion-Exchange Capacities. *Polymer*, 45: 3037–3043

El-Lawindy, A. M. Y and El-Guiziri, S. B (2000). Strain energy density of carbon-black-loaded rubber vulcanizates. *Journal of Physics, D: Applied Physics*, 33: 1894–1901

El-Lawindy, A.M.Y (2002). Static Deformation of Low Structure HAF Black-Loaded (SBR+NR) Rubber Blend. *Egypt. Journal of Solids*, 25(1).

Erik, T., Thostenson, C. L., and Tsu-Wei, C (2005). Nanocomposites in context. *Composites Science and Technology*, 65: 491–516

Fahlman, I. T (2007): Fullerene chemistry for materials science applications. *Journal of Material Chemistry*, 7(6): 1097–1109

Finnigan, B., Jack, K., Campbell, K., Halley, P., Truss, R., Casey, P., Cookson, D., King, S and Martin, D (2005). Segmented Polyurethane Nanocomposites: Impact of Controlled Particle Size Nanofillers on the Morphological Response to Uniaxial Deformation. *Macromolecules*, 38: 7386-7396

Foster, N C (1997). Sulfonation and Sulfation Processes. *The Chemithon Corporation*

Furtado, C. R.G., Nunes, R. C.R and Siqueira Filho, A. S (1995). SBR-mica-silica compositions and their physico-mechanical behavior. *Polymer Bulletin*, 34: 627-633

Gao Y, Robertson G.P, Guliver M.D, Jian X, Serguei D.M, Wang K, Kaliaguine S (2003): Sulphonation of poly (pthalaziones) with fuming sulfuric acid mixtures for proton exchange materials. *Journal of Membrane Science*, 227: 39-50.

Gillin, L. M and Kelly, A (1969). Effect of Twins on Deformation of Graphite Single Crystals. *Journal Of Materials Science*, 4: 439-449

Gong, C., Guan, R., Shu, Y., Chuang, F and Tsen, W (2007). Effect of sulphonic group on solubility parameters and solubility behavior of poly(2,6-dimethyl-1,4-phenylene oxide). *Polymer Advanced Technology*, 18: 44–49

Green, J. F and Spain, I. L **(**1973**).** The Theory Of C-Axis Elastic Moduli Of Graphite And Their Strain Dependence Using Simple Models Of The Interplanar Interaction. *Journal of Physical Chemistry. Solids,* 34: 2177-2191

Gibson, H. W and Bailey, F. C (1980). Chemical Modification of Polymers, Sulfonation of Polystyrene Surfaces. *Macromolecules***,** 13: 34-41

Guan, R., Gong, C., Lu, D., Zou, H and Lu W (2005). Development and Characterization of Homogeneous Membranes Prepared from Sulfonated Poly(phenylene oxide). *Applied Polymer Sciences, 98*: 1244 - 1250

Guillermo, A.J (2007). Characterization of Poly(Methyl Methacrylate) and Thermoplastic Polyurethane-Carbon Nanofiber Composites Produced By Chaotic Mixing. Department of Polymer Engineering, University of Poliuna, Costa Rica.

Gwaze, P., Schmida, O., Annegarnb, H. J., Andreaea M. O., Huthc, J and Helasa, G (2006) Comparison of three methods of fractal analysis applied to soot aggregates from wood combustion. *Aerosol Science,* 37: 820–838

Haghighat, M., Zadhoush, A and Khorasani, S. N (2005). Physicomechanical Properties of _-Cellulose–Filled Styrene–Butadiene Rubber Composites. *Journal of Applied Polymer Science*, 96: 2203–2211

He, X., Wu, F., Zheng, M (2007). The synthesis of carbon nanoballs and its electrochemical performance. *Diamond and Related Materials* 16: 311 – 315.

Hickner, M. A., Ghassemi, H., Kim, Y. S., Einsla, B. R and McGrath, J. E (2004). Alternative Polymer Systems for Proton Exchange Membranes (PEMs). *Chemistry Review,* 104: 4587-4612

Ho, C., Zydney A. Protein fouling of asymmetric and composite microfiltration membranes. *Ind Eng Chem Res*. 40: 1412-1421.

Hornig, J and Schoop, H (2003). Closed form analysis of wrinkled membranes with linear stress–strain relation. *Computational Mechanics,* 30: 259–264

Hooper, J. B and Schweizer, K. S **(**2006). Theory of Phase Separation in Polymer Nanocomposites, *Macromolecules*, 39: 5133-5142

Hua, N., Karube, Y., Yan, C., Masuda, Z and Fukunaga, H (2008). Tunneling effect in a polymer/carbon nanotube nanocomposite strain sensor. *Acta Materialia,* 56: 2929–2936

Huang, X., Solasi, R., Zou, Y., Feshler, M., Reifsnider, K., Condit, D., Burlatsky, S and Madden, T (2006). Mechanical Endurance of Polymer Electrolyte Membrane and PEM Fuel Cell Durability. *Journal of Polymer Science: Part B: Polymer Physics*, 44: 2346–2357

Hussain, F., Hojjati, M., Okamoto, M and Gorga R.E (2006). Polymer-matrix Nanocomposites, Processing, Manufacturing and Application: An Overview. *Journal of Composite Materials*, 40: 1511-1565.

Idibie, C. A (2009). Sulphonation Of Synthetic Rubber As An Alternative Membrane For Proton Exchange Membrane Fuel Cell. PhD Thesis, University of Witwatersrand, South Africa

Ikeda, Y., Akira, T and Kohjiyab, S (1997). Reinforcement of styrene–butadiene rubber vulcanizate by in situ silica prepared by the sol–gel reaction of tetraethoxysilane. *Journal of Material Chemistry,* 7(8): 1497–1503

Iyuke S.E (2005): "Swirled Fluidized Bed Chemical Vapour Deposition Reactor", University of Witwatersrand, Johannesburg. *SA Patent Appl. No*: 200503438.

Iyuke S.E, Abdulkareem A.S, Afolabi A.S, Pienaar C.H (2007): Catalytic production carbon nanotubes in a swirled fluid chemical vapour deposition reactor. *International Journal of Chemical Engineering*.

Jacob J., Pradanos P., Calvo J.I, Hernandez A., Jonsson G. Fouling kinetics and associated dynamics of structural modifications. *J. Coll and Surf.*, 138: 173-183.

Jancar, J., Douglas, J. F., Starr, F.W., Kumar, S.K., Cassagnau, P., Lesser, A.J., Sternstein, S.S and Buehler, M.J (2010). Current issues in research on structure property relationships in polymer nanocomposites. *Polymer,* 51: 3321-3343

Janowska, G. A. and Jastrzabek, K (2010). The effect of chlorosulphonated polyethylene on thermal properties and combustibility of butadiene–styrene

rubber. *Journal of Thermal Analytical Calorimetry*

Jannasch, P (2003). Recent developments in high-temperature proton conducting polymer electrolyte membranes. *Current Opinion in Colloid and Interface Science, 8:* 96–102

Jayasree, T. K and Predeep, P (2008). Effect of Fillers on Mechanical Properties of Dynamically Crosslinked Styrene Butadiene Rubber/High Density Polyethylene Blends. *Journal of Elastomers and Plastics,* 40: 127

Jeriera, J., Richefeua, V., Imbaulta, D and Donz, F (2010). Packing spherical discrete elements for large scale simulations. Computer *Methods in Applied Mechanics and Engineering*

Jia, Q., Wu, Y., Wang, Y., Lu, M., Yang J and Zhang L (2007). Organic Interfacial Tailoring of Styrene Butadiene Rubber–Clay Nanocomposites Prepared by Latex Compounding Method. *Journal of Applied Polymer Science,* 103: 1826–1833

Jiang, J., Oberdo¨rster, G and Biswas, P (2009). Characterization of size, surface charge, and agglomeration state of nanoparticle dispersions for toxicological studies. *Journal of Nanoparticle Resources*, 11:77–89

Jin, Y. Z., Gao, C., Hsu, W. K., Zhu, Y., Huczko, A., Bystrzejewski, M., Roe, M., Lee, C.Y., Acquah, S., Kroto, H and Walton, D. R. M (2005). Large-scale synthesis and characterization of carbon spheres prepared by direct pyrolysis of hydrocarbons. *Carbon 43:* 1944–1953,

Johnson P.S (2001): Rubber Processing: An Introduction. *Hanser Gardner Publications*, Cincinnati, OH.

Jornitz, M. W (2006). *Sterile Filtration*, Springer, Germany, 2006

Joyce, G **(**2009). Advances in Structure Measurements of Carbon Black. *The Carbon Aggregate,* 9(1).

Kang, Z. C and Wang Z. L (1996). On Accretion of Nanosize Carbon Spheres. *Journal of Physical Chemistry,* 100: 5163-5165

Kim, D. P., Suhng, Y and Labes, M. M **(**1992). Mechanical Properties Of Pyrolytic Graphite Flakes. *Carbon.* 30: (5) 729-737

Kim, J and Reneker, D. H (1999). Mechanical Properties of Composites Using Ultrafine Electrospun Fibers. *Polymer Composites*, 20(1).

Kaur, S., Florio, G., and Michalak, D (2002). Cross-linking of sulfonated styrene–ethylene/butylene–styrene triblock polymer via sulfonamide linkages. *Polymer*, 43: 5163–5167

Knaggs E. A and Nepras M. J (2005). Sulfonation and Sulfation. *Kirk-Othmer Encyclopedia of Chemical Technology*, 23: 1-52

Koter, S., Piotrowski, P and Keresi J (1999). Comparative Investigations of ion exchange membrane. *Journal of Membrane Science*, 153: 83.

Kozako, M., Kuge, S., Imai, T., Ozaki, T., Shimizu, T and Tanaka, T (2005). Surface Erosion Due to Partial Discharges on Several Kinds of Epoxy Nanocomposites. *Annual Report Conference on Electrical Insulation and Dielectric Phenomena*

Kramb, R. C and Zukoski, C. F (2008). A Metastable van der Waals Gel: Transitioning from Weak to Strong Attractions. *Langmuir*, 24(14).

Lach, R., Adhikari, R., Weidisch, R., Huy, T. A., Michler, G. H., Grellmann, W and Knoll, K (2004). Crack toughness behaviour of binary poly(styrene-butadiene) block copolymer blends. *Journal of Material Science*, 39: 1283-1295.

Levin, V. M., Petronyuk, J. S and Ponomareva, I. V (2003). Modeling mechanical properties of carbon molecular clusters and carbon nanostructural materials. *Materials Research Society Symposium Proceedings*, 740.

Lee, H., Kim, C., Yang, K. S and Lee, W (2004). Electrical Characteristics of Polypyrrole/Sulfonated poly(styrene-co-butadiene) Composite Electrode for Polymer Battery. *Applied Chemistry*, 8(1): 175 – 178.

Liang, J and Yang, Q (2007). Aggregate structure and percolation behavior in polymer/carbon black conductive composites. *Journal of Applied Physics, 102.*

Lorenz, G and Günther, G. S (2008). A Proton-Conducting Polymer Membrane as Solid Electrolyte – Function and Required Properties. *Adv Polym Sci*, 215: 1–14

Luzanov, A. V., Ivanov V. V., Klimko, G. T and Mestechkin, M. M (1998). Semiempirical estimations of van der Waals interactions of fullerenes C_{60}, C_{70}, and C_{80}. *Journal of structural Chemistry*, 39(2)

Madaeni S.S (2001). The effect of large particles on microfiltration of small particles J. *Por Mat*. 8: 143-148.

Marangoni, A. G (2000). Elasticity of high-volume-fraction fractal aggregate networks: A thermodynamic approach. *Physical Review B*, 62 (1).

Martins, C. R., Ruggeri, G and De Paoli, M (2003). Synthesis in Pilot Plant Scale and Physical Properties of Sulfonated Polystyrene. *Journal of Brazilian Chemical Society,* 14(5): 797-802.

Manivannan, S., Jeong, O., Ryu, J. H., Lee, C. S., Kim, K. S., Jang, Jin and Park, K. C (2009). Dispersion of single-walled carbon nanotubes in aqueous and organic solvents through a polymer wrapping functionalization, *Journal of Material Science,* 20:223–229

Meier-Haack, J., Taeger, A., Vogel, C., Schlenstedt, K., Lenk, W and Lehmann, D (2005). Membranes from sulfonated block copolymers for use in fuel cells. *Separation and Purification Technology,* 41: 207–220.

Martinez F., Martin A., Pradanos P., Calvo J.I., Palacio L.., Hernandez A. Protein adsorption and deposition onto microfiltration membranes: the role of solute-solid interactions. *J. Coll Interf Sci*., 221: 254-261.

Mhlanga, S. D., Coville, N. J., Iyuke, S. E., Afolabi, A. S., Abdulkareem, A. S and Kunjuzwa, N (2010). Controlled syntheses of carbon spheres in a swirled floating catalytic chemical vapour deposition vertical reactor. *Journal of Experimental Nanoscience*, 5(1): 40–51

Miao, J., Hwang, D. W., Chang, C., Lin, S., Narasimhulu, K.V and Hwang, L (2003). Uniform carbon spheres of high purity prepared on kaolin by CCVD. *Diamond and Related Materials,* 12: 1368–1372

Miao, J., Hwang, D. W., Narasimhulu, K. V., Lin, P., Chen, Y., Lin, S and Hwang, L (2004). Synthesis and properties of carbon nanospheres grown by CVD using Kaolin supported transition metal catalysts. *Carbon 42*: 813–822

Miller, S. G (2008). Effects of nanoparticle and matrix interface on nanocomposite properties. *PhD Dissertation,* The Graduate Faculty of The University of

Akron

Mitova, S., Delmer, O., Kerres, J and Roduner, E (2006). Oxidative and Photochemical Stability of Ionomers for Fuel-Cell Membranes. *Helvetica Chimica Acta*, 89.

Mohamad, N., Muchtar, A., Ghazali, M. J., Mohd, D. H and Azhari C. H (2008). The Effect of Filler on Epoxidised Natural Rubber-Alumina Nanoparticles Composites. *European Journal of Scientific Research*, 24(4): 538-547

Mokrini, A., Del, R. J and Acosta J. L (2004). Synthesis and characterisation of new ion conductors based on butadiene styrene copolymers. *Solid State Ionics* 166: 375-381.

Moniruzzaman, M and Winey, K. I (2006). Polymer Nanocomposites Containing Carbon Nanotubes. *Macromolecules 39:* 5194-5205

Moodley, V. K (2007). The synthesis, structure and properties of polypropylene nanocomposites. *MTech Thesis*, Durban University of Technology, South Africa

Mulder, M (1996). Basic Principles of Membrane Technology. *Kluwer Academic Publishers, Netherlands*, 1996.

Nagarale, R. K., Gohil, G. S and Shahi V. K (2006). Recent developments in ion exchange membranes and electron-membrane processes. *Advances in Colloid and Interface Science*, 119: 97-130.

Nasef, M. M and Hegazy E.A (2004). Preparation and applications of ion exchange membranes by radiation-induced graft copolymerization of polar monomers onto non-polar films. *Prog. Polym. Sci.*, 499–561.

Odegard, G. M., Clancy, T. C and Gates, T.S (2005). Modeling of the mechanical properties of nanoparticle/polymer composites. *Polymer* 46: 553–562

Oden, J. T., Fung, Y.C., Simo, J. C., Padovan, J and Bauer, R. F (2005). Nonlinear Finite Element Analysis of Elastomers, Nonlinear Finite Element Analysis of Elastomers

Oren, Y., Freger, V and Linder, C (2004). Highly conductive ordered heterogeneous ion-exchange membranes. *Journal of Membrane Science,* 239: 17-26.

Osada, Y and Nakagawa, T (1992). Membrane Science and Technology, *New York: Marcel Dekker, Inc,* 1992.

Osman, H. M., Ghani, S. A. A., Madkour, T. M and Mohamed, A. R (2000). Stress Relaxation in Carbon Black Loaded Butyl Rubber. *Journal of Applied Polymer Science,* 77: 1067–1076.

Owzhera, J. K. I and Cerfontain, H (1968). Aromatic Sulphonation With Sulphur Trioxide In Trichlorofluoromethane As A Solvent. *Tetrahedron,* 24: 6543 – 6555

Palacio, L., Ho, C., Pradanos, P., Calvo, J. I., Kherif, G., Larbot, A and Hernandez A (1998). Fouling, structure and charges of composite inorganic microfiltration membrane. *J. Coll and Surf.* 138: 291-299.

Palza, H., Vergara, R and Zapata, P (2010). Improving the Thermal Behavior of Poly(propylene) by Addition of Spherical Silica Nanoparticles, *Macromolecular. Materials Engineering,* 295: 000–000

Patwardhan, S. V (2002). Review on Silica- Fullerene Hybrid Materials: Synthesis, Properties and Applications. *SJC Research Group*.

Pavlina, E. J and Van Tyne C. J (2008). Correlation of Yield Strength and Tensile Strength with Hardness for Steels. *Journal of Materials Engineering and Performance*, 17(6)

Perry, R.H., Green D.H., *Perry's Chemical Engineers' Handbook*, 7th edition, McGraw-Hill, 1997.

Pinnau, I., Freeman, B.D., *Membrane Formation and Modification*, ACS, 1999.

Prato, M (1997). [60] Fullerene chemistry for materials science applications. *Journal of Material Chemistry*, 7(7): 1097–1109.

Qiu, J., Li, Y and Wang, Y (2004). Novel fluffy carbon balls obtained from coal which consist of short curly carbon fibres. *Letter to the Editor Carbon 42*: 2329-2366.

Quan, P., Zhou, B., Sobiesiak, A and Liu Z (2005). Water behaviour in serpentine micro-channel for proton exchange membrane fuel cell cathode. *Journal of Power of Sources, 150:* 131-144.

Rabia, I., Zerouk, J., Bencheikh, Z., Iayadene, F., Guettaf, H and Saggou, A (1996). Chemical and Textural Characteristics of Chlorosulfonated Porous Stvrene-Divinylbenzene Copolymer Beads. *Polymers for Advanced Technologies,* 7: 543-547

Ramanathan, T., Stankovich, S., Dikin, D. A., Liu H., Shen H., Nguyen S. T and Brinson, L. C (2007). Graphitic Nanofillers in PMMA Nanocomposites—An Investigation of Particle Size and Dispersion and Their Influence on Nanocomposite Properties. Journal of Polymer Science: Part B: Polymer Physics, 45: 2097–2112

Recio, R., Lozano, A. E., Pra´danos, P., Marcos, A., Tejerina, F and Herna´ndez, A (2008). Effect of Fractional Free Volume and T_g on Gas Separation Through Membranes Made with Different Glassy Polymers. *Journal of Applied Polymer Science,* 107: 1039–1046

Reyes, Y., Paulis, M and Leiza, J. R (2010). Modeling the equilibrium morphology of nanodroplets in the presence of nanofillers. *Journal of Colloid and Interface Science,* 352: 359–365

Ripperger S and Schulz G. Microporous membranes in biotechnical applications. *Bioprocess Eng*. 1(1986): 43-49.

Rothon, R. N (2008). Particulate fillers for polymers

Ruoff, R. S and Hickman, A. P (1993). van der Waals Binding of Fullerenes to a Graphite Plane, *The Journal of Physical Chemistry,* 11: 2494-2496

Saeb, M. R and Ramezani-Dakhel, H (2010). Improving Thermo-mechanical Properties of Styrene Butadiene Rubber Nanocomposites Using Eggshell Bio-filler. *Fourth International Conference on Quantum, Nano and Micro Technologies*

Sakr, E. M., Zayed, H.A., El-Mawla, S.A., Kenawy, M.A and Nagy, M.R (1995). Study Of Stress-Strain Characteristics Of SBR And Blended NR/SBR Rubber. Czech. *Journal of Physics,* 45

Sata, T (1986). Recent trends in ion exchange membrane research. *Pure and Appl.*

Chem, 58(12): 1613-1626.

Sata, T (1991): Ion exchange membranes and separation processes with chemical reactions. *Journal of Applied Electrochemistry,* 21: 283-294.

Seon, H. A., Seong H. K., Byoung C. K.**,** Kwang B. S and Bong G. C (2004). Mechanical Properties of Silica Nanoparticle Reinforced poly(ethylene 2, 6-naphthalate). *Macromolecular Research,* 12(3): 293-302

Shaltout, N. A (2009). Effect of electron beam irradiation and degree of boric acid loading on the properties of styrene-butadiene rubber. *Reactive and Functional Polymers,* 69: 229–233

Shanov, V., Schulz, M and Yeo-Heung, Y (2007). Developing A New Grade of CTIC Carbon Nanosphere Chains And Processing This Material In Nanocomposites. *CleanTechnology International Corp.*

Shatalov, V. V., Savel'eva, T. I., Karlashchuk, L. V and Ramzina, T.A (2007): Modification of Ion Exchange Membranes. *Theoretical Foundations of Chemical Engineering, 41 (5)*: 703-705.

Sheikh-Ali, B and Wnek, G. E (2000). Ion conducting Membrane for Fuel Cell. *Patent No:* 6,110,616, American Patents

Strathmann H (2004): Ion Exchange Separation Processes. *Elsevier Ltd, USA.*

Sobkowicz, M. J., Dorgan, J. R., Gneshin, K. W., Herring, A. M and McKinnon, J. T (2009). Controlled dispersion of carbon nanospheres through surface functionalization. Carbon, 47: 622 – 628

Sue, H. J., Wilchester, J. W., Wang, C. H and Caldwell, D. L (1994). Fatigue Fracture Behaviour of Chlor-Alkali Membranes. *Journal of Polymer Research,* 1(2): 205 – 209.

Tabor, D (1969). Recent Studies of Short Range Forces. *Journal of Colloid and Interface Science,* 31: No. 3

Tagmatarchis, N and Prato, M (2005): Carbon based materials: From fullerene nanostructures to functionalized carbon nanotubes. *Pure Appl. Chem, 77(10)*: 1675-1684.

Tanaka, T (2005). Dielectric Nanocomposites with Insulating Properties. *IEEE Transactions on Dielectrics and Electrical Insulation,* 12(5).

Templin, T., Johnston, D., Singh, V., Tumbleson, M. E., Belyea, R. L and Rausch, K. D (2006). Membrane separation of solids from corn processing streams. *Biores Tech*. 97: 1536-1545.

Thostenson, E. T., Li, C and Chou T-W (2005). Nanocomposites in context. *Composites Science and Technology,* 65: 491–516.

Tonanon, N., Intarapanya, W., Tanthapanichakoon, W., Nishihara, H., Mukai, S. R and Tamon, H (2008). Submicron mesoporous carbon spheres by ultrasonic emulsification. *Journal of Porous Materials,* 15:265–270

Tripathi, B. P., Kumar, M and Shahi, K (2008): Highly stable proton conducting nanocomposite polymer electrolyte membrane prepared by pore modifications: An extremely low methanol permeable PEM. *Journal of Membrane Science 327*: 145-154.

Tuichiev, Sh., Tabarov, S. Kh and Ginzburg. B. M (2008). Effect of C60 Fullerene Additions on the Mechanical Properties of a Polybutadiene- Styrene Raw Rubber. *Technical Physics,* 53(7):956 – 958.

Van Reis, R and Zydney, A (2007). Bioprocess membrane technology. *J Mem Sci*., 297: 16-50.

Vassiliou, A., Bikiaris, D., Chrissafis, K., Paraskevopoulos, K.M., Stavrev, S.Y and Docoslis, A (2008). Nanocomposites of isotactic polypropylene with carbon nanoparticles exhibiting enhanced stiffness, thermal stability and gas barrier properties. *Composites Science and Technology,* 68: 933–943

Walsby, N., Paronen, M., Juhanoja, J and Sundholm, F (2001). Sulfonation of Styrene-Grafted Poly(vinylidene fluoride) Films. *Journal of Applied Polymer Science,* 81: 1572–1580

Wan, Y and Wen, D (2004). Thermo-sensitive properties of carbon-black-loaded styrene butadiene rubber composite membranes. *Smart Materials and Structures,* 13: 983–989

Wan, Y and Wen, D (2005). Stability of thermo-sensitive properties of carbon-black/styrene-butadiene-rubber composite membranes. *Smart Materials and Structures,* 14: 941–948

Wang, S., Sun, G., Wang, G., Zhou, Z., Zhao, X., Sun, H., Fam, X., Yi, B and Xin, Q (2005): Improvement of direct methanol fuel cell performance. *Electrochemistry Communication*, 7: 1007 – 1012.

Wang, Y., Nepal, D and Geckeler, K. E (2005). Hollow porous carbon nanospheres with large surface area and stability, assembled from oxidized fullerenes. *Journal of Materials Chemistry,* 15: 1049–1054

Wang, Y., Wu Y., Zhang, H., Zhang, L., Wang, B and Wang, Z (2004). Free Volume of Montmorillonite/Styrene-Butadiene Rubber Nanocomposites Estimated by Positron Annihilation Lifetime Spectroscopy. *Macromolecular Rapid Communications,* 1974 – 1977.

Wang, Z. L and Kang, Z. C **(**1996). Pairing of Pentagonal and Heptagonal Carbon Rings in the Growth of Nanosize Carbon Spheres Synthesized by a Mixed-Valent Oxide-Catalytic Carbonization Process. *Journal of Physical Chemistry*, 100(45).

Wang, Z.F., Wang, B., Qia, N., Zhang, H.F and Zhang, L.Q (2005). Influence of fillers on free volume and gas barrier properties in styrene-butadiene rubber studied by positrons. *Polymer*, 46: 719–724

Williams, J. M., Bartos, J. J and Wilkerson, M. H (1990). Elastic modulus dependence on density for polymeric foams with systematically changing microstructures. *Journal of Materials Science,* 25: 5134-5141

Winey, L. S and Vaia, P. T (2007). Common nanomaterials structures for polymer nanocomposites. *Journal of Nanotechnology,* 20(1).

Wu, H., Hong, C., Chiu, H and Li, Y (2009). Continuous synthesis of carbon spheres by a non-catalyst vertical chemical vapor deposition. *Diamond & Related Materials*, 18: 601–605

Xing, P., Robertson G. P., Guiver, M. D., Mikhailenko, S. D., Wang, K and Kaliaguine, S (2004). Synthesis and characterisation of sulphonated poly (ether ketone) for proton exchange membrane. *Journal of Membrane Science,* 229: 95 – 106.

Xie, H., Liu D and Xie, D (2005). Preparation, Characterization, and Some Properties of Ionomers from a Sulfonated Styrene–Butadiene–Styrene Triblock Copolymer without Gelation. *Applied Polymer Sciences*, 96:1398–1404.

Xu, R., Manias, E., Snyder A. J and Runt, J (2003). Low permeability biomedical polyurethane nanocomposites. *Journal of Biomedical Material Resources,* 64A: 114-119.

Xu, T (2005): Ion exchange membranes: State of their development and perspective. *Journal of Membrane Science,* 263:1-29.

Xu, T., Yang, W and He, B (2002). Effect Of Solvent Composition On The Sulphonation Degree Of Poly(Phenylene Oxide) (PPO). *Chinese Journal of Polymer Science,* 20(1): 53-57

Yan, W., Lin, R. J. T and Bhattacharyya, D (2006). Particulate reinforced rotationally moulded polyethylene composites – Mixing methods and mechanical properties. *Composites Science and Technology,* 66: 2080–2088

Yasmin, A., Luo, J and Daniel, I. M (2006). Processing of expanded graphite reinforced polymer nanocomposites. *Composites Science and Technology,* 66: 1179–1186

Zeaman, L. J and Zydney, A, L (1996). Microfiltration and Ultrafitration, Principles and Applications. *New York: Marcel Dekker, Inc, 1996.*

Zeng, Q.H., Yu, A.B and Lu, G.Q (2008). Multiscale modeling and simulation of polymer nanocomposites. *Progress in Polymer Science,* 33: 191–269

Zetl, A and Cumings, J (2001). Elastic Properties of Fullerenes. *Handbook of Elastic Properties of Solids, Liquids and Gases,* 11: Chapter 11.

Zhang, B., Wang, T., Zhang, S., Jieshan, Q and Jian X (2006). Preparation and Characterisation of carbon membranes made from poly(phthalazinone ether sulfone ketone). *Carbon,* (44): 2764 – 2769.

Zhang, F., Busnaina, A. A., Fury, M. A and Wang, S (2000). The Removal of Deformed Submicron Particles from Silicon Wafers by Spin Rinse and Megasonics. *Journal Of Electronic Materials.*

Zhang, G., Liu, L., Wang, H and Jiang, M (2000). Preparation and association behavior of diblock copolymer ionomers based on poly(styrene-b-ethylene-co-propylene). *European Polymer Journal,* 36: 61- 68

Zhang, X., Wang, Z., Sun, X., Han, W and Hong, C (2008). Effect of graphite flake on the mechanical properties of hot pressed ZrB2–SiC ceramics. *Materials Letters*, 62: 4360–4362

Zhanga, Z., Zhang, L., Li, Y and Xu, H (2005). New fabricate of styrene–butadiene rubber/montmorillonite nanocomposites by anionic polymerization. *Polymer*, 46: 129–136

Zhou, Z and Magriotis, P. A (2005): A New Method for the functionalisation of [60] Fullerene: An Unusual 1,3-Dipolar Cycloaddition Pathway Leading to a C_{60} Housane Derivative. *Organic Letters*, 7(26): 5849-5851.

Zydney, A. L and Ho, C (2003). Effect of Membrane Morphology on System Capacity During Normal Flow Microfiltration. *Biotechnol, Bioeng*., 83: 537-543.

APPENDICES

Appendix 1

Table i.i: NCCVD reactor dimensions

Reactor I. D (mm)	Length(mm)	Furnace Diameter (mm)
50	780	72
19	300	29
16	300	29
22	300	29

Table i. ii: Average carbon ball size estimation

		%Frequency of occurrence						
Sample No.	**Flow Ratio (η_{AC})**	**40-80nm**	**80-120nm**	**120-180nm**	**180 – 280nm**	**280 – 380nm**	**380-500nm**	**Average Diameter(nm)**
22-1	0.48	0	0	0	0	0	0	-
22-2	0.51	3	10	75	6	3	3	150
22-3	0.61	1	3	10	76	6	4	200
22-4	0.65	0	10	80	10	3	2	160
22-5	0.72	35	45	11	5	3	1	80
22-6	0.85	4	6	5	82	3	0	200
22-7	0.87	0	2	4	11	73	10	300
22-8	1	0	1	2	5	22	70	450
19-1	0.32	0	0	0	0	0	0	-
19-2	0.48	0	0	0	0	0	0	-
19-3	0.61	2	4	4	85	3	2	250
19-4	0.66	0	3	2	15	75	5	300
19-5	0.72	70	25	3	2	1	0	70
19-6	0.82	10	85	2	2	1	0	100
19-7	0.90	0	1	8	85	2	1	200
19-8	1	0	0	3	2	93	5	350
16-1	0.50	0	0	0	0	0	0	-
16-2	0.61	2	3	90	3	1	1	140
16-3	0.66	1	2	2	94	1	0	250
16-4	0.72	80	18	1	1	0	0	80
16-5	0.82	95	4	1	0	0	0	60
16-6	0.90	2	80	18	0	0	0	120
16-7	1	0	0	0	2	95	3	300

Calculation of parameters of CNBs produced from the NCCVD equipment

Rotameter Flow Rate *Adjustments Factors* for *Argon* and *Acetylene* are *1.18* and *0.95* respectively.

Therefore, Adjusted Flow rate for any Gas Flow was calculated as *Rotameter Flow Rate/Adjustment Factor*

E.g,

i) Acetylene Flow rate = 181ml/min, Adjusted Flow Rate, Q_{ac} *= (181/0.95) = 191ml/min*

ii) Argon Flow rate = 248ml/min, Adjusted Flow Rate,Q_{arg} *= (248/1.18) = 210 ml/min*

iii) Total Flow Rate, Q_T *= Acetylene Adjusted Flow Rate + Argon Adjusted Flow Rate = 191+210 = 401ml/min*

iv) Acetylene Flow Ratio, η_{AC} *= Adjusted Acetylene Flow Rate (*Q_{ac}*)/ Total Flow Rate,* Q_T *= 191/401 = 0.48*

Production Measures

Production Rate, M_p *= Sum of Mass of CNBs from Reactor and Cyclone/Production Run Time.*

Table i.iii: Carbon ball production rate

Sample No.	Flow Ratio (η_{AC})	CNB Mass (Cyclone) (g)	CNB Mass (Reactor) (g)	Total CNB Mass (g)	Run Time(g/min)	Prod Rate (M_p) (g/min)
22-1	0.48	0	0	0	10	0
22-2	0.51	0.143	0.137	0.28	10	0.028
22-3	0.61	0.235	0.0088	0.24	10	0.024
22-4	0.65	0.112	0.0306	0.14	10	0.014
22-5	0.72	0.484	0.1784	0.66	10	0.066
22-6	0.85	0.26	0.19	0.45	10	0.045
22-7	0.87	0.216	0.42	0.64	10	0.064
22-8	1	0.17	0.398	0.57	10	0.057
19-1	0.32	0	0	0	10	0
19-2	0.48	0	0	0	10	0
19-3	0.61	0.15	0.0047	0.15	10	0.015
19-4	0.66	0.036	0.0013	0.04	10	0.004
19-5	0.72	0.051	0.045	0.10	10	0.010
19-6	0.82	0.242	0.2445	0.49	10	0.049
19-7	0.90	0.138	0.3258	0.46	10	0.046
19-8	1	0.128	0.45	0.58	10	0.058
16-1	0.50	0	0	0	10	0
16-2	0.61	0.1	0.009	0.11	10	0.011
16-3	0.66	0.0418	0.0095	0.05	10	0.005
16-4	0.72	0.10	0.3	0.40	10	0.040
16-5	0.82	0.382	0.7135	1.1	10	0.11
16-6	0.90	0.2176	0.41	0.63	10	0.063
16-7	1	0.211	0.513	0.72	10	0.072

Calculation of Carbon Ball Yield

The following assumptions were made;

i) Carbon balls are 100% carbon

ii) Acetylene is 100% pure

iii) Ideal Gas Law Equation applies since the compressibility factors for argon and acetylene are close to unity (R = 8.3144Nm/molK).

iv) Rotameter flow rates were calibrated at T = 293K (20°C) and 101.3kPa

Calculation of mass flow rate of carbon in acetylene entering the reactor, M_{aci}

Let the Volumetric flow rate of acetylene entering the reactor be Q_{ac};

Using the ideal gas law equation and assumptions given,

$pQ_{ac} = M_{aci}RT/M_{wac}$*, which implies that,*

$M_{aci} = pQ_{ac} M_{wac}/RT$*, where* M_{aci}, M_{wac} *and* Q_{ac} *are the mass flow rate and molecular weight of acetylene and volumetric flow rate of acetylene respectively.*

Therefore mass flow rate of carbon into reactor, $M_{ci} = 2xM_{wC}xM_{aci}/M_{wac}$*, where* M_{ci} *and* M_{wC} *are the mass flow rate of carbon into the reactor and atomic weight of carbon respectively. Substituting the values,*

$M_{ci} = 2xM_{wC}xM_{aci}/M_{wac} = 2x12xM_{aci} / 26 = 0.923M_{aci}$*;*

Substituting $Q_{ac} = 456ml/min$,

$M_{aci} = 101300x456x26x10^{-6}/(8.3144x293) = 0.49g/min$

And $M_{ci} = 0.923x0.49 = 0.455g/min$

Therefore Yield,γ*. calculated as,* $M_p/M_{ci} = 0.11/0.455 = 0.24 = 24\%$

Table i.iv: Carbon ball productivity measures

η_{AC}[a]	Φ_{CB}(nm)[b]	M_{ci} (g/min)[c]	M_{CBc}(g/min)[d]	M_R(g/min)[e]	M_F(g/min)[f]	M_G(g/min)[g]	M_P(g/min)[h]	γ_{cyc}(%)[j]	β(%)[k]	ω[m]	γ_G(%)[n]	γ(%)[p]	γ_F(%)[q]
22mm Φ x 300mm Length Reactor													
0.48	-	0.19	0.0000	0.0000	0.0048	0.005	0.000	0	0	-	3	0	3
0.51	150	0.32	0.0143	0.0137	0.0092	0.037	0.028	4	75	0.51	12	9	3
0.61	200	0.32	0.0235	0.0009	0.0002	0.025	0.024	7	99	0.96	8	8	0
0.65	160	0.39	0.0112	0.0031	0.0003	0.015	0.014	3	98	0.79	4	4	0
0.72	60	0.39	0.0484	0.0178	0.0004	0.067	0.066	12	99	0.73	17	17	0
0.85	200	0.32	0.0260	0.0190	0.0010	0.046	0.045	8	98	0.58	14	14	0
0.87	300	0.39	0.0216	0.0421	0.0037	0.067	0.064	6	95	0.34	17	16	1
1.00	450	0.45	0.0170	0.0399	0.0044	0.061	0.057	4	93	0.30	13	13	1
19mm Φ x 300mm Length Reactor													
0.32	-	0.19	0.0000	0.0000	0.0059	0.006	0.000	0	0	-	3	0	3
0.48	-	0.19	0.0000	0.0000	0.0020	0.002	0.000	0	0	-	1	0	1
0.61	250	0.32	0.0150	0.0005	0.0090	0.024	0.015	5	63	0.97	8	5	3
0.66	300	0.36	0.0036	0.0001	0.0011	0.005	0.004	1	77	0.97	1	1	0
0.72	70	0.39	0.0051	0.0045	0.0002	0.010	0.010	1	98	0.53	3	2	0
0.82	100	0.45	0.0242	0.0245	0.0283	0.077	0.049	5	63	0.50	17	11	6
0.90	200	0.51	0.0138	0.0326	0.0109	0.057	0.046	3	81	0.30	11	9	2
1.00	350	0.57	0.0128	0.0450	0.0900	0.148	0.058	2	39	0.22	26	10	16
16mm Φ x 300mm Length Reactor													
0.50	-	0.26	0.0000	0.0000	0.0020	0.002	0.000	0	0	-	1	0	1
0.61	140	0.32	0.0100	0.0009	0.0081	0.019	0.011	3	57	0.92	6	3	3
0.66	250	0.36	0.0042	0.0009	0.0038	0.009	0.005	1	58	0.82	3	1	1
0.72	80	0.39	0.0100	0.0300	0.0270	0.067	0.040	3	60	0.25	17	10	7
0.82	60	0.45	0.0382	0.0714	0.0480	0.158	0.110	8	70	0.35	35	24	11
0.90	120	0.51	0.0218	0.0410	0.0176	0.080	0.063	4	78	0.35	16	12	3
1.00	300	0.57	0.0211	0.0513	0.0190	0.091	0.072	4	79	0.29	16	13	3

Appendix 2

Dilution of Chlorosulphonic Acid Calculations (Analytical Grade, Merck Chemicals, SA)

Let purity of purchased chlorosulphonic acid be P (97%), Density, D = 1.75kg/l and M_{wcsa} *= 116.52g/mol*

Let desired chlorosulphonic acid concentration and Volume of diluted acid be C_{csa} *(M) and* V_d *(ml) respectively, therefore the required volume of CSA,* V_{csa} *to make this concentration is given by;*

$V_{csa} = C_{csa} x V_d x M_{wcsa}/(10 x D x P)$*, Taking for example Ccsa and Vd of 1.6M and 500mls respectively,*

$V_{csa} = 1.6x500x116.52/(10x1.75x97) = 54.91ml$

Table ii.i: Dilution of chlorosulphonic acid

V_d(ml)	D(kg/l)	P(%)	M_{wcsa}(g/mol)	C_{csa}(M)	V_{DCE}(ml)[a]	V_{csa}(ml)	C_0(M)[b]
500	1.75	97	116.52	1.8	438	62	14.57
500	1.75	97	116.52	1.6	445	55	14.57
500	1.75	97	116.52	1.4	452	48	14.57
500	1.75	97	116.52	1.2	459	41	14.57
500	1.75	97	116.52	1	466	34	14.57
500	1.75	97	116.52	0.8	473	27	14.57
500	1.75	97	116.52	0.6	479	21	14.57
500	1.75	97	116.52	0.4	486	14	14.57
500	1.75	97	116.52	0.2	493	7	14.57
500	1.75	97	116.52	0.1	497	3	14.57
500	1.75	97	116.52	0.09	497	3	14.57
500	1.75	97	116.52	0.05	498	2	14.57

a - the volume of DCE solvent required for dilution; b – concentration of undiluted CSA

Stoichiometry of SBR Sulphonation

Let the mass of SBR dissolved in DCE, be M_{sbr}, and the %ge of styrene by weight in SBR = 23.5% (Karbochem Pty Ltd).

Therefore mass of styrene dissolved, $M_{st} = 0.235x\ M_{sbr}$

And number of moles of styrene dissolved, $n_{st} = M_{st}/M_{wst}$

Where M_{wst} = molecular weight of styrene unit = 104g/mol

Therefore $n_{st} = 0.235xM_{sbr}/M_{wst} = 0.235xM_{sbr}/104 = 0.00226M_{sbr}$

If 10g SBR is dissolved, $n_{st} = 0.0226\ x10 = 0.0226$ moles and so on.

Molar ratio, M.R = n_{csa}/n_{st}, where n_{csa} is the number of moles of chlorosulphonic acid to be added to the SBR solution in DCE.

Therefore for any given M.R, $n_{csa} = n_{st}\ x\ M.R$ (moles)

Therefore Volume of diluted acid required for sulphonation, V_{sulph} (ml), is given by;

$V_{sulph} = n_{st}\ x\ M.Rx1000/C_{csa}$ *(ml)*

E.g for M.R = 1.12, $C_{csa} = 0.09M$ and 10g SBR,

$V_{sulph} = 0.0226x1.12x1000/0.09 = 281mls$

Measurement of instantaneous Degree Of Mismatch (DOM) between CSA and Styrene moles

Experimentally, the average volume of a drop of CSA was found to be 0.084375ml. Therefore at any given concentration of chlorosulphonic acid, C_{csa}, the number of moles of acid per drop, n_{csa}, is given by;

$$n_{csa} = 0.084375xC_{csa}/1000$$

Given that the concentration of SBR solution in DCE (w/v) is given by C_{sbr} (g/l), and assuming that the volume of contact of a drop of SBR solution with CSA is equal to the volume of a drop of CSA, then;

The number of styrene units per volume of contact,

$$n_c = 0.235x\ 0.084375xC_{sbr}/(1000x104) = 0.00226x\ 0.084375xC_{sbr}/1000$$

Therefore, DOM, given by $n_{csa}/n_c = 442.5C_{csa}/C_{sbr}$

For example for 1.6M CSA and 40g/l SBR solution,

$$DOM = 442.5 \times 1.6/40 = 17.7$$

Appendix 3

Table iii.i: Dispersion data for SSBR-CNB blended at different amplitudes

Sample	Amplitude (%)	% Frequency of occurrences of Agglomerates (Estimated from SEM Images		
		60 – 100nm	100 – 200nm	>300nm
1-CNB-20	20	10	80	10
2.5-CNB-20	20	5	70	25
4-CNB-20	20	1	70	29
1-CNB-60	60	80	15	5
2.5-CNB-60	60	60	30	10
4-CNB-60	60	50	40	10
1-CNB-75	75	85	10	5
2.5-CNB-75	75	65	30	5
4-CNB-75	75	55	40	5

Appendix 4

Mechanical Testing

Testing Set Up

Maximum Force Setting = 10.624 N

Maximum Displacement = 150mm

Displacement Rate = 100μm/s

Table iv.i: Dimensions of strip specimens for nanotensile testing

Specimen	L(cm)	W(cm)	t(cm)	V(cm^3)	M(g)	ρ(g/cm^3)
S-0-1	3	0.44	0.013	0.01716	0.0205	1.19
S-0-2	3.2	0.5	0.015	0.024	0.0226	0.94
S-0-3	3	0.45	0.015	0.02025	0.0215	1.06
S-0.25-1	3	0.44	0.015	0.0198	0.0223	1.13
S-0.5-1	3	0.44	0.015	0.0198	0.0194	0.98
S-1-1	3	0.45	0.0145	0.019575	0.0221	1.13
S-1-2	3	0.44	0.015	0.0198	0.0203	1.03
S-1-3	3	0.45	0.0165	0.022275	0.0242	1.09
S-1-4	3.1	0.4	0.016	0.01984	0.0227	1.14
S-2.5-1	3	0.44	0.0135	0.01782	0.02	1.12
S-2.5-2	3	0.44	0.016	0.02112	0.0243	1.15
S-2.5-3	3	0.4	0.014	0.0168	0.02	1.19
S-2.5-4	3.1	0.4	0.015	0.0186	0.0191	1.03
S-4-1	3	0.44	0.0165	0.02178	0.0222	1.02
S-4-2	3.2	0.4	0.015	0.0192	0.0226	1.18
S-4-3	3.2	0.45	0.015	0.0216	0.024	1.11

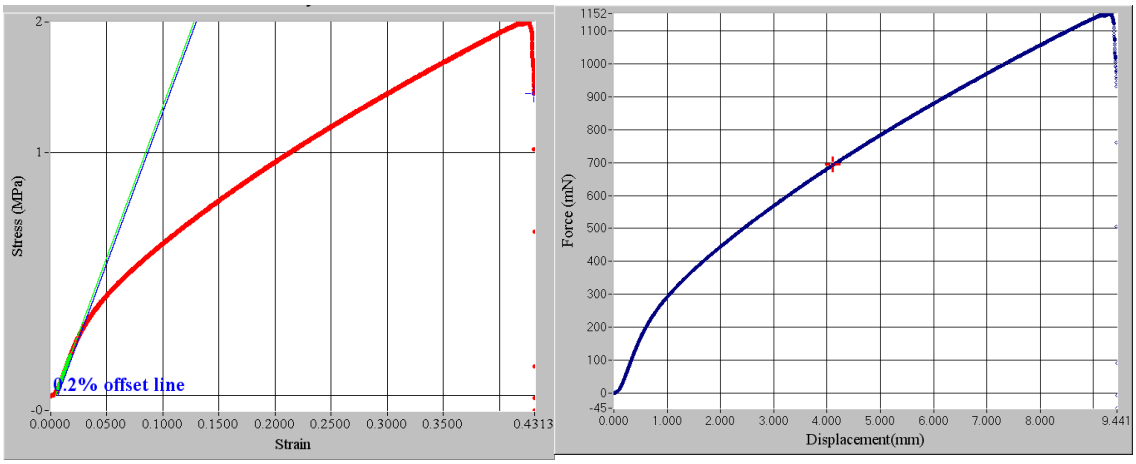


Figure iv.i: Stress- Strain and Force Displacement graphs for aged plain SSBR membranes

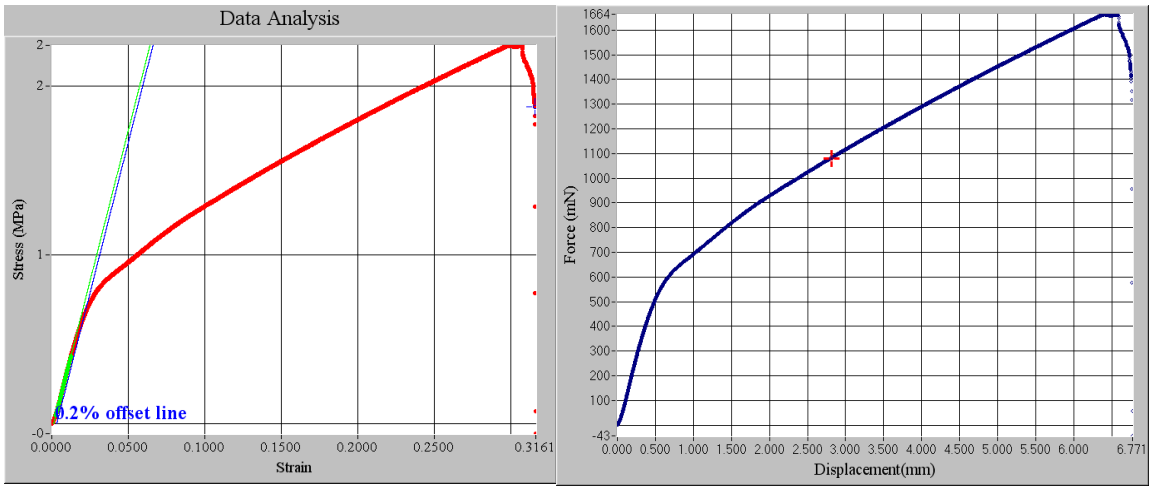


Figure iv.ii: Stress- Strain and Force Displacement graphs for aged 2.5wt% SSBR-CNB nanocomposite ion exchange membranes

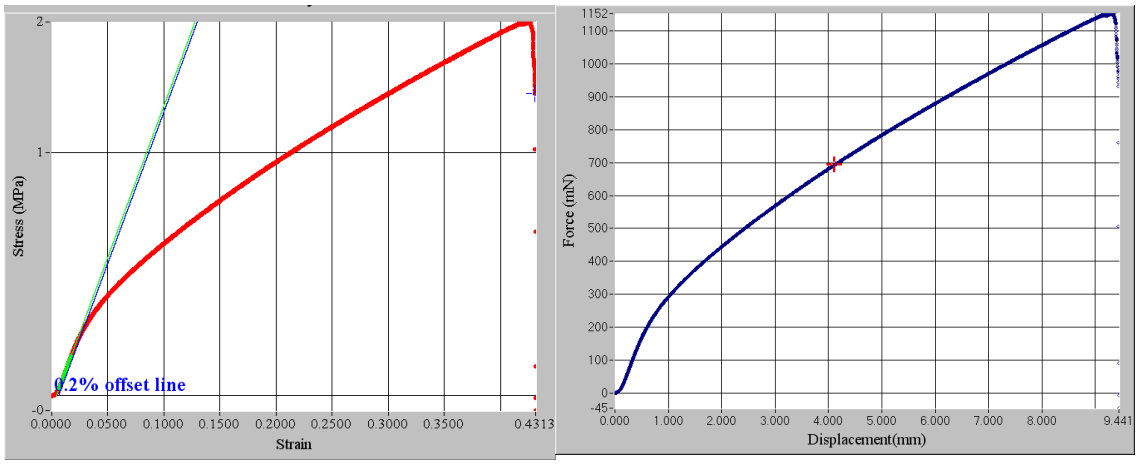


Figure iv.iii: Stress- strain and Force Displacement graphs for aged 1wt% SSBR-CNB nanocomposite ion exchange membranes

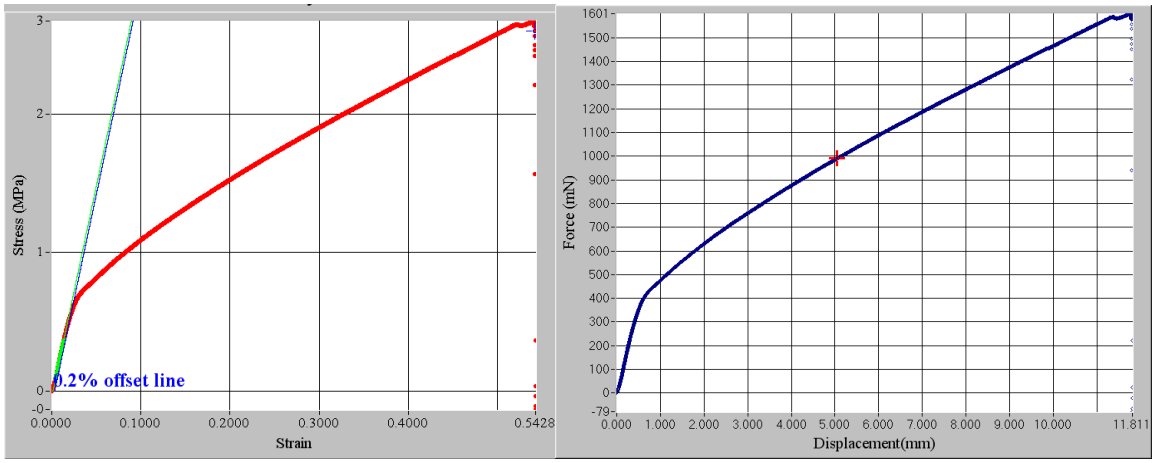


Figure iv.iv: Stress- Strain and Force Displacement graphs for aged 4wt% SSBR-CNB nanocomposite ion exchange membranes

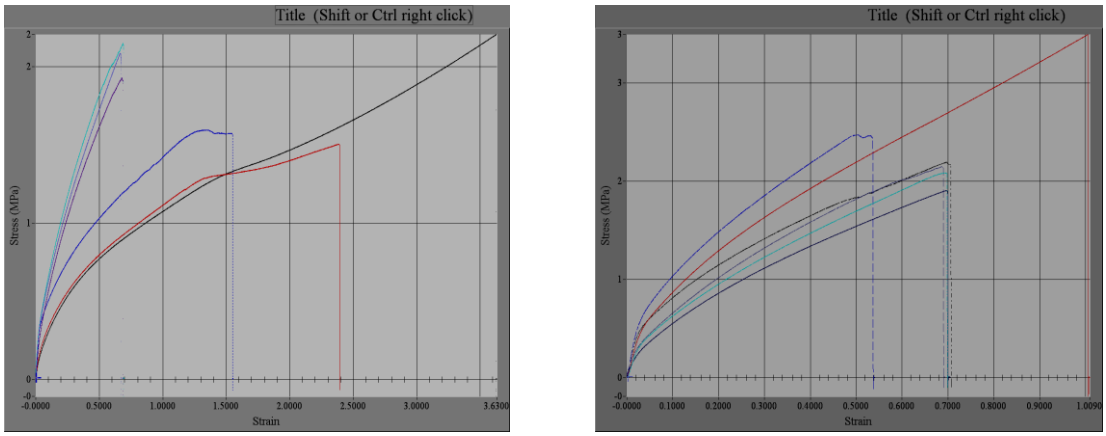
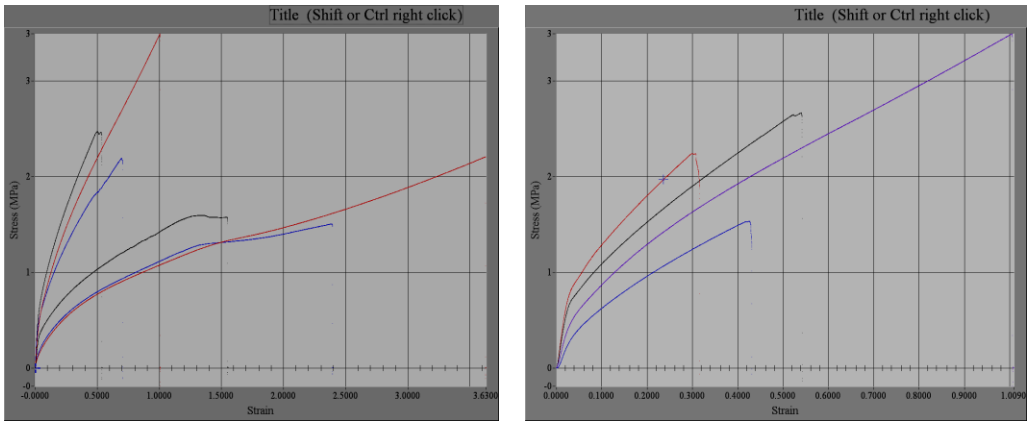


Figure iv.v: Stress- strain graphs of; a) 20% and b) 60% Amplitude SSBR-CNB nanocomposite ion exchange membrane



a) b)

Figure iv.vi: a) Comparison of Stress-Strain graphs for a) 20% and 60% amplitude of Sonication, b) different filler concentrations

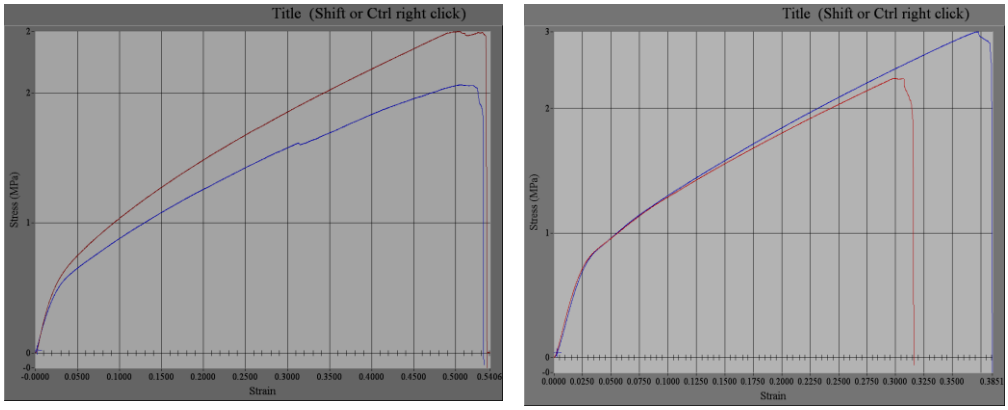


Figure iv.vii: Isotropy results (Stress-Strain) for 1wt% loaded SSBR-CNB nanocomposite ion exchange membrane

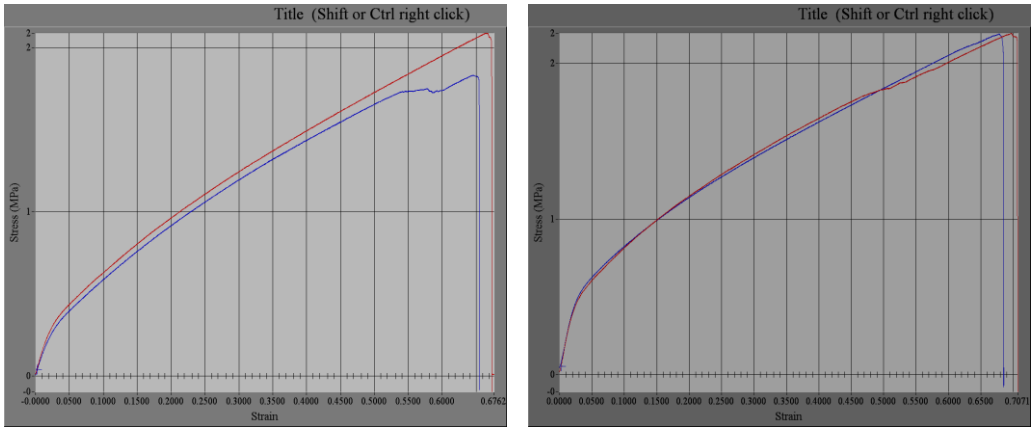
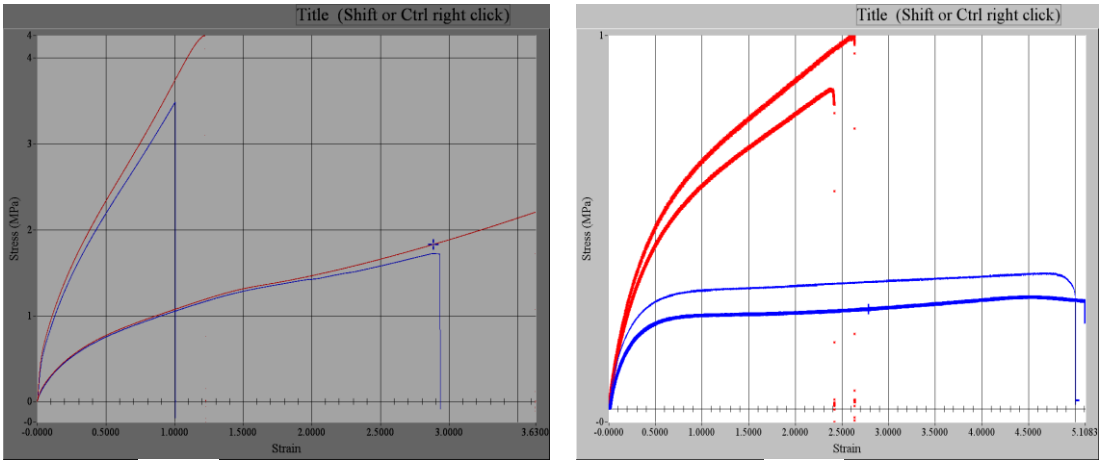


Figure iv.viii: Isotropy results (Stress-Strain) for plain SSBR membranes



a) b)

Figure iv.ix: Isotropy results on a) 2.5 and 4wt% loaded CNB, b) unsulphonated plain SBR (red) and 1wt%SBR-CNB nanocomposite (blue)

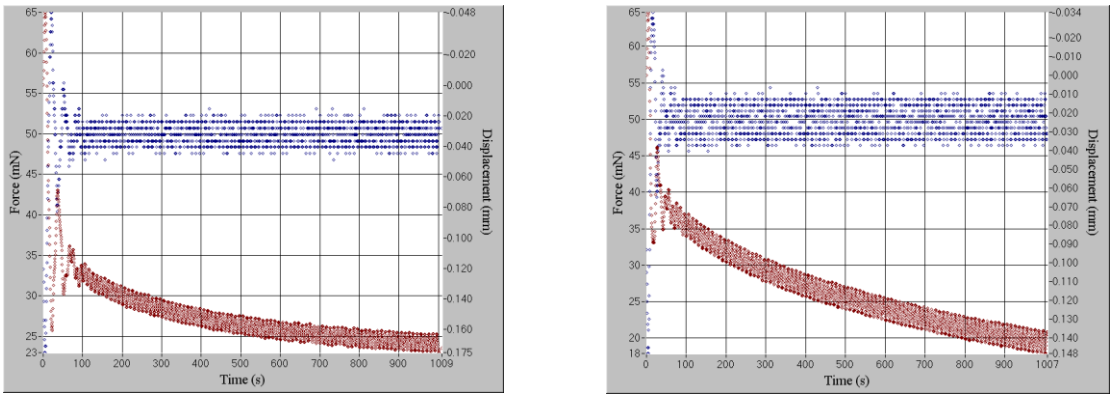


Figure iv.x: Force Time graphs of 20%A, 2.5wt% loaded SSBR-CNB IEM at 0.14MPa mean stress

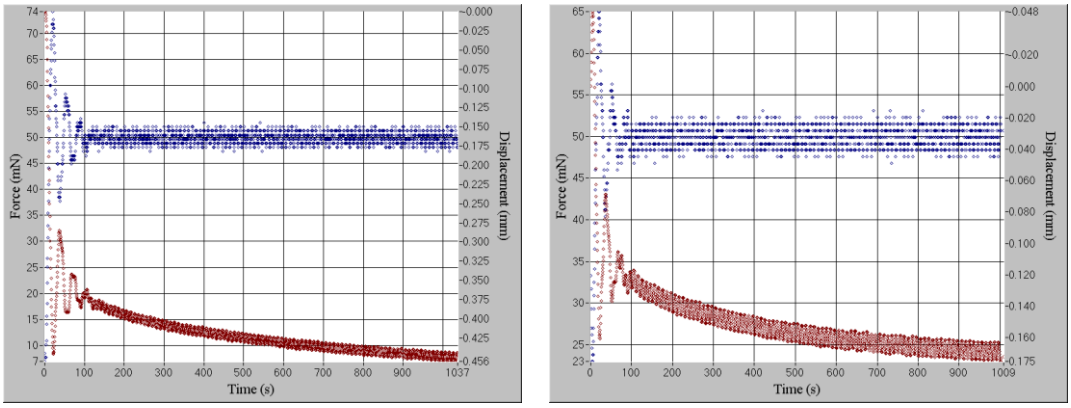
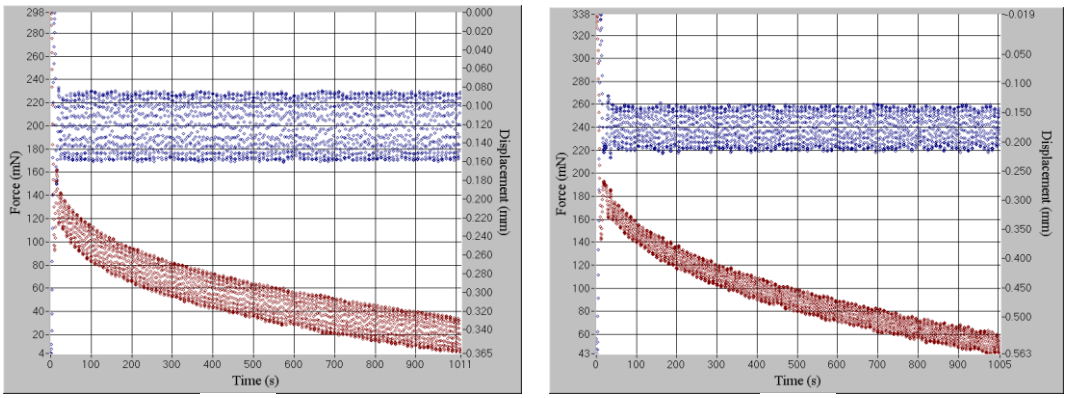


Figure iv.xi: Force Time graphs for 20%A, 1wt% loaded SSBR-CNB IEM at 0.14MPa mean stress



a) b)

Figure iv.xii: Force Time graphs for 60%A; a) 1wt% loaded SSBR-CNB IEM at 0.63MPa mean stress and b) 2.5wt% loaded SSBR-CNB IEM at 0.81MPa mean stress

Table iv.ii: Young's modulus experimental results (60% amplitude, 20 days after drying)

V_f	wt%CNB	E_1(MPa)	E_2(MPa)	E_3(MPa)	E(MPa)	Deviation	%Dev
0.000	0.00	14.02	13.28	13.84	13.71	0.29	2
0.008	0.25	14.12	14.50	14.40	14.34	0.15	1
0.017	0.50	16.89	17.43	17.13	17.15	0.19	1
0.025	0.75	21.67	21.88	22.18	21.91	0.18	1
0.033	1.00	25.01	24.32	24.40	24.58	0.29	1
0.058	1.75	21.97	22.14	22.04	22.05	0.06	0
0.086	2.50	19.56	19.42	20.21	19.73	0.32	2
0.142	4.00	20.16	20.95	19.42	20.18	0.52	3

Table iv.iii: Yield strength experimental results (60% amplitude, 20 days after drying)

V_f	wt%CNB	σ_{y1}(MPa)	σ_{y2}(MPa)	σ_{y3}(MPa)	σ_{ya}(MPa)	Deviation	%Dev
0.000	0.00	0.23	0.26	0.27	0.25	0.02	6
0.008	0.25	0.22	0.24	0.26	0.24	0.01	6
0.017	0.50	0.26	0.26	0.29	0.27	0.01	5
0.025	0.75	0.33	0.35	0.34	0.34	0.01	2
0.033	1.00	0.47	0.48	0.46	0.47	0.01	1
0.058	1.75	0.44	0.43	0.48	0.45	0.02	4
0.086	2.50	0.44	0.43	0.45	0.44	0.01	2
0.142	4.00	0.41	0.42	0.43	0.42	0.01	2

Table iv.iv: Tensile strength experimental results (60% amplitude, 20 days after drying)

V_f	wt%CNB	σ_{s1}(MPa)	σ_{s2}(MPa)	σ_{s3}(MPa)	σ_{sa}(MPa)	Deviation	%Dev
0.000	0.00	1.98	2.13	1.89	2.00	0.09	4
0.008	0.25	1.82	1.90	2.13	1.95	0.12	6
0.017	0.50	2.02	1.93	2.29	2.08	0.14	7
0.025	0.75	2.01	2.15	2.35	2.17	0.12	6
0.033	1.00	2.25	2.34	2.52	2.37	0.10	4
0.058	1.75	2.48	2.40	2.44	2.44	0.03	1
0.086	2.50	2.52	2.53	2.59	2.55	0.03	1
0.142	4.00	3.92	4.06	3.65	3.88	0.15	4

Table iv.v: Engineering strain experimental results (60% amplitude, 20 days after drying)

V_f	wt%CNB	e_{u1}	e_{u2}	e_{u3}	e_{ua}	Deviation	%Dev
0.000	0.00	0.63	0.69	0.71	0.68	0.03	4
0.008	0.25	0.57	0.66	0.72	0.65	0.05	8
0.017	0.50	0.68	0.66	0.74	0.69	0.03	5
0.025	0.75	0.63	0.71	0.70	0.68	0.03	5
0.033	1.00	0.66	0.68	0.85	0.73	0.08	11
0.058	1.75	0.69	0.73	0.80	0.74	0.04	5
0.086	2.50	0.77	0.82	0.94	0.84	0.06	7
0.142	4.00	1.13	1.10	1.11	1.11	0.01	1

Table iv.vi: Fracture toughness experimental results (60% amplitude, 20 days after drying)

V_f	wt%CNB	$U_{f.t1}$ (J/cm^3)	$U_{f.t2}$ (J/cm^3)	$U_{f.t3}$ (J/cm^3)	$U_{f.ta}$ (J/cm^3)	Deviation	%Dev
0.000	0.00	0.77	0.83	0.87	0.82	0.04	4
0.008	0.25	0.68	0.71	0.68	0.69	0.01	2
0.017	0.50	0.73	0.75	0.89	0.79	0.07	8
0.025	0.75	0.88	0.82	0.85	0.85	0.02	2
0.033	1.00	0.89	0.87	0.97	0.91	0.04	4
0.058	1.75	0.91	0.96	1.10	0.99	0.07	7
0.086	2.50	1.44	1.39	1.41	1.41	0.02	1
0.142	4.00	2.67	2.47	2.80	2.65	0.12	4

Table iv.vii: Young's modulus experimental results (20% amplitude, 20 days after drying)

V_f	wt%CNB	E_1(MPa)	E_2(MPa)	E_3(MPa)	E(MPa)	Deviation	%Dev
0.000	0.00	13.01	13.55	14.39	13.65	0.49	4
0.008	0.25	13.92	14.25	14.19	14.12	0.13	1
0.017	0.50	17.36	16.87	17.22	17.15	0.19	1
0.025	0.75	12.36	11.55	11.91	11.94	0.28	2
0.033	1.00	13.61	12.47	12.76	12.95	0.44	3
0.058	1.75	11.35	10.01	9.93	10.43	0.61	6
0.086	2.50	6.80	6.92	6.83	6.85	0.05	1
0.142	4.00	6.50	5.23	5.37	5.70	0.53	9

Table iv.viii: Yield strength experimental results (20% amplitude, 20 days after drying)

V_f	wt%CNB	σ_{y1}(MPa)	σ_{y2}(MPa)	σ_{y3}(MPa)	σ_{ya}(MPa)	Deviation	%Dev
0.000	0.00	0.25	0.24	0.27	0.25	0.01	4
0.008	0.25	0.24	0.23	0.25	0.24	0.01	3
0.017	0.50	0.27	0.28	0.26	0.27	0.01	2
0.025	0.75	0.24	0.22	0.23	0.23	0.01	3
0.033	1.00	0.25	0.23	0.27	0.25	0.01	5
0.058	1.75	0.16	0.18	0.20	0.18	0.01	7
0.086	2.50	0.11	0.12	0.15	0.13	0.01	11
0.142	4.00	0.11	0.09	0.12	0.11	0.01	10

Table iv.ix: Tensile strength experimental results (20% amplitude, 20 days after drying)

V_f	wt%CNB	σ_{s1}(MPa)	σ_{s2}(MPa)	σ_{s3}(MPa)	σ_{sa}(MPa)	Deviation	%Dev
0.000	0.00	1.95	2.02	2.03	2.00	0.03	2
0.008	0.25	1.88	1.78	2.03	1.90	0.09	5
0.017	0.50	1.92	1.77	2.06	1.92	0.10	5
0.025	0.75	2.12	2.05	2.25	2.14	0.07	3
0.033	1.00	1.48	1.67	1.40	1.52	0.10	7
0.058	1.75	1.66	1.43	1.80	1.63	0.13	8
0.086	2.50	1.48	1.55	1.49	1.51	0.03	2
0.142	4.00	1.88	1.94	2.09	1.97	0.08	4

Table iv.x: Engineering strain experimental results (20% amplitude, 20 days after drying)

V_f	wt%CNB	e_{u1}	e_{u2}	e_{u3}	e_{ua}	Deviation	%Dev
0.000	0.00	0.67	0.65	0.71	0.68	0.02	3
0.008	0.25	0.59	0.53	0.59	0.57	0.03	5
0.017	0.50	0.65	0.64	0.79	0.69	0.06	9
0.025	0.75	0.93	0.99	1.02	0.98	0.03	3
0.033	1.00	1.22	1.38	1.81	1.47	0.23	15
0.058	1.75	2.05	2.15	2.19	2.13	0.05	3
0.086	2.50	2.63	2.48	2.59	2.57	0.06	2
0.142	4.00	3.17	3.30	3.37	3.28	0.07	2

Table iv.xi: Fracture toughness experimental results (20% amplitude, 20 days after drying)

V_f	wt%CNB	$U_{f.t1}$ (J/cm^3)	$U_{f.t2}$ (J/cm^3)	$U_{f.t3}$ (J/cm^3)	$U_{f.ta}$ (J/cm^3)	Deviation	%Dev
0.000	0.00	0.78	0.86	0.89	0.84	0.04	5
0.008	0.25	0.70	0.69	0.73	0.71	0.01	2
0.017	0.50	0.75	0.84	0.89	0.83	0.05	6
0.025	0.75	1.09	1.10	1.17	1.12	0.03	3
0.033	1.00	1.66	1.63	1.53	1.61	0.05	3
0.058	1.75	2.22	2.13	2.10	2.15	0.05	2
0.086	2.50	2.77	2.80	2.80	2.79	0.01	0
0.142	4.00	4.23	4.16	4.18	4.19	0.03	1

Table iv.xii: Young's modulus experimental results (60% amplitude, 40 days after drying)

V_f	wt%CNB	E_1(MPa)	E_2(MPa)	E_3(MPa)	E(MPa)	Deviation	%Dev
0.000	0.00	12.45	12.42	12.24	12.37	0.09	1
0.008	0.25	13.87	14.11	15.04	14.34	0.47	3
0.017	0.50	19.07	18.56	17.00	18.21	0.81	4
0.025	0.75	25.32	25.11	24.69	25.04	0.23	1
0.033	1.00	33.99	34.17	34.77	34.31	0.31	1
0.058	1.75	32.36	32.28	32.35	32.33	0.03	0
0.086	2.50	28.79	30.67	30.54	30.00	0.81	3
0.142	4.00	24.97	25.06	24.97	25.00	0.04	0

Table iv.xiii: Yield strength experimental results (60% amplitude, 40 days after drying)

V_f	wt%CNB	σ_{y1}(MPa)	σ_{y2}(MPa)	σ_{y3}(MPa)	σ_{ya}(MPa)	Deviation	%Dev
0.000	0.00	0.30	0.29	0.25	0.28	0.02	7
0.008	0.25	0.31	0.33	0.32	0.32	0.01	2
0.017	0.50	0.35	0.39	0.40	0.38	0.02	5
0.025	0.75	0.54	0.48	0.54	0.52	0.03	5
0.033	1.00	0.66	0.69	0.66	0.67	0.01	2
0.058	1.75	0.62	0.63	0.58	0.61	0.02	3
0.086	2.50	0.58	0.53	0.63	0.58	0.03	6
0.142	4.00	0.44	0.51	0.52	0.49	0.03	7

Table iv.xiv: Tensile strength experimental results (60% amplitude, 40 days after drying)

V_f	wt%CNB	σ_{s1}(MPa)	σ_{s2}(MPa)	σ_{s3}(MPa)	σ_{sa}(MPa)	Deviation	%Dev
0.000	0.00	1.57	1.70	1.68	1.65	0.05	3
0.008	0.25	1.78	2.07	1.84	1.90	0.12	6
0.017	0.50	1.90	1.81	2.04	1.92	0.08	4
0.025	0.75	2.11	2.13	2.21	2.15	0.04	2
0.033	1.00	2.45	2.26	2.57	2.43	0.11	5
0.058	1.75	2.47	2.61	2.45	2.51	0.07	3
0.086	2.50	2.60	2.70	2.71	2.67	0.05	2
0.142	4.00	3.51	3.48	3.48	3.49	0.01	0

Table iv.xv: Engineering strain experimental results (60% amplitude, 40 days after drying)

V_f	wt%CNB	e_{u1}	e_{u2}	e_{u3}	e_{ua}	Deviation	%Dev
0.000	0.00	0.43	0.47	0.53	0.48	0.03	7
0.008	0.25	0.55	0.52	0.64	0.57	0.05	8
0.017	0.50	0.63	0.69	0.76	0.69	0.04	6
0.025	0.75	0.49	0.67	0.67	0.61	0.08	13
0.033	1.00	0.33	0.42	0.29	0.35	0.05	14
0.058	1.75	0.61	0.55	0.61	0.59	0.03	5
0.086	2.50	0.51	0.47	0.65	0.54	0.07	13
0.142	4.00	0.66	0.69	0.73	0.69	0.03	4

Table iv.xvi: Fracture toughness experimental results (60% amplitude, 40 days after drying)

V_f	wt%CNB	$U_{f.t1}$ (J/cm^3)	$U_{f.t2}$ (J/cm^3)	$U_{f.t3}$ (J/cm^3)	$U_{f.ta}$ (J/cm^3)	Deviation	%Dev
0.000	0.00	0.46	0.47	0.53	0.49	0.03	5
0.008	0.25	0.73	0.69	0.70	0.71	0.02	2
0.017	0.50	0.81	0.77	0.90	0.83	0.05	6
0.025	0.75	0.77	0.75	0.82	0.78	0.03	3
0.033	1.00	0.85	0.83	0.84	0.84	0.01	1
0.058	1.75	0.87	0.90	0.81	0.86	0.03	4
0.086	2.50	0.96	0.88	0.98	0.94	0.04	4
0.142	4.00	0.97	0.99	1.14	1.03	0.07	7

Table iv.xvii: Effect of amplitude of sonication on mechanical properties

V_f	E(MPa)			σ_y(MPa)			σ_s(MPa)			e_u			$U_{f.t}$(J/cm^3)		
	20% A	60%A	75%A	20% A	60%A	75%A	20% A	60%A	75%A	20% A	60%A	75%A	20% A	60%A	75%A
0.000	14	14	16	0.25	0.25	0.25	2.0	2.0	2.1	0.68	0.68	0.73	0.8	0.8	1.0
0.008	14	14	15	0.24	0.24	0.25	1.9	2.0	2.0	0.57	0.65	0.78	0.7	0.7	0.9
0.017	17	17	16	0.27	0.27	0.28	1.9	2.1	2.2	0.69	0.69	0.83	0.8	0.8	1.1
0.025	12	22	22	0.23	0.34	0.36	2.2	2.2	2.3	0.98	0.68	0.87	1.1	0.9	1.2
0.033	13	25	25	0.25	0.47	0.48	1.5	2.4	2.4	1.47	0.73	0.99	1.6	0.9	1.4
0.058	10	22	22	0.18	0.45	0.47	1.6	2.5	2.5	2.13	0.74	1.15	2.2	1.0	1.5
0.086	7	20	21	0.13	0.44	0.44	1.5	2.6	2.6	2.57	0.84	1.23	2.8	1.4	1.8
0.142	6	20	20	0.11	0.42	0.43	2.0	3.9	3.8	3.28	1.11	1.41	4.2	2.7	2.9

Table iv.xviii: Effect of age on SSBR nanocomposite ion exchange membrane

V_f	E(MPa)		σ_y(MPa)		σ_s(MPa)		e_u		$U_{f.t}$(J/cm^3)	
	20dys	40dys	20dys	40dys	20dys	40dys	20dys	40dys	20dys	40dys
0.000	13.71	12.37	0.25	0.28	2.00	1.65	0.68	0.48	0.82	0.49
0.008	14.34	14.34	0.24	0.32	1.95	1.90	0.65	0.57	0.69	0.71
0.017	17.15	18.21	0.27	0.38	2.08	1.92	0.69	0.69	0.79	0.83
0.025	21.91	25.04	0.34	0.52	2.17	2.15	0.68	0.61	0.85	0.78
0.033	24.58	34.31	0.47	0.67	2.37	2.43	0.73	0.35	0.91	0.84
0.058	22.05	32.33	0.45	0.61	2.44	2.51	0.74	0.59	0.99	0.86
0.086	19.73	30.00	0.44	0.58	2.55	2.67	0.84	0.54	1.41	0.94
0.142	20.18	25.00	0.42	0.49	3.88	3.49	1.11	0.69	2.65	1.03

Table iv.xix: % Change in reinforcement property with age (20 days to 40days)

V_f	ΔE	$\Delta\sigma_y$	$\Delta\sigma_s$	Δe_u	$\Delta U_{f.t}$
0	-10%	12%	-18%	-29%	-40%
0.008	0%	33%	-3%	-12%	3%
0.017	6%	41%	-8%	0%	5%
0.025	14%	53%	-1%	-10%	-8%
0.033	40%	43%	3%	-52%	-8%
0.058	47%	36%	3%	-20%	-13%
0.086	52%	32%	5%	-36%	-33%
0.142	24%	17%	-10%	-38%	-61%

Table iv.xx: Comparison of experimental profile for Young's modulus with existing models

wt%CNB	V_f	E(MPa)	Einstein	Guth	Mooney	Thomas	Frankie-A	Quemada	Nielsen	Kerner
0	0.00	13.7	13.7	13.7	13.7	13.7	13.7	13.7	13.7	13.7
0.25	0.01	14.3	14.0	14.0	14.0	14.0	18.5	14.0	14.0	14.0
0.5	0.02	17.2	14.3	14.3	14.3	14.4	20.2	14.3	14.3	14.3
0.75	0.02	21.9	14.6	14.7	14.6	14.7	21.6	14.6	14.6	14.6
1	0.03	24.6	14.8	15.0	14.9	15.0	22.8	14.9	14.9	14.8
1.75	0.06	22.1	15.7	16.4	16.1	16.3	26.3	15.9	15.9	15.8
2.5	0.09	19.7	16.7	18.1	17.6	17.8	29.9	17.2	17.1	16.8
4	0.14	20.2	18.6	22.5	21.6	21.7	37.5	20.3	19.8	19.2

Table iv.xxi: Comparison of experimental profile for tensile strength with existing models

wt%CNB	V_f	$\sigma_{s20\%}$(MPa)	$\sigma_{s60\%}$(MPa)	Nielsen	Nicolais and Narkis
0	0.00	2.00	2.00	2.00	2.00
0.25	0.01	1.90	1.95	1.92	1.90
0.5	0.02	1.92	2.08	1.87	1.84
0.75	0.02	2.14	2.17	1.83	1.79
1	0.03	1.52	2.37	1.80	1.75
1.75	0.06	1.63	2.44	1.70	1.64
2.5	0.09	1.51	2.55	1.61	1.53
4	0.14	1.97	3.88	1.46	1.34